Heriot-Watt University, Edinburgh UK

Doctoral Thesis

Temperature control in a multi-tubular fixed bed Fischer-Tropsch reactor using encapsulated phase change materials

Author:
Ademola O. Odunsi

Supervisors:
Dr. Tadhg S. O'Donovan &
Prof. David A. Reay

A thesis submitted in partial fulfilment of the requirements for the degree of Doctor of Philosophy

in the

Department of Chemical Engineering
School of Engineering and Physical Sciences

January 2017

Declaration of Authorship

I, Ademola O. Odunsi, declare that this thesis titled, 'Temperature control in a multi-tubular fixed bed Fischer-Tropsch reactor using encapsulated phase change materials ' and the work presented in it are my own. I confirm that:

- This work was done wholly or mainly while in candidature for a research degree at this University.
- Where any part of this thesis has previously been submitted for a degree or any other qualification at this University or any other institution, this has been clearly stated.
- Where I have consulted the published work of others, this is always clearly attributed.
- Where I have quoted from the work of others, the source is always given. With the exception of such quotations, this thesis is entirely my own work.
- I have acknowledged all main sources of help.
- Where the thesis is based on work done by myself jointly with others, I have made clear exactly what was done by others and what I have contributed myself.

Signed: _____

Date: _____

"The time to begin writing an article is when you have finished it to your satisfaction. By that time you begin to clearly and logically perceive what it is that you really want to say.

Mark Twain, Notebook (1902-1903)

Abstract

The Fischer-Tropsch synthesis is a highly exothermic, indirect, catalytic, gas (syngas) liquefaction chemical process. Temperature control is particularly critical to the process in order to ensure longevity of the catalyst, optimise the product distribution, and to ensure thermo-mechanical reliability of the entire process. This thesis proposes and models the use of encapsulated, phase change material, in conjunction with a supervisory temperature control mechanism, as diluents for the catalytic, multi-tubular fixed bed reactor in order to help mitigate the heat rejection challenges experienced in the process. The modelling was done using the Finite Element Analysis (FEA) software, COMSOL Multiphysics. In the main, three studies were considered in this thesis.

In the first study, a two dimensional quasi-homogeneous, reactor model, without and with the dissipation of the enthalpy of reaction into a near isothermal phase change material (silica encapsulated tin metal) heat sink, in a wall-cooled, single-tube fixed bed reactor was implemented and the results were presented. The encapsulated phase change material was homogeneously mixed with the active catalyst pellets. The thermal buffering provided by the phase change material were found to induce up to 7% increase in selectivity towards the C_{5+} and a 2.5% reduction in selectivity towards CH_4. Although there was a reduction in the conversion per pass of the limiting reactant and hydrocarbon productivity due to a reduction in reactor temperature, it was observed that for a unit molar reduction in the productivity of C_{5+}, there was a corresponding 1.5 moles reduction in methane production.

In the second study, a modified, one dimensional, α-model was derived which accounted for the heat sink effect of the phase change material diluent. The resulting, less computationally cumbersome, yet sufficiently accurate model was benchmarked against the more rigorous two-dimensional quasi-homogeneous model in order to check its fidelity in predicting the reactor performance. As in the first case study, a homogeneous distribution of the phase change material and active catalyst pellets was assumed. The α-model was able to approximate the reactor temperature profile of the 2D-quasi-homogeneous reactor model to within 4% error, and consistently, slightly over-predicted the limiting reactant conversion by about 3%. Based on these comparisons, the α-model was deemed sufficiently accurate to predict the reactor performance in place of the 2D model for the optimisation simulation in the third study.

The third case study entailed simultaneously maximising the production of long chain hydrocarbon molecules and ensuring proper heat rejection from the reacting system, two desirable yet often conflicting operational requirements. The homogeneous distribution of the active catalyst pellets and the phase change material diluents was abandoned for a

multi-zonal axial distribution in which, individual zones of the catalyst bed were diluted to varying extents. The best dilution and distribution "recipe" was determined using optimisation techniques and the previously derived modified α-model. The multi-zonal axial dilution of the catalyst bed brought about a marked increase (up to 19%) in the productivity of the long chain hydrocarbons, while ensuring a more judicious use of the catalyst bed in contrast to the homogeneous catalyst/phase change material arrangement in the previous two studies. The latent enthalpy of the metallic phase change material combined with its good thermal conductivity helped push the limits of the catalyst bed by increasing the conversion per pass beyond the typical 20-30% reported in literature, with less likelihood of either early catalyst deactivation or thermal unreliability of the reacting system.

In the main, it was observed that the overall productivity of the desired C_{5+} could be enhanced by reducing the quantity of the catalyst pellets by a pre-defined reactor volume. In addition, the reactor productivity benefits from a highly active zone situated at the reactor entrance, immediately followed by a less reactive zone. This arrangement has the effect of ramping the reaction rate (and in effect the reactor temperature) early on, and this is kept in check by the less reactive zone immediately adjacent to the reactive one at the reactor entrance.

Acknowledgements

I wish to express my sincerest thanks and gratitude to my supervisors, Dr. Tadhg S. O'Donovan and Professor David A. Reay for their invaluable and very useful advice and guidance, which contributed substantially to the successful birthing of this thesis.

I am extremely thankful to both of my parents, and my siblings who believed in me and gave me the opportunity to further my education. Your love and sacrifice are peerless.

Finally, I will like to thank all my former colleagues at work in Aberdeen, and friends at the Anglican Cathedral in Aberdeen: Your encouragement and perfectly timed social breaks are greatly appreciated.

ACADEMIC REGISTRY
Research Thesis Submission

Name*:*	Ademola O. Odunsi		
School:	Engineering and Physical Sciences		
Version: *(i.e. First, Resubmission, Final)*	Final	Degree Sought:	PhD (Chemical Engineering)

Declaration

In accordance with the appropriate regulations I hereby submit my thesis and I declare that:

1) the thesis embodies the results of my own work and has been composed by myself
2) where appropriate, I have made acknowledgement of the work of others and have made reference to work carried out in collaboration with other persons
3) the thesis is the correct version of the thesis for submission and is the same version as any electronic versions submitted*.
4) my thesis for the award referred to, deposited in the Heriot-Watt University Library, should be made available for loan or photocopying and be available via the Institutional Repository, subject to such conditions as the Librarian may require
5) I understand that as a student of the University I am required to abide by the Regulations of the University and to conform to its discipline.
6) I confirm that the thesis has been verified against plagiarism via an approved plagiarism detection application e.g. Turnitin.

* *Please note that it is the responsibility of the candidate to ensure that the correct version of the thesis is submitted.*

Signature of Candidate*:*	A.O. Odunsi	Date:	6th February 2017

Submission

Submitted By *(name in capitals):*	ADEMOLA O. ODUNSI
Signature of Individual Submitting:	A.O. Odunsi
Date Submitted:	6th February 2017

For Completion in the Student Service Centre (SSC)

Received in the SSC by *(name in capitals):*			
Method of Submission *(Handed in to SSC; posted through internal/external mail):*			
*E-thesis Submitted (**mandatory for final theses)***			
Signature:		Date:	

Please note this form should be bound into the submitted thesis.
Academic Registry/Version (1) August 2016

List of Publications

Published papers

(1) Odunsi, A.O., O'Donovan, T.S., Reay, D.A. Temperature Stabilisation in Fixed Bed Fischer-Tropsch reactors using Phase change Material (PCM) *Applied Thermal Engineering*, 93: 1377-1393, 2016

(2) Odunsi, A.O., O'Donovan, T.S., Reay, D.A. Dynamic Modelling of Fixed Bed Fischer-Tropsch Reactors with Phase Change Material Diluents *Chemical Engineering & Technology*, 2016

Papers under Peer Review

(1) Odunsi, A.O., O'Donovan, T.S., Reay, D.A. Optimal Distribution of Phase Change Diluents and Catalysts in Tubular Fischer-Tropsch Reactors *Chemical Engineering & Technology*, 2016

Conferences attended

(1) 13$^{\text{th}}$United Kingdom Heat Transfer Conference held at Imperial College London, September 2013

(2) 1$^{\text{st}}$ Chemistry in Energy Conference held at Heriot-Watt University, Edinburgh, July 2015

(3) 14$^{\text{th}}$ United Kingdom Heat Transfer Conference Edinburgh, September 2015

(4) European Symposium on Chemical Reaction Engineering (ESCRE), Veranstaltungsforum Fürstenfeld, Fürstenfeldbruck (nearby Munich), Germany October 2015

Contents

List of Figures

List of Tables

Abbreviations

ARGE	**AR**beits**GE**meinschaft (consortium) Ruhrchemie/Lurgi
ASF	**A**nderson **S**chulz **F**lory
BDF	**B**ackward **D**ifferential **F**ormula
BTL	**B**iomass **T**o **L**iquid
CFB	**C**irulating **F**luidised **B**ed reactor
CTL	**C**oal **T**o **L**iquid
FEA	**F**inite **E**lement **A**nalysis
FFB	**F**ixed **F**luidised **B**ed reactor
FTS	**F**ischer **T**ropsch **S**ynthesis
GCI	**G**rid **C**onvergence **I**ndex
GTL	**G**as **T**o **L**iquid
GHSV	**G**as **H**our **S**pace **V**elocity
HTFT	**H**igh **T**emperature **F**ischer **T**ropsch
LPG	**L**iquefied **P**etroleum **G**as
LHHW	**L**angmuir **H**inshelwood **H**ougen **W**atson
LTFT	**L**ow **T**emperature **F**ischer **T**ropsch
MTFBR	**M**ulti **T**ubular **F**ixed **B**ed **R**eactor
PCM	**P**hase **C**hange **M**aterial
PID	**P**roportional **I**ntegral **D**ifferential
PTT	**P**hase **T**ransition **T**emperature
QP	**Q**uadratic **P**rogramming
SBC	**S**lurry **B**ubble **C**olumn reactor
SQP	**S**equential **Q**uadratic **P**rogramming
STP	**S**tandard **T**emperature and **P**ressure
WGS	**W**ater **G**as **S**hift

TES	**T**hermal **E**nergy **S**torage
TP	**T**rigonal **P**rismatic
XTL	**X** **T**o **L**iquid

Physical Constants

Acceleration due to gravity	g	=	$9.81\,\mathrm{m\,s^{-2}}$
Mathematical constant	π	=	3.14159
Universal molar gas constant	R_g	=	$8.31446\,\mathrm{J\,(mol\,K)^{-1}}$

Symbols

A	α-model Taylor's expansion parameter	$[\mathrm{K}^{-1}]$
a	Adsorption constant	[-]
A_c	Cross sectional area	$[\mathrm{m}^2]$
a_0	Adsorption pre-exponential factor	$[\mathrm{mol}^{1-n}\mathrm{m}^{3n}\mathrm{kg}^{-1}\mathrm{s}^{-1}]$
$A_\mathrm{p,ex}$	External surface area of catalyst pellet	[m]
B	α-model Taylor's expansion parameter	$[\mathrm{K}^{-2}]$
Bi_w	Thermal Biot number at the wall	[-]
c	Molar concentration	$[\mathrm{mol\,m}^{-3}]$
$\overline{\mathbf{c}}$	Vector of average concentrations of reactants and products	$[\mathrm{mol\,m}^{-3}]$
c_mol	Total molar feed concentration	$[\mathrm{mol\,m}^{-3}]$
C_p	Heat capacity of feed mixture concentration	$[\mathrm{J\,kg}^{-1}\,\mathrm{K}^{-1}]$
D	Normalised pulse function	$[^\mathrm{o}\mathrm{C}]$
Da_I	1st Damköhler number	[-]
Da_II	2nd Damköhler number	[-]
Da_III	3rd Damköhler number	[-]
D_eff	Effective diffusion coefficient of particle	$[\mathrm{m}^{-2}\mathrm{s}^{-1}]$
$D_{\mathrm{K}j}$	Knudsen diffusion coefficient for species j	$[\mathrm{m}^{-2}\mathrm{s}^{-1}]$
D_mol	Molecular diffusion coefficient	$[\mathrm{m}^{-2}\mathrm{s}^{-1}]$
D_r	Radial diffusion coefficient	$[\mathrm{m}^{-2}\mathrm{s}^{-1}]$
$D_\mathrm{r\,T}$	Molecular, radial, transition diffusion coefficient	$[\mathrm{m}^{-2}\mathrm{s}^{-1}]$
D_z	Axial diffusion coefficient	$[\mathrm{m}^{-2}\mathrm{s}^{-1}]$
d_p	Diameter of catalyst particle	[m]
d_t	Tube diameter	[m]
E_act	Activation energy	$[\mathrm{J\,mol}^{-1}]$
$\overline{E_\mathrm{act}}$	Average activation energy for a number of reactions	$[\mathrm{J\,mol}^{-1}]$

E_{eff}	Effective activation energy	$[\text{J mol}^{-1}]$
f	Friction factor	[-]
G	Superficial mass velocity	$[\text{kg m}^2\,\text{s}^{-1}]$
GHSV	Gas hour space velocity	$[\text{NmL g}_{\text{cat}}^{-1}\,\text{h}^{-1}]$
$\mathcal{H}_{\text{H}_{2,\text{c}}}$	Henry's coefficient for hydrogen in FT wax	$[\text{Pa m}^3\,\text{mol}^{-1}]$
h	Mesh size parameter	[-]
h_{s}	Interfacial heat transfer coefficient	$[\text{W m}^{-2}\,\text{K}^{-1}]$
h_{w}	Wall heat transfer coefficient	$[\text{W m}^{-2}\,\text{K}^{-1}]$
J_{cat}	Diffusive molar flux	$[\text{mol m}^{-2}\text{s}^{-1}]$
J_{int}	Interfacial molar flux	$[\text{mol m}^{-2}\text{s}^{-1}]$
K_{eq}	Reaction equilibrium constant	[-]
K_{ewg}	Water gas shift reaction equilibrium constant	[-]
K_{HW}	Coefficient of LHHW equation for FT on Fe	[-]
K_{v}	Water gas shift reaction coefficient	[-]
k	Reaction rate constant	$[\text{s}^{-1}]$
k_0	Pre-exponential factor	$[\text{mol}^{1-n}\text{m}^{3n}\text{kg}^{-1}\text{s}^{-1}]$
k_s	Interfacial mass transfer coefficient	$[\text{m s}^{-1}]$
L	Length of tube	[m]
M	Methanation reaction	[-]
MW	Molecular weight	$[\text{kg mol}^{-1}]$
N	Total number of reactions/number of catalytic zones	[-]
Nu	Nusselt number	[-]
n	Order of reaction	[-]
Pe_{r}	Radial Peclet number	[-]
$Pe_{\text{z,h}}$	Heat transfer axial Peclet number	[-]
$Pe_{\text{z,m}}$	Mass transfer axial Peclet number	[-]
p_0	Total pressure	$[\text{Nm}^{-2}]$
p_{vap}	Vapour pressure	$[\text{Nm}^{-2}]$
Pr	Prandtl number	[-]
Pt	Prater number	[-]
Q	Reaction heat energy	[J]
$\dot{Q}$	Heat flux	$[\text{Wm}^{-2}\text{K}^{-1}]$
R_{pore}	Pore radius	[m]

$\Re$	Rate of reaction	$[\mathrm{mol\,m^{-3}s^{-1}}]$
$\Re_{\mathrm{i}}^{\mathrm{m}}$	Reaction rate of reaction i per unit mass of catalyst	$[\mathrm{mol\,kg^{-1}s^{-1}}]$
$\Re_0$	Dimensionless reaction rate	[-]
R_{p}	Catalyst pellet radius	[m]
Re_{p}	Particle Reynolds number	[-]
R	Inner radius of encapsulated PCM capsule	[m]
R_{g}	Universal gas constant	$[\mathrm{J\,mol^{-1}\,K^{-1}}]$
R_{prop}	Rate of chain growth or propagation	$[\mathrm{mol\ m^{-2}\ s^{-1}}]$
R_{t}	Internal radius of reactor tube	[m]
R_{term}	Rate of chain termination	$[\mathrm{mol\ m^{-2}\ s^{-1}}]$
R_{w}	External radius of capsule	[m]
r_{SL}	Radial distance of the solid-liquid boundary	[m]
r	Radial coordinates	[m]
S_j	Selectivity of component j	[%]
Sc	Schmidt number	[-]
Sh	Sherwood number	[-]
T	Temperature	[$^{\mathrm{o}}$C]
T^*	Temperature at hotspot	[$^{\mathrm{o}}$C]
$\overline{T}$	Average temperature	[$^{\mathrm{o}}$C]
T_{m}	Fusion point of phase change material	[$^{\mathrm{o}}$C]
$T_{\mathrm{r=R_t}}$	Temperature of fluid contiguous to the wall	[$^{\mathrm{o}}$C]
$\overline{T_{\Re}}$	Reaction averaged temperature	[K]
t	time	[s]
U_{wall}	Overall heat transfer coefficient	$[\mathrm{W\,m^{-2}\,K^{-1}}]$
u_{s}	Superficial velocity	$[\mathrm{m\,s^{-1}}]$
u_{z}	Axial velocity	$[\mathrm{m\,s^{-1}}]$
$V_{\mathrm{f,\,STP}}$	Volumetric flow rate at STP	$[\mathrm{m^3\,s^{-1}}]$
$V_{\mathrm{H_2}}$	Molar volume of H_2 at normal boiling point	$[\mathrm{m^3\,kgmol^{-1}}]$
V	Volume	$[\mathrm{m^3}]$
w_i	weighted heat release for reaction i	[-]
wx_j	Mass fraction of species j	[-]
X	Conversion	[-]
x_{cn}	Molar distribution of hydrocarbon products	[-]

y_{H_2}	Mole fraction of H_2 in feed	[-]
y_{CO}	Mole fraction of CO in feed	[-]
z	Axial coordinates	[m]
α	α-model dimensionless heat loss parameter	[-]
α_{FT}	Carbon chain growth probability factor	[-]
α_{rs}	Radiation coefficient for catalyst	[$kWm^{-2}K$]
α_{rv}	Void to void radiation coefficient	[$kWm^{-2}K$]
β	Particle geometry and packing density coefficient	[-]
β_f	feed flow factor	[-]
γ	Thermal conductivity ratio coefficient	[-]
γ_{FT}	Olefins to paraffins ratio	[-]
ΔG^{θ}	Standard Gibbs free energy	[$J\,mol^{-1}$]
ΔH_{ad}	Enthalpy of adsorption	[$J\,mol^{-1}$]
ΔH_r	Enthalpy of reaction	[$J\,mol^{-1}$]
ΔS	Entropy change	[$J\,mol^{-1}$]
ΔT_{ad}	Adiabatic temperature rise	[^oC]
ϵ	Catalyst bed void fraction	[-]
η_i	Effectiveness factor for reaction i	[-]
η_{pore}	Pore effectiveness factor	[-]
Θ	Dimensionless temperature rise	[-]
Θ_{ad}	Normalised temperature (using adiabatic temperature rise)	[-]
θ	Azimuthal coordinates	[m]
κ_{cat}	Catalyst pellet thermal conductivity	[$W\,m^{-1}K^{-1}$]
$\kappa_{eff,r}$	Effective radial thermal conductivity	[$W\,m^{-1}K^{-1}$]
$\kappa_{eff,z}$	Effective axial thermal conductivity	[$W\,m^{-1}K^{-1}$]
$\kappa^0_{eff,r}$	Static effective radial thermal conductivity	[$W\,m^{-1}K^{-1}$]
κ_f	Fluid thermal conductivity	[$W\,m^{-1}K^{-1}$]
κ_{rf}	Fluid radial thermal conductivity	[$W\,m^{-1}K^{-1}$]
κ_z	Axial thermal conductivity	[$W\,m^{-1}K^{-1}$]
λ_{em}	Catalyst emissivity	[-]
μ_f	Fluid viscosity	[$kg\,m^{-1}s^{-1}$]
μ_i	Chemical potential	[$J\,mol^{-1}$]

μ_{wax}	Viscosity of Fischer-Tropsch wax	$[\text{kg m}^{-1}\text{s}^{-1}]$
$\nu_{\text{i,j}}$	Stoichiometric coefficient of component j in reaction i	[-]
ξ	Normalised bed length	[-]
ρ_{b}	Catalyst bed bulk density	$[\text{kg m}^{-3}]$
σ	Relative mass fraction of catalyst	[-]
τ	Modified residence time	[s]
Φ	Packing density factor	[-]
Φ_{obj}	Optimisation objective function	[-]
ϕ	Thiele modulus	[-]
χ_{th}	Encapsulating wall thickness	[m]
Ψ_{a}	Association parameter	[-]
ψ	Liquid melt fraction	[-]
ω_{r}	Ratio by mass of catalyst to phase change material	[-]
$\in$	Is a member/an element of a set	[-]

Subscripts and superscripts

α	Alpha model	[-]
abs	Absorbed	[-]
ad	Adiabatic	[-]
av	Average	[-]
cat	Catalyst	[-]
cr	Critical	[-]
CO_{g}	Gaseous carbon monoxide	[-]
CO_2	Carbon dioxide	[-]
dif	Diffusion	[-]
eff	Bulk fluid phase	[-]
f	Bulk fluid phase	[-]
fus	Fusion	[-]
g	Gas phase	[-]
H_2O	Water	[-]
$\text{H}_{2\text{g}}$	Gaseous hydrogen	[-]
i	Reaction index	[-]

int	Internal	[-]
in, cool	Feed and/or coolant	[-]
intf	Interfacial	[-]
j	Chemical species j	[-]
max	Maximum	[-]
obs	Observed	[-]
out	Outer	[-]
p	Catalyst pellet	[-]
react	Reactor	[-]
rxn	Reaction	[-]
vap	vaporisation	[-]
w	Wall	[-]
wax	Wax	[-]

***To Father, Son and Holy Ghost**:*

"Oh how shall words, with equal warmth,
The gratitude declare,
That glows within my ravished heart:
But Thou canst read it there."

"Through all eternity to Thee
A joyful song I'll raise;
For, oh, eternity's too short
To utter all Thy praise!"

ADDISON, J. (1712; CH. 169)

Chapter 1

Introduction

"Begin at the beginning," the King said gravely, "and go on till you come to the end; then stop."

Lewis Caroll, Alice in Wonderland.

The Fischer-Tropsch synthesis, a strongly exothermic, indirect, catalytic gas (synthesis gas or syngas) liquefaction process is set to play a crucial role in the supply of clean and sustainable liquid fuel and petrochemical feedstock for the future. The Fischer-Tropsch process is able to convert greenhouse gases such as methane and carbon dioxide into useful liquid fuels and starting materials for the production of other useful chemical products. The intermediate synthesis gas which serves as feed for the Fischer-Tropsch reaction is usually produced from the gassification of biomass or the reforming of natural gas. A schematic of a generic Fischer-Tropsch process and production of synthesis gas via gassification is depicted in Figure 1.1[1]. The BP Plc. 2016 global energy outlook to 2035 [2] highlights three key features in its consideration of how the energy landscape might evolve over the next twenty years:

(i) There will be a continued increase in global energy requirements as a concomitant of, and commensurate with the growth in the world's population over the next twenty years in order to enable economic prosperity.

(ii) The world's fuel mix is on a sliding scale. Fossil fuels, and in particular gas, look set to continue to be the dominant source of energy (supplying up to 60% of energy increase out to 2035). Renewables are however growing rapidly (with their share in primary energy source increasing from 3% in 2016 to 9% in 2035, see Figure 1.2) owing to their falling costs and pledges made for their widespread adoption at the 2016 Paris climate change conference.

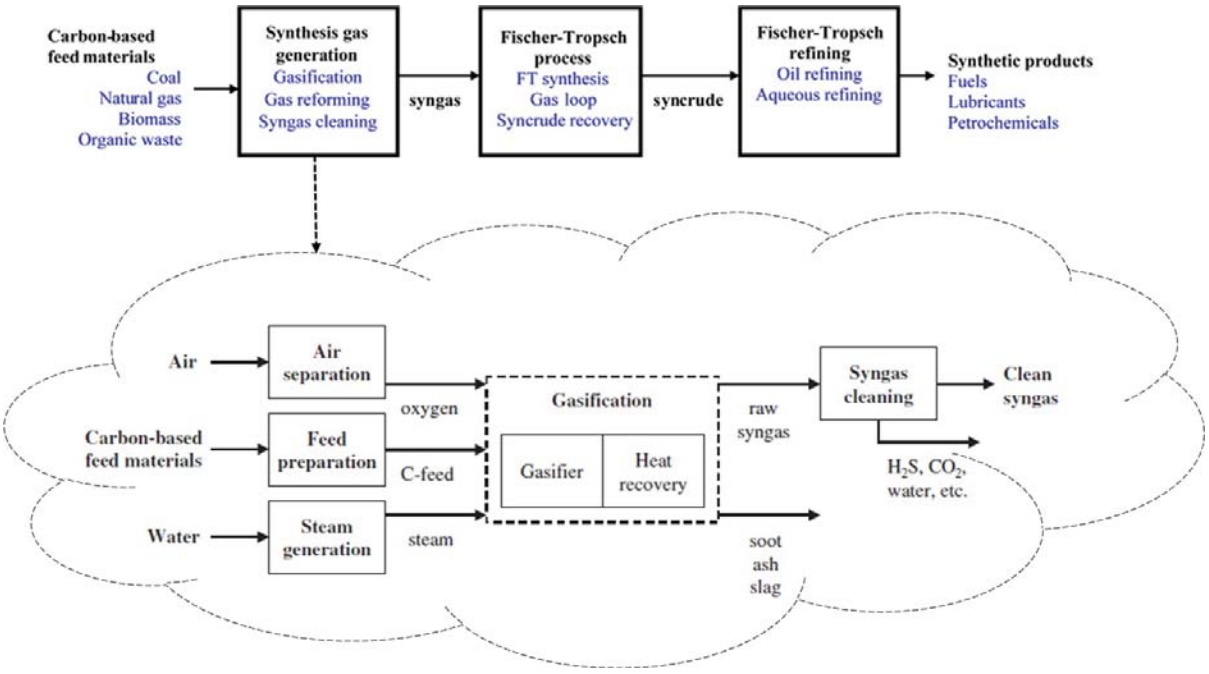

FIGURE 1.1: A generic indirect liquefaction process using the Fischer-Tropsch synthesis and production of syngas through the gassification of a solid precursor [1]

(iii) The rate of growth of carbon emissions are expected to halve over the outlook period (2016-2035) in comparison to the previous twenty years. This is as a result of improved energy efficiencies and a change in taste from higher to lower carbon fuels.

The Fischer-Tropsch synthesis technology is well placed to play important roles in each of the three key features outlined by BP. On the first point, as energy needs rise with increasing population, and as petroleum resources dwindle, the Fischer-Tropsch synthesis technology is stood in good stead to provide an alternative, i.e. synthetic crude oil (syncrude) which can be refined into liquid fuels and petrochemical feedstock. In the second feature, the flexibility of the Fischer-Tropsch process makes it an ideal vehicle for utilising the various energy sources. In a wider sense, the Fischer-Tropsch synthesis lends itself to a variety of traditional precursors including, stranded/shale/associated/flared/-natural gas, and renewable feedstock such as: waste organic matter, waste plastics and more latterly, CO_2 [3]. On the third point raised by BP, more recent applications of the Fischer-Tropsch have seen the intensification of the process. Small scale plants including bio-refineries are being developed by companies such as Velocys® [4], which could provide for "on-demand" liquid fuel from what might otherwise be stranded or underutilised local resources. In addition, the fuel obtained from the Fischer-Tropsch process is ultra-clean, being devoid of nitrogen based compounds, aromatics, sulphur, particulates, etc. This quality of being able to produce ultra-pure fuels gives the technology an edge and

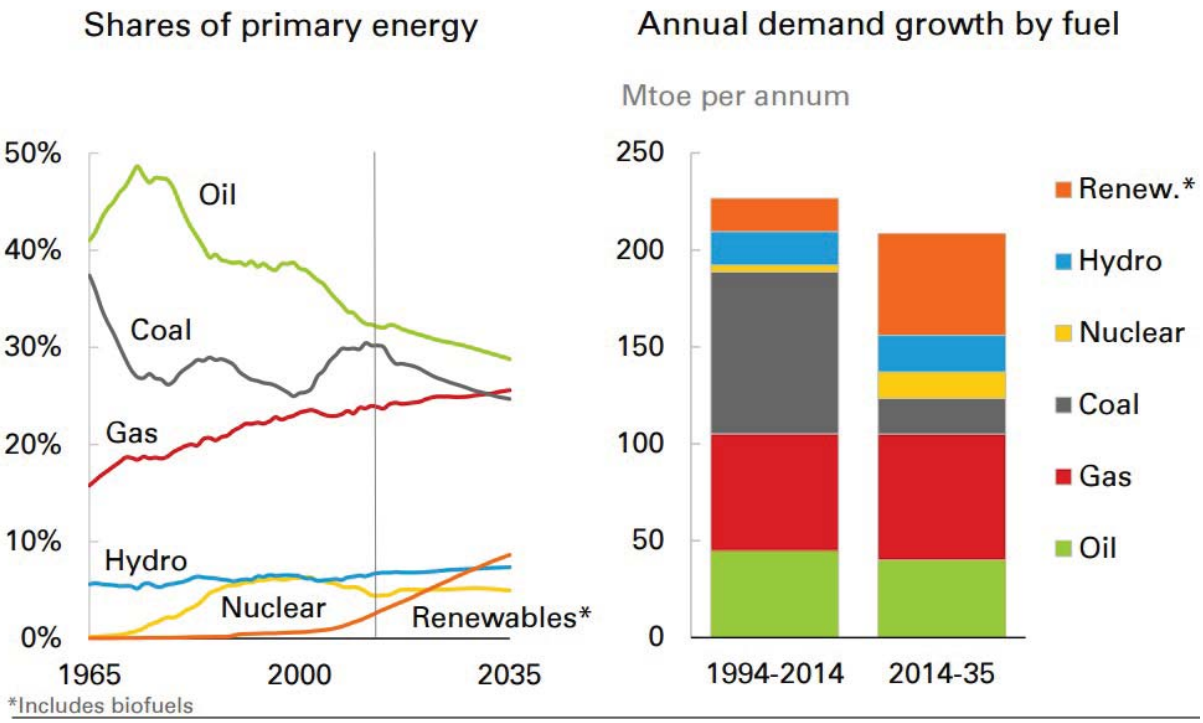

FIGURE 1.2: Historical and predicted future share of primary energy and annual demand growth by fuel to 2035 [2]

puts it in a place where it is able to meet the present and future strict environmental policies and changing tastes in energy sources.

Based on this report, the Fischer-Tropsch synthesis has the potential of not only straddling but bridging the present and the future of the world's energy use. A useful maxim therefore is that, improvements to the Fischer–Tropsch synthesis are desirable, possible, and necessary and should be developed as soon as practicable.

1.1 Fischer-Tropsch synthesis and temperature control

Ordinarily, the production of liquid fuels, lubricants, petrochemical feedstock, etc., is less capital intensive and complex starting from conventional crude oil relative to the Fischer-Tropsch process. There are however, a number of circumstances under which the Fischer-Tropsch process becomes attractive:

(i) There has latterly been a deliberate determination across the globe to shift away from petroleum to more sustainable sources of energy. This "shift" has seen a recent resurgence of interest in the Fischer-Tropsch technology. The process may be viewed as a useful transition from total dependence on petroleum to total dependence on zero-carbon energy sources such as solar, wind, etc. It is also pertinent

to state that the Fischer-Tropsch process will continue to be relevant even upon complete transition to zero carbon as there is the need to continue to produce petrochemical precursors for the production of important chemicals and materials used daily such as plastics, polymers, etc. In fact, as at 2015, the estimated, annual worldwide production of chemicals and liquid fuels via the Fischer-Tropsch process was put at about 30 million tonnes [5].

(ii) Every nation is intent on achieving energy independence; however, not all are endowed with petroleum resources. Such nations may however possess other carbonaceous energy sources including coal, agricultural waste, etc. It may become attractive for such nations under these circumstances to embark on the Fischer-Tropsch technology to produce fuels which may arguably be more economical, compared to the importation of fuels, which otherwise, renders them vulnerable to fluctuating oil prices and political instability in the countries from which the imported fuels derive. It will be recalled that historically, the strategic benefit of energy independence was the impetus for the industrial implementation of the Fischer-Tropsch process in Germany during the world wars and in Apartheid South Africa.

(iii) The Fischer-Tropsch synthesis technology also makes "stranded" and under-utilised energy resources more economically attractive as sources of liquid fuels. Stranded energy resources refer to those potential energy sources such as associated natural gas, flared natural gas, agricultural waste, etc., which are geographically and/or economically far removed from energy markets. The Fischer-Tropsch technology is able to add value to these low energy density raw materials by converting them to high volumetric energy density products, which makes their transportation more efficient and without the need for expensive transportation infrastructure [1].

Central to the Fischer-Tropsch synthesis is the economic incentive of the process, i.e., it must be able to convert low energy density raw materials to a high value spectrum of products (usually long chain hydrocarbon molecules). It is therefore important that the reactor conditions must be such that they favour the production of these high end products; it is also important that the reactor is maintained within this regime for the preponderance of its on-stream time. Locating and staying within the optimal conditions of the Fischer-Tropsch synthesis entails a consistent attempt to balance out competing forces, including: the operating conditions (temperature, pressure, gas hour space velocity (GHSV), etc.) and the factors controlling them such as: catalyst properties and reactor structure.

The available Fischer-Tropsch technologies differ principally on the bases of catalyst type, reactor type and operating temperature. Of these distinguishing characteristics,

TABLE 1.1: Influence of some process conditions on the selectivity characteristics of the Fischer-Tropsch Synthesis (adapted from Schulz[6]and Röper [7]). Key: ↑: increase; ↓: decrease and *: complex relationship

	Chain growth probability (α_{FT})	Olefin/Paraffin ratio	Carbon deposition	Methane selectivity
Temperature (↑)	↓	↓	↑	↑
Pressure (↑)	↑	*	*	↓
H_2/CO ratio (↑)	↓	↓	↓	↑
Conversion (↑)	*	↓	↑	↑
Space velocity (↑)	*	↑	*	↓
Alkali content (Fe-catalyst) (↑)	↑	↑	↑	↓

the temperature is the most influential property on the composition of the Fischer-Tropsch syncrude [1]. The dominant and possibly detrimental effects of a sustained increase in reaction temperature on the Fischer-Tropsch synthesis are borne out in table 1.1. These detrimental effects include: (i) a reduction in the value of the carbon chain growth probability factor (α_{FT}), i.e. ability of the carbon atoms to catenate and form long chain molecules, (ii) an increased tendency of carbon laydown- a process which clogs the catalyst active sites and prevents further reaction and, (iii) an increased production of methane gas, an undesired product.

The cardinal challenge experienced in the design of Fischer-Tropsch reactors is the combination of the high enthalpy of reaction ($-152\text{kJ mol}^{-1}\text{H}_2$, with an adiabatic temperature rise, $\Delta T_{ad} \geq 1600\text{K}$) and the high sensitivity of the product selectivity to the prevalent reactor temperature. It is thus crucial to ensure that the Fischer-Tropsch reactor has a well-designed heat rejection mechanism [5, 8]. This requirement for excellent heat removal has inspired the wide variety of Fischer-Tropsch reactor designs available on the market today such as: the multi-tubular fixed bed [9–12], fluidised beds (circulating and fixed) [9, 10], slurry/bubble phase [9, 10, 12], monolith [13], micro-reactors [14, 15], etc. The Multi-Tubular Fixed Bed Reactor (MTFBR) has been selected for this study, principally because, it presents the greatest challenge of all the Fischer-Tropsch reactors in terms of heat rejection [10, 11, 16, 17].

The challenge of exothermicity in the Fischer-Tropsch fixed bed reactor is traditionally tackled by: (I) recycling fluid effluents at high velocity in order to generate turbulent flow [18], (II) Reduction of the upper limit of the tube diameters [10, 18] and, (III) Reducing catalyst activity [19, 20]; achieved by mixing of inert substances such as silicon carbide with the catalyst. This thesis specifically examines the dilution of the catalyst bed in a fixed bed reactor using inert, encapsulated phase change materials, which act as thermally functional additives for removing the enthalpy of reaction at near isothermal

conditions. In order to do this effectively, it is often instructive to simulate the reactor from first principles in order to generate a truly predictive model, capable of addressing issues such as non-uniform temperature distributions, reactor performance in terms of conversion, selectivity, productivity, etc., and open to modifications for optimising the reactor performance.

1.2 Research Aim

In general, none of the Fischer-Tropsch synthesis mathematical models available in open literature specifically accounts for the effects of catalyst dilution with inert substances or indeed phase change material for the purpose of temperature control. The advent of more powerful computers has also meant that the physico-chemical processes that occur in the fixed bed reactor can be simulated in more detail.

The aim of this research therefore is to present a new methodology of controlling the temperature within a multi-tubular fixed bed Fischer-Tropsch reactor by diluting the catalyst bed with thermally functional, encapsulated phase change materials and by extension, to maintain the selectivity to the spectrum of products within a narrow optimal window. Specifically, the simulation of a multi-tubular fixed bed Fischer-Tropsch reactor, catalysed by iron, with temperature modulation using the combined effect of encapsulated phase change material (PCM) and traditional saturated water wall-cooling will be presented. This simulation provides the chemical engineer with a useful, predictive tool for ascertaining the reactor performance, including reactant conversion, product selectivity, product yield, etc. under the influence of phase change material.

This simulation exercise also affords a measure of flexibility in the sense that its complexity may be adjusted by reducing or increasing the number of spatial dimensions considered, without overtly sacrificing computational accuracy for convenience. In the main, the more rigorous two dimensional reactor model comes with increased fidelity required for reactor design because it considers concentration and temperature gradients along the axial and radial directions. The modified one dimensional α-model, which accounts for temperature and concentration gradients along only the axial direction, however provides sufficiently accurate and less computationally cumbersome models useful for the iterative exercise of optimising the best catalyst-phase change material arrangement in the reactor.

1.3 Research Scope/Outline

While it is possible (and could be the aim of future work) to extrapolate and apply the knowledge gained from this simulation exercise to other reactor configurations, this thesis is limited to the multi-tubular fixed bed reactor configuration. An industrial scale fixed bed reactor with design and operational parameters/properties obtained from literature [5] will be modelled in this work. The chemical kinetics/reaction occurring within the sphere of influence of the physical transport phenomena in the reactor and in particular, how these physico-chemical phenomena occurring in the reactor are influenced by the presence of the phase change material will be the subject of investigation. Typical reactor performance indices including: conversion, product selectivity and yield will be used as yardsticks for comparing the "basecase" reactor scenario without any phase change material to instances where the effect of phase change material on the reactor performance is considered. Outlined below is the organisation of this thesis into its constituent chapters and a synopsis of each chapter.

- Chapter 2 is dedicated to salient background literature survey on the Fischer-Tropsch process, classifications of the technology, reactor configurations and design, reaction kinetics and mechanisms, reactor modelling, heat transport challenges peculiar to the multi-tubular fixed bed reactor configuration, historical and present day measures of tackling heat rejection limitations.
- Chapter 3 puts forward the mathematical formulation of the study in hand, including the governing conservation and constitutive equations. It also sets about implementing the mathematical equations as numerical models on the Finite Element Analysis (FEA) platform, COMSOL Multiphysics [21], including the initial and boundary conditions.
- Chapter 4 presents the validation of the mathematical formulations and the verification of the numerical simulations. In order to ascertain the robustness of the model, three test cases were modelled, validated and verified namely, an industrial scale Fe-catalysed multi-tubular fixed bed reactor, a laboratory scale, single-tube, Co-catalysed fixed bed Fischer-Tropsch reactor, and finally, a laboratory scale fixed bed reactor for the exothermic Pt/SiO_2 catalysed, partial oxidation of methanol, with silica encapsulated indium as diluent.
- Chapter 5 presents a rigorous two-dimensional quasi-homogeneous model for the fixed bed reactor in which the bed is assumed to be homogeneously diluted with encapulated phase change material. The results compare and contrast the reactor behaviour without, and under the influence of phase change materials as catalytic bed diluents.

- Chapter 6 develops a sufficiently accurate one-dimensional model, the modified α-model. The results obtained from simulating the reactor (i.e. for a homogeneous dilution of the bed with phase change material) with this modified α-model are compared with the more rigorous two dimensional and less accurate, conventional one dimensional quasi-homogeneous reactor model.

- Chapter 7 looks at other catalyst-PCM arrangements apart from the homogeneous mixing of both materials, informed by the need to simultaneously maximise desired product yield while preventing thermal runaway. The modified α-model developed in chapter 6 was employed in the optimisation problem posed.

- Chapter 8 entails the relevant conclusions drawn from the thesis. It also outlines limitations of the work done, while suggesting areas for future work.

Chapter 2

Background and literature review

"Everything has been thought of before, but the problem is to think of it again."

Johann Wolfgang Goethe, (1749-1832).

This chapter sets out the relevant literature review for this work. The Fischer-Tropsch synthesis and its complexities are presented.

2.1 The Fischer-Tropsch synthesis process description

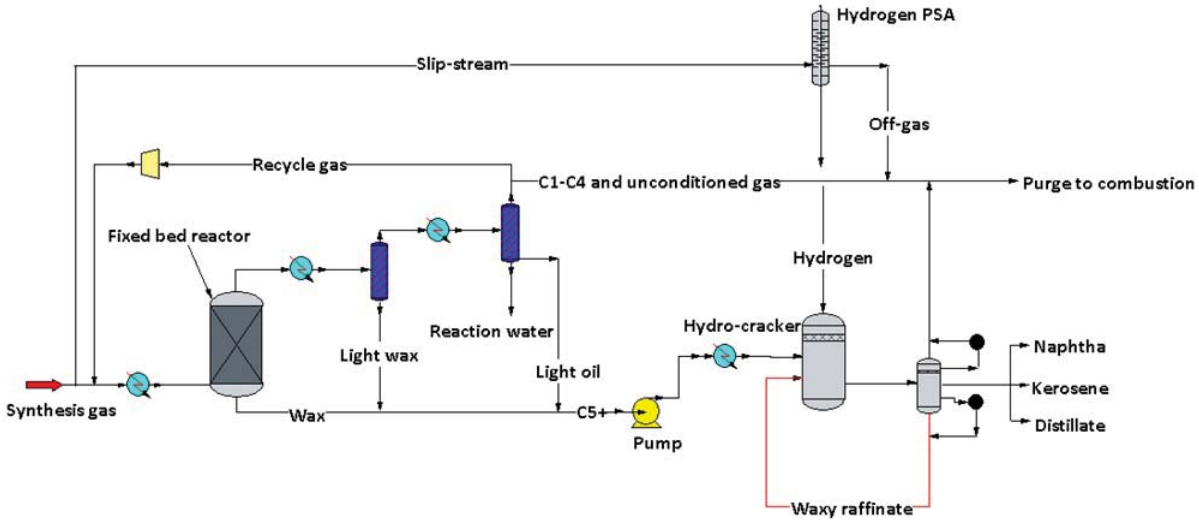

FIGURE 2.1: Fischer-Tropsch synthesis process flow diagram, adapted from [22, 23]

TABLE 2.1: Major overall reactions in the Fischer-Tropsch synthesis, adapted from [26]

Main reactions	
1. Paraffins	$(2n+1)H_2 + nCO \longrightarrow C_nH_{2n+2} + nH_2O$
2. Olefins	$2nH_2 + nCO \longrightarrow C_nH_{2n} + nH_2O$
3. WGS reaction	$CO + H_2O \leftrightharpoons CO_2 + H_2$
Side reactions	
4. Alcohols	$2nH_2 + nCO \longrightarrow C_nH_{2n+2}O + (n\text{-}1)H_2O$
5. Catalyst oxidation/reduction	(a) $M_xO_y + yH_2 \leftrightharpoons yH_2O + xM$ (b) $M_xO_y + yCO \leftrightharpoons yCO_2 + xM$
6. Bulk carbide formation	$yC + xM \leftrightharpoons M_xC_y$
7. Boudouard reaction	$2CO \longrightarrow C + CO_2$

The Fischer-Tropsch synthesis, discovered by Professor Franz Fischer and Dr Hans Tropsch [24] in the early twentieth century, refers to an indirect, chemical process for liquefying synthesis gas. It entails an aggregate of simultaneous, surface polymerisation chemical reactions, occurring *in situ* on the active sites of principally group VIII transition metals, which act as catalysts e.g. iron, cobalt, ruthenium, nickel, etc. [11, 25].

Synthesis gas, commonly called syngas is predominantly made up of carbon monoxide and hydrogen gas, and can be sourced from a wide variety of raw materials including: coal, natural gas, biomass (agricultural waste products, etc.). The Fischer-Tropsch process is a key element in the composite industrial technologies referred to as XTL, where "X" stands for the first letter of the raw material processed into syngas e.g. GTL for gas (natural) to liquid, BTL, for biomass to liquid, etc. Figure 2.1 depicts a commercial Fischer-Tropsch process occurring in a fixed bed reactor, with downstream processing.

A summary of the overall reactions occurring in a Fischer-Tropsch synthesis process is outlined in table 2.1. The process, which typically operates at conditions of 200-350°C and 1-6MPa, generates a complex, multi-component spectrum of products comprising predominantly, straight chain aliphatic paraffins and α-olefins. Oxygenates and some cycloalkanes are also produced in smaller quantities [18, 27, 28]. This complex multi-component mixture is referred to as synthetic crude or syncrude. The Fischer-Tropsch process is often categorised on the basis of the operating temperature (T) as either low-temperature Fischer-Tropsch (LTFT), where $200 \leq T \leq 250$°C or High-temperature Fischer-Tropsch (HTFT), where $250 \leq T \leq 350$°C. A typical spectrum of constituent products of the syncrude produced by either of the two Fischer-Tropsch processes is outlined in table 2.2.

TABLE 2.2: Syncrude properties from the two main classes of Fischer-Tropsch processes based on typical current industrial operation [1]

FTS syncrude property	HTFT	LTFT
Carbon number range	C_1-C_{30}	C_1-C_{120}
Main product	C_2-C_{10} olefins	waxes
Normal product phases[a]		
Gases (C_1-C_4)	20-25%	5-10%
Oil	20-25%	15-20%
Wax	0%	20-25%
Aqueous organics	∼5%	1-2%
Water	45-50%[b]	50-55%[b]
Organic compound classes[a]		
Paraffins (alkanes)	20-30%	major product (> 70%)
Naphthenes (cycloalkanes)	< 1%	< 1%
Olefins (alkenes)	major product (> 50%)	15-20%
Aromatics	1-5%	< 1%
Oxygenates	10-15%	∼ 5%

a All percentages are on a mass basis
b Closed gas loop, i.e. no wet water gas shift conversion

The syncrude produced from the Fischer-Tropsch process is not available for immediate use in internal combustion engines, etc., this is because the syncrude comprises primarily straight chain aliphatic hydrocarbons. This amounts to low octane number, poor flow properties (compared to branched chains) and low lubricity. In order to overcome these challenges, the syncrude is usually sent for further downstream separation, processing and refining, which could involve reactions such as isomerisation, hydro-cracking, alkylation, blending with crude oil or blending with other finished products, etc. [29].

The post-processed fuels produced from the Fischer-Tropsch synthesis are however ultra-pure and of superior quality to their crude-oil derived counterparts. For example, the Fischer-Tropsch fuels are devoid of particulates, nitrogen based compounds, aromatics and sulphur. In addition, the gasoil or diesel obtained from the Fischer-Tropsch process has a cetane number of ≥ 70 compared to 50 for the crude oil derived gasoil [27]. A particularly crucial aspect of the Fischer-Tropsch reaction is its exothermicity, i.e., it possesses a large enthalpy of reaction ($-152\text{kJ}\,\text{mol}^{-1}$ of H_2 or $-167\text{kJ}\,\text{mol}^{-1}$ of CO) and could lead to the process suffering thermal runaway if proper heat rejection is not ensured. This feature plays a significant role in the design and operation of large scale Fischer-Tropsch units and will be central to the research work presented in this thesis.

2.1.1 Prospects and commercial aspects of the Fischer-Tropsch synthesis

The Fischer-Tropsch synthesis was first commercialised during World War II as a means of generating liquid transportation fuels from coal when access to conventional crude oil was constrained. Although interest waned in the process after the war years, it became popular again in South Africa when the country was subjected to economic sanctions during the Apartheid era. This synergy between isolation and the availability of an alternative carbonaceous source of energy has always provided the characteristically ideal recipe on which the Fischer-Tropsch process thrives economically.

In today's context, the reasons for the recent resurgence of interest in the Fischer-Tropsch process are no different. Most of the Fischer-Tropsch process in operation today are located near remote gas fields in order to process stranded gas, which will otherwise be abandoned, as the cost of putting transportation infrastructure in place to move the raw gas to the market could prove prohibitive [13].

Shell [27] and South Africa's SASOL [16, 28] run between them four gas to liquid (GTL) and coal to liquid (CTL) plants. Other major players including EXXON Mobil [30], BP and Conoco Phillips [31] as well as some smaller companies including Rentech [32] have large pilot plants. Velocys[4] has developed a microchannel reactor and demonstrated their technology using wood chip feedstock. Table 2.3 outlines a number of commercial and demonstration Fischer-Tropsch plants in existence. Figures 2.2-2.3 show the microchannel reactor and the test skid of Velocys in Austria respectively.

2.2 The chemistry of the Fischer-Tropsch synthesis

2.2.1 Fischer-Tropsch Catalysis

The commonest catalysts used in the Fischer-Tropsch synthesis are the group VIII transition metals including Co, Fe and Ru. Iron and cobalt are the most commercially viable. Iron is particularly attractive for reasons of being the cheapest option; table 2.4 shows the relative costs of different metal catalysts to Fe. It is commonplace to promote Fe-catalysts with salts of alkali metals [34]. The water-gas shift activity and selectivity towards olefins of such promoted catalysts are typically high and they seem to be quite stable when synthesis gas with a high H_2:CO ratio (i.e. approaching a value of 2) is used [18, 35].

Cobalt generally gives the highest yield of straight chain aliphatic hydrocarbons and also has the longest cycle time. The cycle time of a catalyst in a multi-tubular fixed

Table 2.3: A summary of commercial Fischer-Tropsch facilities [33]

Name	**Place**	**Dates**	**FTS Techn.**	**Feed-stock**	**Prod. volume*** **(bbl/day)**	**Prod.**
Sasol 1 (Sasol)	Sasolburg, S. Africa	1955-date	Fe-LTFT SBC & Fe-LTFT MTFBR	Coal & Natural gas	6,750	Gasoline, wax & chemicals
Sasol 2&3 (Sasol)	Secunda, S. Africa	1980-date	Fe-HTFT CFB (From 1995)	Coal	120,000	Gasoline
Mossgas (PetroSA)	Mossel Bay, S. Africa	1993-date	Fe-HTFT CFB	Natural gas	24,000	Gasoline & Diesel
Shell Bintulu (Shell)	Bintulu, Malaysia	1993-date	Co-LTFT MTFBR	Natural gas	12,000	Distillate
Pearl GTL (Shell)	Qatar	2011-date	Co-LTFT MTFBR	Natural gas	140,000	Distillate
Oryx GTL (Qatar Pet.)	Qatar	2007-date	Co-LTFT SBC	Natural gas	24,000	Distillate
Escravos GTL (Chevron)	Nigeria	2013-date	Co-LTFT SBC	Natural gas	34,000	Distillate
Sinopec/ Syntroleum Demo. Facility	Zhenhai, China	2011	Unknown	Coal, coke, asphalt	80	Chemicals
Syntroleum Catoosa Demo. Plant	Catoosa, OK	2003-2006	SBC	Natural gas	70	Diesel for blending
Rentech PDU	Commerce City, CO	2008-date	Fe-LTFT SBC	Natural gas & petroleum coke	7-10	Jet fuel &Diesel

*Production volume numbers given as crude oil equivalent and only include products made by the FTS process.

FIGURE 2.2: Velocys Commercial FT reactor capable of producing 125 barrels per day and microchannels. Photos by Velocys [4]

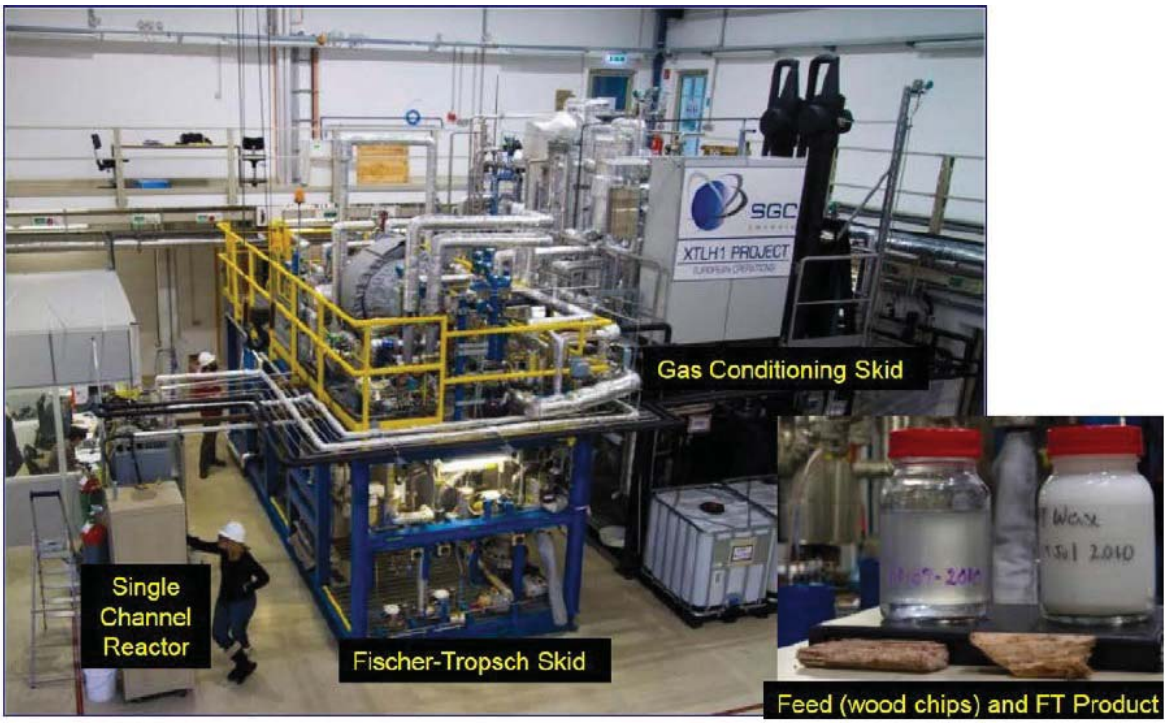

FIGURE 2.3: Velocys demonstration unit at Gussing, Austria, in 2010 [33]

TABLE 2.4: Relative price of metals, adapted from [34]
(a)Dry 1990 [36], (b)Dry 2004 [37]

Metal	Price ratio (Fe-basis)
Fe	1.0
Co	$230^{(a)}$-$1000^{(b)}$
Ni	250
Ru	31,000
Rh	570,000

bed reactor, is defined as the interval of time within which a catalyst delivers on pre-set performance criteria before requiring rejuvenation, regeneration or replacement [1]. The cycle times of Fe and Co in a low temperature Fischer-Tropsch process are 70-100 days [38] and 9-12 months [39] respectively. Co is however between 230-1000 times more expensive than iron (see table 2.4) and supports very little to no water-gas shift activity. Cobalt has been found to be better suited to natural gas based Fischer-Tropsch processes for the production of middle distillates and high molecular weight products [40–42].

Nickel, apart from being expensive at 250 times the cost of Fe, is not recommended because of its high selectivity for methane [36]. Ruthenium is about 31,000 times more expensive than iron, although it is extremely active. It is particularly selective towards high molecular weight waxes at low temperatures and high pressures ($>$ 10MPa), while the converse is true at lower pressures ($<$ 10MPa), in which case, methane becomes the preferred product [23, 43]. According to the findings of Vannice [44], the activity of

Al_2O_3-supported group VIII metals decreased in the order: Ru, Fe, Co, Rh, Pd, Pt and Ir. Sasol measured the activities of Cr and Mo, but found them to be much lower than that of Fe [43].

In general, Co, Ni, and Ru remain in the metallic state under Fischer-Tropsch conditions [45]. Iron on the other hand exhibits a series of phases when subjected to Fischer-Tropsch conditions. These phases include: metallic iron (α-Fe), iron oxides (hematite, α-Fe_2O_3, magnetite Fe_3O_4 and Fe_xO), and five different forms of iron carbides, O-carbides (carbides with carbon atoms in octahedral interstices, ε-Fe_2C, ε'-$Fe_{2.2}C$ and Fe_xC) and Trigonal prismatic (TP) carbides (carbides with carbon atoms in trigonal prismatic interstices, χ-$Fe_{2.5}C$ and Fe_3C) [43, 46–49] . The process conditions, catalyst deactivation and composition largely determine the formation and composition of these iron phases. The exact catalytic activity of the individual phases also remains a subject for debate in literature [43, 49, 50].

All Fischer-Tropsch catalysts are susceptible to irreversible sulphur poisoning, as such industrial operators including Sasol reduce the sulphur contents of their inlet gas to < 0.5ppm. Where the Fischer-Tropsch process is applied in the chemical liquefaction of sour gas, then the longer life and superior performance of cobalt compared to iron may not necessarily be realised and the extra cost of Co may become unjustifiable [33, 36]. In addition, historically, companies have favoured the use of iron despite its shorter cycle time because of its low cost and ease of disposal compared to cobalt. Iron catalysts are more often than not replaced, rather than rejuvenated or regenerated [1].

2.2.2 Water-gas shift activity

The water gas shift activity is an equilibrium, catalytic, exothermic reaction represented as follows:

$$CO + H_2O \rightleftharpoons CO_2 + H_2 \tag{2.1}$$

It is particularly important when synthesis gas with non stoichiometric amounts of hydrogen is used, since by virtue of its forward reaction, it is able to make up the hydrogen deficit. The reaction may reach equilibrium at operational temperatures, $T > 250^oC$ on catalysts with a high water-gas shift activity [51, 52]. Cobalt and Ruthenium are not very active toward the water gas shift reaction unlike iron based Fischer-Tropsch catalysts [53]. Magnetite, Fe_3O_4 has been proposed as the most active phase of iron for the water gas shift reaction [47, 48, 53–56].

Put together with its relatively low cost, the ability of iron to handle a wide range of non-stoichiometric combinations of hydrogen to carbon monoxide in the feed synthesis

gas, by reason of facilitating the water gas shift reaction to make up for hydrogen deficits, renders it a very versatile catalyst choice for the Fischer-Tropsch synthesis (even though its on stream life is much shorter than that of cobalt). As such, the modelling exercise presented subsequently in this work (chapters 3-7) will assume reaction kinetics based on Fe-catalysis.

2.2.3 Fischer-Tropsch synthesis reaction mechanism

Literature is replete with several postulations regarding the mechanism by which the Fischer-Tropsch process proceeds [57–60]. Despite the reaction having been discovered nearly one hundred years ago, researchers have not come to a consensus as to which reaction mechanism is to be universally adopted. This section looks at a number of plausible ones often put forward in published literature to explain the formation of straight chain hydrocarbons. According to Adesina [60], a synopsis of the mechanism for the formation of straight chain aliphatic hydrocarbon molecules are as follows:

1. The adsorption of the reactants, CO and H_2 on to the catalytic metal surface
2. Initiation of the carbon chain
3. Propagation or growth of the carbon chain
4. Termination of the carbon chain
5. Desorption of the product from the catalyst active site
6. Readsorption of desorbed (but still chemically active) molecules on to the catalyst active site and possible further reaction.

A succinct description of some of the most plausible mechanisms in literature are as follows:

2.2.3.1 The Carbide Mechanism

Figure 2.4 shows a schematic representation of the carbide mechanism for the Fischer-Tropsch synthesis. The underlying assumption is the dissociative adsorption of CO and H_2. The methylene group $*CH_2$, serves as the monomer or building block for the polymerisation reaction and long chain hydrocarbon molecules are formed by the successive coupling of the methylene group. This monomer ($*CH_2$) is formed by the hydrogenation of the surface carbide. Termination reactions bring about the product formation, examples of these termination reactions include: hydrogenation to form straight chain

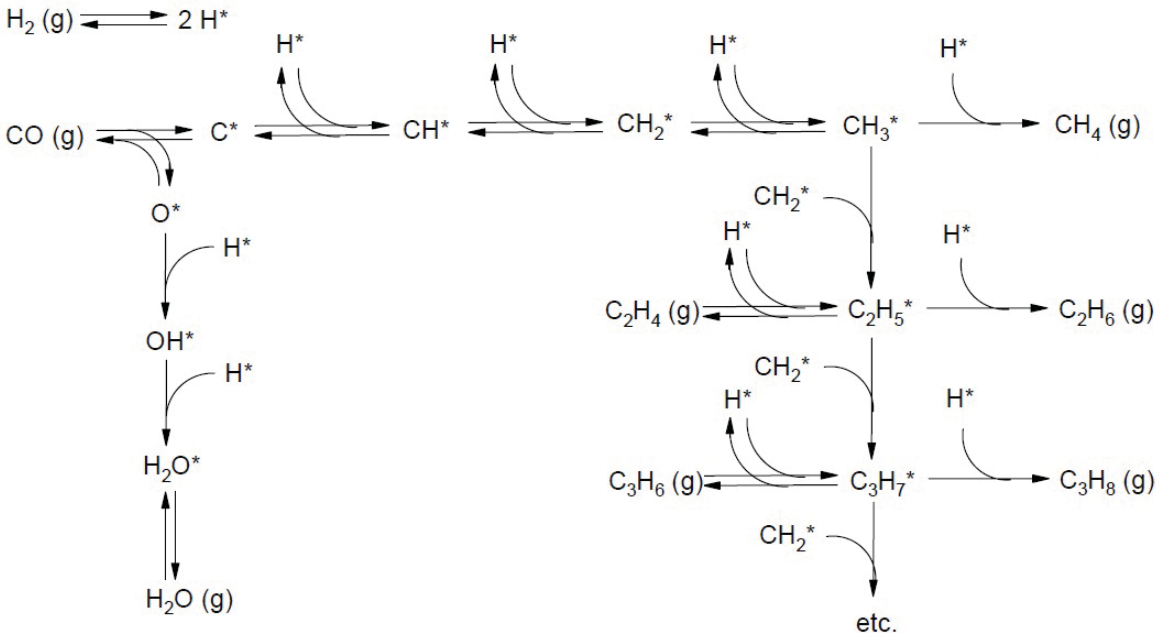

FIGURE 2.4: Schematic representation of the carbide mechanism [13, 61]

paraffins or hydrogen abstraction to form linear α-olefins. Table 2.5 sets out a series of elementary reactions that are thought to take place in the formation of linear hydrocarbons; in the table, s represents the catalyst active site.

Other products like aldehydes and alcohols may be formed through termination reactions with oxygen laden surface species [61]. Secondary reactions also take place when primary products desorb from the catalyst active site and interact with another active site before exiting the reactor. Examples of such reactions include: isomerisation, cracking and hydrogenolysis, insertion into growing chains and re-adsorption and initiation of hydrocarbon chains [26, 62, 63].

2.2.3.2 The Enolic Mechanism

In this mechanism, the monomer is an oxygen carrying intermediate as opposed to the carbidic methylene group in the carbide mechanism. As seen in Figure 2.5, there is no dissociative adsorption of CO, rather, after the reaction of the adsorbed CO with hydrogen, a new intermediate HC*OH is formed and it serves as the building block or monomer. Chain propagation is achieved by coupling the monomers in conjunction with hydrogen, while oxygen is expelled in the form of water. Termination occurs via the same primary and secondary reactions outlined in the carbide mechanism. It is also pertinent to note that a mechanism involving a combined enol/carbide mechanism has been proposed in which, a methylene species is formed via the hydrogenation of the hydroxylated enolic HC*OH intermediate [67].

TABLE 2.5: Proposed carbide mechanism of the hydrocarbon synthesis from CO and H_2 adapted from [54, 64–66]

Adsorption	
1	$CO + s \rightleftharpoons CO s$
2	$CO s + s \rightleftharpoons C s + O s$
3	$H_2 + 2s \rightleftharpoons 2Hs$
Surface reactions	
Water formation	
4	$Os + Hs \rightleftharpoons HOs + s$
5	$HOs + Hs \rightleftharpoons H_2O + 2s$
or	$Os + H_2 \rightleftharpoons H_2O + s$
Chain initiation	
6	$Cs + Hs \rightleftharpoons CHs + s$
7	$CHs + Hs \rightleftharpoons CH_2s + s$
8	$CH_2s + Hs \rightleftharpoons CH_3s + s$
or	$COs + H_2 \rightleftharpoons CHOHs$
	$CHOHs + H_2 \rightleftharpoons CH_2s + H_2O$
Methanation	
9	$CH_3s + Hs \rightleftharpoons CH_4 + s$
Chain growth	
10	$C_nH_{2n+1}s + CH_2s \rightleftharpoons C_{n+1}H_{2n+3}s + 2s$
Hydrogenation to paraffins	
11	$C_nH_{2n+1}s + Hs \rightleftharpoons C_nH_{2n+2} + 2s$
β-Dehydrogenation to olefins	
12	$C_nH_{2n+1}s \rightleftharpoons C_nH_{2n} + Hs$

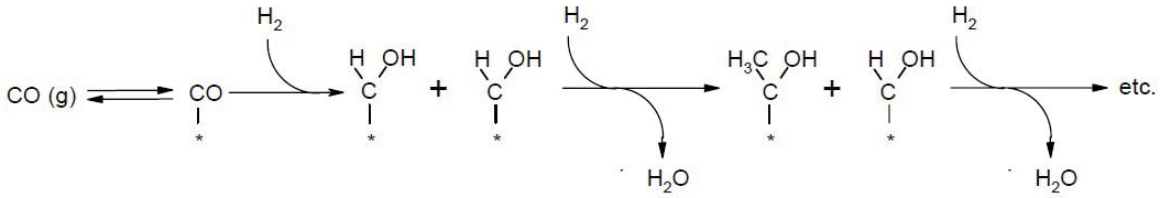

FIGURE 2.5: Schematic representation of the enolic mechanism [13, 61]

2.2.3.3 The CO insertion Mechanism

Figure 2.6 shows the schematic for the CO insertion mechanism. Like the enolic mechanism, the building block or monomer also carries an oxygen atom. This monomer, O^*CH_3 is formed in two steps, first, there is the reaction between carbon monoxide and a surface hydroxyl group and secondly, a hydrogenation reaction. Propagation of the hydrocarbon chains is brought about by the reaction of the intermediate with a carbon monoxide molecule and two hydrogen molecules. Termination occurs through the same primary and secondary reactions outlined in the carbide mechanism.

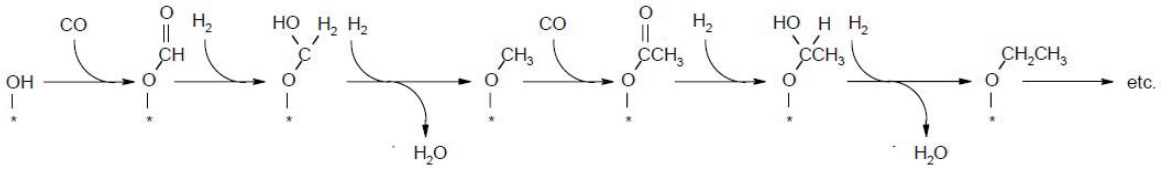

FIGURE 2.6: Schematic representation of the CO insertion mechanism [13, 61]

2.2.3.4 The mechanism for the water-gas shift reaction

As previously highlighted in section 2.2.2, the water-gas shift activity is important in Fe-catalysed Fischer-Tropsch synthesis. Rethwisch et al [55] have studied the water-gas reaction extensively on both supported and unsupported iron oxide catalysts. From their findings they concluded that the water gas shift reaction proceeded over unsupported magnetite via a direct oxidation mechanism, while on supported iron catalysts, it proceeded via the formate species. van der Laan et al [26] in their in-depth literature review posited that the formate species mechanism was the more plausible of the two.

Figure 2.7 shows a schematic of the formate species mechanism. The formate species are produced by the reaction of the hydroxy species with either of water or carbon dioxide in the gas or adsorbed state. The formate intermediate is reduced to adsorbed or gaseous carbon dioxide.

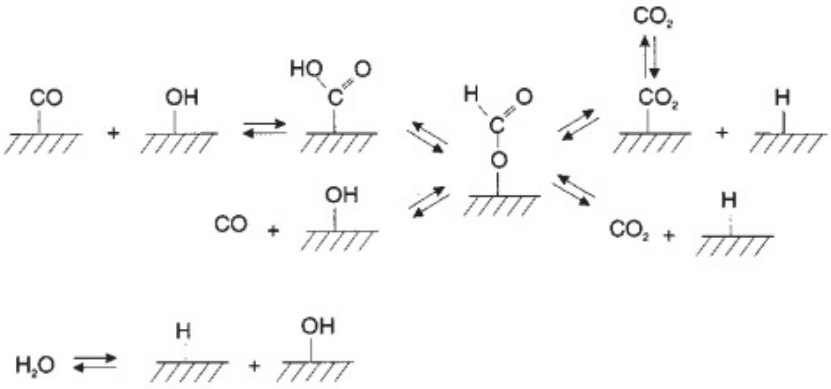

FIGURE 2.7: Water gas shift reaction mechanism via formate species [54, 55]

2.2.4 Fischer-Tropsch synthesis kinetics

The kinetics of the Fischer-Tropsch synthesis is inherently complex because of the complicated reaction mechanisms and the myriad of products obtained from the reactants. In general, the intrinsic kinetics of the Fischer-Tropsch reaction may be expressed in the

form of empirical power laws [68, 69] or in the Langmuir-Hinshelwood-Hougen-Watson (LHHW) and Eley-Rideal forms, based on a reaction mechanism for the hydrocarbon forming reactions [64, 70–72]. The main differentiating features of these kinetic expressions for the consumption of syngas derive from the nature of the monomer (whether it is oxygen bearing or not), and the adsorption of the reactants (CO and H_2) and products (H_2O and CO_2) on the catalyst surface.

The Fischer-Tropsch synthesis may be reduced to two principal equations, i.e., the main Fischer-Tropsch reaction and the water gas shift reaction, with overall reaction equations as follows:

$$CO + \left(1 + \frac{m}{2n}\right)H_2 \longrightarrow \frac{1}{n}C_nH_m + H_2O \qquad (\Re_{FT}) \qquad (2.2)$$

$$CO + H_2O \rightleftharpoons CO_2 + H_2 \qquad (\Re_{WGS}) \qquad (2.3)$$

where, n is the average carbon number and m is the average number of hydrogen atoms of the hydrocarbon product. van der Laan et al [26] have published a selection of kinetic expressions proposed by various researchers as shown in table 2.6, where a and b in the expressions are temperature dependent constants. It should be stated that the expressions in table 2.6 have been derived using different experimental approaches, including the use of fixed bed, slurry and Berty reactors (see table 2.7), it is however interesting to note that there is broad similarity amongst the expressions [13, 26]. In almost all the expressions, H_2 is observed to have an overall positive order, while CO, when it appears in the expressions, mainly plays an inhibiting role (in the denominator) in most of the expressions.

2.2.4.1 Fischer-Tropsch kinetics on iron based catalysts

The rate of reaction of a Fe-catalysed Fischer Tropsch reaction generally increases with a corresponding increase in the partial pressure of H_2, while the converse is true for an increase in the partial pressure of water vapour [82]. Precipitated iron catalyst is often used in low temperature Fischer-Tropsch synthesis, while fused iron catalysts are used for high temperature Fischer-Tropsch synthesis [1, 43]. A detailed description of the catalyst synthesis procedures may be found elsewhere [11, 28, 43, 83]. Table 2.7 presents various kinetic studies on both iron and cobalt catalysts.

Several kinetic equations have been suggested by various researchers, most of them based on the carbide or combined carbide and enolic mechanisms [65, 69]. The main underlying assumptions of these mechanistic kinetic rate expressions include [65, 73]:

TABLE 2.6: Reaction rate equations for overall synthesis gas consumption rate [26]

Kinetic expression	Ref.
(a) kP_{H_2}	[45, 52, 73]
(b) $kP_{H_2}^{a}\,P_{CO}^{b}$	[68]
(c) $\dfrac{k\,P_{H_2}\,P_{CO}}{P_{CO}+aP_{H_2O}}$	[45, 52, 74, 75]
(d) $\dfrac{k\,P_{H_2}^{2}\,P_{CO}}{P_{CO}\,P_{H_2}+aP_{H_2O}}$	[70, 74, 76, 77]
(e) $\dfrac{kP_{H_2}^{2}\,P_{CO}}{1+aP_{CO}P_{H_2}^{2}}$	[45]
(f) $\dfrac{kP_{H_2}P_{CO}}{P_{CO}+aP_{CO_2}}$	[52, 72, 76, 78]
(g) $\dfrac{kP_{H_2}P_{CO}}{P_{CO}+aP_{H_2O}+bP_{CO_2}}$	[52, 72, 78]
(h) $\dfrac{kP_{CO}^{\frac{1}{2}}P_{H_2}^{\frac{1}{2}}}{\left(1+aP_{CO}^{\frac{1}{2}}+bP_{H_2}^{\frac{1}{2}}\right)^{2}}$	[71]
(i) $\dfrac{kP_{CO}P_{H_2}^{\frac{1}{2}}}{\left(1+aP_{CO}+bP_{H_2}^{\frac{1}{2}}\right)^{2}}$	[64]
(j) $\dfrac{kP_{CO}P_{H_2}}{(1+bP_{CO})^{2}}$	[79–81]

1. The reaction between dihydrogen and a carbon intermediate serves as the rate determining step
2. There is a strong adsorption of carbon monoxide and water on the catalyst surface
3. Hydrogen reacts in a molecular fashion and does so in either the gaseous phase or the associated adsorbed state

Anderson [45] put forward equation (2.4), which incorporates a water vapour inhibition term, this was later corroborated Dry [75] and Huff et al [85]

$$\Re_{FT} = \frac{kP_{CO}P_{H_2}}{P_{CO}+aP_{H_2O}} \tag{2.4}$$

TABLE 2.7: Kinetic studies for the Fischer-Tropsch synthesis on iron and cobalt catalysts [26]

Catalyst	Reactor	Operating conditions			Kinetic expression (Table 2.6)	E_{act} (k) (kJmol^{-1}) (equation (2.5))	$-\Delta H_{ad}$ (a) (kJmol^{-1}) (equation (2.6))	Ref.
		T(°C)	P (MPa)	H_2:CO_{feed}				
Fused Fe/K	Fixed bed	225-265	1.0-1.8	1.2-7.2	(a)	71	-	[73]
Prec. Fe/K/Cu	Slurry	235-265	1.5-3.0	0.6-1.0	(a)	86	-	[52][a]
Prec. Fe/K/Cu	Slurry	250	1.5-3.0	0.6-1.0	(c)	-	-	[52]
Iron	Fixed bed	?	?	?	(c)	-	-	[45]
Fused Fe/K	‡Fixed bed	250-315	2.0	2.0	(c)	85	8.8	[84]
Fused iron	Slurry	232-263	0.4-1.5	0.5-1.8	(d)	83	100	[70]
Prec. iron	Slurry	220-260	1.0	0.5-0.6	(f)	103	0	[78][b]
Prec. iron	Slurry	220-280	0.5-1.2	0.5-3.5	(c)	89	-	[72] [b]
Fused iron	Slurry	210-270	0.5-5.5	0.5-3.5	(f)	81	-	[72][b]
Co/Kieselguhr	Berty	190	0.2-1.5	0.5-8.3	(h, i)	-	-	[64][71][c]
Co/MgO/ SiO_2	Slurry	220-240	1.5-3.5	1.5-3.5	(j)	-	-	[80]
Co/Zr/ SiO_2	Slurry	220-280	2.1	0.5-2.0	(d)	97	-	[77]
Prec. Fe/Cu/K	‡Fixed bed	230-264	1.0-2.6	1.1-2.4	(d)	56	-62	[74]
Prec. Fe/Cu/K	‡Fixed bed	230-264	1.0-2.6	1.1-2.4	(c)	56	-60	[74]
Prec. iron	Slurry	220-260	-	0.5-0.8	(f)	105	0	[76][b]
Prec. iron	Slurry	220-260	-	0.8-2.0	(c)	80	55	[76][b]
Prec. iron	Fixed bed	250-350	0.6- 2.1	3.0- 6.0	-	-	-	[54][d]

a No temperature dependence of optimal rate equations (c) (Fe/Cu/K) and (g) (100 Fe/0.3Cu/0.2K) is given
b Rate equations expressed in liquid concentrations
c Only measurements at 190°C are reported. Conversions and space velocities are not mentioned by Sarup et al [71]
d Kinetic expressions not mentioned in Table 2.6.
‡ Gradientless.

where P_{CO}, P_{H_2}, P_{H_2O} are respectively the partial pressures of gaseous CO, H_2 and H_2O. The reaction rate constant, k and the adsorption parameter a are defined using the Arrhenius expression [84]. Atwood et al [84] determined the activation energy (E_{act}) and enthalpy of adsorption, ($-\Delta H_{ad}$) to be 85kJ mol^{-1} and 8.8kJ mol^{-1} respectively by fitting their kinetics data on fused nitrided iron catalyst to equation (2.4).

$$k = k_0 \exp\left(-\frac{E_{act}}{R_g T}\right) \tag{2.5}$$

$$a = a_0 \exp\left(-\frac{\Delta H_{ad}}{R_g T}\right) \tag{2.6}$$

Anderson [45] and Dry [75] also suggested that where there was a high water gas shift activity, resulting in a high removal rate of water vapour from the Fischer-Tropsch synthesis and channelled towards the water gas shift reaction instead, then the water vapour concentration becomes sufficiently low, such that, $P_{CO} >> P_{H_2O}$, and if in addition, there is less than 60% per pass conversion, equation (2.4) may be reduced to a first order dependency in H_2 as follows:

$$\Re_{FT} = kP_{H_2} \tag{2.7}$$

In order to account for their observation of a linear decrease in the adsorption parameter a in equation (2.4) with hydrogen pressure on a fused iron catalyst, Huff et al [85] modified equation (2.4) and put forward the following equation:

$$\Re_{FT} = \frac{kP_{CO}P_{H_2}^2}{P_{CO}P_{H_2} + \frac{a}{P_{H_2}}P_{H_2O}} \tag{2.8}$$

Deckwer et al [76], however found that equation (2.8) was unable to predict the kinetic data for low H_2:CO feed ratios (< 0.8) on a potassium-promoted iron catalyst owing to high water gas shift activity. Shen et al [74] modelled their kinetic data on equation (2.8) and reported $E_{act} = 56\text{kJmol}^{-1}$ and $-\Delta H_{ad} = -62\text{kJmol}^{-1}$, they were however silent on any discrimination between the models in equations (2.4) and (2.8) in terms of which gave the better fit.

The water gas shift reaction by altering the activities of reactants and products can have have either a promoting or inhibiting effect on the Fischer-Tropsch synthesis. Typically, CO_2 is less of an inhibitor to the Fischer-Tropsch reaction relative to H_2O owing to the large difference in their respective adsorption coefficients [52, 86]. Iron catalysts with a high water shift reaction are however able to convert a large amount of water vapour into CO_2, and were thought to significantly increase the CO_2 inhibiting influence under these circumstances. To that end, Ledakowicz et al [78] (using precipitated iron catalyst,

100Fe/1.3K, with high water gas shift activity), Nettelhoff et al [72] (using a commercial fused iron ammonia synthesis catalyst, BASF S6-10) and Deckwer et al [76], put forward equation (2.9), which accounts for CO_2 inhibition.

$$\Re_{FT} = \frac{kP_{CO}P_{H_2}}{P_{CO} + aP_{CO_2}} \tag{2.9}$$

Ledakowicz et al [78] also put forward a generalised reaction rate expression to cater for catalysts with high and low water gas shift activities:

$$\Re_{FT} = \frac{kP_{CO}P_{H_2}}{P_{CO} + aP_{H_2O} + bP_{CO_2}} \tag{2.10}$$

Further experimental evidence however, from co-feeding of CO_2 to the feed synthesis gas revealed that the syngas consumption/rate of reaction was not significantly affected by adding CO_2 in this fashion [87, 88]. This led Yates et al [88] to conclude that the inhibition effect attributed to CO_2 by previous researchers was probably due in fact to H_2O, since the water gas shift reaction is either at, or close to equilibrium on these catalysts.

$$P_{CO_2} = K_{ewgs}\frac{P_{CO}P_{H_2O}}{P_{H_2}} \tag{2.11}$$

Where, K_{ewgs} is the equilibrium constant for the water gas shift reaction. From the foregoing, it is clear that no one reaction rate expression set out by previous researchers universally satisfies/describes all the Fe-catalysed Fischer-Tropsch reactions and their individual nuances (of catalyst type, catalyst formulation, process conditions, etc.). In other words, the rate expressions are catalyst specific.

Jess et al [5, 89–91], Popp[92], Kuntze [93] and Raak et al [94] have widely researched and published on Fischer-Tropsch synthesis in industrial, multi-tubular, fixed bed reactors. They have also derived reaction rate expressions (similar to equation (2.4)) based on systematic experiments with commercial Fe catalysts in their original form, specific to the catalyst and process, and validated their work using data from commercially operating plants including the Arbeitsgemeinschaft (consortium) Ruhrchemie/Lurgi(ARGE) plant and presented their results. A full description of these equations are presented in subsection 5.1.2 of chapter 5. Therefore, in the absence of any experimental work in this thesis, the works of Jess et al [5, 89–91] have been chosen as a benchmark for the modelling exercise carried out in chapters 3-7 of this thesis.

2.2.4.2 Fischer-Tropsch kinetics on cobalt based catalysts

The reaction kinetic expressions developed for a Co-catalysed Fischer-Tropsch synthesis are quite different in form from those of Fe-catlysed FTS. The Co-catalysed FTS kinetic

expressions, often of the form of LHHW, are premised on the rate determining step being a bimolecular surface reaction, between a dissociated hydrogen species and a carbon intermediate, yielding a quadratic denominator in the reaction rate expression. As mentioned previously in section 2.2.2, Co is not very active towards the water gas shift reaction, as such, no CO_2 is formed and inhibition terms due to H_2O in the reaction rate expressions are not recorded in literature [26].

Similar to the Fe-catalysed FTS, the mechanistic reaction rate expressions have also been developed on the bases of the carbide and/or combined carbide/enolic reaction mechanisms. Between them, Wojciechowski [64] and Sarup et al [71] developed six different reaction rate equations from experiments in a Berty reactor at 190°C, partial pressure of hydrogen maintained within the region of $0.07 \leq P_{H_2} \leq 0.68$MPa and the partial pressure of CO held within $0.003 \leq P_{H_2} \leq 0.93$MPa. All of their six reaction rate expressions may be generalised as follows:

$$-\Re_{CO} = \frac{kP_{CO}^{a}P_{H_2}^{b}}{\left(1 + \sum_i K_i P_{CO}^{c_i} P_{H_2}^{d_i}\right)^2} \tag{2.12}$$

where, a and b are the orders of the reaction, K_i is the adsorption constant for the i^{th} adsorption term, c_i and d_i represent the dependency of surface coverage on the reactant pressure of the i^{th} adsorption term. Wojciechowski [64] and Sarup et al [71] proceeded to carry out model discrimination by testing their six models against experimental data, whittling the expressions down to two:

$$-\Re_{CO} = \frac{kP_{CO}^{\frac{1}{2}}P_{H_2}^{\frac{1}{2}}}{\left(1 + K_1 P_{CO}^{\frac{1}{2}} + K_2 P_{H_2}^{\frac{1}{2}}\right)^2} \tag{2.13}$$

$$-\Re_{CO} = \frac{kP_{CO}P_{H_2}^{\frac{1}{2}}}{\left(1 + K_1 P_{CO} + K_2 P_{H_2}^{\frac{1}{2}}\right)^2} \tag{2.14}$$

After optimising the parameters of equations (2.13) and (2.14), and further comparisons were made with experimental data, the relative variance between model and experiment was greater than 40%, indicating a significant lack of fit and was ultimately rejected [71].

Yates et al [80] carried out Co-catalysed FTS experiments in a slurry reactor and obtained a simpler, yet more accurate Langmuir-Hinshelwood form equation involving a

bimolecular surface reaction as the rate determining step:

$$-\Re_{CO} = \frac{kP_{CO}P_{H_2}}{(1 + K_1 P_{CO})^2} \tag{2.15}$$

An equation similar to (2.15) had previously been developed by Sarup et al [71], with a larger number of inhibition terms, but it was jettisoned because one of the adsorption constants had been negative; a situation which had no physical meaning. Remarkably, the linearised form of the rate equation (2.15), due to Yates et al [80] fiited Sarup et al's [71] data well.

Overall, relative to kinetic studies on Fe catalysts, research on Co catalysts are more comprehensive, due principally to the simpler kinetics, stemming from the absence of any significant water gas shift activity [26]. It should also be stated that the kinetic equations set out in this section have principally been intrinsic kinetics, in reality however, reactions carried out on an industrial scale often occur in the region of the sphere of influence of transport phenomena limiting effects. As such, when these equations are used in the subsequent modelling to be presented, they will be appropriately qualified to reflect this.

2.2.5 Product distribution and selectivity

Left to its own devices thermodynamically, the Fischer-Tropsch synthesis will under the prevalent process conditions of temperature, pressure, reactants, etc., most favour the production of methane and coke. In table 2.8, a measure of the spontaneity of some of the constituent reactions of the Fischer-Tropsch process are shown using the standard Gibbs free energies (ΔG^{θ}) of the reactions. Essentially, the reactions may be imagined as being driven by the formation of water. The formation of hydrocarbons and alcohols is spontaneously favoured (i.e. $\Delta G^{\theta} << 0$), so long as there is the simultaneous formation water, see reactions (a)-(e) in table 2.8. In the same vein, the spontaneous formation of longer chain hydrocarbons wanes as the number of carbon atoms increase (see reactions (a)-(b) of table 2.8). Reaction (f) shows that the Boudouard reaction, i.e. carbon laydown is readily spontaneous. This fact shows the critical role of the catalyst in controlling the kinetic factors in order avoid the reaction settling for what would otherwise be the thermodynamic (equilibrium) tendencies, i.e. methane, carbon and water formation.

The selectivity of a chemical species j in the Fischer-Tropsch process refers to the process preferring the production of molecule j over any another. On a carbon basis, this may be defined mathematically as follows:

TABLE 2.8: Energetics of CO hydrogenation, adapted from[25]

(a) $3H_2 + CO \longrightarrow H_2O + CH_4$	$\Delta G^{\theta} = -94 \text{kJmol}^{-1}$
(b) $2H_2 + CO \longrightarrow H_2O + \frac{1}{3}C_3H_6$	$\Delta G^{\theta} = -31 \text{kJmol}^{-1}$
(c) $3H_2 + CO \longrightarrow CH_3OH$	$\Delta G^{\theta} = +21 \text{kJmol}^{-1}$
(d) $3H_2 + 2CO \longrightarrow HOCH_2OH$	$\Delta G^{\theta} = +66 \text{kJmol}^{-1}$
(e) $4H_2 + 2CO \longrightarrow CH_3CH_2OH + H_2O$	$\Delta G^{\theta} = -27 \text{kJmol}^{-1}$
(f) $2CO \rightleftharpoons CO_2 + C$	$\Delta G^{\theta} = -120 \text{kJmol}^{-1}$
(g) $H_2O + CO \rightleftharpoons H_2 + CO_2$	$\Delta G^{\theta} = -28 \text{kJmol}^{-1}$

$$S_j = \frac{\text{moles of hydrocarbon } j \times cn}{\text{moles of CO converted}} \tag{2.16}$$

where, cn is the carbon number of species j. It is therefore clear that the selectivity of the Fischer-Tropsch process to desirable molecules lies at the heart of its economical success. The catalyst conditions, reactor configurations and process conditions wield the greatest influence on the process selectivity [95]. The theoretical description of the selectivity to a particular species with some carbon number, cn using a carbon number, independent, chain growth probability parameter (α_{FT}), has been put forward by Anderson et al [45] in the familiar Anderson-Schulz-Flory (ASF) equation (full derivation can be found elsewhere [11]):

$$x_{cn} = (1 - \alpha_{\text{FT}}) \times \alpha_{\text{FT}}^{(cn-1)} \tag{2.17}$$

where, x_{cn} is the mole fraction of a hydrocarbon of chain length cn. The chain growth probability parameter (α_{FT}) is given by the expression:

$$0.0 \leq \left(\alpha_{\text{FT}} = \frac{R_{\text{prop}}}{R_{\text{prop}} + R_{\text{term}}} \right) \leq 1.0 \tag{2.18}$$

where, R_{prop} is the rate of chain growth or chain propagation and R_{term} is the rate of chain termination. A value of $\alpha_{\text{FT}} = 0.0$ signifies no chain growth, while $\alpha_{\text{FT}} = 1.0$ implies infinite chain growth. According to Dry [95], the range of α_{FT} is a function of the reaction conditions and nature of catalyst. Typical ranges for α_{FT} Fe and Co are: 0.70-0.80 and 0.50-0.70 respectively. The α_{FT}-value also determines the total carbon number distribution of the Fischer-Tropsch products as depicted in Figures 2.8 and 2.9.

The chief underlying assumptions of the ASF description of the carbon number distribution are as follows:

1. The carbon chain growth probability factor, α_{FT} is independent of the carbon chain length

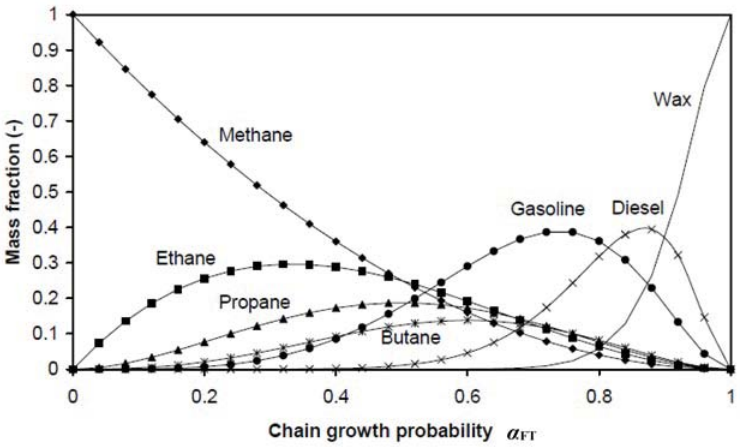

FIGURE 2.8: Hydrocarbon selectivity as a function of the chain growth probability parameter, adapted from [13, 26]

2. The chain growth occurs only from a single point

3. Chain growth that has been terminated cannot be re-initiated.

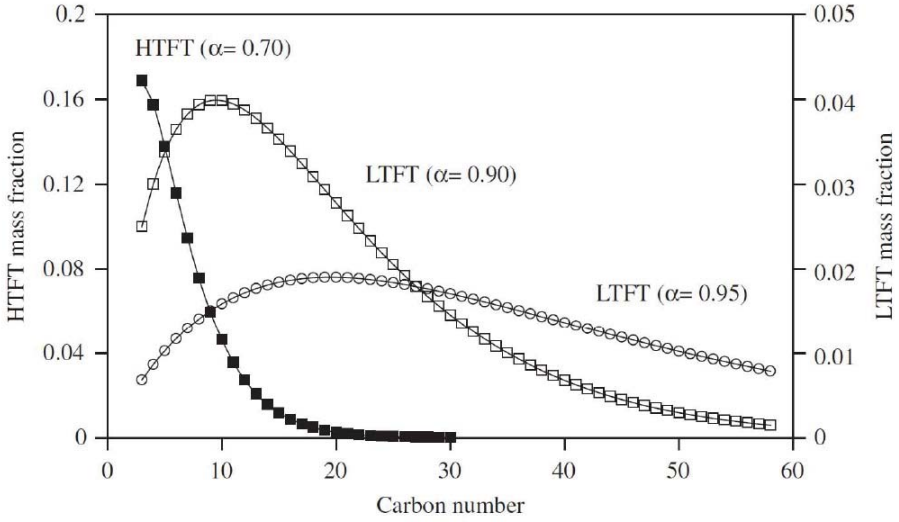

FIGURE 2.9: Theoretical ASF distributions for three different Fischer-Tropsch reactors: High temperature FT (HTFT) and two low temperature FT (LTFT), adapted from [96]

To a large extent, the ASF equation describes the carbon number distributions for real Fischer-Tropsch synthesis data quite well [1]. Some deviations do exist however in reality, for example the selectivity towards methane is usually higher than that predicted by the ASF, the selectivity to the C_2 products, ethene and ethane is lower than predicted by the ASF, much higher C-number molecules seem to have their own α_{FT} values and there is also olefin re-adsorption. Nevertheless, the α_{FT} values continue to be widely used as a standard way of reporting product distribution in the Fischer-Tropsch synthesis

TABLE 2.9: Selectivity control in Fischer-Tropsch synthesis by process conditions and catalyst modifications, adapted from Röper [7], van der Laan et al[26]

Parameter	Chain length	Chain brainching	Olefin selectivity	Alcohol selectivity	Carbon deposition	Methane selectivity
Temperature	↓	↑	*	↓	↑	↑
Pressure	↑	↓	*	↑	*	↓
H_2:CO	↓	↑	↓	↓	↓	↑
Conversion	*	*	↓	↓	↑	↑
Space velocity	*	*	↑	↑	*	↓
Alkali content (iron catalyst)	↑	↓	↑	↑	↑	↓

Key: Increases with increasing parameter: ↑; Decreases with increasing parameter: ↓; Complex relationship: *

products and thus, a measure of the effectiveness of the reactor in question [26, 33] and will be used for predicting product distribution in this thesis.

2.2.5.1 Effect of reactor design and process conditions on catalyst selectivity

In the main, the selectivity of the Fischer-Tropsch synthesis may be influenced through the reactor/catalyst design or through the process conditions. Some design-based methods of influencing reactor selectivity include:

- recycling un-reacted reactants and some of the effluent fluid products into the reactor, with the aim of increasing the hydrocarbon yield and possibly driving short chain molecules towards further polymerisation, thus enhancing the overall output of long chain hydrocarbon molecules.
- co-feeding products from other processes e.g. ethane gas may be fed into the reactor simultaneously with the syngas with the intent of encouraging the polymerisation process and by extension the selectivity to higher molecular weight hydrocarbons.
- the use of staged reactors, with multiple access and egress points along the reactor length, where syngas is fed and products are removed respectively.
- A combination of these methods may also be applied.

Table 2.9 presents a summary of how process conditions influence the selectivity of the Fischer-Tropsch process.

1. *Temperature*

   An increase in temperature displaces the selectivity towards the shorter chain hydrocarbon molecules, especially methane. This observation is true for the main catalysts: Fe [97, 98] and Co [43]. Of all the process conditions, a sustained increase in temperature has a consistent deleterious effect on the process, including carbon deposition, reactor uncontrollability and ultimately, thermal runaway. The reason for this lies in the thermodynamic fundamentals of the process.

   The Fischer-Tropsch reaction is not of itself an equilibrium/reversible reaction, neither is the syncrude generated an equilibrium mixture of products. It may however, be instructive to analyse the FTS in equilibrium reaction terms. The Fischer-Tropsch reaction is a strongly exothermic reaction i.e., the forward reaction converting reactants to products generates a large amount of heat. The Le Châtelier's principle suggests that if the temperature of such an exothermic reaction is further raised, then the reacting system responds in such a way as to annul the effect of the temperature increase. One of the ways it does this is to terminate the carbon chain lengths rather abruptly, thus preventing further polymerisation which would otherwise result in more heat generation.

   The enthalpies of reaction of both the main synthesis reaction (equation 2.19) and the water gas shift reaction (equation 2.20) in their monomolecular forms are quite substantial:

$$\mathrm{CO} + 2\mathrm{H_2} \longrightarrow -(\mathrm{CH_2}) - +\mathrm{H_2O} \quad \Delta H_{\mathrm{r},\,227^{\circ}\mathrm{C}} = -165\mathrm{kJ\,mol^{-1}\,CO\ converted} \tag{2.19}$$

$$\mathrm{CO} + 2\mathrm{H_2O} \rightleftharpoons \mathrm{CO_2} + \mathrm{H_2} \quad \Delta H_{\mathrm{r},\,227^{\circ}\mathrm{C}} = -40\mathrm{kJ\,mol^{-1}\,CO\ converted} \tag{2.20}$$

   The Gibbs free energy equation is given by:

$$\Delta G = \Delta H - T\,\Delta S = -R_{\mathrm{g}} T\,\log_e(K_{\mathrm{eq}}) \tag{2.21}$$

   and the partial molar Gibbs free energy or chemical potential (μ_{i}) is given by:

$$\mu_{\mathrm{i}} = \left(\frac{\partial G}{\partial N_i}\right)_{T,p,N_{j\neq 1}} \tag{2.22}$$

   where, $\Delta H = \Delta H_{\mathrm{r},\,227^{\circ}\mathrm{C}}$ is the enthalpy of reaction at 227°C, ΔS is the entropy change for the synthesis reaction with an order of magnitude -0.2kJ $\mathrm{mol^{-1}CO}$ converted at 227^{o}C [99], R_{g} is the universal molar gas constant, K_{eq} is the reaction

equilibrium constant where, $K_{eq} > 0$, for $T \leq 400^{o}$C [99], T is absolute temperature, p is absolute pressure, N_i is the number of moles of species i and N_j is is the number of moles of species j. It can clearly be seen that the sheer magnitude of the enthalpy of reaction of the Fischer-Tropsch synthesis disproportionately dominates the Gibbs free energy and by extension the chemical potential calculations and indeed the overall thermodynamic description of the Fischer-Tropsch synthesis. Temperature exacerbates this exothermic dominance, as such it is a critical reaction system property to be controlled.

It is pertinent to mention that controlling temperature is a delicate balancing act, which must be considered carefully with some trade-offs. For example, on one hand, severely reducing the temperature results in very slow kinetics, which decreases hydrocarbon productivity and may even extinguish the reaction altogether, while on the other hand, excessive temperature rise leads to thermal runaway and in extreme cases, explosions. Subsequent sections and chapters of this thesis will look at methods of maintaining a narrow optimal window of temperature in order to maximally benefit the reaction system.

2. *Partial pressure of H_2 and CO*

   The preponderance of research works reveal that the selectivity is displaced in favour of heavier molecular weight hydrocarbon compounds and oxygenates as the total pressure of the reacting system is increased [43]. Increasing the H_2:CO ratio has also been reported to increase the volume of lighter hydrocarbon products and reduce the olefin contents [97, 98].

3. *Space Velocity*

   Essentially, the olefin-to-paraffin ratio increases with increasing space velocity (or reducing residence time), in other words, a reduction in conversion per pass [100]. Iglesia et al [101] also reported an increase in the molecular weight of products with reducing space velocity (or increasing residence time). The selectivity to methane and olefins decreases with decreasing space velocity, while the selectivity towards paraffins was observed to be constant [101].

4. *Time on stream*

   As the catalyst remains on stream, it gets deactivated with time and the selectivity also changes over time owing to carbonaceous deposits on the active sites of potassium promoted catalysts (often reversible by hydrogen treatment at 350^{o}C) [43]. As deactivation occurs, oxygenates become more selectively produced according to Donnelly et al [97], while selectivity towards methane and low molecular weight hydrocarbons also rises on iron catalysts [97, 102, 103].

5. *Reduction of catalyst*

   Pre-treatment methods which the catalyst is subjected to also affects its selectivity. Pre-treatments involving CO and CO/H_2 have been reported to show high selectivity towards diesel fuel and wax (C_{12+}) to the disadvantage of methane and other short chain molecules C_2-C_4 [26, 50, 104–107]

2.3 The Fischer-Tropsch reactor configurations

The cardinal challenge in the design of Fischer-Tropsch synthesis reactors is the high exothermicity coupled with the high sensitivity of the product selectivity to the prevalent reactor temperature. The heat released during the CO hydrogenation and polymerisation reaction is in the order of 20-25% of the calorific value of synthesis gas [27]. As such, an excellent heat rejection system is required. This quest for proper thermal management of the reaction has informed the various reactor designs available on the market [33].

This section briefly reviews the typical Fischer-Tropsch reactors currently in commercial use. Subsection 2.3.1 provides a brief overview of the structure of the multii-tubular fixed bed reactor (MTFBR); the chosen reactor for this thesis. Section 2.4 will be devoted to the heat transport challenges, suggested mitigations and mathematical modelling of the MTFBR.

2.3.1 Multi-tubular fixed bed reactor

Figure 2.10 is the schematic diagram of a multi-tubular fixed bed reactor (MTFBR). It is built like a vertically oriented shell and tube heat exchanger, except that the tube side is packed with stationary catalyst pellets for carrying out the chemical reaction; the reactions are assumed to take place only on, or within the catalyst pellets. The MTFBR is able to handle both gas-solid-liquid (three-phase) reactions and gas-solid (2-phase) reactions. Typical measurements include up to 5cm inner diameter tubes of length 2-12m and catalyst pellets in the diameter range of 2-3mm.

Being a gas-limited reaction (i.e. high liquid reactant flux to the catalyst particle, low gas reactant flux to the particle [108–110]), the reactor is often operated in the trickle bed hydrodynamic regime during the LTFT synthesis, i.e. a continuous gas (syngas and other recycled gaseous effluents) phase and a distributed liquid (recyclyed liquid effluents) phase in which both fluids flow co-currently in a downward flow and the main

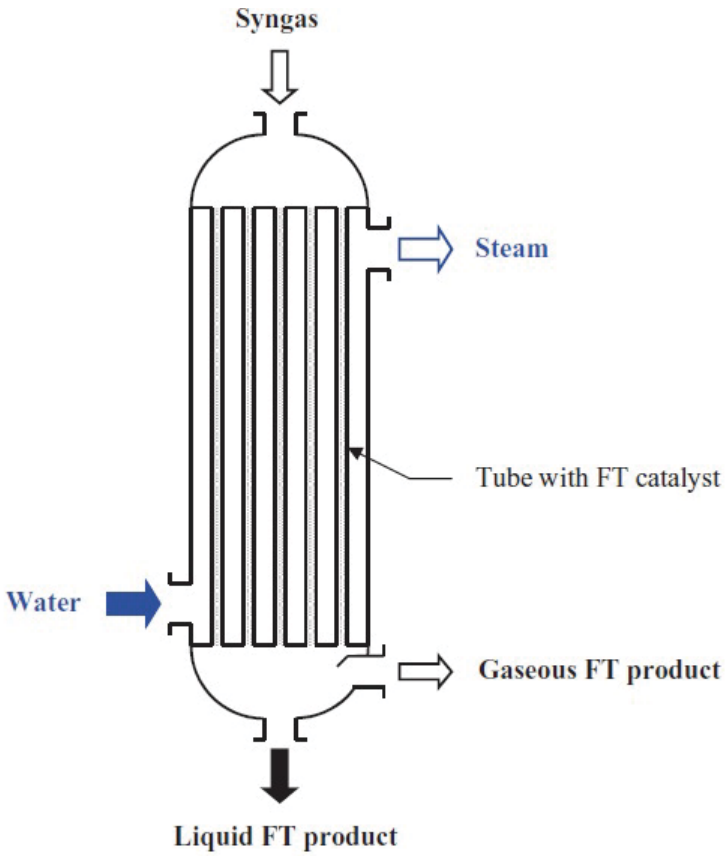

FIGURE 2.10: Multi-tubular fixed bed reactor [1]

mass transport resistance occurs in the gaseous phase. Gas-liquid separation occurs at the bottom of the reactor.

The pressure drop across the reactor more than any other factor, determines the particle size of the Fischer-Tropsch catalyst. While very small catlyst particles ($\leq$ 1.0mm) may reduce the mass transfer resistance by reducing the diffusion length, they greatly increase pressure drop and the converse is true for larger particles. Traditionally, on-line replacement of catalysts had been impossible and catalyst had to be changed out during shutdown. Ansorge [22] however reports that Shell has developed an automated catalyst loading system with *in situ* regeneration.

The principal operational constraint of the MTFBR in the Fischer-Tropsch synthesis is its ability to control temperature through efficient heat transfer. This operational requirement in effect limits the upper diameter of the tubes and the volumetric productivity of the catalyst. Apart from its relatively high capital cost and poor heat transfer characteristics, the MTFBR is still in commercial use and has the following advantages over other reactors:

1. The MTFBR is robust and has the longest proven track record of carrying out stable and reliable Fischer-Tropsch synthesis
2. The MTFBR of all Fischer-Tropsch reactors best approximates plug flow behaviour, as such, it is generally more efficient in terms of the achieved conversion per unit reactor volume for positive ordered chemical reactions [111].
3. It obviates the need for separating the reaction products form the catalyst [112]
4. Kinetic data, catalyst performance and hydrodynamics from a single tube are largely representative at the pilot plant scale [112]
5. It features low fluid inventory [17]

2.3.1.1 Micro-channel reactor

A subset of the multi-tubular fixed bed reactor are the microchannel reactors. These intensified reactors have smaller diameter tubes/channels, of the order of millimetres, which come in a wide variety of geometries other than circular. The tubes are packed or coated with much smaller catalyst pellets ($\leq 100\mu$m) and the linear velocity of the syngas is significantly increased. With the heat and mass transport resistances significantly reduced, it comes as no surprise that these reactors have superior heat and mass transfer characteristics. They are often marketed as being modular and more compact. Velocys [4], a subsidiary of Oxford catalysts, has been at the vanguard of this technology.

A major drawback of this technology is the danger of the tubes fouling up, causing immense pressure drops and they can be very difficult to clean.

2.3.2 Slurry bubble column reactor

Figure 2.11 is a schematic representation of the slurry bubble column reactor (SBC). This reactor is a vertically oriented vessel which contains a slurry (fine catalyst powder suspended in Fischer-Tropsch wax in the liquid state). There is a gas distributor at the bottom of the reactor through which syngas accesses the vessel and bubbles up through the slurry mixture. This reactor is designed to operate strictly in the three phase regime, i.e. gas-liquid-solid reactions.

The reactor is equipped with several heat exchanger/cooling tubes on the inside of the reactor, through which the heat generated by the reaction is rejected. The heat removal is greatly enhanced by the turbulent and constant movement of the slurry- this enhanced heat removal capability particularly makes the reactor attractive. The

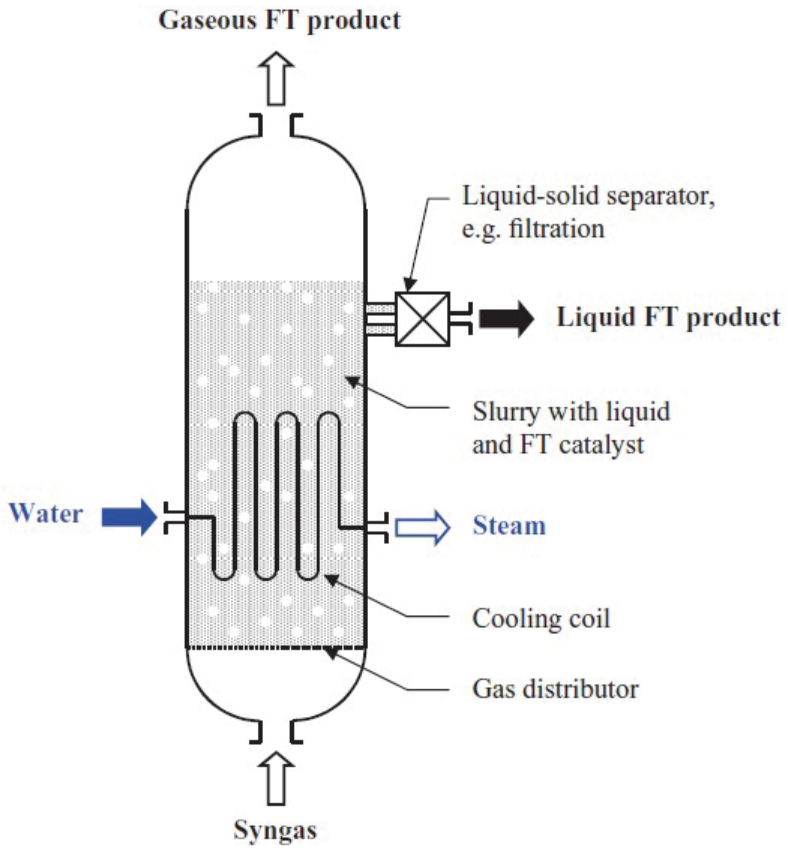

FIGURE 2.11: Slurry bubble column reactor [1]

slurry is constantly produced alongside the products from the reactor, it is therefore very important to have an efficient phase separation unit operation downstream, which separates the products from the fine catalyst powder. This constitutes the cardinal drawback of this reactor as the the separation process almost always invariably involves catalyst loss. Catalyst loss means that the reactor is in principle, economically better suited to the use of the cheaper and more ubiquitous Fe catalyst as opposed to the more expensive Co. The upside to this arrangement however is that the catalysts can be regenerated and re-introduced into the process without having to shut down the process. The constant movement of the catalysts and collision with the walls of the reactor will require them to have good mechanical strength and attrition resistance. The pressure drop in the reactor is dependent on the hydrostatic height of the slurry in the column, as opposed to the catalyst pellet size.

A cross between the MTFBR and SBC is called an ebullated or moving bed reactor. In this reactor, advantage is taken of the positive sides of both the MTFBR and SBC, including doing away with the need to separate catalyst from products and achieving good temperature control at the same time. Syntroleum Corporation is one of the comapnies looking to develop this concept further [113].

2.3.3 Fixed fluidised bed reactor

The fixed fluidised bed reactor (FFB), depicted in Figure 2.12, is one of the two reactors categorised under the Fluidised bed reactors for the Fischer-Tropsch synthesis. This category of reactors are strictly two-phase (gas-solid) reactors, as such they are only employed in the HTFT synthesis. Like the SBC, the catalyst particles are dispersed and suspended in an upward movement of flow of a continuous phase fluid; however, the catalyst particles are extracted from the products. The design constraint of the fluidised bed reactors to operate in the gaseous phase means that the Fischer-Tropsch products are necessarily restricted to lower α_{FT} selectivities as shown in Figure 2.9.

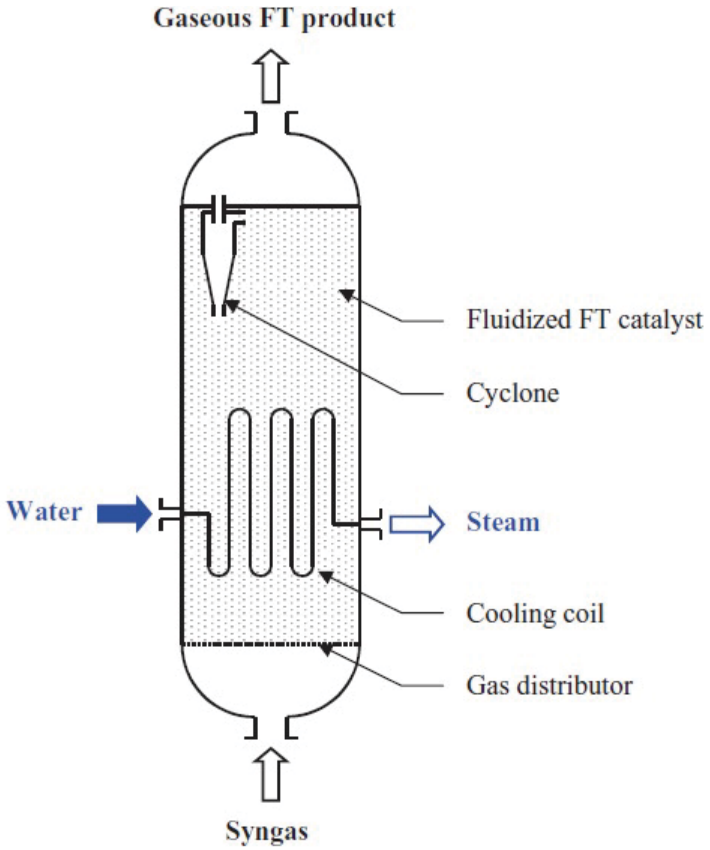

FIGURE 2.12: Fixed fluidised bed reactor [1]

The fixed fluidised bed is the simpler of the two designs in this category. It comprises a vertical vessel equipped with: a gas distributor at the bottom of the vessel, through which syngas is supplied to the process, several heat exchanger cooling coils on the inside of the reactor and cyclones at the top for separating the catalyst from the products. The fixed fluidised beds are generally more difficult to control and are constrained by the strict gas flow rate and catalyst particle size requirements ; they have however been shown to be more efficient than their circulating bed counterparts.

2.3.4 Circulating fluidised bed reactor

The circulating fluidised bed (CFB) reactor is shown in Figure 2.13, with the same basic design elements as its fixed fluidised variation. Its design and operation are however more complex than the fixed fluidised bed reactor; it operates at a higher gas velocity and the catalyst pellets are entrained. the pressure drop is determined by the gas phase flow.

Theoretically, the CFB reactor has a wider window of operation, but it is subject to many operational challenges. the catalyst particles must be mechanically strong in order to withstand the high rate of attrition and mechanical stresses experienced through the circulating motion in the reactor. In general, the catalyst particle size distribution is a compromise between the catalyst activity, fluidisation properties of the bed and the ease of separation from the products.

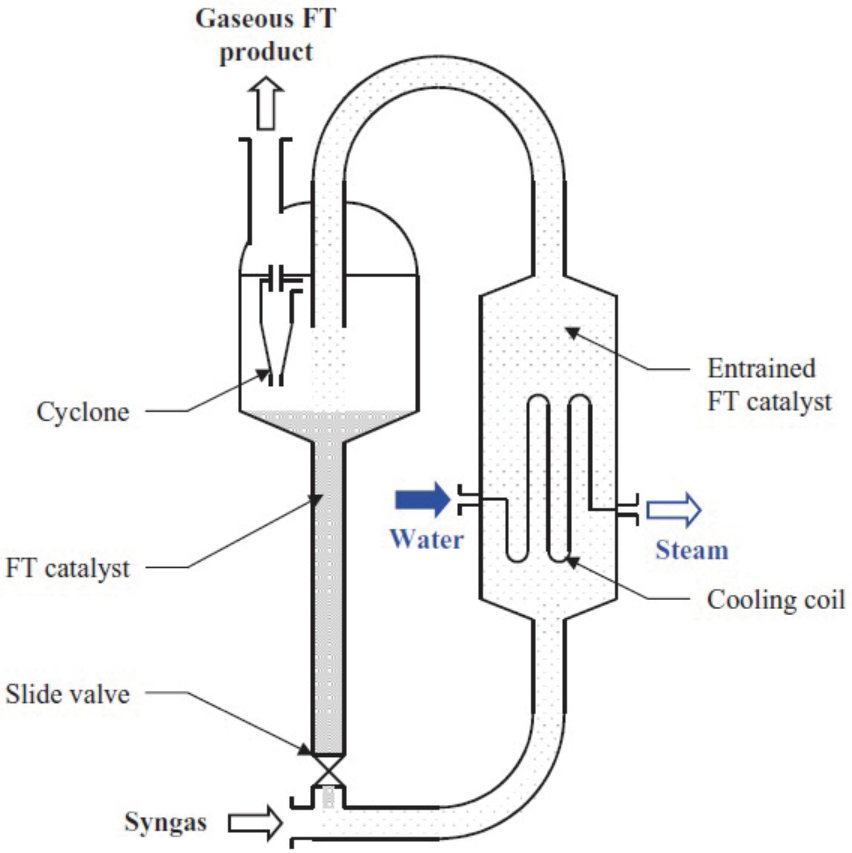

FIGURE 2.13: Circulating fluidised bed reactor [1]

2.4 Modelling the multi-tubular fixed bed reactor

From section 2.3, it is clear that no one reactor perfectly meets all the operational requirements of the Fischer-Tropsch synthesis and as such, compromises and trade-offs have to be made. This thesis is focussed on the requirement to control temperature with the intention of maintaining an optimal, narrow window of catalyst selectivity to the desired spectrum of products. The multi-tubular fixed bed reactor quite clearly is the most deficient in this respect, as such it will be the case study for the remainder of this work.

As pointed out earlier in subsection 2.2.5.1, temperature (and in effect selectivity) control may be achieved through managing process conditions better, or the outright reconfiguration of the reactor/catalyst arrangement or indeed a combination of both. The second approach may not always be available to plants already in existence as the capital cost of shutting down and swapping unit operations and ancillary facilities out for more modern ones may prove prohibitive. In such a situation, retrofitting the existing plant may be a cheaper and less dramatic option. The work done in this thesis may therefore find useful practical applications in the so-called "brown-field" Fischer-Tropsch synthesis plants seeking to improve their productivity.

Finally, if the methods suggested in this work can find use in the "worst" case scenario as far as heat rejection is concerned, then such techniques may become useful transferable engineering skills, possibly informing the design of future reactors. The next subsections will briefly look at traditional methods of handling the challenge of exothermic reactions in multi-tubular fixed bed reactors, and how, well engineered, encapsulated phase change materials can add to this mix of strategies.

2.4.1 Exothermic reactions in the multi-tubular fixed bed reactor

The multi-tubular fixed bed reactor is the work horse of the chemical processing industry, used to carry out reactions with large heat effects. For the preponderance of industrial syntheses, MTFBRs are typically operated in a steady state fashion, i.e. under constant operations, over protracted operational runs. The design strategy is therefore to achieve an optimum steady state operation [17].

The MTFBR belongs to the class of reactors called "isothermal" reactors. This classification is not because they are actually isothermal in operation, rather, it is because they are designed with integrated and indirect heat exchange/cooling mechanisms with the aim that they will be isothermal [17, 114]. In order to ensure proper control of the reactor and avoid irreversible damage to the catalyst, indirect heat exchange is carried

out through external cooling around the tubes in the reactor. This requirement can only be met if:

1. The temperature of the coolant fluid (saturated water in the case of the FTS) is close to the desired catalyst temperature
2. There are large heat exchange surfaces per unit catalyst volume and,
3. A sufficiently large molar flow rate of the synthesis gas in order to ensure good heat transport from the packing to the heat exchange surface.

This removal of heat while an exothermic chemical reaction is in progress has the effect of adapting the temperature profile over the flow path and thereby, influencing the course of the reaction, i.e. the conversion, selectivity, yield, etc. The competition between reaction heat generation and its removal through the tube walls gives rise to axial and radial temperature profiles, and in particular, single-humped, temperature profile peaks, occurring near the entrance of the reactor. This hump, often referred to as a hotspot, is associated with the peak conversion rates. In other words, most of the reaction occurs near the entrance of the reactor, at the location of hotspot and very little, if at all any reaction occurs further down the axial length of the reactor, thus under-utilising the catalyst bed [115].

The challenge of exothermicity in MTFBRs is normally tackled by:

1. Recycling fluid effluents from the reactor at high velocity in order to generate turbulent flow- this however comes at high re-compression cost and conversion is necessarily limited to 20-30% per pass. In addition, it is vital to ensure the even distribution of the liquid in order to avoid thermal runaway and blockages in "dry" tubes [12, 115].
2. Reducing the upper limit of the tube diameters- this is the next option once all possibilities of heat transport improvement by recycling have been exhausted. Although this facilitates the production of higher pressure steam, it comes at an increased cost of manufacturing the reactor [10, 115].
3. Reducing catalyst activity: this is achieved by using catalysts of different activities over the reactor length, by diluting them with inert substances such as silicon dioxide, silicon carbide, etc.

This thesis seeks to explore option (3) further. In particular, it looks to propose the use of new inert materials- "active-inert", thermally functional, phase change materials.

The next section looks at some previous work done in the area of catalyst dilution with respect to the Fischer-Tropsch reaction and sets the scene ready for the introduction of this new catalyst diluent.

2.4.2 Reactor modelling

Reactor modelling is essential in order to optimise the reactor's productivity and safety elements. It comprises two interdependent aspects: in the first, there is the macroscopic description of the hydrodynamics of how the different phases participating in the reaction behave, including the heat and mass transport effects. In the second, the Fischer-Tropsch reaction model, involving the consumption and production of chemical species in the region of influence of mass and heat transfer.

Owing to the heat extraction at the tube walls by the cooling medium, temperature (and by extension, concentration) gradients are set up in a direction perpendicular to the direction of flow. In addition to the axial concentration and temperature gradients, the turbulent effect of the packings may induce an axial diffusion of heat (Fourier's law) and mass (Fickian diffusion law) which opposes the fluid flow [116]. It is therefore vital for any mathematical model attempting to describe the spatial distribution of mass and heat in the reactor to take into account both the radial and axial dimensions.

A rigorously comprehensive model will seek to describe the fluid on a microscopic scale, take into account the spatial distribution of each catalyst particle (and encapsulated phase change material), as well as the discontinuous arrangement in the bed. Not only will this level of detail require infinitely large computing resources, it is also unnecessary. A more practical approach will be to treat the catalyst bed as a pseudo/quasi-homogeneous-dispersion-continuum, with its physical properties averaged out. It then becomes possible to write differential equations describing the bed using effective transport parameters. Although the bed properties are space averaged, the heat and mass transfer equations within the catalyst pellet are solved for the actual pellet size being used [116]. In effect, the volumetric rates of reaction and heat generated can be computed at any location within the bed as though a catalyst pellet and its associated voidage were acting at the location in question.

Several researchers have put forward Fischer-Tropsch reactor models of sundry complexities. Atwood et al [84] put forward a one-dimensional heterogeneous plug flow model to study the effects of parameters on industrial reactors. A two-dimensional pseudo-homogeneous plug flow model, neglecting the limitations of intra-particle diffusion was examined by Bub et al [68]. Jess et al [89] considered a two-dimensional pseudo-homogeneous model exclusive to the Fe-catalysed conversion of N_2-rich syngas. Wang

et al [117] proposed a one-dimensional heterogeneous model, using the modified Soave-Redlich-Kwong equation of state and accounting for pore diffusion limitations. Marvast et al [118] proposed one-dimensional and two-dimensional pseudo-homogeneous models using bi-functional catalysts. De Swart et al [119] presented a one-dimensional heterogeneous model for a cobalt catalysed reaction. Philippe et al [120] studied the effects of the operating conditions and thermal properties of Co-based catalyst on the behaviour of the MTFBR using a gas-solid two-dimensional homogeneous model. Güettel and Turek [121] compared one-dimensional models of various Fischer-Tropsch reactor types. Jess and Kern [5, 90, 91] compared Co and Fe catalysts using two-dimensional pseudo-homogeneous models, accounting for mass transfer limitations and radial heat transfer within the MTFBR. Rafiq et al [122] presented a two-dimensional pseudo-homogeneous model for bio-syngas conversion over Co as catalyst. Many of these models have their specific drawbacks including: neglecting the mass transfer limitations (pore diffusion, etc.), not accounting for radial heat transfer gradients in the MTFBR (as in the one-dimensional models) and leaving out the effect of radial dispersion (two-dimensional models).

Figure 2.14 presents graphical algorithm for working through the complexities of modelling a fixed bed reactor in order to arrive at the appropriate reactor model, needed to describe the system in hand. The cut-off points for the relevance of various internal and external heat and mass transport limiting factors are pre-determined based on the feed and reactor design entry conditions using dimensionless quantities/ratios put together by Mears [123, 124]. This algorithm will be put to practical use in chapter 3 during the mathematical model formulation.

None of the MTFBR Fischer-Tropsch synthesis mathematical models available in open literature specifically considers the effects of catalyst dilution with inert substances or indeed phase change material for the purpose of temperature control. Previous studies involving other exothermic reactions which either catalyst dilution or the use of phase change materials have been adopted as strategies for modulating chemical reactions are as follows: Luyben [19], Nie et al [126] and Calverley et al [127] have examined the concept of catalyst dilution using zoned/graded catalytic reactor arrangements for various exothermic reactions such as the partial oxidation of ortho-xylene in multi-tubular fixed beds, but none of them has specifically considered the Fischer-Tropsch reaction nor explored the use of encapsulated phase change materials as diluents and potential distributed temperature controllers. Pattison et al [128, 129] considered the use of phase change material as a temperature control strategy in an autothermal, steam methane reforming, catalytic plate micro-reactor, but not in a fixed bed reactor or specifically for the Fischer-Tropsch reaction. Mittal et al [130] presented a one-dimensional model

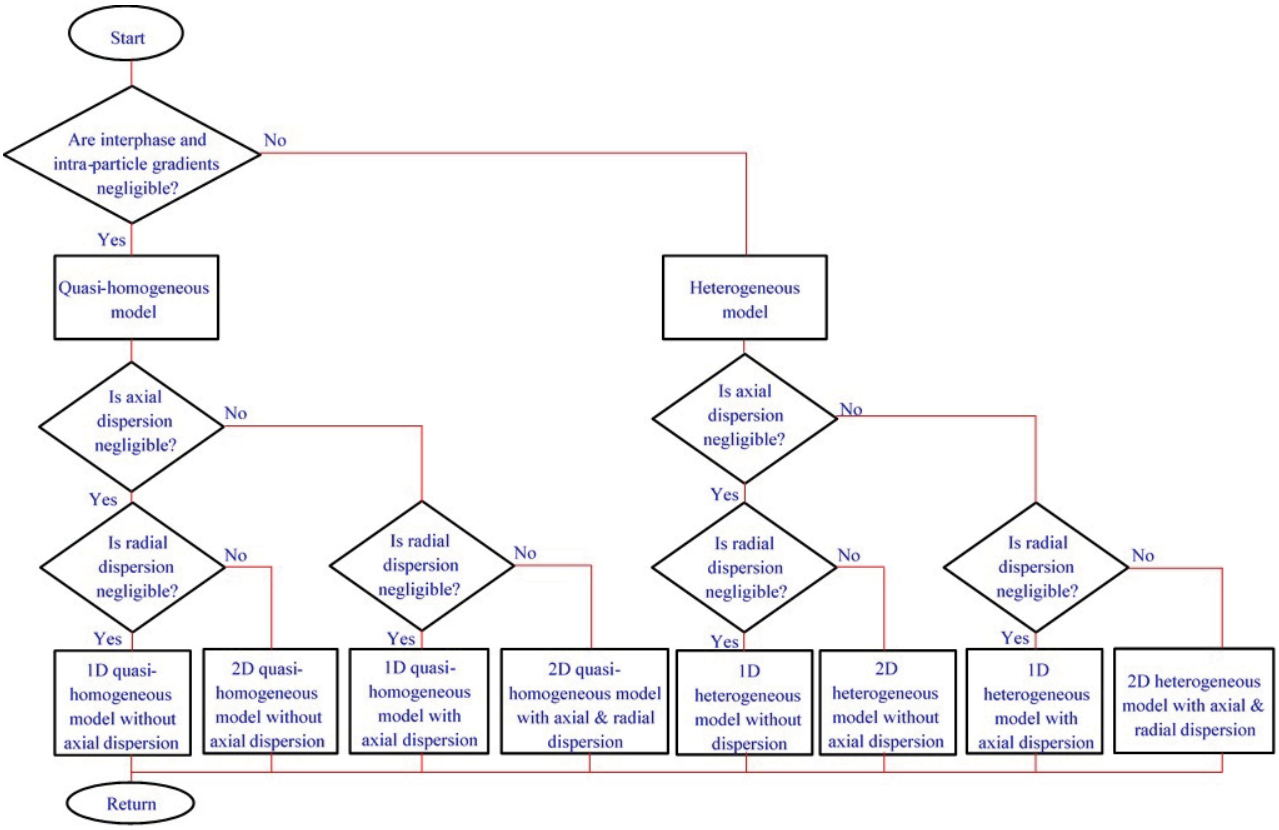

FIGURE 2.14: Algorithm for selecting appropriate reactor model, adapted from [125]

of a novel process concept entailing the time-segregated, hybridisation of biomass gasification/combustion in a monolith, micro-fluidised bed reactor with alternating reaction and phase change material filled channels, arranged in a "chequerboard" pattern, they however did not consider the Fischer-Tropsch aspect of processing the resultant syngas. Zhang et al [131] examined the use of paraffin wax nano-PCM for controlling excess temperature from heat accumulation caused by auto-acceleration or gel effects in the polymerisation of methyl methacrylate in a stirred batch reactor. Zhang et al [131] have also considered the use silica-encapsulated indium particles for temperature control in the catalytic oxidation of methanol in a fixed bed reactor. The current research examines the concept of maintaining the Fischer-Tropsch multi-tubular fixed bed reactor within a narrow, optimum temperature range, using carefully selected phase change material as a catalyst bed diluent. The phase change material unlike other inert catalyst diluents can operate not only in the sensible temperature region, but in addition, brings with it the added advantage of its latent enthalpy of fusion, acting as a temperature buffer and delaying any significant temperature rise in the reactor in the course of the reaction.

Encapsulated phase change material in Fischer-Tropsch synthesis fixed bed reactors may be looked upon as an "active inert". "Inert" in this case means that they do not promote, inhibit or directly participate in the chemical reactions. "Active" refers

to the fact that when the reactor temperature reaches the fusion temperature of the phase change material, the fusion enthalpy, which is up to two orders of magnitude of the normal thermal capacity, of the phase change material acts as a temporary buffer for the reaction heat, thus preventing local temperature rises which would under other circumstances give rise to hotspots.

This thesis specifically examines this concept of catalyst dilution to bring about temperature modulation, using the combined effect of the phase change material and traditional saturated water wall-cooling in a Fe-catalysed, Low Temperature Fischer Tropsch (LTFT), fixed bed reactor.

2.4.3 Phase change materials in chemical reactors

Before concluding this chapter, it is pertinent to make some remarks about phase change materials and how they can be adapted for use in chemical reactors.

Phase change materials have found application in the transient thermal management of micro-electronics [128, 132], thermal energy storage (TES) [133] and temperature stabilisation in modern buildings [134]. With modifications, they may also be used in chemical reactors. Proportional-integral-differential (PID) units used for supervisory temperature control in reactors may be limited by the size and location of thermocouples within the reactor; it is also impractical on an industrial scale to have thermocouples in all the tubes of the MTFBR [17]. This is especially true for heterogeneous reactions like the Fischer-Tropsch synthesis, where chemical reactions occur on active catalyst sites. A phase change material, with a phase transition temperature (ptt) lying between a nominal operating temperature (e.g. the lower end of the temperature spectrum for the LTFT, 200°C) and the onset temperature of catalyst sintering ($\approx$ 260°C [93]) or catalyst de-activation (whichever occurs first) can act as a rapid-responding, distributed temperature controller. In the simulation presented in this thesis, tin (ptt= 231.9°C) is the phase change material of choice.

Unlike in TES applications, bulk or large PCM is not very useful in reactors because of non-uniform heat transfer. For phase change material to find relevance in a MTFBR, it should:

(i) as in the case of TES applications, it should ideally have properties as summarised in table 2.10

(ii) be small enough to melt swiftly (nano to millimetre-sized). As a rule of thumb, a unit reduction in the characteristic length of the phase change material reduces the melt time by a factor of 10 [139, 140],

Table 2.10: Desirable qualities of phase change materials, adapted from [135–138]

Thermodynamic properties	(a) Melt in the desired temperature range (b)High latent enthalpy per unit volume (c) High thermal conductivity (d) Small volume changes on phase transition and small vapour pressure at operating temperature in order to reduce containment problems (e) Congruent melting
Kinetic properties	(a) No super-cooling or super-heating
Chemical properties	(a) Complete reversible freezing and melting (b)Chemical stability (c) No degradation after a large number of freezing melting cycles (d) Non-corrosive (e) Non-toxic, non-flammable and non-explosive
Economic properties	(a) Effective cost (b) Large scale availability

(iii) be encapsulated in an inert shell (e.g. SiO_2), in order to avoid agglomeration, leakage or contamination. It is noteworthy that silica has been found to be particularly advantageous in Fe-catalysed Fischer-Tropsch synthesis reactors. This is because silica supported Fe catalysts are more stable and are far less susceptible to deactivation and sintering due to the SiO_2 acting as a spacer, preventing the catalyst grains from growing together [11, 141, 142].

(iv) maintain very close contact with the catalyst in order to quench local temperature rises.

In summary, this chapter has extensively, qualitatively considered the Fischer-Tropsch synthesis and possibilities of catalyst bed dilution with phase change material. The next chapter will look at developing the mathematical model for describing the reaction system in a MTFBR.

Chapter 3

Mathematical and Numerical Model Formulation

"It is not wise to violate the rules
until you know how to observe them."

T.S. Eliot, (1888-1965).

This chapter presents the mathematical formulation, governing equations, and numerical implementation of the conservation equations describing the Fischer-Tropsch reaction in a multi-tubular fixed bed reactor. The various types of mathematical models employed in simulating fixed bed reactors range from basic to the comparatively complicated. The methods and assumptions deployed in computing properties (concentration, pressure and temperature) in each discretisation node bring about the distinction between the various reactor models. The chemical and transport phenomena encountered in fixed bed reactors are inherently complex. This chapter however attempts to systematically work through the physico-chemical peculiarities of the system in order to arrive at a relatively simple yet sufficient model which, adequately captures the essential mechanisms involved. Section 3.1 examines the description of the reactor geometry and the transport phenomena occurring on the bulk and catalytic/sub-catalytic scales. Section 3.2 looks at the model selection criteria for the different types of reactor models and simplifying assumptions, while section 3.3 sets out the governing conservation equations as well as the additional energy balance for the phase change material diluent. Finally, section 3.4 puts forward the numerical implementation of the preceding mathematical model in COMSOL MULTIPHYSICS 4.4 [21].

3.1 Reactor Geometry

Figure 3.1 shows a single, typical reactor tube packed with stationary catalyst pellets and inert diluents. The coolant fluid, saturated water in this case, runs on the shell side of the reactor, maintaining the walls at isothermal conditions by absorbing the reaction heat. Multi-tubular fixed bed reactors typically comprise several thousand tubes which are identically packed [17] and as there are neither inter-tube interactions nor rotational effects, it is sufficient to represent the entire reactor with a single tube in a mathematical model. The assumption of identical packing in each tube, such that, there is no variation of porosity in the angular direction [143], suggests that the tube may be considered to be symmetrical, thus enabling a reduction in the computational effort. Figure 3.2 shows the geometric basis of the mathematical model.

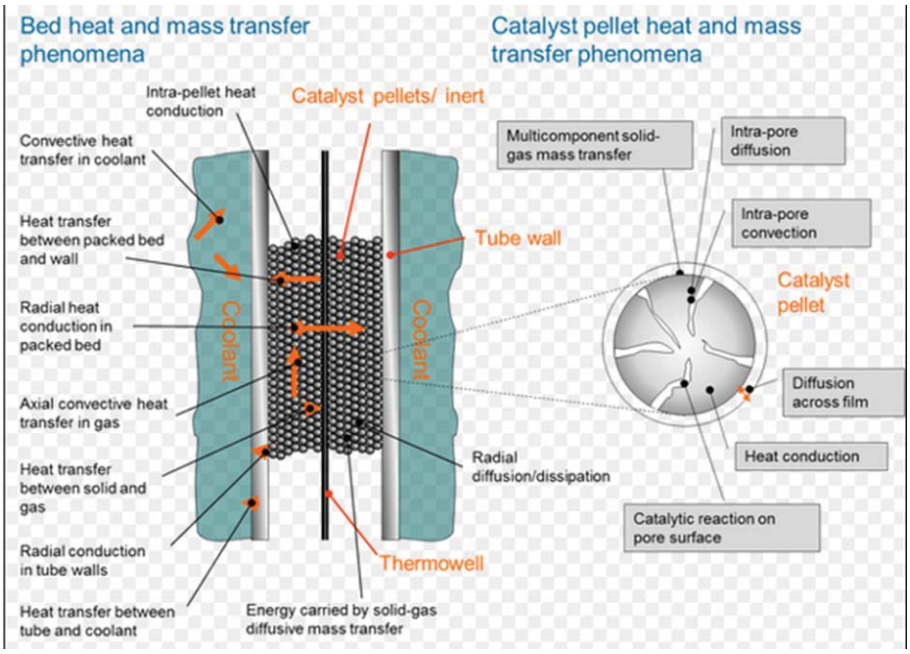

FIGURE 3.1: Reactor tube packed with catalyst [144]

The principal challenge with modelling a heterogeneous reactor is that the reaction and transport phenomena occur in dimensions of different orders of magnitude namely: (I) the inter-catalyst macro-pores or bulk scale and, (II) the intra catalyst micro-pores. The reaction is however, usually assumed to take place only on, or within the catalyst pellets.

3.1.1 Macro-scale transport phenomena effects

The packing in each tube, in the multi-tubular fixed bed reactor, may be divided into a core zone and a wall zone, as shown in Figure 3.3. The temperature profile in the

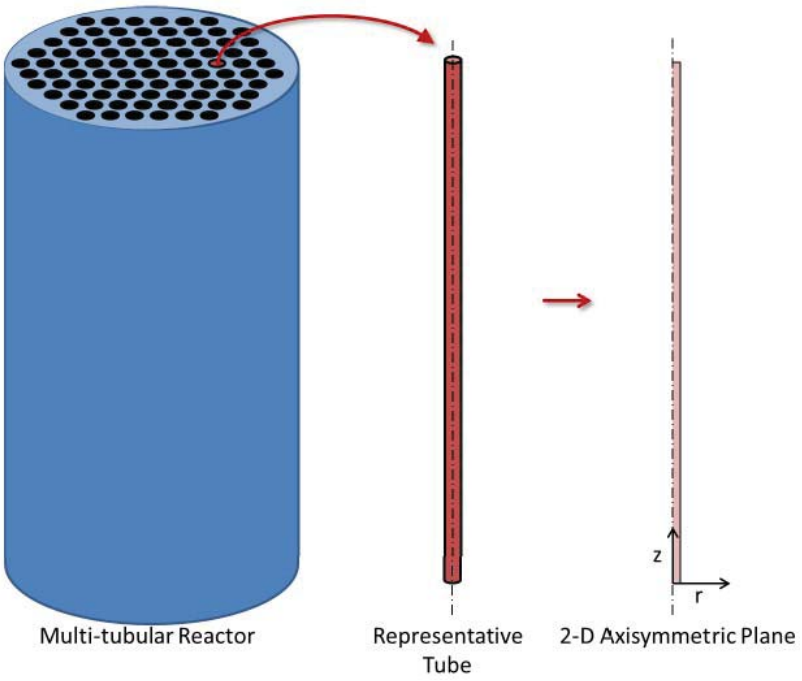

FIGURE 3.2: Model geometry represented by the 2D-axisymmetric plane of a single tube [33]

core zone is parabolic, while the wall zone shows a sharp dip in temperature. The heat transfer coefficient and thermal conductivity at the wall are individually made up of the sum of their respective flow-dependent and non-flow-dependent aspects; some of the correlations showing this are recorded in Appendix A. The heat flux at the wall ($\dot{Q}_{\mathrm{w}}$) is a function of the difference between the temperature of the wall (T_{w}) and that of the fluid inside the bed/tube, contiguous to the wall ($T_{\mathrm{r=R_t}}$) according to:

$$\dot{Q}_{\mathrm{w}} = h_{\mathrm{w}}(T_{\mathrm{r=R_t}} - T_{\mathrm{w}}) \tag{3.1}$$

where, h_{w} is the wall heat transfer coefficient. The radial mass flux at the wall is zero, as the wall is impermeable.

The temperature and pressure gradient across the bed could lead to the variation of fluid density over the bed, which leads to free convection, which in turn brings about additional dispersion of heat and mass (or molar) in the axial direction[145, 146]. Heat and mass transport occur in both the fluid (reactants/products) and solid (catalyst) phases in parallel and series concurrently. Bulk fluid transport in the axial direction gives rise to convective molar ($J_{\mathrm{z,\,bulk}}$) and heat ($Q_{\mathrm{z,\,bulk}}$) transport which are represented by the following quantities respectively:

$$J_{\mathrm{z,\,bulk}} = -u_{\mathrm{z}}\frac{\partial c_j}{\partial z} \tag{3.2}$$

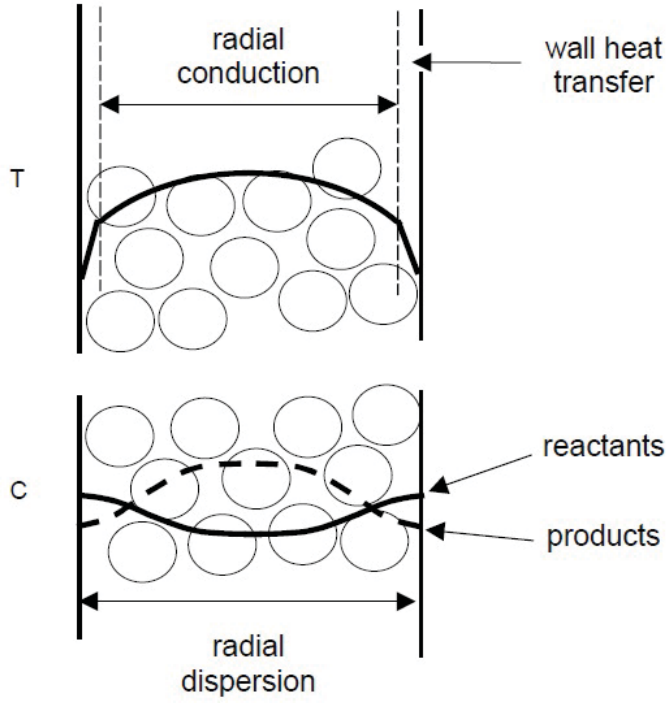

FIGURE 3.3: Radial concentration and temperature profiles in a fixed bed reactor [143]

$$Q_{\mathrm{z,\,bulk}} = -u_{\mathrm{z}}\rho_{\mathrm{f}}C_{\mathrm{p,f}}\frac{\partial T}{\partial z} \tag{3.3}$$

where, u_z is the axial component of the velocity vector, c_j is the concentration of any generic chemical species j, ρ_{f} is the average fluid density, $C_{\mathrm{p,f}}$ is the effective fluid heat capacity and z is the unit vector in the axial direction. The reaction fluid flows

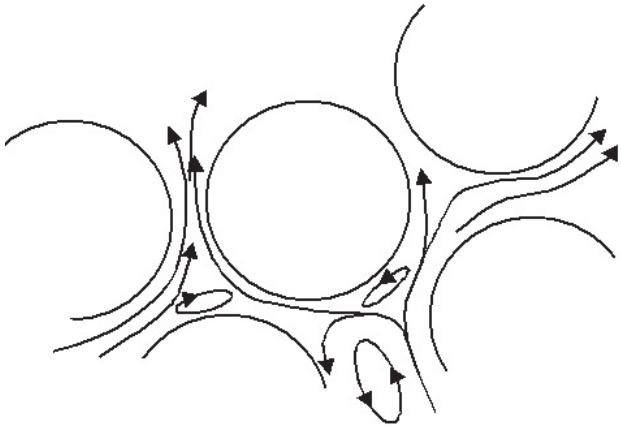

FIGURE 3.4: Mixing of fluid elements in between catalyst particles [143]

through a tortuous, inter-particle path in a chaotic fashion (see Figure 3.4), bringing about axial and transverse mixing due to turbulence and molecular diffusion and conduction; this form of transport, particularly at high flow rates, is known as heat and

mass "dispersion"[111]. Where there is a temperature gradient in the fluid immediately surrounding the catalyst pellets, a temperature gradient also develops over the catalyst pellets. Heat is transported between any two adjacent particles by direct exchange (conduction), through the interstitial fluid in between the pellets (conduction/convection) or by radiation (see Figure 3.5, radiation not shown). Radiation is negligible at temperatures below 400°C [147], a temperature well above the ceiling temperature of the LTFT.

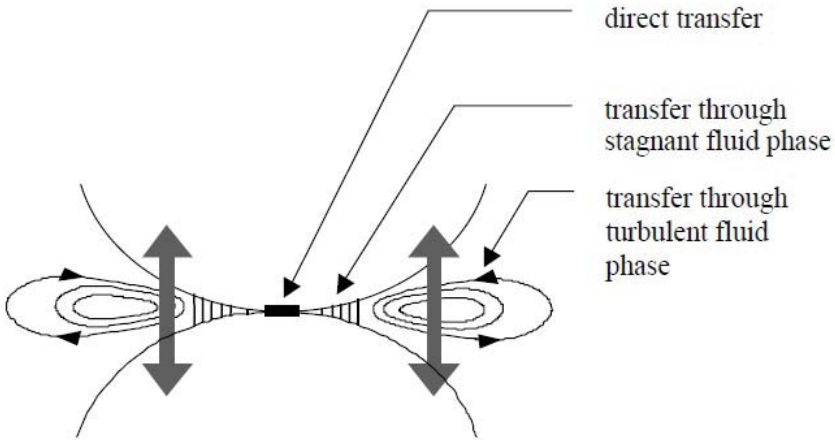

FIGURE 3.5: Inter-particle heat transfer in between two catalyst particles in contact[143]

3.1.2 Micro-scale transport phenomena effects

Inside the catalyst pellet is a tortuous network of pores which increases the specific surface area available for adsorption and reaction. The diffusion of mass and heat from the bulk fluid phase, through the stationary boundary layer of fluid around the catalyst pellet, and eventually through these pores, is therefore crucial to the observed rate of reaction. A summary of the steps followed by a chemical species in a heterogeneous reactor is given below [148] and shown schematically in Figure 3.6:

(1) Convective transport of the reactant species form the bulk reaction mixture to the surface of the catalyst pellet

(2) Diffusion of reactants from the pores of the catalyst to the active sites

(3) Adsorption of the reactants to the active site

(4) Chemical reaction and formation of adsorbed products

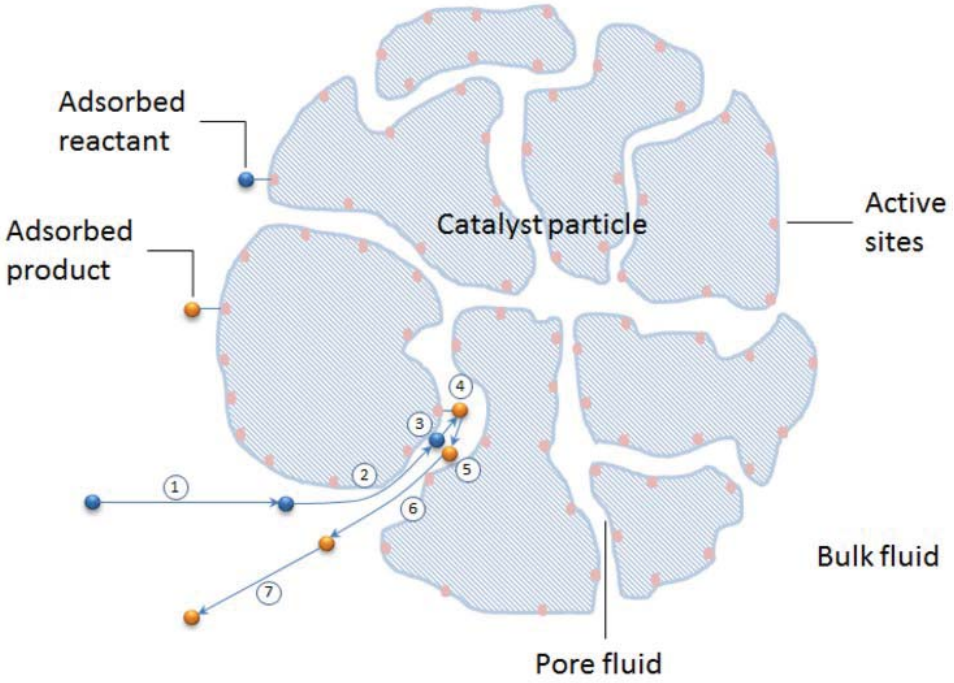

FIGURE 3.6: Heteregeneous reaction mechanism [149]

(5) Desorption of products from active sites

(6) Diffusion of products from the catalyst pores to the surface

(7) Convective transport of products from the catalyst to the bulk reaction mixture

It should be stated that steps (3)-(5) have been dealt with under the discussion regarding the Fischer-Tropsch kinetics in subsections 2.2.4 through to 2.2.4.2 in chapter 2. If there is a difference in temperature and/or concentration at the interface of the fluid and the catalyst pellet, mass/heat transport will occur at this interface. The interfacial molar (J_{intf}) and heat ($\dot{Q}_{\text{intf}}$) flux, proportional to their respective driving forces, are calculated as follows:

$$J_{\text{intf}} = -k_{\text{s}}(c_{\text{f}} - c_{\text{s}}^{i}) \tag{3.4}$$

$$\dot{Q}_{\text{intf}} = -h_{\text{s}}(T - T_{\text{s}}^{i}) \tag{3.5}$$

where, k_{s} and h_{s} are respectively the averaged values of particle to fluid mass and heat transfer coefficients over the surface of the pellets (obtainable from correlations [150]), c_{f} is the bulk fluid concentration, c_{s}^{i} is the concentration at the surface of the catalyst and T_{s}^{i} is the catalyst surface temperature. Inside the catalyst pellet, the radial heat flux ($\dot{Q}_{\text{cat}}$) is due solely to conduction and is calculated using the Fourier's law of heat conduction (equation 3.6), while the molar flux (J_{cat}) due solely to diffusion is calculated

using Fick's law of molecular diffusion (equation 3.7):

$$\dot{Q}_{\text{cat}} = -\kappa_{\text{eff,r}} \frac{\partial T}{\partial r} \tag{3.6}$$

$$J_{\text{cat}} = -D_{\text{r T}} \frac{\partial c_j}{\partial r} \tag{3.7}$$

where $\kappa_{\text{eff,r}}$ and $D_{\text{r T}}$ are respectively, the effective radial thermal conductivity and the transition, molecular, radial diffusion coefficient of the two phase (fluid-solid) medium. They are determined by a combination of the physical properties of both phases at the prevalent operating conditions and the geometry of both the reactor tube and catalyst. If the mean free path of the gas molecules diffusing into the catalyst pores is comparable or exceeds the dimensions of the catalyst pores, then the gas molecules will collide more often with the pore walls, and the radial molecular diffusion coefficient must take into account the Knudsen diffusion (see Figure 3.7).

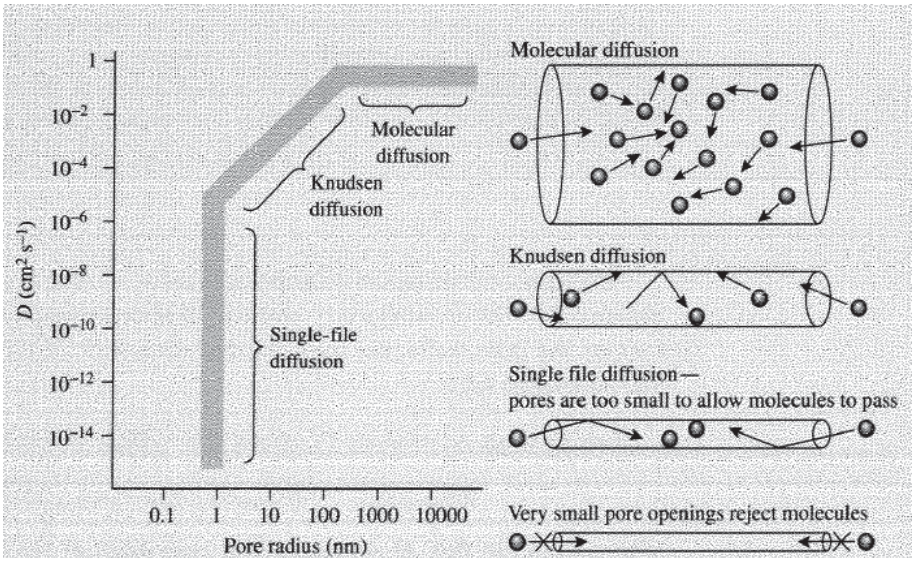

FIGURE 3.7: Influence of pore size on diffusivity of gas phase molecules[151]

The Knudsen diffusion ($D_{\text{K}j}$) of any component j is given by:

$$D_{\text{K}j} = 9.7 R_{\text{pore}} \sqrt{\frac{T}{MW_j}} \left[\frac{\text{m}^2}{\text{s}}\right] \tag{3.8}$$

where, R_{pore} is the pore radius, T is the absolute temperature and MW_j is molecular weight of component j. The combined molecule-molecule and Knudsen diffusion coefficient for a component j can be approximated by the Bosanquet equation to give a radial, transition diffusivity ($D_{\text{r T}\,j}$) of component j:

$$\frac{1}{D_{\text{r T}\,j}} = \frac{1}{D_j} + \frac{1}{D_{\text{K}j}} \tag{3.9}$$

The non-solid parts of catalyst pellets are made up of pores or voidages. The mass flux equation (3.7) must therefore be modified to reflect the fact that catalytic molar flux, J_{cat} is based only on the area of a pore by including the porosity (ϵ_{p}) in the equation. In addition, the random and tortuous nature of the path lengths of the pores must be accounted for using the tortuosity (τ_{p}). The effective radial diffusion coefficient thus becomes:

$$D_{\text{eff,r}} = \frac{\epsilon_{\text{p}}}{\tau_{\text{p}}} D_{\text{r T}\,j} \tag{3.10}$$

and a more general form of equation (3.7) may be re-written as follows:

$$J_{\text{cat}} = -D_{\text{eff,r}} \frac{\partial c_j}{\partial r} \tag{3.11}$$

Experimental evidence [46, 101, 152–157] suggests that in the LTFT, the pores of the catalysts pellets become completely filled with liquid wax after a short start-up period. The reactant syngas therefore has to diffuse into, and dissolve in the liquid wax at the pore entrance in order to access the active sites for reaction, while the desorbed products exit the catalyst by diffusing through the liquid wax. Therefore the reaction rate is dependent on the rate of diffusion/dissolution of the reactant gas in the liquid filled pores of the catalyst. The gas-liquid wax solution is assumed to behave ideally (i.e. negligible enthalpy of mixing and volume increment)[158], as such, Henry's law can be used to describe the gas-liquid solubility.

3.1.2.1 Thiele modulus and effectiveness factor

The Thiele modulus (ϕ), a dimensionless quantity compares the reaction rate to the diffusion rate and determines which is rate limiting. The Fischer-Tropsch reaction may be considered to be a pseudo-first order reaction[5] and the Thiele modulus for a first-order reaction occurring in a spherical pellet is given by:

$$\phi = \frac{V_{\text{p}}}{A_{\text{p,ex}}} \sqrt{\frac{k}{D_{\text{eff,r}}}} \tag{3.12}$$

where, V_{p} is the volume of the catalyst pellet, $A_{\text{p,ex}}$ is the external surface area of the catalyst pellet and k is the reaction rate constant. The full derivation of equation (3.12) may be found elsewhere[111, 151, 159].

Figure 3.8 depicts the normalised concentration profile of hydrogen from the catalyst core ($r/R_{\text{p}} = 0$) to the catalyst wall ($r/R_{\text{p}} = 1$), where R_{p} is the radius of the catalyst. As ϕ reduces, the effect of diffusional transport reduces, the reaction becomes dominant and the observed reaction rate is significantly increased- the converse is equally true.

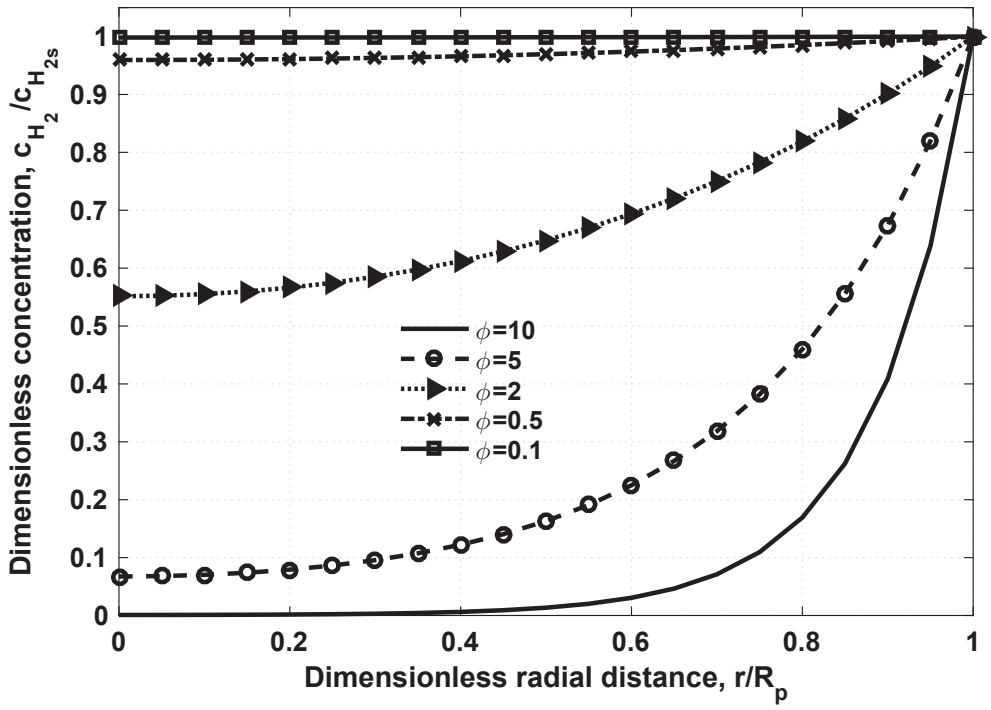

FIGURE 3.8: Effect of Thiele modulus on the normalised concentration profiles in a spherical catalyst particle with first order Fischer-Tropsch reaction

How efficiently the catalyst pellet is used is characterised by the effectiveness factor (η). The effectiveness factor is the ratio of the observed reaction rate ($\Re_{\text{obs}}$) to that which would be observed if there were no diffusion transport limitations ($\Re_{\text{max}}$), i.e. at the external surface of the catalyst[151]. Mathematically, for a species j in a spherical pellet, it is given by:

$$\eta = \frac{\Re_{\text{obs}}}{\Re_{\text{max}}} = \frac{\int_0^{V_\text{p}} \Re(c_j) dV}{V_\text{p}\Re(c_{j\text{s}})} = \frac{\int_0^{R_\text{p}} \Re(c_j) 4\pi r^2 dr}{V_\text{p}\Re(c_{j\text{s}})} = \frac{A_{\text{p,ex}}\int_0^{R_\text{p}} \Re(c_j) \left(\frac{r}{R_\text{p}}\right)^2 dr}{V_\text{p}\Re(c_{j\text{s}})} \tag{3.13}$$

The full derivations of the effectiveness factors for different regular geometries can be found elsewhere [111, 151, 159]. In most cases for a spherical pellet, the effectiveness factor can be approximated by a hyperbolic tangent function of the Thiele modulus[160] as follows:

$$\eta = \frac{\tanh(\phi)}{\phi} \tag{3.14}$$

The relationship is plotted in Figure 3.9. Equipped with a good understanding of the transport phenomena and how they interplay with the reaction kinetics, it is now possible to systematically choose an appropriate dispersion reactor model for describing the Fischer-Tropsch synthesis; this will be considered in the next section.

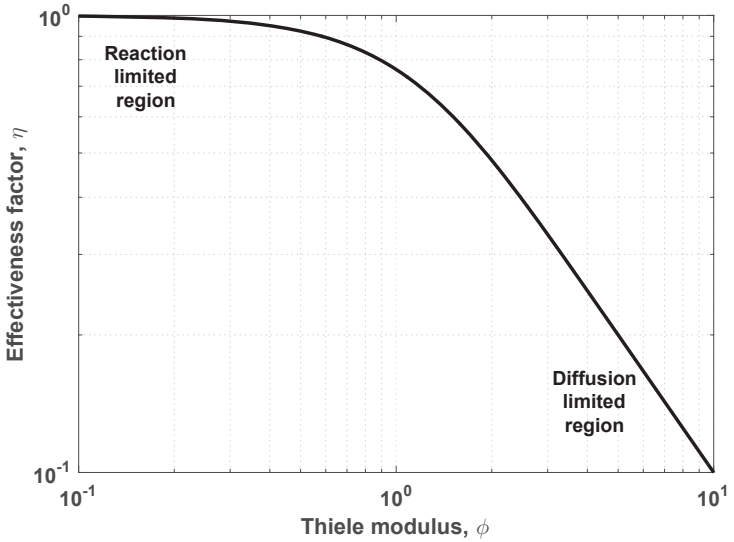

FIGURE 3.9: Effectiveness factor for a first order reaction in a spherical catalyst particle a function of the Thiele modulus

3.2 Reactor Model Selection Criteria

The choice of reactor model for a MTFBR is made on the bases of the desired accuracy, available information and considerations for computational effort. There are, in the main, two major approaches to the continuum modelling of a fixed bed reactor:

(1) Quasi-homogeneous or Pseudo-homogeneous model: the catalyst conditions of chemical species concentration and temperature are assumed to be in equilibrium with that of the surrounding fluid. The interparticle and intraparticle gradients are also assumed to be insignificant. The catalyst packing is thus considered from the fluid dynamics perspective and its effect on fluid flow.

(2) Heterogeneous model: the presence of the catalyst pellets are accounted for explicitly by writing additional conservation equations. Usually, the rates of reaction are modified using an effectiveness factor obtained from a catalyst pellet model [116].

Each of the aforementioned models could either be one dimensional (where only the concentration and temperature gradients along the reactor axial direction are considered) or two dimensional (where both the axial and radial concentration and temperature gradients are considered). This section attempts to select a model based on the systematic criteria set out by Mears [123, 124]. In order to do this, the base case design parameters for the Fischer-Tropsch reaction were obtained from the work of Jess et al [5] and outlined in Table 3.1. Table 3.2 shows some dimensionless quantities and other calculated quantities obtained from the process parameters of Jess et al [5]; these values

are used in the subsequent model selection criteria. The main Fischer-Tropsch synthesis reaction, which was assumed to be a pseudo-first order reaction in $H_{2(g)}$, was used as the principal reaction in the model selection exercise.

TABLE 3.1: Design Parameters and reaction conditions for the Fischer-Tropsch synthesis [5]

Parameter	**Value**	**Description**
T_0	240°C	Feed temperature
T_w	240°C	Wall temperature
p_0	2.40MPa	Total pressure
c_{mol}	$0.563 kmol\,m^{-3}$	Total molar feed concentration
$d_{t,int}$	0.046m	Internal tube diameter
L	12m	Length of tube
d_p	0.003m	Diameter of catalyst particle
ρ_b	$790 kg\,m^{-3}$	Bulk density of catalyst bed
y_{H_2}	0.666	Feed mole fraction
y_{CO}	0.334	Feed mole fraction
MW_{av}	$0.010681 kg\,mol^{-1}$	Average molecular weight
C_p	$2808 J\,kg^{-1}\,K^{-1}$	Heat capacity of feed mixture
ΔH_r	$-152 kJ\,mol^{-1}$	Reaction enthalpy
$\kappa_{eff,r}$	$6.3 W\,m^{-1}\,K^{-1}$	Effective radial thermal conductivity
κ_f	$0.16 W\,m^{-1}\,K^{-1}$	Fluid thermal conductivity
μ_f	$2.4032 \times 10^{-5} kg\,m^{-1}\,s^{-1}$	Fluid viscosity
E_{eff}	$52000 J\,mol^{-1}$	Effective activation energy
U_{wall}	$1380 W\,m^{-2}\,K^{-1}$	Overall heat transfer coefficient
D_{eff}	$1.2 \times 10^{-7} m^2\,s^{-1}$	Effective diffusion coefficient
u_s	$0.55 m\,s^{-1}$	Superficial velocity

3.2.1 Effect of interfacial gradients

A necessary but insufficient condition for using a quasi-homogeneous model is that the interfacical gradients of temperature and chemical species concentration between the catalyst surface and the bulk fluid, must be negligible, i.e. $T_f \approx T_{cat}$ and $c_f \approx c_{cat}$. This holds true if the inequalities (3.15) and (3.16) are satisfied:

$$\left| \frac{\Re_{eff} d_p}{2\, y_{H_2}\, c_{mol}\, k_s} \right| < \frac{0.15}{n} \tag{3.15}$$

$$\left| \frac{(-\Delta H_r)\, \Re_{eff} d_p}{2 T_0 h_s} \right| < \frac{0.15 R_g T_0}{E_{eff}} \tag{3.16}$$

TABLE 3.2: Parameters and dimensionless quantities computed and/or assumed based on reaction and design conditions specified by Jess et al [5]

Parameter	**Value**	**Description**
ϵ	$0.4 {m_f}^3/{m_r}^3$	Catalyst bed void fraction
κ_{cat}	$0.243 \mathrm{Wm^{-1}K^{-1}}$	Catalyst thermal conductivity
G	$3.304 \mathrm{kg\,m^{-2}\,s^{-1}}$	Superficial mass velocity
$Pr = \left(\frac{C_p \mu_f}{\kappa_f}\right)$	0.422	Prandtl number
$Re_p = \left(\frac{G d_p}{\mu_f}\right)$	412.5	Reynolds number
$Sc = \left(\frac{\mu_f}{\rho_f D_{eff}}\right)$	33.3	Schmidt number
$Nu = \left(\frac{h_s d_{t,int}}{\kappa_f}\right)$	102.8	Nusselt number
$Sh = \left(\frac{k_s d_{t,int}}{D_{eff}}\right)$	134.8	Sherwood number
$Da_I = \left(\frac{\Re_{eff}\, d_p}{u_s c_{H_2}}\right)$	1.12×10^{-4}	1st Damköhler number
$Da_{II} = \left(\frac{\Re_{eff}\, {d_p}^2}{4 D_{eff} c_s}\right)$	0.384	2nd Damköhler number
$Da_{III} = \left(\frac{-\Delta H_r\, \Re_{eff}\, d_p}{\rho_f\, u_s\, T_w\, C_p}\right)$	7.36×10^{-4}	3rd Damköhler number
$Pt = \left(\frac{-\Delta H_r\, D_{eff}\, c_s}{\kappa_{cat}\, T_s}\right)$	0.055	Prater number
$Pe_{z,m} = \left(\frac{u_s\, d_p}{D_z}\right)$	2	Mass transfer axial Peclet number
$Pe_{z,h} = \left(\frac{\rho_f\, u_s\, d_p\, C_p}{\kappa_z}\right)$	1.25	Heat transfer axial Peclet number
$Pe_r = \left(\frac{\rho_f\, u_s\, d_p\, C_p}{\kappa_r}\right)$	9	Radial Peclet number
$Bi_w = \left(\frac{h_w\, d_{t,int}}{\kappa_{eff,r}}\right)$	10	Thermal Biot number at the wall
$\Delta T_{ad} = \left(\frac{-\Delta H_r\, c_{H_2}}{\rho_f\, C_p}\right)$	3378K	Adiabatic temperature rise
κ_{rf}	$3.093 \mathrm{Wm^{-1}K^{-1}}$	Radial thermal conductivity of fluid
k_s	$5.39 \times 10^{-4} \mathrm{ms^{-1}}$	Interfacial mass transfer coefficient
h_s	$357.6 \mathrm{Wm^{-2}s^{-1}}$	Interfacial heat transfer coefficient
T^*	1189K	Reaction temperature at hotspot
$\Re^*_{eff}$	$7.84 \mathrm{\,kmol\,m^{-3}s^{-1}}$	Reaction rate at hotspot

If the inlet concentration of H_2O is negligible, so that $c_{H_2O} = 1 \times 10^{-12} \mathrm{mol\,m^{-3}}$, the effective reaction rate is given by:

$$\Re_{eff} = \rho_b \frac{5.1 \exp\left(\frac{-E_{eff}}{R_g T_0}\right)}{1 + 1.6 \frac{c_{H_2O_g}}{c_{CO_g}}} c_{H_2} = 7.69 \times 10^{-3} \left[\frac{\mathrm{kmol}}{\mathrm{m^3\,s}}\right] \tag{3.17}$$

The interfacial mass transfer coefficient between the fluid and catalyst, k_s and interfacial heat transfer coefficient, h_s between the fluid and catalyst are respectively calculated using the correlations in equations (3.18) and (3.19):

$$\epsilon Sh = \epsilon \left(\frac{k_\mathrm{s}\, d_\mathrm{t,int}}{D_\mathrm{eff}} \right) = 0.357 Re_\mathrm{p}^{0.641} Sc^{0.33} \tag{3.18}$$

$$\epsilon Nu = \epsilon \left(\frac{h_\mathrm{s}\, d_\mathrm{t,int}}{\kappa_\mathrm{f}} \right) = 1.0 \left(\frac{Re_\mathrm{p}}{\epsilon} \right)^{0.563} Pr^{0.22} \tag{3.19}$$

For the interfacial species concentration gradient:

$$\begin{aligned} \left| \frac{\Re_\mathrm{eff} d_\mathrm{p}}{2\, y_{\mathrm{H}_2}\, c_\mathrm{mol}\, k_\mathrm{s}} \right| &< \frac{0.15}{n} \\ 0.057 &< \frac{0.15}{1} \end{aligned} \tag{3.20}$$

For the interfacial temperature gradient:

$$\begin{aligned} \left| \frac{(-\Delta H_\mathrm{r})\, \Re_\mathrm{eff} d_\mathrm{p}}{2 T_0 h_\mathrm{s}} \right| &< \frac{0.15 R_\mathrm{g} T_0}{E_\mathrm{eff}} \\ 9.55 \times 10^{-3} &< 0.012 \end{aligned} \tag{3.21}$$

Inference: The interfacial gradients are negligible. The intraparticle gradients must also be considered in order to satisfy the necessary and sufficient conditions for using the quasi-homogeneous reactor model.

3.2.2 Effect of intraparticle gradients

The next stage of the model complexity is accounting for the species concentration and temperature gradient within the catalyst particle. Having shown that the interfacial gradients are negligible, it is sensible to assume that the surface conditions of species concentration c_s and temperature T_s of the catalyst pellets are the same as those at the feed conditions. According to Mears [123], the intraparticle heat and mass transfer resistances may be neglected in a first order (or quasi-first order) reaction if the following inequality is satisfied:

$$\begin{aligned} Da_\mathrm{II} \left| n - \frac{E_\mathrm{eff}}{R_\mathrm{g} T} Pt \right| &< 1 \\ 0.127 &< 1 \end{aligned} \tag{3.22}$$

Inference: The intraparticle gradients are negligible, i.e. an isothermal catalyst pellet with, a pseudo-steady state intraparticle concentration profile may be assumed. A combination of insignificant intraparticle and interfacial gradients provides the *necessary and sufficient conditions* for applying a quasi-homogeneous model.

3.2.3 Effect of axial dispersion

Hitherto, the flow in the reactor has been assumed to be devoid of mixing or any eddy effects. Mixing in the axial direction may be superimposed on the plug flow hydrodynamics in order to account for non-ideal flow conditions. The axial thermal conductivity, κ_z (represented by $Pe_{z,h}$) and axial diffusion coefficient, D_z (represented by $Pe_{z,m}$) implicitly bring the effect of the velocity profile to bear on the reaction process. Mears [124] reports that the effects of axial dispersion is vanishingly small if:

$$\left|\frac{n.Da_I}{Pe_{z,m}} - \frac{E_{eff}.Da_{III}}{R_g T\, Pe_{z,h}}\right| < 0.05$$
$$7.14 \times 10^{-3} < 0.05 \tag{3.23}$$

The axial mass transfer Peclet number, $Pe_{z,m}$ was computed using the correlation in equation (3.24):

$$\frac{1}{Pe_{z,m}} = \frac{0.3}{Re_p\, Sc} + \frac{0.5}{\left(1 + \frac{3.8}{Re_p\, Sc}\right)} \tag{3.24}$$

In order to evaluate the axial heat transfer Peclet number, the axial thermal conductivity, κ_z was first calculated using the correlation in equation (3.25):

$$\frac{\kappa_z}{\kappa_f} = 9 + 0.75\, Re_p\, Pr \tag{3.25}$$

Inference: Mixing in the axial direction is inconsequential on the overall process as the pre-set (inequality) condition is fulfilled. Therefore the effect of axial dispersion may be ignored.

3.2.4 Model dimension and effect radial dispersion

The importance of lateral mixing in the radial direction, brought about by the chaotic fluid flow through the catalyst bed, must also be considered. If the radial dispersion is found to be of little consequence, then a one-dimensional model can be be applied, as otherwise, a two dimensional model, which takes into account the axial and radial

gradients in the reactor must be used instead. In general, there are often negligible radial concentration gradients as radial diffusion occurs quite rapidly, and radial concentration symmetry can often be assumed in tubular reactors of this nature, such that $\frac{\partial c_j}{\partial r} \approx 0$ [161]. Therefore, the more likely radial gradient to occur in the reactor is that of temperature. According to Mears [123], a one-dimensional model may be adopted if:

$$\left|\frac{-\Delta H_{\mathrm{r}}\,\Re^{*}_{\mathrm{eff}}\,d_{\mathrm{t}}^{2}}{\kappa_{\mathrm{rf}}\,T_{\mathrm{w}}}\right|\frac{E_{\mathrm{eff}}}{R_{\mathrm{g}}T_{0}} < \frac{1.6}{\left(1+\frac{8}{Bi_{\mathrm{w}}}\right)}$$

$$82.36 \not< 0.89 \tag{3.26}$$

The fluid radial thermal conductivity, κ_{rf} was computed by assuming a value of 9 for the radial Peclet number, Pe_{r}[114]. The effective reaction rate at the hotspot $\Re^{*}_{\mathrm{eff}}$ was calculated at some modified temperature, $T^{*} = T_0 + 0.2.\Delta T_{\mathrm{ad}}$.

Inference: The condition for using a one dimensional model has not been satisfied hence, the effect of radial dispersion must necessarily be accounted for. A two dimensional model will therefore be applied.

3.2.5 Effect of pressure drop

The effect of pressure drop on the operations of a gas limited fixed bed reactor is quite important. Reactors with significant pressure drop often require the recycling of effluent fluid products in order to maintain the reaction pressure and to drive conversion to economically worthwhile levels [12, 18]. The Ergun equation (3.27) is customarily used to predict the pressure drop in a packed bed reactor [162]:

$$-\frac{\mathrm{d}p}{\mathrm{d}z} = f\frac{\rho_{\mathrm{f}}u_{\mathrm{s}}^{2}}{d_{\mathrm{p}}} \tag{3.27}$$

Typically, the Ergun equation is used to estimate pressure drop in single fluid phase problems in packed beds [114, 163]. Under the low temperature Fischer-Tropsch (LTFT) reaction conditions ($p \geq 2.0$MPa and $T > 200^{\mathrm{o}}$C), more than 99mol% of the reacting species are in the gaseous phase, based on thermodynamic equilibrium calculations, even though wax is the desired product. Based on these findings, Phillipe et al [120] in their work reported that a gas-solid system can be assumed with minimal error. Therefore, the Ergun equation may be used to approximate the pressure drop across the reactor. In order to further corroborate the assertions of Phillipe et al [120], flash calculations were carried out in this work at different pressures and inlet/coolant temperatures; the results are presented in Figure 3.10.

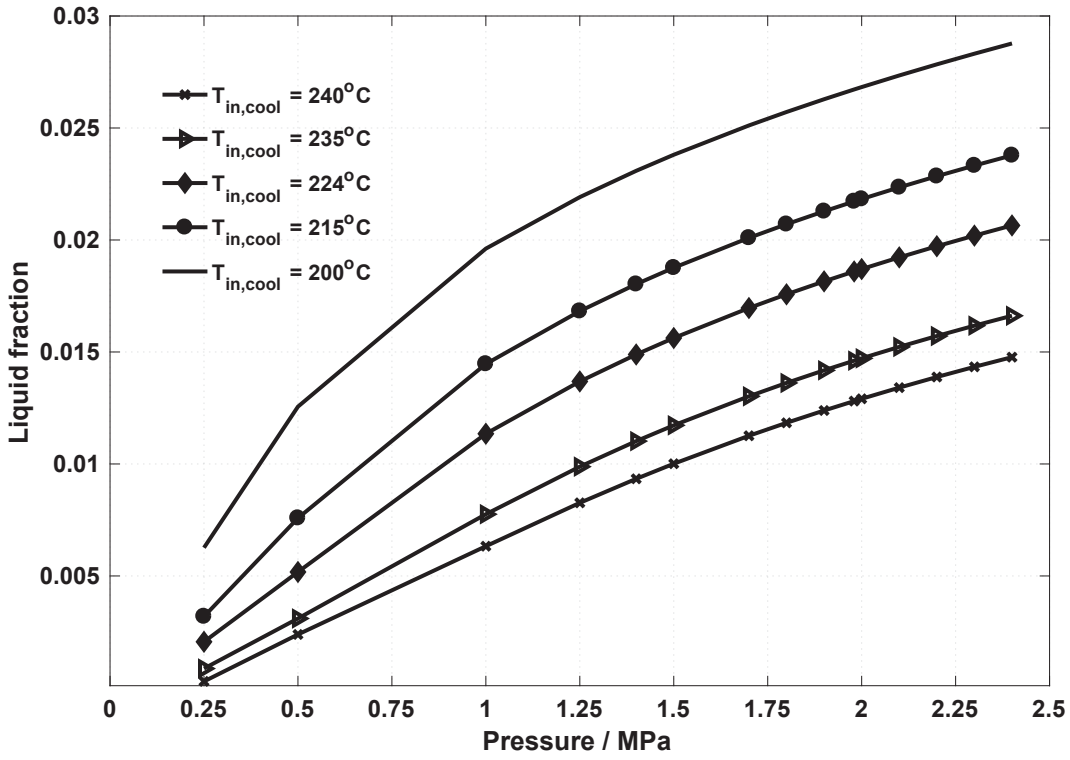

FIGURE 3.10: Liquid volume fraction at different pressures for various inlet/coolant temperatures

As seen in Figure 3.10, the liquid fraction in the reactor increases with increasing pressure and reducing temperature. The maximum liquid fraction is about 2.8% (i.e. vapour fraction = 97.2%), occurs at conditions of $T_{\text{in, cool}} = 200^{\text{o}}\text{C}$ and $p = 2.4\text{MPa}$; the floor conditions of the LTFT. These values are very close to those suggested by Phillipe et al [120], i.e. 99%. The flash calculations also reveal that the maximum liquid fraction diminishes even further at higher inlet temperatures.

In addition to the foregoing, Jess et al [90] in their work suggest that the Ergun equation may be used to determine the trends, providing the pressure drop does not exceed $5 \times 10^5\text{Pa}$ (= 5 bar). Again, this condition is fulfilled in equation (3.29).

Using the reactor bed and feed entry conditions, the friction factor f in equation (3.27) may be computed as follows:

$$\begin{aligned} f &= \frac{1-\epsilon}{\epsilon^3}\left(1.75 + 4.2\, Re_{\text{p}}^{\frac{5}{6}}\frac{1-\epsilon}{Re_{\text{p}}}\right) \\ &= 25.07 \end{aligned} \tag{3.28}$$

The pressure drop along the reactor is given by:

$$\begin{aligned}\Delta p &= \int_0^L f\frac{\rho_\mathrm{f}\, u_\mathrm{s}^2}{d_\mathrm{p}}\mathrm{d}z \\ &= 1.82\times 10^5\mathrm{Pa}\end{aligned} \tag{3.29}$$

The expression in equation (3.28) is well suited to spherical particle packings over a relatively wide range of particle Reynolds numbers [18].

The percentage change in pressure drop is:

$$\frac{\Delta p}{p_0} = \frac{1.82\times 10^5}{2.4\times 10^6}\times 100 = 8\% \tag{3.30}$$

Inference: An 8% pressure drop is relatively modest, showing that an axial, multi-tubular fixed bed reactor can be used in the process.

3.3 Governing Reactor Model Equations

From the inferences in the foregoing subsections (3.2.1) - (3.2.5), a two dimensional, quasi-homogeneous reactor model, without axial dispersion is the appropriate model to be applied. The respective governing molar balance, enthalpy balance, momentum balance, state and continuity equations are given by equations (3.31), (3.32) and (3.33a-3.33c) respectively. The rate of change of the fluid density with respect to the reactor length was computed by applying the chain rule to the ideal gas law as in equation (3.33b), while the gas velocity was calculated from the continuity equation as in equation (3.33c).

$$-\frac{\partial c_j}{\partial t} + \epsilon D_\mathrm{r}\left(\frac{\partial^2 c_j}{\partial r^2} + \frac{1}{r}\frac{\partial c_j}{\partial r}\right) - \frac{\partial(u_s\, c_j)}{\partial z} - \sum_{i=1}^{N}\nu_{i,j}\,\Re_{i,j}(c,T) = 0 \tag{3.31}$$

$$-\rho_\mathrm{f} C_\mathrm{p}\frac{\partial T}{\partial t} + \kappa_\mathrm{r}\left(\frac{\partial^2 T}{\partial r^2} + \frac{1}{r}\frac{\partial T}{\partial r}\right) - \rho_\mathrm{f} u_\mathrm{s} C_\mathrm{p}\frac{\partial T}{\partial z} + \sum_{i=1}^{N}\nu_{i,j}\,\Re_{i,j}(c,T)(-\Delta H_\mathrm{r}) = 0 \tag{3.32}$$

$$-\frac{\mathrm{d}p}{\mathrm{d}z} = \frac{1-\epsilon}{\epsilon^3}\left(1.75 + 4.2\,Re_{\mathrm{p}}^{\frac{5}{6}}\frac{1-\epsilon}{Re_{\mathrm{p}}}\right)\frac{\rho_{\mathrm{f}}u_{\mathrm{z}}^2}{d_{\mathrm{p}}} \tag{3.33a}$$

$$\frac{\partial\rho_{\mathrm{f}}}{\partial z} = \frac{MW_{\mathrm{av}}}{R_{\mathrm{g}}}\left(\frac{1}{T}\frac{\partial p}{\partial z} - \frac{p}{T^2}\frac{\partial T}{\partial z}\right) \tag{3.33b}$$

$$\frac{1}{\rho_{\mathrm{f}}}\frac{\partial\rho_{\mathrm{f}}}{\partial t} + \frac{\partial u_{\mathrm{z}}}{\partial z} = -\frac{u_{\mathrm{z}}}{\rho_{\mathrm{f}}}\frac{\partial\rho_{\mathrm{f}}}{\partial z} \tag{3.33c}$$

In equations (3.31) and (3.32), the average values of the macro-scale radial diffusion coefficient (D_{r}) and the macro-scale radial thermal conductivity (κ_{r}), are defined for the multi-phase continuum (i.e. quasi-homogeneous) reaction system with the aid of correlations given by Skaare [164] and Xu et al [165] respectively as follows:

$$D_{\mathrm{r}} = \left[\frac{1}{1.1Pe_{\mathrm{r,m}}^{\mathrm{p}}}\left(\frac{1}{u_{\mathrm{z}}.d_{\mathrm{p}}} - \frac{\rho_{\mathrm{f}}.(1-\sqrt{1-\epsilon})}{Re_{\mathrm{p}}.\mu_{\mathrm{f}}}\right)\right]^{-1} \tag{3.34}$$

$$\kappa_{\mathrm{r}} = \kappa_{\mathrm{eff,r}}^{0} + 0.14\kappa_{\mathrm{f}}Re_{\mathrm{p}}Pr \tag{3.35}$$

where, the mass transfer, radial, particle Peclet number is given by:

$$Pe_{\mathrm{r,m}}^{\mathrm{p}} = 8\left[2 - \left(1 - \frac{2.d_{\mathrm{p}}}{d_{\mathrm{t,int}}}\right)^2\right] \tag{3.36}$$

and the static radial thermal conductivity ($\kappa_{\mathrm{eff,r}}^{0}$) is as defined in Appendix A.

The initial and boundary conditions are as follows,

At time $t = 0$:

$$\left.\begin{aligned} c_j &= c_{j0} \\ T &= T_0 \\ p &= p_0 \\ u_{\mathrm{z}} &= u_{\mathrm{s}} \\ \rho_{\mathrm{f}} &= \rho_{\mathrm{f}\,0} \end{aligned}\right\} \quad \forall \text{ values of } z \text{ and } r \tag{3.37}$$

At time $t > 0$:

$$\left.\begin{aligned} c_j &= c_{j1} \\ T &= T_1 \end{aligned}\right\} \quad \text{at } z = 0 \text{ and } 0 \leq r \leq \frac{d_{\mathrm{t,int}}}{2} \tag{3.38}$$

$$\frac{\partial c_j}{\partial r} = 0 \qquad \text{at } r = 0 \text{ and } \quad r = \frac{d_{\mathrm{t,int}}}{2}, \quad \forall\, z \tag{3.39}$$

$$\frac{\partial T}{\partial r} = 0 \qquad \text{at } r = 0, \quad \forall\, z \tag{3.40}$$

$$\frac{\partial T}{\partial r} = -\frac{h_{\mathrm{w}}}{\kappa_r}(T_{\mathrm{react}} - T_{\mathrm{w}}) \qquad \text{at} \quad r = \frac{d_{\mathrm{t,int}}}{2}, \quad \forall\, z \tag{3.41}$$

3.3.1 Chemical reaction and kinetics

The complex Fischer-Tropsch synthesis has been reduced to three representative reactions namely, the main Fischer Tropsch synthesis, methanation and water gas shift reactions, respectively denoted by:

$$\mathrm{CO} + 2\,\mathrm{H_2} \longrightarrow (-\mathrm{CH_2}-) + \mathrm{H_2O} \qquad \Delta H^{\theta}_{298} = -152\,\mathrm{kJ\,mol^{-1}} \tag{3.42}$$

$$\mathrm{CO} + 3\,\mathrm{H_2} \longrightarrow \mathrm{CH_4} + \mathrm{H_2O} \qquad \Delta H^{\theta}_{298} = -206\,\mathrm{kJ\,mol^{-1}} \tag{3.43}$$

$$\mathrm{CO} + \mathrm{H_2O} \longrightarrow \mathrm{CO_2} + \mathrm{H_2} \qquad \Delta H^{\theta}_{298} = -41\,\mathrm{kJ\,mol^{-1}} \tag{3.44}$$

The respective reaction rate equations are as follows:

$$\Re_{\mathrm{FT}} = \rho_{\mathrm{b}} \frac{5.1 \exp\left(\dfrac{-52000}{R_{\mathrm{g}} T}\right)}{1 + 1.6 \dfrac{c_{\mathrm{H_2O_g}}}{c_{\mathrm{CO_g}}}} c_{\mathrm{H_{2,g}}} \tag{3.45}$$

$$\Re_{\mathrm{M}} = 27.3\,\rho_{\mathrm{b}} \exp\left(\frac{-70000}{R_{\mathrm{g}} T}\right) c_{\mathrm{H_{2,g}}} \tag{3.46}$$

$$\Re_{\mathrm{WGS}} = \rho_{\mathrm{b}} \times \frac{10^3 \times k_{\mathrm{v}} (R_{\mathrm{g}} T)^{\frac{3}{2}} \left(\dfrac{c_{\mathrm{CO}}\, c_{\mathrm{H_2O}}}{c_{\mathrm{H_2}}^{\frac{1}{2}}} - \dfrac{1}{K_{\mathrm{ewg}}}\, c_{\mathrm{CO_2}}\, c_{\mathrm{H_2}}^{\frac{1}{2}} \right)}{\left(1 + K_{\mathrm{v}} (R_{\mathrm{g}} T)^{\frac{1}{2}} \dfrac{c_{\mathrm{H_2O}}}{c_{\mathrm{H_2}}^{\frac{1}{2}}} \right)^2} \tag{3.47}$$

The water gas shift equilibrium constant, K_{ewg} is given by the expression of Lox et al [54]:

$$\exp\left(\frac{5078.0045}{T} - 5.8972089 + 13.958689 \times 10^{-4} T - 27.592844 \times 10^{-8} T^2\right) \tag{3.48}$$

The following lumps have been defined as Fischer-Tropsch products in this thesis: C_1, C_2, Liquefied Petroleum Gas ($C_3 - C_4$), gasoline/naphtha ($C_5 - C_{11}$), diesel ($C_{12} - C_{20}$) and wax (C_{21+}). The wax fraction is represented by the hydrocarbon $C_{28}H_{58}$ in the model for simplification purposes. The Anderson Schulz Flory (ASF) molar distribution of hydrocarbon products x_{cn} was obtained by substituting the appropriate, constant-valued, carbon chain growth probability factor, α_{FT} into the Schulz-Flory [166] equation

(3.49).

$$x_{\mathrm{cn}} = (1 - \alpha_{FT}) \times \alpha_{\mathrm{FT}}^{(\mathrm{cn}-1)} \tag{3.49}$$

It is important to note that the sum of mole fractions (x_{cn}) for $1 \leq cn \leq \infty$ is unity.

The rate of consumption of CO may be correlated with the mole fraction of the hydrocarbons produced (equation 3.49) using the following C-atom balance:

$$\begin{aligned} [\text{Molar consumption rate of C as CO}] &= [\text{Molar production rate of C as } CO_2] \\ &+ [\text{Molar production rate of C as hydrocarbons}] \end{aligned} \tag{3.50}$$

In order to account for both olefin and paraffin production for each carbon number (cn) greater than 2, an olefin to paraffin ratio, γ_{FT} is defined and incorporated into the atom balance. For a Fe-catalysed Fischer-Tropsch reaction, a typical value of olefin to paraffin ratio is $\gamma_{\mathrm{FT}} = 0.35$ [156, 167]. The total number of moles of hydrocarbon (N_{tot}) produced per unit time as reported by Panahi et al [168] is given by:

$$N_{\mathrm{tot}} = \frac{\left(\dfrac{-\Re_{\mathrm{FT}} - \Re_{\mathrm{M}} - \Re_{\mathrm{WGS}}}{MW_{\mathrm{CO}}} + \dfrac{\Re_{\mathrm{WGS}}}{MW_{\mathrm{CO_2}}}\right) V_{\mathrm{react}}}{\dfrac{x_{(cn=1)}}{MW_{\mathrm{CH_4}}} + \displaystyle\sum_{cn=2}^{cn} cn \times x_{cn} \times \left(\frac{1}{(1+\gamma_{\mathrm{FT}})} . \frac{1}{MW_{\mathrm{C_{cn}H_{2cn+2}}}} + \frac{\gamma_{\mathrm{FT}}}{(1+\gamma_{\mathrm{FT}})} . \frac{1}{MW_{\mathrm{C_{cn}H_{2cn}}}}\right)} \tag{3.51}$$

The carbon-atom balance may then be re-written as follows:

$$\begin{aligned} (-\Re_{\mathrm{FT}} - \Re_{\mathrm{M}}).V_{\mathrm{react}} &= 2\Re_{\mathrm{WGS}}.V_{\mathrm{react}} + x_{(cn=1)}.N_{\mathrm{tot}} + N_{\mathrm{tot}} \times x_{cn} \times cn \\ &\times \sum_{cn=2}^{cn} \left(\frac{1}{(1+\gamma_{\mathrm{FT}})} . \frac{1}{MW_{\mathrm{C_{cn}H_{2cn+2}}}} + \frac{\gamma_{\mathrm{FT}}}{(1+\gamma_{\mathrm{FT}})} . \frac{1}{MW_{\mathrm{C_{cn}H_{2cn}}}}\right) \end{aligned} \tag{3.52}$$

The rate of production (or consumption) of the various chemical species participating in the reaction can therefore be summarised as below:

$$\Re_{H_2} = -\Re_{FT} - 3\Re_M + \Re_{WGS} \tag{3.53}$$

$$\Re_{CO} = -\Re_{FT} - \Re_M - \Re_{WGS} \tag{3.54}$$

$$\Re_{CH_4} = \Re_M \tag{3.55}$$

$$\Re_{C_{cn}H_{2cn+2}} = x_{(cn>2)} \times N_{tot} \times V_{react} \times \frac{1}{(1+\gamma_{FT})} \tag{3.56}$$

$$\Re_{C_{cn}H_{2cn}} = x_{(cn>2)} \times N_{tot} \times V_{react} \times \frac{\gamma_{FT}}{(1+\gamma_{FT})} \tag{3.57}$$

$$\Re_{H_2O} = \Re_{FT} + \Re_M - \Re_{WGS} \tag{3.58}$$

$$\Re_{CO_2} = \Re_{WGS} \tag{3.59}$$

3.3.2 Effect of phase change material

This subsection attempts to incorporate the effect of the phase change material (PCM) into the reactor enthalpy balance. If the concept of the multi-phase fluid continuum adopted for modelling the reactor, is extended to include the encapsulated PCM packed alongside the catalyst pellets in the reactor, then a continuous, pseudo-homogeneous, fluid-catalyst-PCM system may be defined.

Figure 3.11 shows a schematic representation of the metallic PCM encased in a spherical silica shell and immersed in the reaction fluid. In Figure 3.11, r_{SL} is the radial distance of the solid-liquid boundary, R_w is the external radius of the capsule and R is the inner radius of the capsule. Vitorino et al [169, 170] have extensively studied the absorption and/or desorption of heat and coolth from encapsulated phase change materials of sundry geometries and properties under mixed control, and made the following assumptions which will be upheld for the purpose of modelling:

(i) Symmetric discharge/absorption of heat in the radial direction

(ii) The solid-liquid interface of the PCM does not depart significantly from the PCM fusion temperature, and there is no significant under-cooling. In a similar fashion, the liquid PCM remains close to the PCM melting temperature with negligible overheating.

(iii) The boundary temperatures (inner shell wall/solid PCM interface, outer shell wall and reaction fluid, etc.) are determined by the continuity of heat flux.

(iv) The relevant physical properties of the PCM are constant.

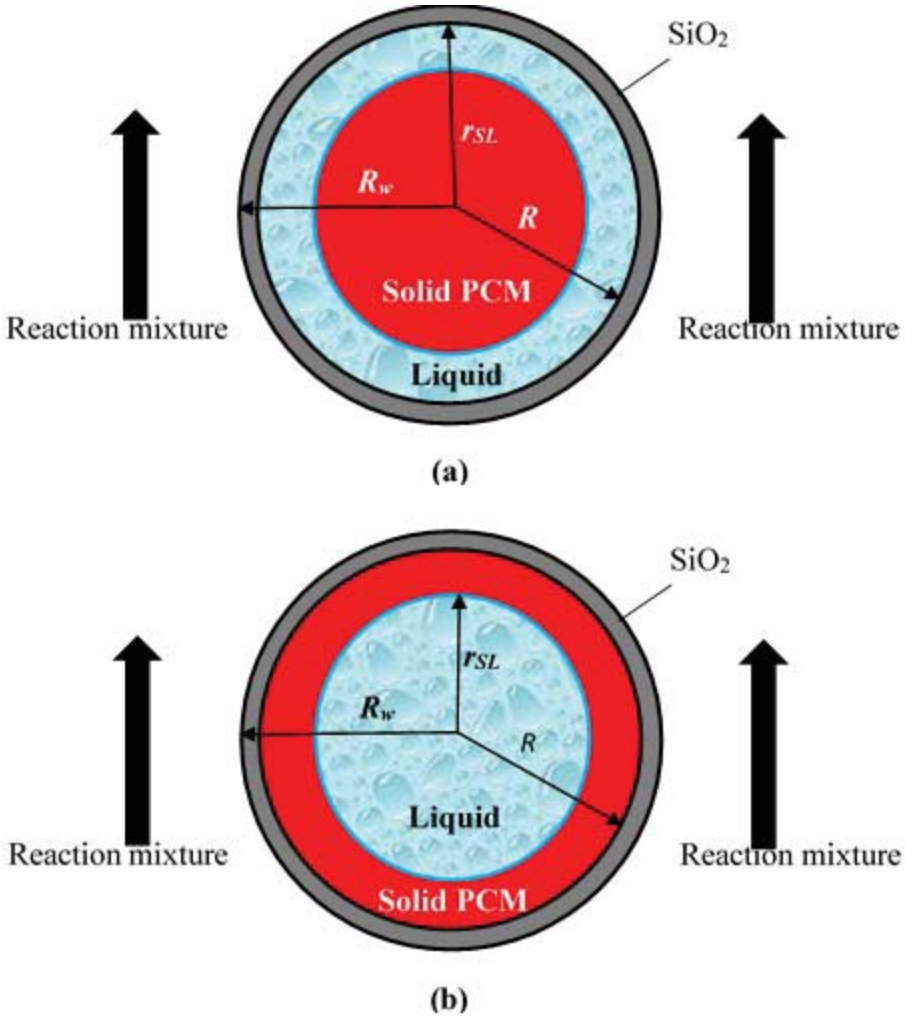

FIGURE 3.11: Schematic of a silica encapsulated phase change material: (a)Melting (b) Solidification

The overall effect of the PCM is to provide a near isothermal sink into which the enthalpy of reaction may be dissipated temporarily. This buffering effect of the PCM may be reflected in the enthalpy balance by expanding the last term on the LHS of equation (3.32) as follows:

$$\begin{aligned}\sum_{i=1}^{N} \nu_{i,j}\, \Re_{i,j}(c,T)(-\Delta H_{\mathrm{r},i}) \;&=\; \nu_{\mathrm{FT},j}\, \Re_{FT}(-\Delta H_{\mathrm{FT}}) + \nu_{\mathrm{M},j}\, \Re_{M}(-\Delta H_{\mathrm{M}}) \\ &\quad + \nu_{\mathrm{WGS},j}\, \Re_{WGS}(-\Delta H_{\mathrm{WGS}}) \\ &\quad - \sum_{i=1}^{N} \nu_{i,j}\, \Re_{i,j}(c,T)(-\Delta H_{\mathrm{pcm}}) \end{aligned} \tag{3.60}$$

For a metallic core enapsulated PCM, as in Figure 3.11, immersed in the flowing reaction mixture, the relative effect of the capsule wall thickness is the limiting step to heat transfer and therefore the controlling resistance. It is also logical to assume that

the rate at which the PCM transitions depends upon the rate at which the chemical reaction proceeds; and by extension the rate at which heat is generated by the reaction. Therefore, the concept of continuity of heat flux may be applied as follows:

$$\begin{aligned}\rho_{\mathrm{pcm}}\Delta H_{\mathrm{pcm}}\frac{\mathrm{d}r_{\mathrm{SL}}}{\mathrm{d}t} &\approx \kappa_{\mathrm{pcm}}\frac{T_{\mathrm{R}}-T_{\mathrm{m}}}{\left(\frac{1}{r_{\mathrm{SL}}}-\frac{1}{R}\right)}\\ &\approx \kappa_{\mathrm{w}}\frac{T_{\mathrm{RW}}-T_{\mathrm{R}}}{\left(\frac{1}{R}-\frac{1}{R+\chi_{\mathrm{th}}}\right)}\\ &\approx h(T_{\mathrm{RW}}-T_{\mathrm{c}}) \approx \sum_{i=1}^{N}\nu_{i,j}\,\Re_{i,j}(c,T)(-\Delta H_{\mathrm{r},i})\end{aligned} \tag{3.61}$$

where the last term of equation (3.61) is as defined in equation (3.60).

3.3.3 Pseudo-continuum properties in fixed bed reactor

Consistent with the pseudo-homogeneous multi-phase continuum approach for modelling the reactor, the solid particles, including the encapsulated phase change material will not be explicitly accounted for. Rather, the so-called "effective heat capacity method" [130] will be employed in reflecting the heat sink effect of the PCM in the model. In this method, the enthalpy of the PCM, ΔH_{pcm}, used in equations (3.60) and (3.61) will be calculated using the piecewise, temperature dependent, heat capacity of the PCM as depicted in equation (3.62).

$$C_{\mathrm{p(pcm)}}(T) = \begin{cases} C_{\mathrm{p(pcm)s}} & : T < T_{\mathrm{m}}, \\ C_{\mathrm{p(pcm)s}} + \dfrac{\Delta H_{\mathrm{fus}}}{\Delta T} & : T_{\mathrm{m}} \leq T \leq (T_{\mathrm{m}}+\Delta T), \\ C_{\mathrm{p(pcm)_l}} & : T > (T_{\mathrm{m}}+\Delta T). \end{cases} \tag{3.62}$$

In order to facilitate the mathematical definition of pseudo-continuum physical properties of the phase change material (e.g. thermal conductivity, density, etc.), and to alleviate any numerical discontinuities in these physical properties caused by phase transition, a "mushy zone approximation" [171] was used. The approximation entails the definition of a temperature-dependent, piecewise liquid melt fraction (ψ), which ranges

from 0 (completely solid) to 1 (completely liquid) (equation 3.63).

$$\psi = \begin{cases} 0 & : T < T_{\mathrm{m}}, \\ \dfrac{\Delta H_{\mathrm{pcm}} - C_{\mathrm{p,pcm,s}}(T_{\mathrm{m}} - T_0)}{\Delta H_{\mathrm{fus}}} & : T_{\mathrm{m}} = T, \\ 1 & : T > T_{\mathrm{m}}. \end{cases} \tag{3.63}$$

The individual physical properties were then approximated as continuous, smooth, linear combinations of their values in the solid and liquid phases [128, 129], for example,

$$\kappa_{\mathrm{pcm}}(T) = \kappa_{\mathrm{pcm,s}}(1 - \psi) + \kappa_{\mathrm{pcm,l}} \times \psi \tag{3.64}$$

This approach was extended in order to define effective properties of the fluid-catalyst-PCM system by defining an arbitrary catalyst activity coefficient, σ; where $0 \leq \sigma \leq 1$. Hence the system's overall physical properties may be defined as follows:

$$\kappa_{\mathrm{f,cat,pcm}}(T) = \sigma\kappa_{\mathrm{f,cat}} + (1 - \sigma)(\kappa_{\mathrm{pcm,s}}(1 - \psi) + \kappa_{\mathrm{pcm,l}} \times \psi) \tag{3.65}$$

$$\rho_{\mathrm{f,cat,pcm}}(T) = \sigma\rho_{\mathrm{f,cat}} + (1 - \sigma)(\rho_{\mathrm{pcm,s}}(1 - \psi) + \rho_{\mathrm{pcm,l}} \times \psi) \tag{3.66}$$

$$C_{\mathrm{p\,f,cat,pcm}}(T) = \sigma C_{\mathrm{p\,f,cat}} + (1 - \sigma)C_{\mathrm{p\,pcm}}(T) \tag{3.67}$$

where $C_{\mathrm{p,pcm}}(T)$ is defined in equation (3.62).

3.4 Numerical Implementation

This section looks at how the mathematical model is solved using the commericial Finite Element Method (FEM) modelling platform, COMSOL Multiphysics 4.4 [21]. The software possesses a variety of physics modules including: chemical reactions (Transport of diluted species), heat transfer, fluid flow, Livelink with MATLAB$^{\mathrm{TM}}$ [172] and user defined equations which make it possible to specify almost any type mathematical model. Ideally, the "transport of diluted species" interface is used to model systems where the mole fraction of one chemical species dominates, such that the effective fluid properties may be approximated as those of the dominant species. However, central to this interface is the Fickian diffusion law, as opposed to the Maxwell-Stefan diffusion matrix used in the transport of concentrated species interface. Most of the modelling of the Fischer-Tropsch synthesis available in literature have used the Fickian law approximation with results comparing with experimental values to acceptable levels, including the works of: Rafiq et al [122], Jess et al [5], Phillippe et al [120], etc. It was therefore on this basis that the diluted species interface was adopted in this work.

A particularly attractive feature of the software COMSOL Multiphysics 4.4 [21] is its ability to interface these individual pieces of physics modules automatically (providing the numerical model is set correctly), thus enabling the model to bear a closer semblance to reality. COMSOL Multiphysics 4.4 [21] has extensive meshing capabilities and a wide variety of numerical solver routines which can handle problems of varying complexity. These solvers may be optimised by the user as required. False streamline and crosswind diffusion are inbuilt into the COMSOL equations for stability during convergence, this however does not affect the physics of the results. All these features make COMSOL Multiphysics 4.4 [21] an excellent fit for the nature of this work.

3.4.1 Numerical Integration and Homogenisation

The numerical integration of the system of non-linear, time-dependent system of partial differential equations (PDE) (3.31-3.41) and the solution of the non-linear differential algebraic equations (DAE) and constitutive equations must be carried out on each discretisation (meshed) node of the representative reactor geometry. The model was discretised and numerically integrated using the time-dependent Backward Differential Formula (BDF). The relative tolerance was set to a value of 0.001, so as to avoid the solver (which automatically selects the time step) from skipping over the PCM's transition point. The simulations were performed on a HP Compaq desktop with the following specification: Quad core Intel® Core(TM) i7-3770 CPU @ 3.40GHz, 16GB RAM.

A detailed model of the reactor including all the randomly packed particles with their individual multi-scale transport phenomena is not only computationally unreasonable, but unnecessary. COMSOL Multiphysics [21] handles this by treating the porous catalyst packing as a homogeneous slab containing both the fluid and solids, so that the reactions become sources and/or sinks in the molar balance rather than boundary conditions around each catalyst pellet to the fluid domain. The underlying assumption is that each individual catalyst pellet is very small compared to the entire packing in the reactor; this is known as *homogenisation* [149]. Homogenisation is carried out on the micro and macro scales as shown in Figures 3.12 and 3.13 respectively.

3.4.2 Numerical Implementation of the Phase Change Material

The concluding part of this chapter looks at the numerical implementation of the PCM effect in the numerical model.

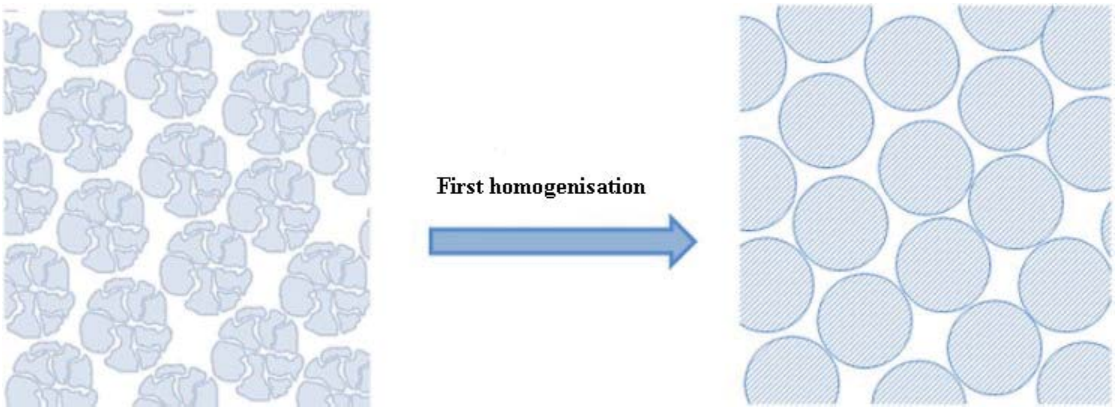

FIGURE 3.12: Micro-scale homogenisation for the inner parts of the catalyst pellets [149]

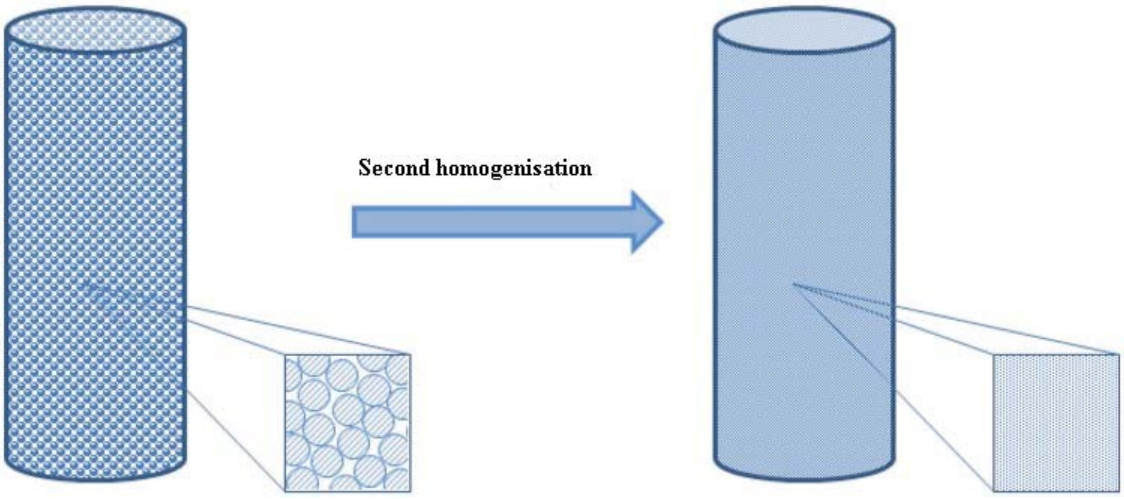

FIGURE 3.13: Macro-scale homogenisation for the fixed bed reactor [149]

The conduction equation without internal heat generation in Lagrangian coordinates is given by:

$$\rho_{\mathrm{pcm,s}}\, C_{\mathrm{p,eff}}\, \frac{\partial T}{\partial t} + \nabla.\left(-\kappa_{\mathrm{eff}}\, \nabla T\right) = 0 \tag{3.68}$$

The effective thermal conductivity in equation (3.68) is the same as that expressed in equation (3.64). The liquid melt fraction, ψ which varies between 0 and 1 is implemented using the in-built smoothed global Heaviside function with continuous second order derivative- this is depicted in Figure 3.14. This has the effect of smoothing any "jumps" which the solver may experience as the PCM's physical properties change with temperature. This facility helps alleviate numerical discontinuities. The effective heat capacity was adjusted in order to incorporate the latent enthalpy of fusion using an analytic pulse function as depicted in Figure 3.15. The amplitude of the pulse function occurs at the fusion temperature of metallic tin, 231.9°C. This effective heat capacity is given by equation (3.69). The latent enthalpy of fusion is reflected using the normalised pulse, $D(^{\mathrm{o}}\mathrm{C}^{-1})$ within the phase change interval from T_0 to T_1 ($T_1 - T_0 = 2.5^{\mathrm{o}}\mathrm{C}$ in this

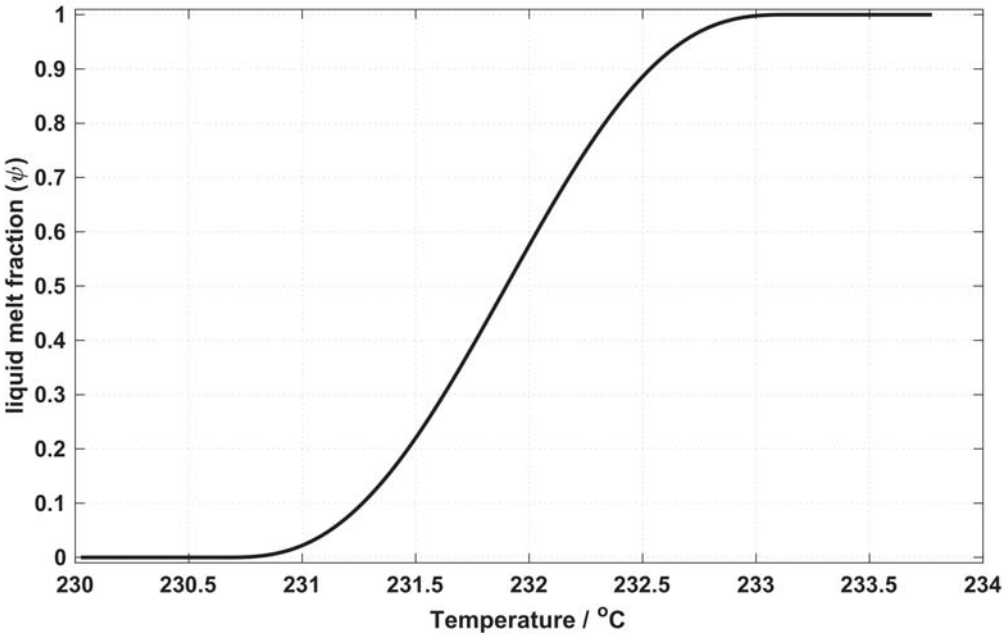

FIGURE 3.14: Liquid melt fraction, ψ represented as a Heaviside function in COMSOL

case).

$$C_{\mathrm{p,eff}} = \sum_i \psi \left(C_{\mathrm{p\,i}} + D\Delta H_{\mathrm{fus}} \right) \tag{3.69}$$

The integral of the pulse function, D must equal unity in order to satisfy equation (3.70), such that the pulse width denotes the range between the solid phase and liquid phase temperatures.

$$\int_{T_0}^{T_1} \rho_{\mathrm{pcm,s}}\, D(T)\, \Delta H_{\mathrm{fus}}\, \mathrm{d}T = \rho_{\mathrm{pcm,s}}\, \Delta H_{\mathrm{fus}} \tag{3.70}$$

In this study, the pulse, D has been conveniently chosen to be the temperature-dependent derivative of the liquid melt fraction ψ in order to satisfy equation (3.70).

The next chapter looks to validate and verify the mathematical and numerical models developed in this chapter. Industrial and laboratory scale basecase scenarios will be considered and modelled using the methods identified in this chapter. The results will be compared to those reported in literature.

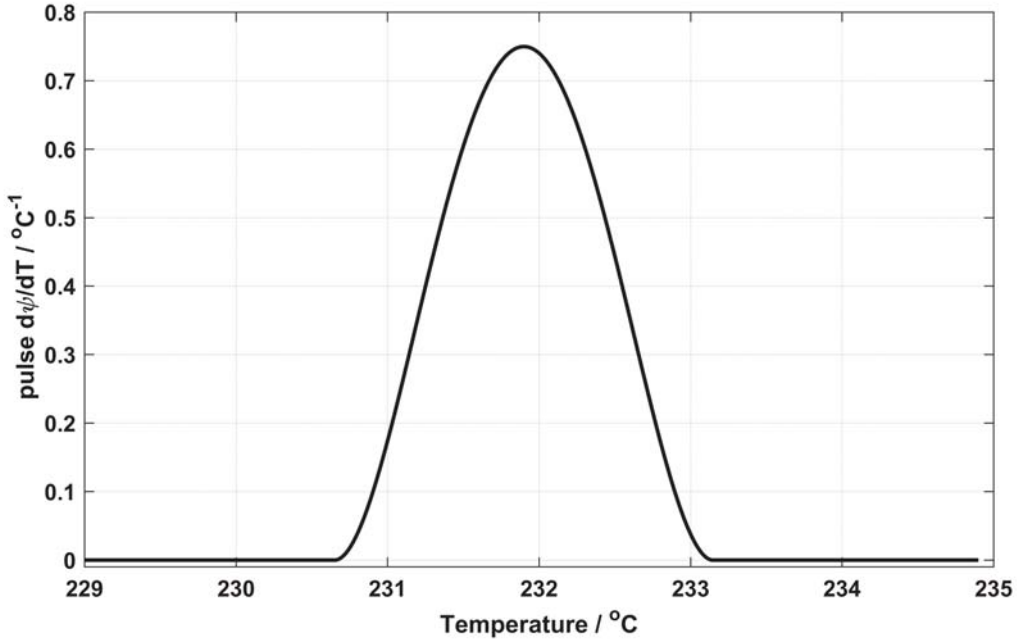

FIGURE 3.15: Pulse function used for numerically implementing the effect of the PCM's latent enthalpy of fusion

Chapter 4

Validation and Verification

"We shall not cease from exploration. And the end of all our exploring will be to arrive where we started and know the place for the first time."

T.S. Eliot, (1888-1965).

This chapter is devoted to the validation of previously developed mathematical models set out in Chapter 3, and verification of the subsequent numerical solutions. To this end, three test categories have been considered for the verification and validation exercise in this work. The evaluation of the capability of the software, COMSOL Multiphysics 4.4 [21], to accurately model the results of experimental and numerical simulations of the Fischer-Tropsch synthesis in a fixed bed reactor as reported in open literature, forms the heart of this chapter. This evaluation implicitly combines into one, the validation and verification steps for each case. Mesh refinement studies are conducted for each case study in order to ensure that the obtained solutions are mesh independent. The layout of this chapter is as follows: section 4.1 looks at the verification of the axial temperature profile and reactant conversion in an industrial scale, Fe-catalysed, Fischer-Tropsch synthesis, multi-tubular fixed bed reactor (MTFBR), against the results of Jess et al [5]. Section 4.2 presents the verification of the product distribution and selectivity in a laboratory scale, single tube, Co-catalysed, Fischer-Tropsch synthesis fixed bed reactor, for four different gas hourly space velocity (GHSV) runs, against the experimental and numerical modelling work of Rafiq et al [122] . Lastly, section 4.3 sets out the verification for the product distribution and the reaction-time-dependent temperature profiles in a laboratory scale, fixed bed reactor, for the exothermic Pt/SiO_2-catalysed, partial oxidation of methanol, with encapsulated indium phase change material as diluent against the experimental work of Zhang et al [131].

4.1 Fixed bed axial temperature profile and reactant conversion (Fe-catalysed)

4.1.1 Numerical model

Figure 4.1 depicts the multi-tubular reactor, while Figure 4.2 is a schematic representation of a single tube in the Fischer-Tropsch multi-tubular fixed bed reactor in space. It will be recalled from Chapter 3 that an underlying assumption was that each of the tubes in the reactor is identically packed with no inter-tube interactions thus, allowing for a single tube to represent the entire reactor [17]. The reactor bed is also assumed to operate in a down-flow trickle bed regime, i.e. the fluid flows (trickles) downward over a packed bed of catalyst particles [148].

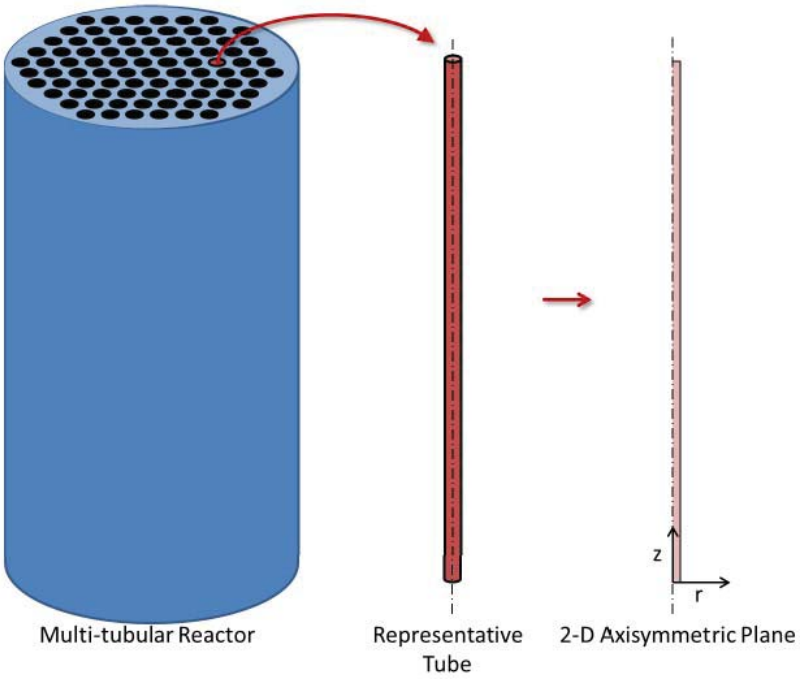

FIGURE 4.1: Model geometry represented by the 2D-axisymmetric plane of a single tube [33]

Cooling saturated water flows around the tube in order to remove the reaction heat. As previously outlined in Chapter 3, a 2D quasi-homogeneous model has been adopted to describe the physico-chemical processes occurring in the reactor; this has been numerically implemented and solved using the COMSOL Multiphysics suite. Equations (4.1 - 4.5) present the initial and boundary conditions for the Initial Boundary Value Problem (IBVP).

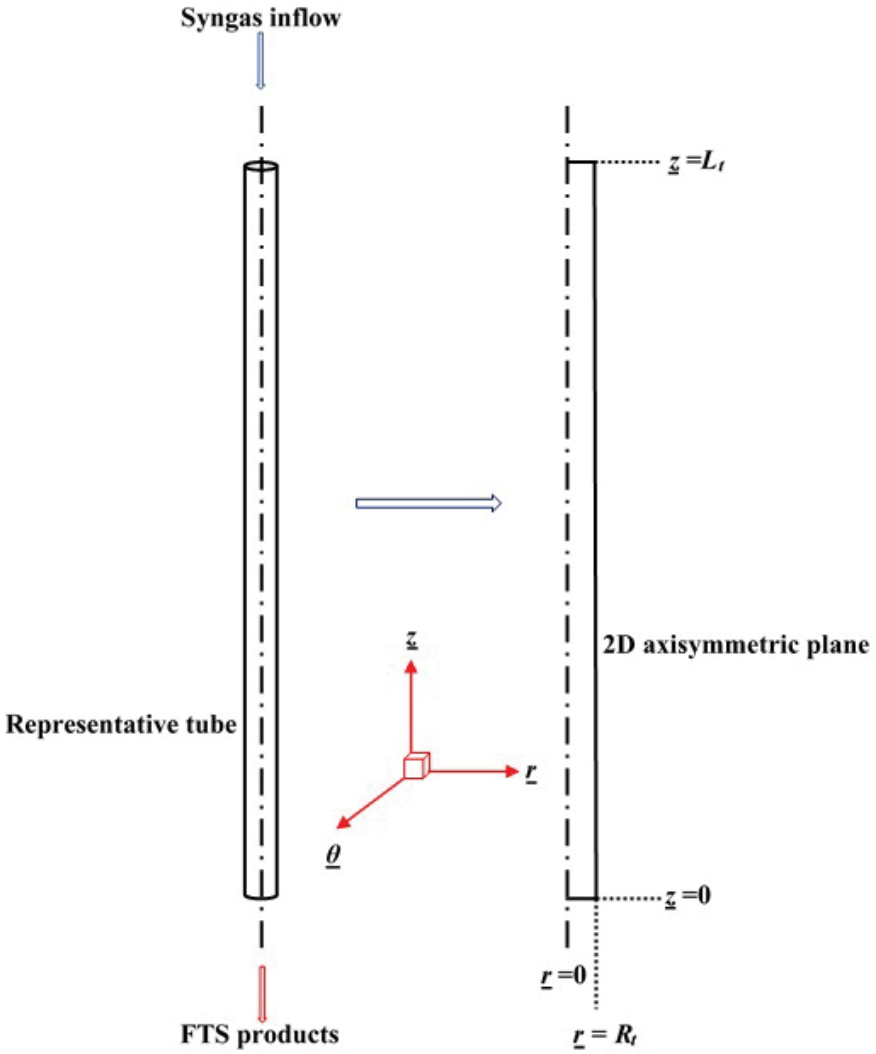

FIGURE 4.2: A representative fixed bed reactor tube on a 2D axisymmetric plane

At time $t = 0$:

$$\left.\begin{aligned} c_j &= c_{j0} \\ T &= T_0 \\ p &= p_0 \\ u_z &= u_s \\ \rho_f &= \rho_{f\,0} \end{aligned}\right\} \quad \forall \text{ values of } z \text{ and } r \tag{4.1}$$

At time $t > 0$:

$$\left.\begin{aligned} c_j &= c_{j1} \\ T &= T_1 \end{aligned}\right\} \quad \text{at } z = 0 \text{ and } 0 \leq r \leq \frac{d_{t,int}}{2} \tag{4.2}$$

$$\frac{\partial c_j}{\partial r} = 0 \qquad \text{at } r = 0 \text{ and } r = \frac{d_{t,int}}{2}, \quad \forall\, z \tag{4.3}$$

$$\frac{\partial T}{\partial r} = 0 \qquad \text{at } r = 0, \quad \forall\, z \tag{4.4}$$

$$\frac{\partial T}{\partial r} = -\frac{h_{\mathrm{w}}}{\kappa_r}(T_{\mathrm{react}} - T_{\mathrm{w}}) \qquad \text{at} \quad r = \frac{d_{\mathrm{t,int}}}{2}, \quad \forall\, z \tag{4.5}$$

4.1.2 Mesh Refinement Studies

The mesh played a crucial role in terms of: convergence, the accuracy of the solution and what may be deemed a "reasonable" computational time for the numerical model. The initial convergence of the numerical model is perhaps the most challenging aspect of the solution process, as such, it was helpful to start with a relatively loose mesh in order to achieve quick convergence and then to tighten the mesh with subsequent computational runs. It is pertinent to state that choosing too coarse a mesh could cause instabilities in the model and lead to erroneous solutions or even non-convergence.

In order to establish the mesh independence of the results in the course of optimising the solution and solution time, it was necessary to carry out a mesh and convergence test according to the Grid Convergence Index (GCI) method of Roache [173]. Unlike in the more traditional methods used in computational fluid mechanics such as the Richardson extrapolation which relies on mesh size doubling i.e. successive mesh sizes change by a factor of two [174], the GCI provides a discretisation error estimate even when the successive mesh refinements are non-integer multiples. In this work, the solution of finest grid or mesh will be used as the "exact" solution and the absolute difference between results from the coarser meshes and this "exact" solution will give an indication of the error estimates in the solution deriving from any variation in spatial discretisation. According to Schwer [175], GCI error estimates may be used with a minimum of two mesh solutions , however better confidence is established with three or more mesh solutions; this work uses a minimum of four mesh solutions.

Figure 4.3(a)-(d) shows a sample progression of how the quadrilateral element meshing is tightened using a mesh size parameter h. The radial axes have been slightly exaggerated for display purposes. The added resolution in the $\vec{r}$ direction helps capture the steep thermal gradient propagating inwards from the exterior wall at the tube circumference.

Quadrilateral elements were chosen instead of the free triangular mesh elements, because their high aspect ratio (ratio of the longest to the shortest edge) facilitated the addition of resolution to areas of particular interest in the reactor, e.g. the walls where the steepest thermal gradient occurs. Triangular elements on the other hand tend to have an aspect ratio of one, resulting in all areas of the reactor being evenly meshed. This may mask interesting results upon computation.

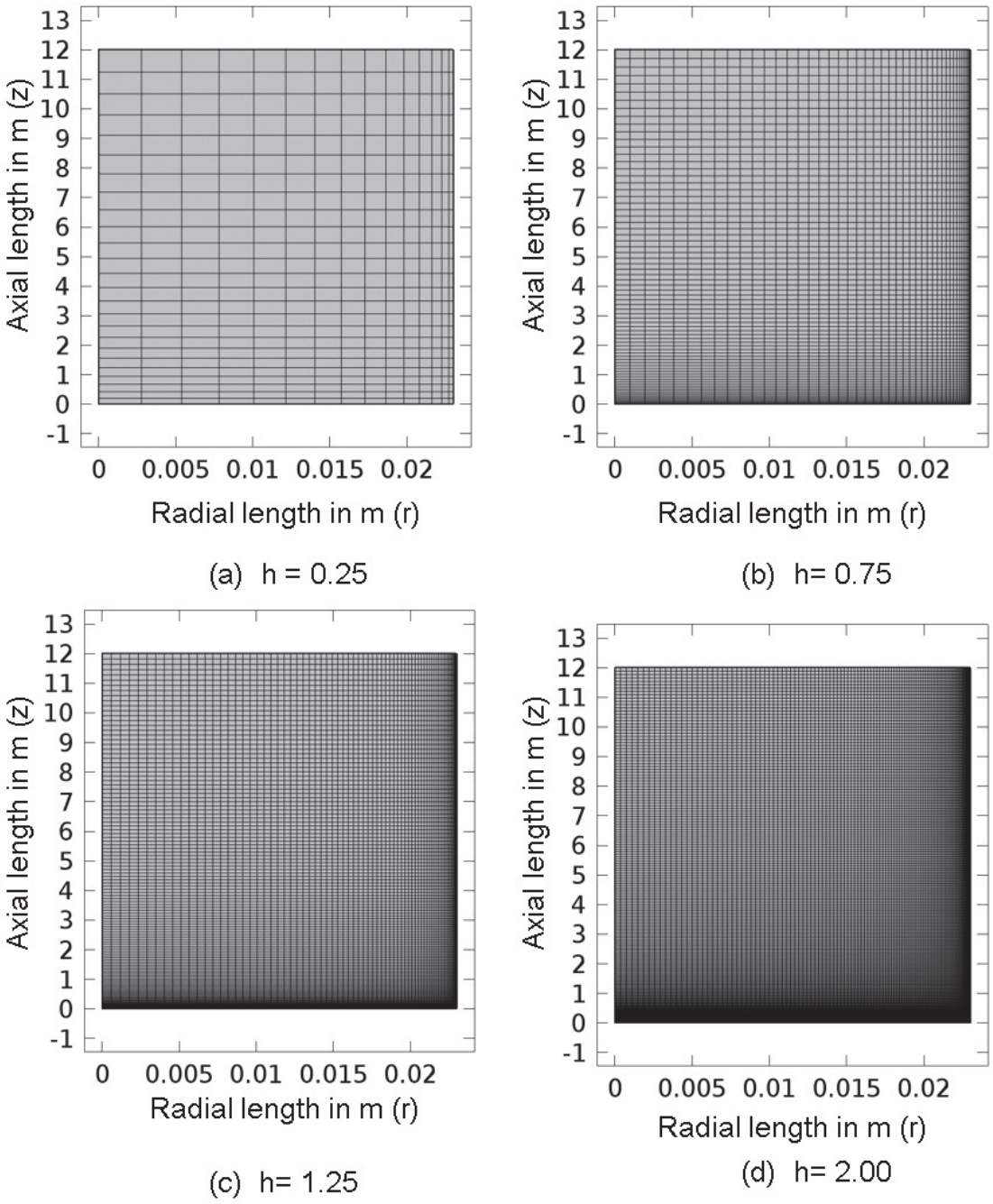

FIGURE 4.3: A selection of meshes used in the mesh-convergence tests: the density of the mesh is proportional to the magnitude of the mesh size parameter h

The results of the mesh refinement test are presented in Fig 4.4. The mesh size parameter, h ranged from the coarse ($h = 0.03$, 3375 quadrilateral elements and 120290 degrees of freedom) to the fine ($h = 2$, 24000 quadrilateral elements and 468530 degrees of freedom). The absolute value of the difference between the hotspot temperature at each mesh size parameter and that at the finest mesh was monitored until the solution converged and remained constant. It is clearly seen that beyond $h = 1$, there was no significant change in the absolute temperature value. Further increments in h, beyond $h = 2$, resulted in the computer running out of random access memory.

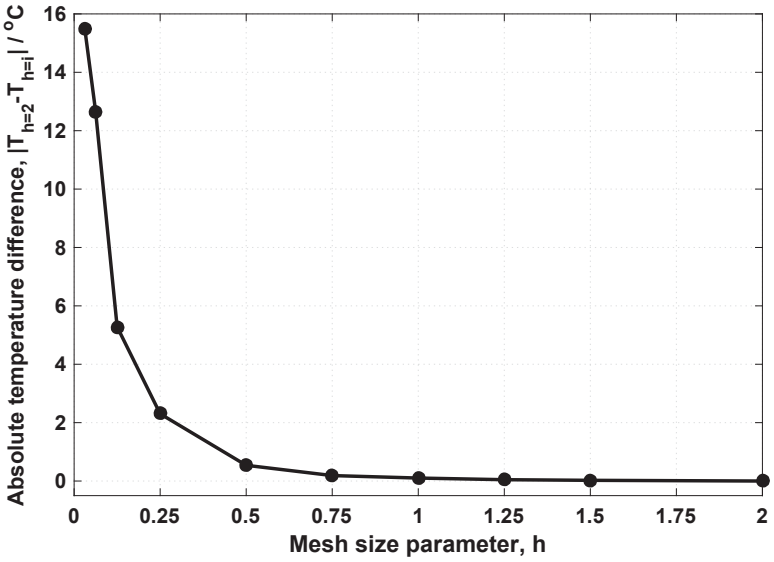

FIGURE 4.4: Mesh independence test for reactor hotspot temperature at $T_{in,\,cool} = 224^{o}C$

4.1.3 Comparison with Literature

Figure 4.5 compares simulation results obtained from the numerical model to results published in literature. In particular, the axial temperature profiles in the reactor for varied inlet or cooling temperatures are compared to the numerical modelling study carried out by Jess et al [5]. As may be observed from Figure 4.5A (Jess et al [5]) and Figure 4.5B (this work), there is good agreement between the results generated and those sourced from literature. In the main, the characteristic hotspot temperature of a high activation energy, exothermic reaction carried out in a tubular wall cooled reactor can be seen to occur near the reactor entrance (i.e. within the first 2m of the reactor axial length). The amplitude of the hotspot temperature is generally exacerbated with increasing cooling temperature, and at an inlet coolant temperature of 250°C, the reactor tends towards instability and a thermal runaway occurs. Figure 4.6 shows a maximum deviation of 1% between the results of this work and those of Jess et al [5]

for the maximum temperature experienced in the reactor. This relatively small error provides confidence in both the numerical model and ability of the software to replicate published results.

Figures 4.7A and B juxtapose the results of Jess et al [5] with this work's reactant conversion profiles in the reactor, for the case of $T_{in,\,cool} = 224^{o}C$. The percentage deviation in the exit conversions of hydrogen and carbon monoxide between the results of Jess et al [5] and that of this study are respectively 1.4% and 1%. A maximum error of 7% was recorded on comparing the conversion per pass for carbon monoxide at various inlet temperatures calculated in this work, with literature values, see Figure 4.8.

4.2 Experimental Co-catalysed Fischer-Tropsch Synthesis

4.2.1 Experimental Studies

In contrast to the previous section 4.2, where the numerical model was checked against another numerical simulation in literature, this section compares results predicted by the numerical model with those obtained from the experimental work of Rafiq et al [122]. Implicit in this aspect of the verification exercise is the establishment of the robustness of the model to handle physical systems of varied dimensions (industrial and laboratory scales) as well as the peculiarities of the kinetics of a cobalt versus iron catalysed Fischer-Tropsch reaction.

Figure 4.9 is a schematic of the experimental setup, comprising a 2m long fixed bed reactor with an inner diameter of 0.0272m. Pressurised water ($200^{o}C$ and $1.6 \times 10^{6}Pa$) in the coolant jacket was used to remove the reaction heat. The temperature of the outer surface of the reactor vessel at the points T_2 to T_8 was measured using K-type thermocouples. The gas phase products were analysed offline using a commercial residual gas analyser (RGA) combined with a gas chromatograph (GC) while the liquid oil/wax product weights were calculated by the overall mass balance within $\pm 2.5\%$ experimental error. A detailed description of the experimental procedure, accuracy, specifications of the operating conditions of the laboratory scale reactor/catalyst and the product analyses may be found in the works of Rafiq et al [122]. The kinetic expressions, constitutive equations and relevant correlations are recorded elsewhere [80, 120, 176].

4.2.2 Mesh Refinement Studies

As in subsection 4.1.2, the results obtained from this particular model were also subjected to mesh sensitivity tests in order to confirm their reliability. The result of the mesh

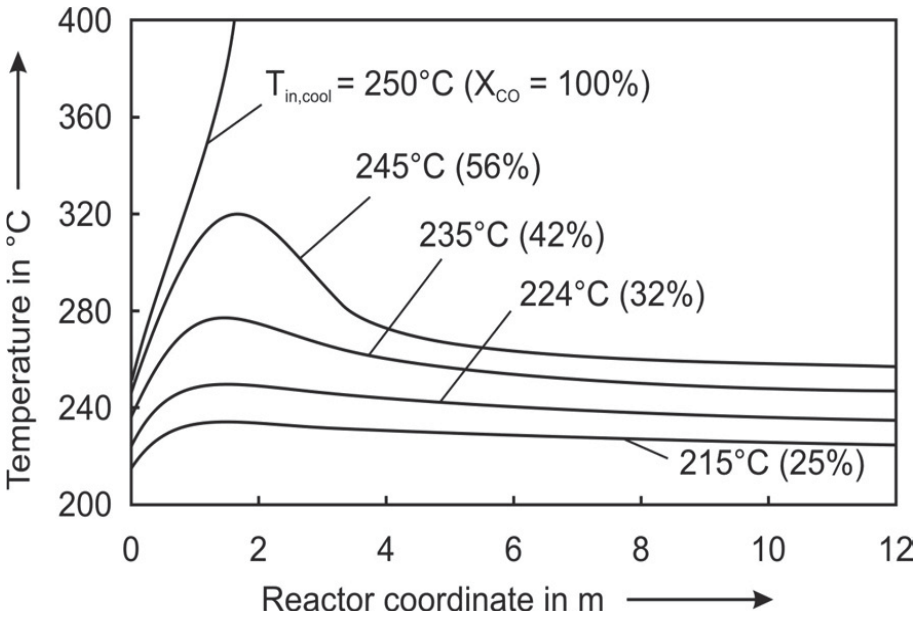

(A) Influence of cooling temperature on axial temperature profiles (Jess et al [5])

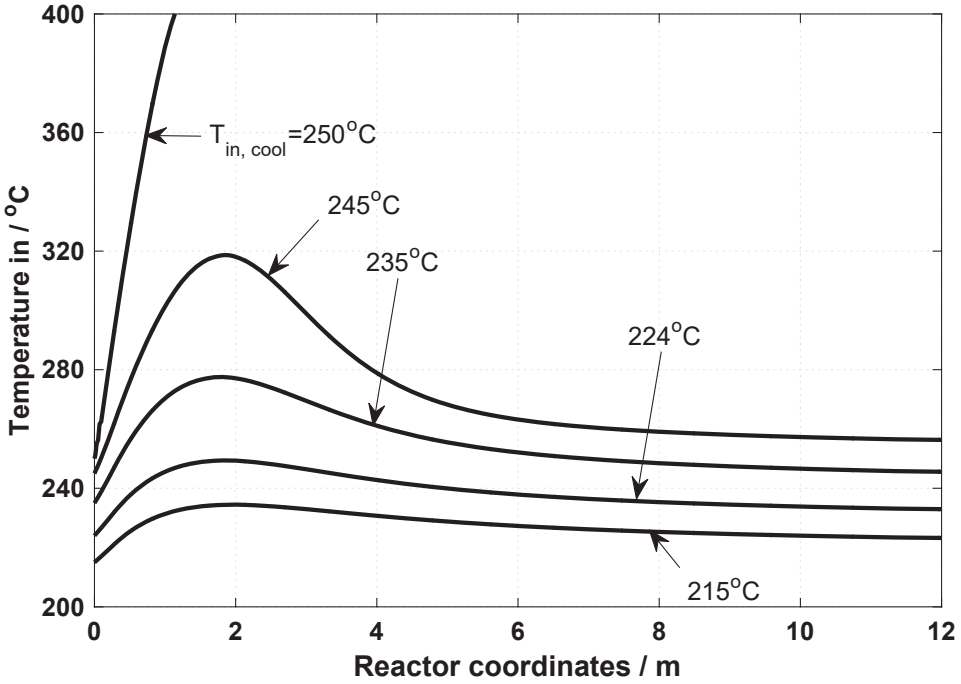

(B) Influence of cooling temperature on axial temperature profiles, (This work)

FIGURE 4.5: 2 Comparison of the influence of cooling temperature on axial temperature profiles (Fe-catalyst using a 2D quasi-homogeneous model)

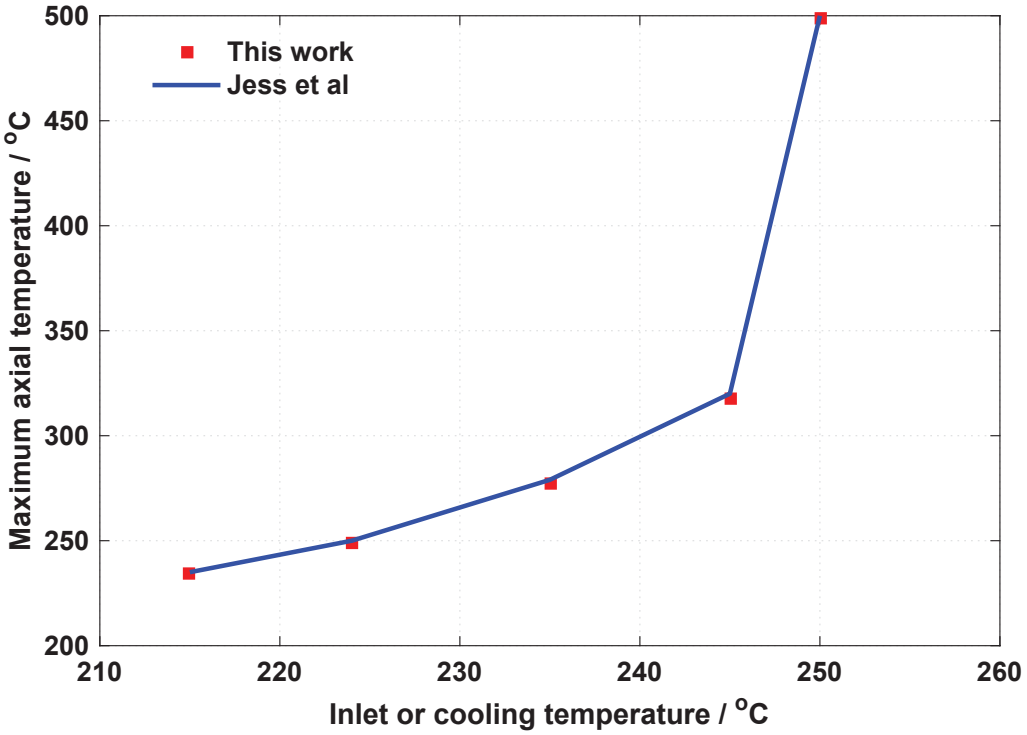

FIGURE 4.6: Comparison of hotspot temperatures for various inlet or cooling temperatures between Jess et al [5] and this work.

refinement test conducted for the exit selectivity of C_{5+} is presented in Fig 4.10. It should be stated that the exit selectivity of C_{5+} has been used for illustration purposes, other quantities may be used to show the same trends described in this section. The mesh element size was fine tuned by systematically increasing the mesh size parameter, h and re-running the simulation for each value of h. The absolute value of the difference between the exit C_{5+} selectivity solution at each successive mesh and that at the finest mesh ($h = 2$) was recorded until the solution converged and stabilised as shown in Fig 4.10. The coarsest mesh consisted of 9375 quadrilateral elements with 275795 degrees of freedom (DOF), while the finest mesh consisted of 24000 quadrilateral elements and 693215 corresponding degrees of freedom (DOF).

4.2.3 Verification of Numerical Model against Experiments

The laboratory scale reactor was modelled for four experimental runs at different Gas Hour Space Velocities (GHSV), and the predicted results from the numerical model were examined against those obtained from the experiment of Rafiq et al [122]. The GHSV values spanned 37 and 148NmL $g_{cat}^{-1}\,h^{-1}$.

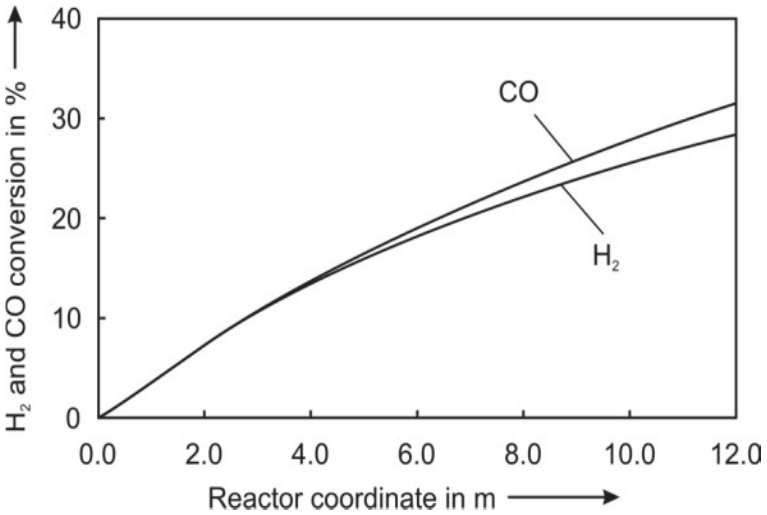

(A) Profiles of H_2 and CO conversion in the multi-tubular FT reactor for $T_{in,\,cool} = 224°C$ (Jess et al [5])

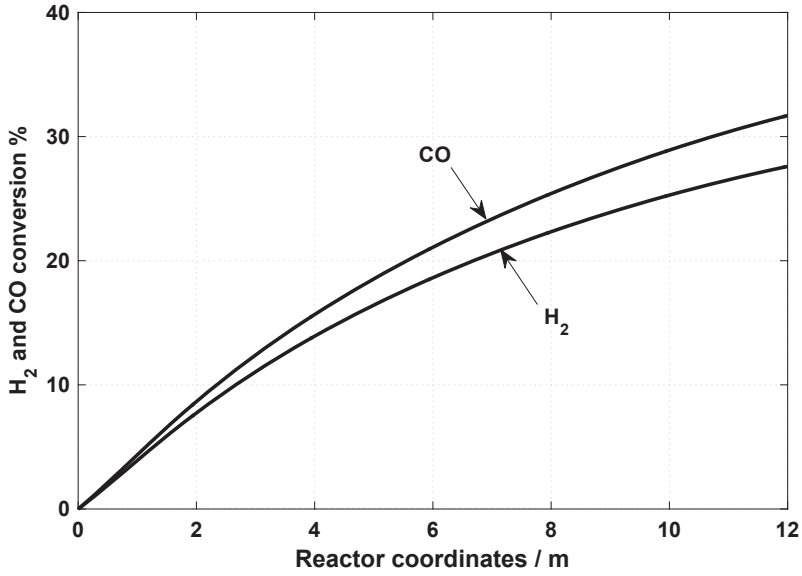

(B) Profiles of H_2 and CO conversion in the multi-tubular FT reactor for $T_{in,\,cool} = 224°C$ (this work)

FIGURE 4.7: Comparison of profiles of H_2 and CO conversion in the multi-tubular FT reactor for $T_{in,\,cool} = 224°C$ (Fe-catalyst using a 2D quasi-homogeneous model)

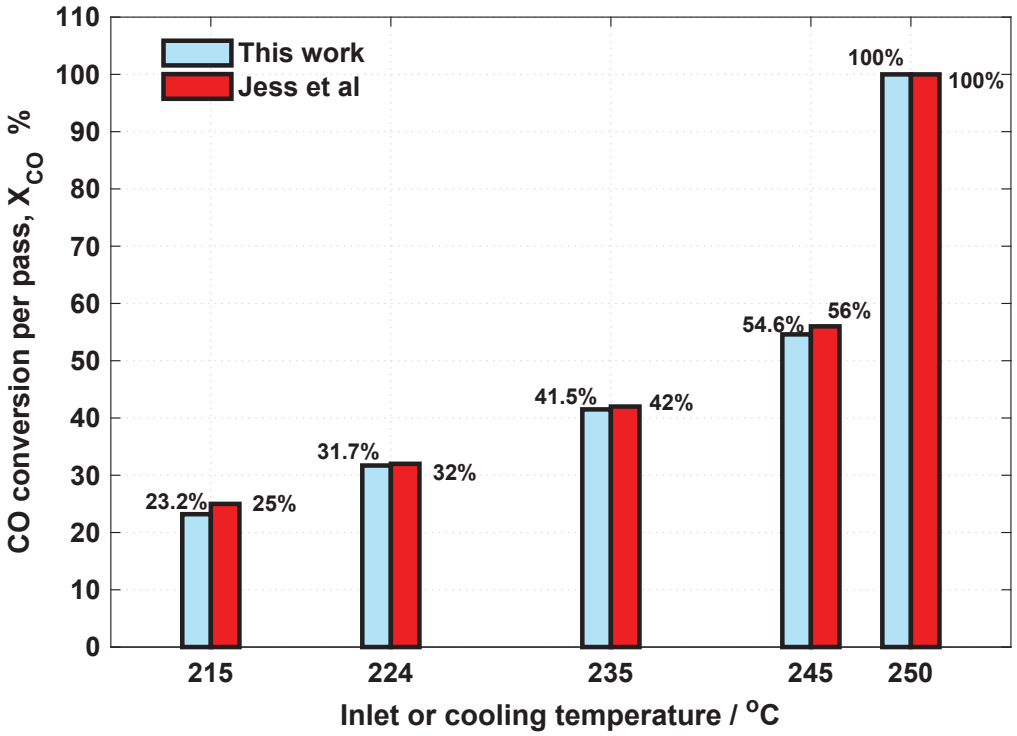

FIGURE 4.8: Comparison of CO conversion per pass for various inlet or cooling temperature between Jess et al [5] and this work.

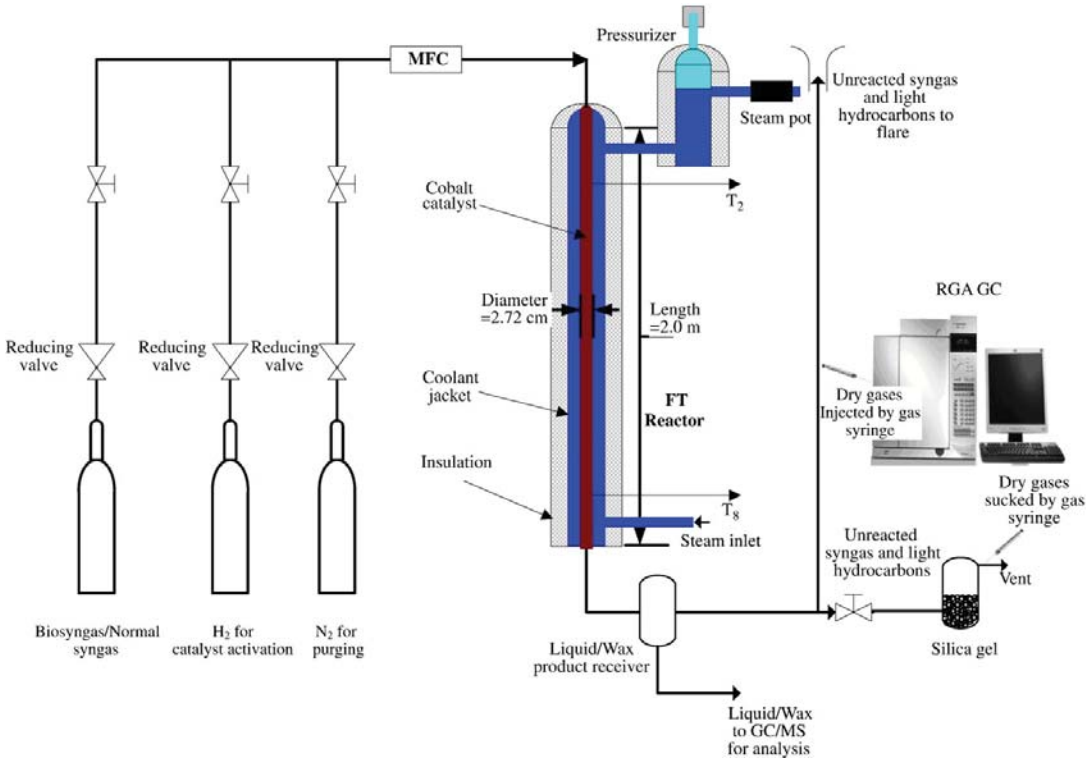

FIGURE 4.9: Schematic diagram of the Fischer Tropsch experimental setup [122]

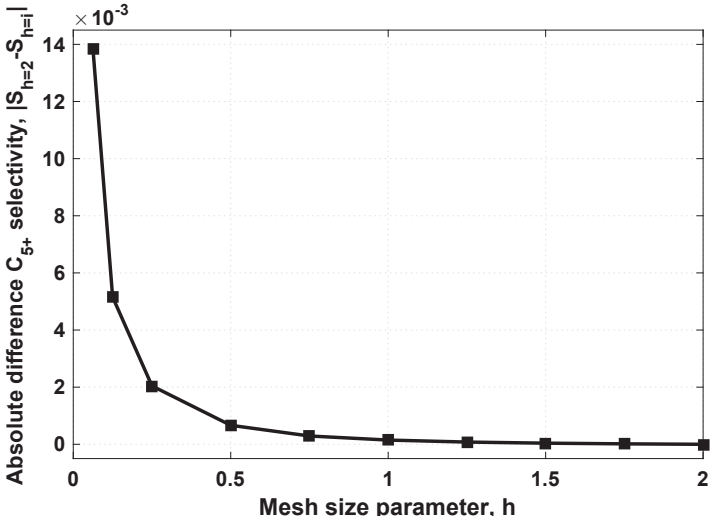

FIGURE 4.10: Mesh independence test for C_{5+} selectivity

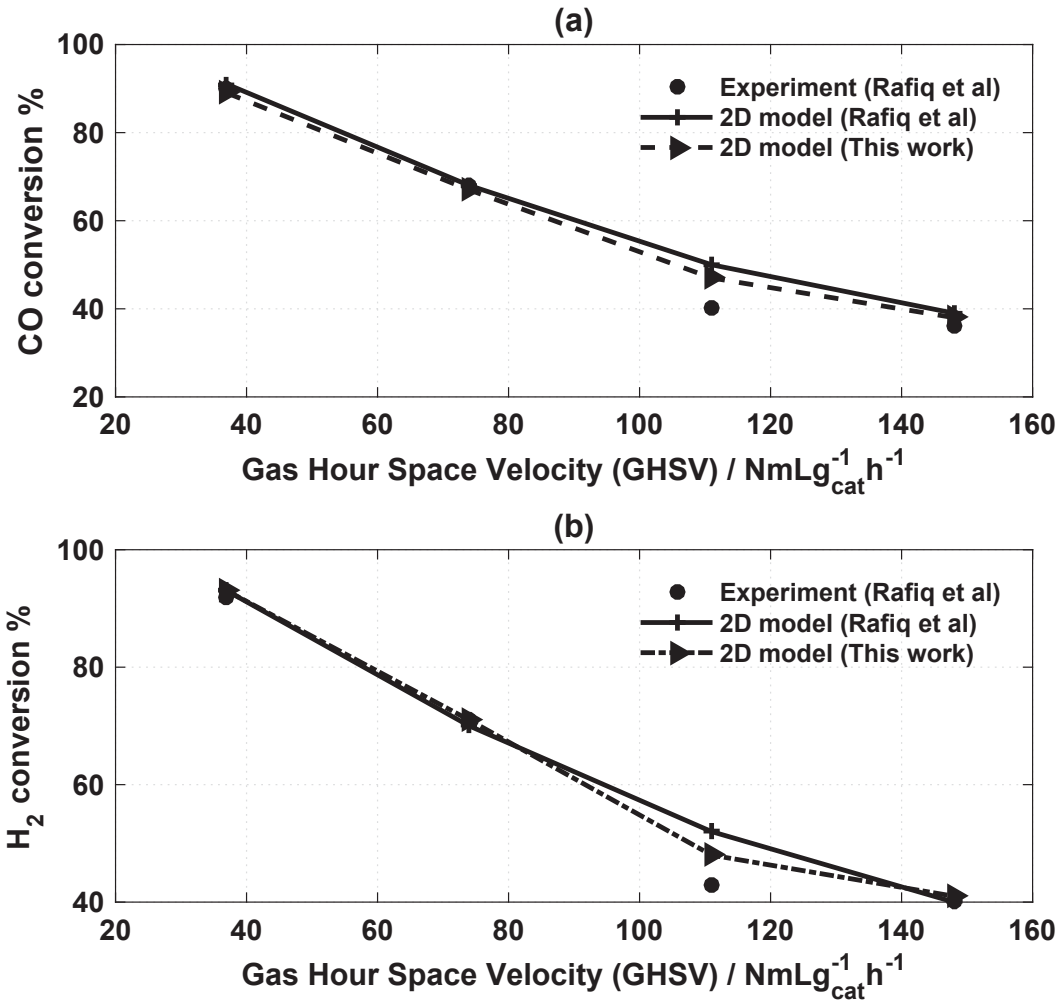

FIGURE 4.11: Comparison of the conversion of CO and H_2 between the experimental work of Rafiq et al [122], the 2D numerical model of Rafiq et al [122] and the 2D model of this work.

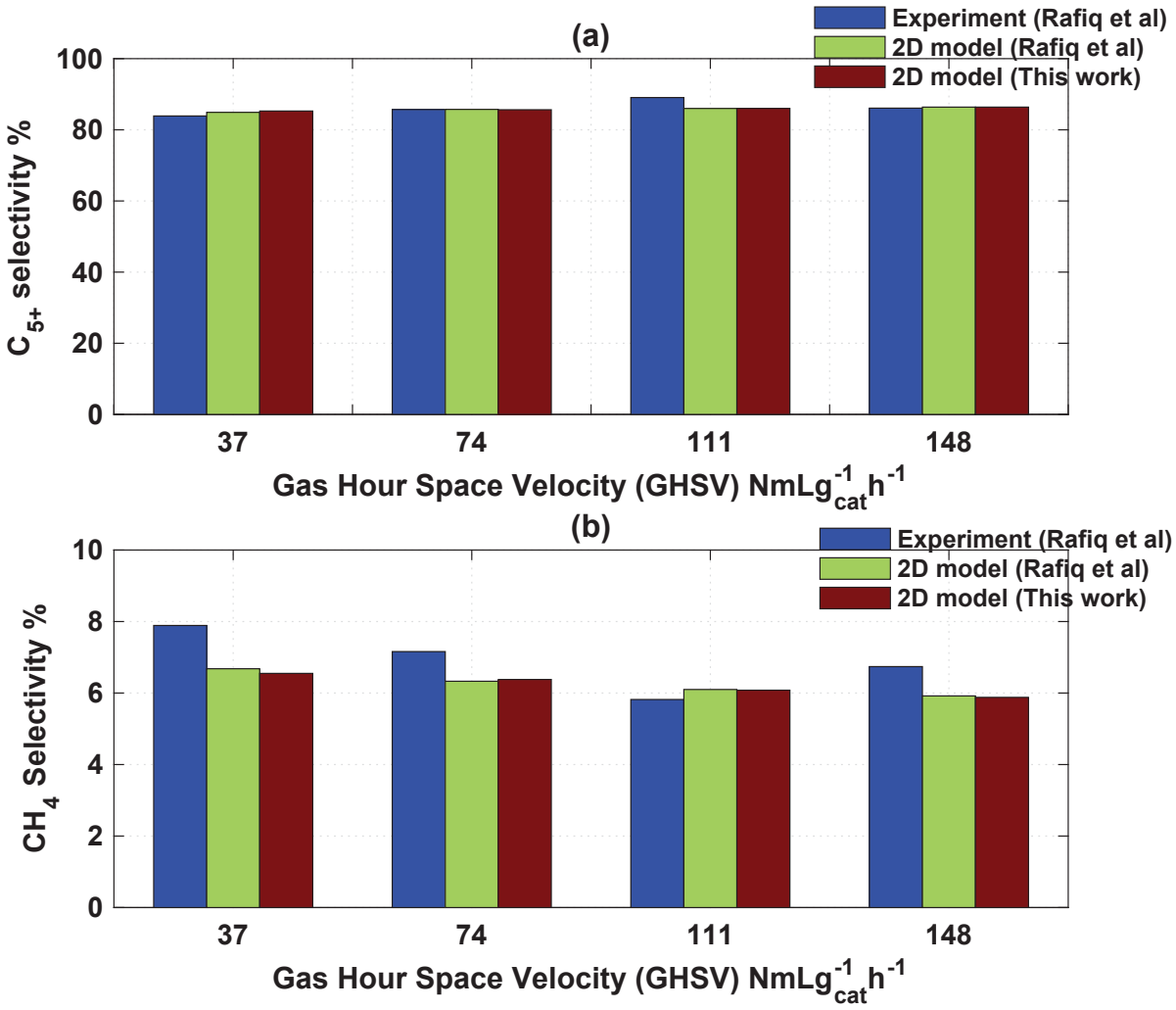

FIGURE 4.12: Comparison of the selectivity to C_{5+} and CH_4 between the experimental work of Rafiq et al [122], the 2D numerical model of Rafiq et al [122] and the 2D model of this work.

Figure 4.11(a) and (b) compares the results of the modelling carried out in this thesis to the experimental work and 2D modelling of Rafiq et al [122], for the conversion of CO and H_2 respectively. As may be seen from the plots, there is good agreement (within 4.5%) between the experimental results and the model put forward in this work. As anticipated, the conversion of either reactant decreases with increasing GHSV (due to reducing residence time with increasing GHSV).

Figure 4.12 (a) and (b) show the comparison of the selectivity to the C_{5+} and CH_4 products of the reaction, between the experiment and models respectively. In Figure 4.12 (a), the results of the experiment and the model put forward in this work are in good agreement (2%). In Figure 4.12 (b), the experimental selectivity to methane is slightly higher than that predicted by either of the models except in the case of GHSV= $111 \mathrm{NmL\,g_{cat}^{-1}\,h^{-1}}$, where it is slightly lower. This slight discrepancy may be

TABLE 4.1: Comparison between experimental data (Co catalysed) and 2Dmodels for GHSV = 37NmL g_{cat}^{-1} h^{-1}.

Parameters	Run 1		
	Experiment [122]	2D model [122]	2D model (This work)
GHSV (NmL g_{cat}^{-1} h^{-1})	37	37	37
X_{CO}	90	91	89
X_{H_2}	92	93	93
C_{5+} (g g_{cat}^{-1} h^{-1})	5.42×10^{-3}	5.69×10^{-3}	5.60×10^{-3}
CH_4 (g g_{cat}^{-1} h^{-1})	5.92×10^{-4}	4.98×10^{-4}	4.81×10^{-4}
C_2 (g g_{cat}^{-1} h^{-1})	7.66×10^{-5}	9.13×10^{-5}	8.82×10^{-5}
C_3 g g_{cat}^{-1} h^{-1})	1.99×10^{-4}	2.12×10^{-4}	2.08×10^{-4}
C_4 (g g_{cat}^{-1} h^{-1})	2.44×10^{-4}	2.26×10^{-4}	2.30×10^{-4}
CO_2 (g g_{cat}^{-1} h^{-1})	1.33×10^{-4}	1.34×10^{-4}	1.34×10^{-4}
H_2O (g g_{cat}^{-1} h^{-1})	8.44×10^{-3}	8.28×10^{-3}	8.24×10^{-3}
% Selectivity (C atom basis)			
CH_4	7.89	6.68	6.55
C_2	1.09	1.30	1.13
C_3	2.90	3.11	3.10
C_4	3.59	3.35	3.31
CO_2	0.64	0.65	0.63
C_{5+}	83.89	84.91	85.28
‡ASF (α_{FT})	0.77	0.77	0.77

‡ The α_{FT} obtained from experiment used directly in 2D model

explained by the fact that the models apply a common and constant carbon chain growth probability factor (α_{FT}), whereas, as highlighted in chapter 2, methane tends to have a different α_{FT} value from the other hydrocarbons produced.

The same trends described above are largely replicated in the other case studies as recorded in Tables 4.1 to 4.4. This demonstrates the robustness of the model to effectively describe the physical process.

4.3 Verification of the Effect of Phase Change Material

The final aspect of this chapter attempts to verify the heat sink effect of encapsulated phase change materials in exothermic packed bed reactors. In order to do this, a numerical model was developed, solved on the COMSOL Multiphysics platform and then compared to the experimental work of Zhang et al [131]. As there has been no experimental work done and reported in open literature regarding the use of phase change

TABLE 4.2: Comparison between experimental data (Co catalysed) and 2Dmodels for GHSV = 74NmL g_{cat}^{-1} h^{-1}.

Parameters	Run 2		
	Experiment [122]	2D model [122]	2D model (This work)
GHSV (NmL g_{cat}^{-1} h^{-1})	74	74	74
X_{CO}	68	68	67
X_{H_2}	71	70	71
C_{5+} (g g_{cat}^{-1} h^{-1})	8.13×10^{-3}	8.58×10^{-3}	8.35×10^{-3}
CH_4 (g g_{cat}^{-1} h^{-1})	8.04×10^{-4}	7.03×10^{-4}	7.13×10^{-4}
C_2 (g g_{cat}^{-1} h^{-1})	1.17×10^{-4}	1.31×10^{-4}	1.27×10^{-4}
C_3 (g g_{cat}^{-1} h^{-1})	2.35×10^{-4}	3.07×10^{-4}	2.96×10^{-4}
C_4 (g g_{cat}^{-1} h^{-1})	2.6983×10^{-4}	3.24×10^{-4}	3.22×10^{-4}
CO_2 (g g_{cat}^{-1} h^{-1})	3.37×10^{-4}	1.32×10^{-4}	1.33×10^{-4}
H_2O (g g_{cat}^{-1} h^{-1})	1.26×10^{-2}	1.24×10^{-2}	1.24×10^{-2}
% Selectivity (C atom basis)			
CH_4	7.16	6.33	6.38
C_2	1.11	1.26	1.22
C_3	2.29	3.02	3.04
C_4	2.65	3.22	3.25
CO_2	1.09	0.43	0.47
C_{5+}	85.70	85.74	85.64
‡ASF (α_{FT})	0.779	0.779	0.779

‡ The α_{FT} obtained from experiment used directly in 2D model

materials as diluents in a fixed bed Fischer Tropsch reactor, a different exothermic reaction was considered; the catalytic partial oxidation of methanol on Pt/SiO_2 catalyst in this case. Zhang et al [131] have also shown that this arrangement of phase change material being used as diluents for the the thermal management of an exothermc reaction may be extended to other reactions with different underlying chemistry principles and rector configurations, providing the phase change material is appropriately selected. They ascertained this by performing other experiments including the exothermic polymerisation reaction of methyl methacrylate in a stirred batch reactor, using silica encapsulated polyethylene phase change material. It is on this basis that this concept will be extended to the Fischer-Tropsch reaction in subsequent chapters.

As the fixed bed reactor configuration is of utmost interest as far as this work is concerned, the catalytic partial oxidation of methanol will be the point of reference for this validation and verification exercise.

TABLE 4.3: Comparison between experimental data (Co catalysed) and 2Dmodels for GHSV = 111NmL $g_{cat}^{-1}\,h^{-1}$.

Parameters	Run 3		
	Experiment [122]	2D model [122]	2D model (This work)
GHSV (NmL $g_{cat}^{-1}\,h^{-1}$)	111	111	111
X_{CO}	40	50	47
X_{H_2}	43	52	48
C_{5+} (g $g_{cat}^{-1}\,h^{-1}$)	7.71×10^{-3}	9.59×10^{-3}	9.46×10^{-3}
CH_4 (g $g_{cat}^{-1}\,h^{-1}$)	5.71×10^{-4}	7.55×10^{-4}	7.42×10^{-4}
C_2 (g $g_{cat}^{-1}\,h^{-1}$)	5.27×10^{-5}	1.47×10^{-4}	1.46×10^{-4}
C_3 (g $g_{cat}^{-1}\,h^{-1}$)	1.54×10^{-4}	3.38×10^{-4}	3.31×10^{-4}
C_4 (g $g_{cat}^{-1}\,h^{-1}$)	2.21×10^{-4}	3.64×10^{-4}	3.60×10^{-4}
CO_2 (g $g_{cat}^{-1}\,h^{-1}$)	8.85×10^{-5}	1.38×10^{-4}	1.37×10^{-4}
H_2O (g $g_{cat}^{-1}\,h^{-1}$)	1.10×10^{-2}	1.38×10^{-2}	1.35×10^{-2}
% Selectivity (C atom basis)			
CH_4	5.82	6.10	6.08
C_2	0.57	1.26	1.24
C_3	1.72	2.98	2.98
C_4	2.49	3.26	3.24
CO_2	0.33	0.44	0.45
C_{5+}	89.07	86.0	86.01
‡ASF (α_{FT})	0.784	0.784	0.784

‡ The α_{FT} obtained from experiment used directly in 2D model

4.3.1 Experimental Description

In this experimental procedure, the phase change material of choice is indium metal (fusion temperature 156.7°C) encapsulated in silica. A full description of the phase change material encapsulation procedure, which is not outlined here, may be found in the works of Zhang et al [131] and Cingarapu et al [177]. The supported Pt/SiO_2 catalyst preparation procedure are also described in detail by Zhang et al [131].

Figure 4.13 is a schematic of the experimental setup. The reactor was initially heated to, and stabilised at a temperature of 120°C under a continuous stream of He gas for 1800 seconds. A gas mixture comprising: He (87% vol.), air (9%vol. of $N_2 + O_2$) and CH_3OH was then charged into the reactor regulated by mass flow controllers at 100ml min^{-1}. Two on-line gas chromatograph systems were used in analysing the effluent products: a Porapak Q packed column with thermal conductivity detector for carbon dioxide and a methyl-silicone capillary column with flame ionisation detector for organic products. Three runs of experiments for three different values of ω_r (ratio by mass of catalyst to encapsulated indium phase change material) were carried out. In addition, two control

TABLE 4.4: Comparison between experimental data (Co catalysed) and 2Dmodels for GHSV = 148NmL $g_{cat}^{-1}\,h^{-1}$.

Parameters	Run 4		
	Experiment [122]	2D model [122]	2D model (This work)
GHSV (NmL $g_{cat}^{-1}\,h^{-1}$)	148	148	148
X_{CO}	36	39	38
X_{H_2}	40	40	41
C_{5+} (g $g_{cat}^{-1}\,h^{-1}$)	9.20×10^{-3}	1.00×10^{-2}	1.00×10^{-2}
CH_4 (g $g_{cat}^{-1}\,h^{-1}$)	8.19×10^{-4}	7.64×10^{-4}	7.57×10^{-4}
C_2 (g $g_{cat}^{-1}\,h^{-1}$)	9.85×10^{-5}	1.52×10^{-4}	1.49×10^{-4}
C_3 (g $g_{cat}^{-1}\,h^{-1}$)	2.63×10^{-4}	3.57×10^{-4}	3.54×10^{-4}
C_4 (g $g_{cat}^{-1}\,h^{-1}$)	3.83×10^{-4}	3.53×10^{-4}	3.52×10^{-4}
CO_2 (g $g_{cat}^{-1}\,h^{-1}$)	1.52×10^{-4}	1.34×10^{-4}	1.37×10^{-4}
H_2O (g $g_{cat}^{-1}\,h^{-1}$)	1.36×10^{-2}	1.44×10^{-2}	1.42×10^{-2}
% Selectivity (C atom basis)			
CH_4	6.74	5.92	5.88
C_2	0.86	1.26	1.25
C_3	2.37	3.02	3.00
C_4	3.48	3.04	3.10
CO_2	0.46	0.38	0.39
C_{5+}	86.09	86.38	86.38
‡ASF (α_{FT})	0.8	0.8	0.8

‡ The α_{FT} obtained from experiment used directly in 2D model

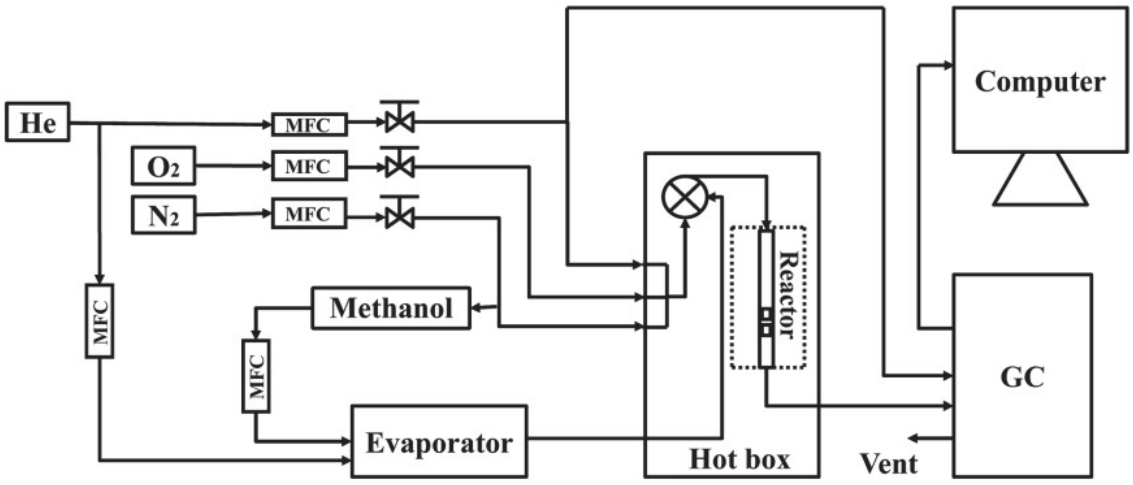

FIGURE 4.13: Experimental setup for the catalytic partial oxidation of methanol reaction system [178]

experiments involving the use of silica and silicon carbide respectively, were used as diluents were also carried out for the purpose of comparison. The catalyst and diluent material were mixed together and then loaded into a quartz reactor to form a 1cm long column. A 1mm diameter thermocouple was inserted into the reactor to measure the temperature of the catalyst bed.

4.3.2 Numerical Model

In general, the transfer of heat from the surrounding reaction fluid mixture to an encapsulated phase change material particle, is a function of the temperature difference between the fluid temperature and the surface temperature of the particles. By setting up an electrical circuit analogy of the external fluid, boundary region and the solid particles system, the heat transport resistances within the system may be grouped as follows to yield the melting time, τ of the phase change material:

$$\tau(T_\mathrm{s} - T_\mathrm{m}) = \rho_\mathrm{pcm}\,\Delta H_\mathrm{fus}\left[\frac{1}{3}\left(\frac{1}{\kappa_\mathrm{pcm} r_\mathrm{pcm}} + \frac{1}{\kappa_{\mathrm{SiO_2}} r_{\mathrm{SiO_2}}}\right) r^3 - \frac{1}{2}\frac{r^2}{\kappa_\mathrm{pcm}} + \frac{1}{6}\frac{r_\mathrm{pcm}^2}{\kappa_\mathrm{pcm}} - \frac{1}{3}\frac{r_\mathrm{pcm}^3}{\kappa_{\mathrm{SiO_2}}\, r_{\mathrm{SiO_2}}} + \frac{r_\mathrm{pcm}^2}{3\kappa_{\mathrm{SiO_2}}}\right] \tag{4.6}$$

Where: T_s is the particle surface temperature, $T_\mathrm{m} = 157.6^\mathrm{o}\mathrm{C}$ is the melting point of indium, $\rho_\mathrm{pcm} = 7300\mathrm{kg\,m^{-3}}$ is the density of phase change material, $\Delta H_\mathrm{fus} = 28520\mathrm{J\,kg^{-1}}$ is the enthalpy of fusion of indium, $\kappa_\mathrm{pcm} = 81.8\mathrm{Wm^{-1}K^{-1}}$ is the thermal conductivity of indium, $\kappa_{\mathrm{SiO_2}} = 1.3\mathrm{Wm^{-1}K^{-1}}$ is the thermal conductivity of the encapsulating silica shell, r is the radius of phase change material at some time t, r_pcm is the radius of phase change material before melting and $r_{\mathrm{SiO_2}}$ is the radius of silica shell.

An in-depth treatment of the kinetics of the partial oxidation of methanol on $\mathrm{Pt/SiO_2}$ may be found in the works of McCabe et al [179] and Lordanidis [180]. If the reaction is treated as a first order reaction (e.g. using excess air) [181], then the instantaneous heat flow from the reaction may be represented as:

$$\frac{\mathrm{d}Q_\mathrm{rel}}{\mathrm{d}t} = \Delta H_\mathrm{r} \times k\left[c_{\mathrm{CH_3OH,\,in}} - \frac{\int_0^t \left(\frac{\mathrm{d}Q_\mathrm{rel}}{\mathrm{d}t} + \frac{\mathrm{d}Q_\mathrm{pcm}}{\mathrm{d}t}\right)}{\Delta H_\mathrm{r}}\right] \tag{4.7}$$

ΔH_r is the enthalpy of reaction, k is reaction rate constant, $c_{\mathrm{CH_3OH,\,in}}$ is the inlet concentration of methanol and $\int_0^t \left(\frac{\mathrm{d}Q_\mathrm{rel}}{\mathrm{d}t} + \frac{\mathrm{d}Q_\mathrm{pcm}}{\mathrm{d}t}\right)$ is the corresponding net heat accumulation of reaction heat, taking into account the buffering effect of the phase change material. Solving equation (4.7) (by method of integrating factors) and integrating the resulting expression gives the net heat released:

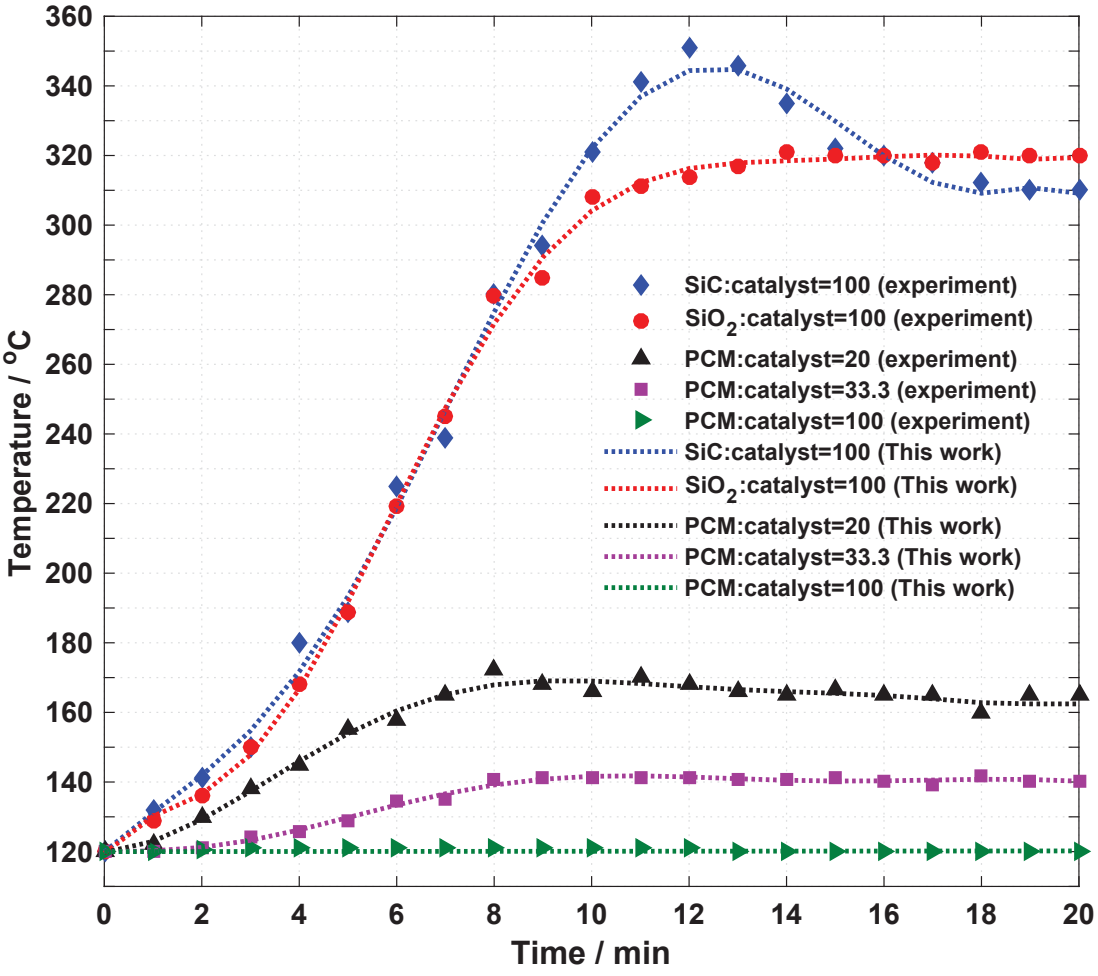

FIGURE 4.14: Reaction temperature of the catalytic oxidation of CH_3OH on Pt/SiO_2 catalyst as a function of time (Experimental[131] and numerical simulation).

$$Q_{\text{rel}} = \Delta H_{\text{r}}\, c_{\text{CH}_3\text{OH,in}}\, [kt + \exp(-kt)] \tag{4.8}$$

It is pertinent to note that the expressions for the heat released by the reaction, as shown in equations (4.7) and (4.8), are slightly different to those outlined in equations (3.32) and (3.60) in chapter 3. The underlying principle is however the same, i.e., the heat generated by the reaction is obtained by the product of the reaction rate and the enthalpy of reaction in question, as shown in equation (4.7). As previously stated, the second term in brackets in equation (4.7) is the effective heat accumulated when the heat sink effect of the phase change material is considered. The heat release term in equation (4.8) has been conveniently re-cast as a time explicit expression in order to facilitate comparison between the available experimental data in literature [131] and the numerical results obtained in this work as shown in Figure 4.14.

The piecewise heat capacity expression for the phase change material in equation (3.62) in chapter 3 has been used to compute the heat absorbed by the phase change material, using the the principle that: the heat released by the reaction is absorbed by the encapsulated phase change material ($Q_{\text{rel}} = Q_{\text{abs}} = Q$) according the following temperature-dependent, piecewise, enthalpy function:

$$Q = \begin{cases} (m_{\text{SiO}_2} C_{\text{p, SiO}_2} + m_{\text{pcm}} C_{\text{p, pcm, s}}) \times (T - T_0) & : T < T_{\text{m}}, \\ (m_{\text{SiO}_2} C_{\text{p, SiO}_2} + m_{\text{pcm}} C_{\text{p, pcm, s}}) \times (T - T_0) + \psi\, m_{\text{pcm}}\, \Delta H_{\text{fus}} & : T_{\text{m}} \leq T \leq (T_{\text{m}} + \Delta T) \\ (m_{\text{SiO}_2} C_{\text{p, SiO}_2} + m_{\text{pcm}} C_{\text{p, pcm, l}}) \times (T - T_0) + m_{\text{pcm}}\, \Delta H_{\text{fus}} & : T > T_{\text{m}}. \end{cases} \tag{4.9}$$

Subsequent computations with respect to the heat sink effect of the phase change material in the reactor are consistent with the steps described in chapter 3. It will be recalled from chapter 3 that the liquid melt fraction, ψ is given by:

$$\psi = \begin{cases} 0 & : T < T_{\text{m}}, \\ \dfrac{\Delta H_{\text{pcm}} - C_{\text{p,pcm,s}}(T_{\text{m}} - T_0)}{\Delta H_{\text{fus}}} & : T_{\text{m}} = T, \\ 1 & : T > T_{\text{m}}. \end{cases} \tag{4.10}$$

Implementing and solving the foregoing and the kinetic equations on the COMSOL Multiphysics platform yields results which were compared with the experimental data. Figure 4.14 depicts a reaction time dependent temperature plot for different scenarios of ω_{r} (ratio of mass of catalyst to phase change material) and two control experiments where the phase change material is replaced with silicon dioxide and silicon carbide in each case. On the same graph, the numerical simulation results are plotted and as may be seen, there is agreement between both sets of data within an error limit of 7%.

In all the scenarios, the reaction systems eventually attain steady state, with the phase change material scenarios reaching equilibrium quicker than their contemporary inert diluent systems. It is worthy of mention that even when high thermal conductivity materials, comparable to copper, such as SiC ($\kappa = 360\text{W m}^{-1}\text{K}^{-1}$, $C_{\text{p}} = 690\text{J kg}^{-1}\text{K}^{-1}$) are used as diluents, the reaction still suffers thermal runaway as shown in Figure 4.14. The reactor temperature ramps up quickly (seeing a maximum ramp rate of about 30K min^{-1}), goes through a maxima before settling down to steady state conditions. In contrast, SiO_2 with a relatively modest thermal conductivity ($\kappa = 1.3\text{W m}^{-1}\text{K}^{-1}$, $C_{\text{p}} = 700\text{J kg}^{-1}\text{K}^{-1}$) and a similar temperature ramp rate, puts the catalyst through a less severe temperature spike and approaches steady state conditions faster. Neither material ultimately prevents thermal runaway. This reveals that under the given circumstances, the heat capacity of the inert material is crucial to preventing runaway.

TABLE 4.5: Comparison between experimental and numerical values of equilibrium temperature and methanol conversion for the partial oxidation of methanol on Pt/SiO_2

Inert substance	ω_r	Equilibrium temperature (°C)		Conversion CH_3OH(%)	
		Experiment	Model	Experiment	Model
SiC		310	308	99.3	98.8
SiO_2		320	319	98.2	97.9
PCM	100	120	120	0.6	0.54
PCM	33.3	140	140	5.5	5.1
PCM	20	165	162	32.5	31.8

Encapsulated phase change materials with fusion temperatures lying within the desired reaction temperature range are thus attractive candidates for use as diluents because of the high thermal capacitance/inertia they are able to provide.

Table 4.5 is a summary of the equilibrium (or steady state) temperature and methanol conversion for both the numerical model and experiment. The maximum, absolute, average error between the experimental and numerical model for the equilibrium temperature and methanol conversion are respectively within 2% and 10%. Expectedly, a high temperature drives the limiting reactant (CH_3OH) to near total conversion as seen in the case of SiC: 99.3% (model, 98.8%) and SiO_2 98.2% (model, 97.9%). These contrast with the far more conservative conversion: 0.6-32.5% (model, 0.54-31.8%) achieved when encapsulated phase change material is mixed with the catalyst; a direct result of the more moderate temperatures experienced under these conditions.

Table 4.6 compares the product distribution of the reaction predicted by the numerical model with that measured in the experiment. A good agreement (within 6% error) is seen to exist between both sets of data. It should be stated that although there are quite a number of other products (intermediary and otherwise) obtained from this reaction, a representative desirable product, formaldehyde and a representative undesirable product such as CO_2 have been chosen to illustrate the underlying principles of the observations made. Put together, tables 4.5 and 4.6 reveal that although the presence of the phase change material reduces reactant conversion as a result of limiting the prevalent equilibrium temperature in the reactor, it equally has the effect of increasing selectivity towards the desired HCHO.

4.3.3 Mesh Refinement

The results generated in this section were as in previous sections, subjected to mesh-convergence tests. The mesh independence test results for the exit concentration of

TABLE 4.6: Comparison between experimental and numerical values of CO_2 selectivity and HCHO selectivity for the partial oxidation of methanol on Pt/SiO_2

Inert substance	ω_r	Selectivity CO_2 (%)		Selectivity HCHO (%)	
		Experiment	Model	Experiment	Model
SiC		83.2	82.4	–	1×10^{-4}
SiO_2		87.7	86.8	–	1×10^{-4}
PCM	100	–	1×10^{-4}	97.3	95.8
PCM	33.3	3.1	2.93	75.2	73.8
PCM	20	14.8	13.9	32.5	31.4

formaldehyde are depicted in Figure 4.15. The absolute value of the difference between the exit concentration values of formaldehyde using the finest mesh $h = 7$ and those using the coarser meshes, $h < 7$, was monitored until stability was achieved and/or the computer ran out of random access memory. There were 668592 mesh elements and 1717036 degrees of freedom.

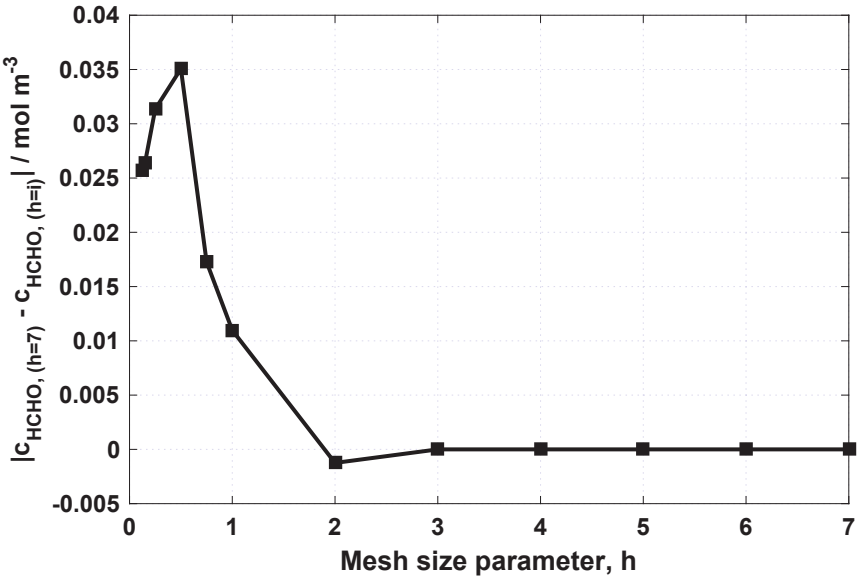

FIGURE 4.15: Mesh refinement study for the exit concentration of formaldehyde

This chapter has provided the needed confidence in both the numerical models developed and the software suite used for generating the solutions. Subsequent chapters will concentrate on modelling the Fischer Tropsch synthesis in fixed bed reactors with the moderating effect of phase change materials under different conditions.

Chapter 5

Homogeneously Distributed Phase Change Material in a Fixed Bed Fischer-Tropsch Reactor

"If you can't stand the heat, get out of the kitchen."

Harry S. Truman, (1884-1972).

The effect of an excessively high temperature in the fixed bed reactor on the Fischer Tropsch synthesis, stemming from poor reaction heat removal, is detrimental to the process. This chapter considers the numerical simulation of the dilution of the catalyst bed using homogeneously dispersed encapsulated phase change material as the diluent in an industrial scale reactor. In general, comparisons will be made between the "control" Fischer-Tropsch reaction, where no phase change material is used (this will serve as the base case), and a phase change material modulated Fischer-Tropsch reaction under various process conditions. Specifically, reactor temperature control, reactant conversion, selectivity to, and productivity of representative desired (C_{5+}) and representative undesired products (CH_4) will be monitored and discussed. In section 5.1, the geometry and mathematical formulation of the problem is presented. Section 5.2 outlines the governing equations, initial and boundary conditions of the initial boundary value problem (IBVP). The validation and the mesh dependency studies conform to the previously discussed test cases set out in chapter 4. The concluding sections of the chapter will set out the results of the numerical simulations.

5.1 Temperature control with phase change material

Figure 5.1a is a schematic diagram of a base case Fischer-Tropsch packed bed reactor filled with stationary spherical catalyst pellets. Figure 5.1b shows the coolant fluid, saturated liquid water, flowing outside the tube. For the purpose of this simulation,

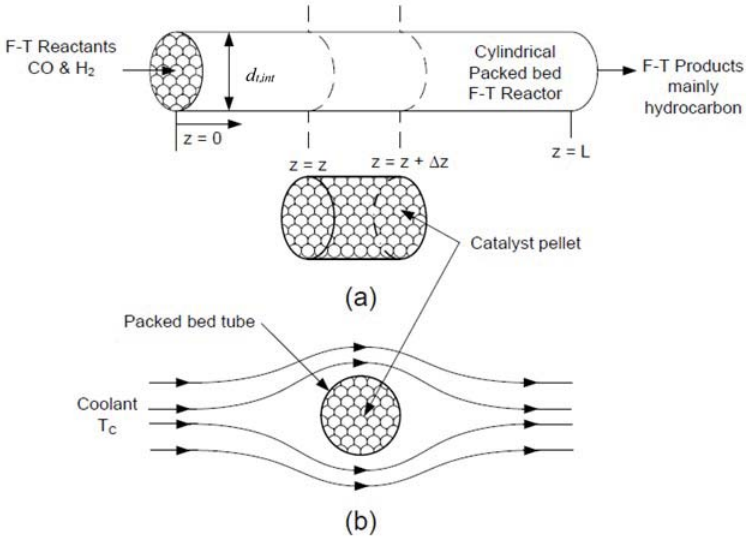

FIGURE 5.1: Schematic packed bed reactor: (a) axisymmetric cylindrical packed bed reactor (b) external coolant flow configuration [182].

the reactor may be imagined to contain a stationary packing of iron catalyst pellets with spherical silica encapsulated metallic tin as phase change material homogeneously dispersed between the catalyst pellets. The phase change material serves as a temperature buffer, preventing any excessive temperature rise within the reactor. The reactant synthesis gas flows over the packing and the hydrocarbon products are collected at the other end of the reactor. Modelling the Fischer-Tropsch chemistry is inherently complex owing to the hundreds of products resulting from just two simple molecules. This difficulty is further heightened by the transport phenomena implications on the reaction chemistry by reason of carrying the reaction out in a fixed bed reactor. Furthermore, in this case, accounting for the effect of the phase change material adds to the complexity. It is therefore necessary to make a number of simplifying assumptions and build on the work presented in the foregoing chapters. The relevant assumptions are as listed:

i Each of the tubes in the reactor is statistically, uniformly packed; there are neither inter-tube interactions nor rotational effects, therefore, a single axisymmetric tube will suffice in modelling the entire reactor

ii The reactor is assumed to be hydrodynamically isotropic, such that channelling does not occur.

iii In order to account for the dynamic nature, i.e. transitioning of the phase change material, the process is cast and solved as a transient numerical model. The simulation time has however been chosen to be long enough in order for the process to attain quasi-steady state.

iv Solid, heavier hydrocarbons have not been accounted for, i.e. all the effluents from the reactor are assumed to either be in liquid or gaseous state.

v The preponderance of products from the reactor are straight chain aliphatic hydrocarbons. Alicyclics, aromatics (e.g. benzene) and oxygenates (e.g. alcohols) are assumed to be formed in negligible quantities.

vi The influence of pore diffusion has been imposed on the lumped, intrinsic, Langmuir-Hinshelwood-Hougen-Watson (LHHW) kinetics equation [89, 93, 94] with an effectiveness factor η_{pore}.

vii Based on the experimental measurements of Kuntze [93] and Raak [94], the influence of external diffusion limitations for Fischer-Tropsch operations under 400°C is negligible and has been neglected (The operational temperature throughout this thesis will lie in this regime).

viii The ideal gas law will serve as the equation of state for the gaseous elements of the process. This is based on the comparison of the results obtained in this work, using the ideal gas law, to previous studies [183] carried out using the Peng-Robinson cubic equation of state, showing no more than 3% deviation.

ix The previously outlined assumptions regarding the phase change material as outlined in subsection 3.3.2 of chapter 3 will be maintained and upheld.

x As was arrived at in chapter 3, an extended quasi-homogeneous multiphase continuum model (comprising the fluid, catalyst and encapsulated phase change material) will be used to represent the physical process.

The next subsection will outline the governing equations. The numerical implementation of the subsequent equations and mesh dependency/convergence tests conform to the methods outlined in chapetrs 3 and 4 and will not be repeated here.

5.1.1 Transport phenonmena governing equations

The governing differential and algebraic constitutive equations used to model the Fischer Tropsch fixed bed reactor with homogeneously dispersed phase change material are outlined in this section. The salient fluid thermodynamic and physical properties such

as density, viscosity, thermal conductivity, specific heat capacity, etc. are allowed to vary with the local temperature. These properties are calculated for the reaction mixture using the individual pure substances properties and local composition. Appendix A outlines a selection of these properties and correlations used in obtaining them.

The fluid velocity is calculated from the continuity equation which is given by:

$$\frac{\partial \rho_{\mathrm{f}}}{\partial t} + \nabla \cdot (\rho_{\mathrm{f}}\, \vec{u_{\mathrm{z}}}) = 0 \tag{5.1}$$

where ρ_{f} is the pseudo-continuum fluid density and $\vec{u}_{\mathrm{z}}$ is the velocity vector of the pseudo-fluid. The momentum balance is approximated using the classical Ergun equation [162], the form of the Ergun equation used in equation 5.2 was one which was valid for spheres over a wide range of particle Reynolds numbers (Re_{p}) as reported by Froment et al [114].

$$-\frac{\partial p}{\partial z} = \frac{1-\epsilon}{\epsilon^3}\left(1.75 + 4.2\, Re_{\mathrm{p}}^{\frac{5}{6}}\, \frac{1-\epsilon}{Re_{\mathrm{p}}}\right)\frac{\rho_{\mathrm{f}}\, u_{\mathrm{z}}^2}{d_{\mathrm{p}}} \tag{5.2}$$

The ideal gas law is expressed as follows:

$$\rho_{\mathrm{f}} = \frac{p\, MW_{\mathrm{av}}}{R_{\mathrm{g}}\, T} \tag{5.3}$$

Applying the chain and quotient rules gives a more useful differential form of the equation, showing how the fluid density varies with reactor axial length:

$$\frac{\partial \rho_{\mathrm{f}}}{\partial z} = \frac{MW_{\mathrm{av}}}{R_{\mathrm{g}}}\left(\frac{1}{T}\frac{\partial p}{\partial z} - \frac{p}{T^2}\frac{\partial T}{\partial z}\right) \tag{5.4}$$

The material balance for the individual species j is as follows:

$$-\frac{\partial c_j}{\partial t} + \epsilon D_{\mathrm{r}}\left(\frac{\partial^2 c_j}{\partial r^2} + \frac{1}{r}\frac{\partial c_j}{\partial r}\right) - \frac{\partial (u_s\, c_j)}{\partial z} - \sum_{i=1}^{N} \nu_{i,j}\, \Re_{i,j}(c,T) = 0 \tag{5.5}$$

The enthalpy balance with the buffering effect of the phase change material incorporated is as follows:

$$-\rho_{\mathrm{f}} C_{\mathrm{p}} \frac{\partial T}{\partial t} + \kappa_{\mathrm{r}}\left(\frac{\partial^2 T}{\partial r^2} + \frac{1}{r}\frac{\partial T}{\partial r}\right) - \rho_{\mathrm{f}} u_{\mathrm{s}} C_{\mathrm{p}} \frac{\partial T}{\partial z} + \sum_{i=1}^{N} \nu_{i,j}\, \Re_{i,j}(c,T)\,(-\Delta H_{\mathrm{r}} + \Delta H_{\mathrm{pcm}}) = 0 \tag{5.6}$$

TABLE 5.1: Properties of phase change material

Parameters	**Value**	**Units**
Phase change material	Sn	-
Fusion temperature, T_{m}	231.9	$^{\mathrm{o}}$C
Latent enthalpy of fusion, ΔH_{fus}	60500	J kg^{-1}
Density of solid phase	7184	kg m^{-3}
Density of liquid phase	6990	kg m^{-3}
Heat capacity of solid phase	214	J kg^{-1}K^{-1}
Heat capacity of liquid phase	212	J kg^{-1}K^{-1}
Thermal conductivity of solid phase	67	W m^{-1}K^{-1}
Thermal conductivity of liquid phase	32.6	W m^{-1}K^{-1}
Differential temperature melting range, ΔT	2.5	$^{\mathrm{o}}$C
Thermal conductivity of SiO_2	1.3	W m^{-1}K^{-1}
Heat capacity of SiO_2	700	J kg^{-1}K^{-1}

whence,

$$\Delta H_{\mathrm{pcm}} = \begin{cases} (m_{\mathrm{SiO_2}}\, C_{\mathrm{p,\,SiO_2}} + m_{\mathrm{pcm}}\, C_{\mathrm{p,\,pcm,\,s}}) \times (T - T_0) & : T < T_{\mathrm{m}}, \\ (m_{\mathrm{SiO_2}}\, C_{\mathrm{p,\,SiO_2}} + m_{\mathrm{pcm}}\, C_{\mathrm{p,\,pcm,\,s}}) \times (T - T_0) + \psi\, m_{\mathrm{pcm}}\, \Delta H_{\mathrm{fus}} & : T_{\mathrm{m}} \leq T \leq (T_{\mathrm{m}} + \Delta T) \\ (m_{\mathrm{SiO_2}}\, C_{\mathrm{p,\,SiO_2}} + m_{\mathrm{pcm}}\, C_{\mathrm{p,\,pcm,\,l}}) \times (T - T_0) + m_{\mathrm{pcm}}\, \Delta H_{\mathrm{fus}} & : T > T_{\mathrm{m}}. \end{cases} \tag{5.7}$$

and the liquid melt fraction, ψ is given by:

$$\psi = \begin{cases} 0 & : T < T_{\mathrm{m}}, \\ \dfrac{\Delta H_{\mathrm{pcm}} - C_{\mathrm{p,pcm,s}}(T_{\mathrm{m}} - T_0)}{\Delta H_{\mathrm{fus}}} & : T_{\mathrm{m}} = T, \\ 1 & : T > T_{\mathrm{m}}. \end{cases} \tag{5.8}$$

Table 5.1 lists the relevant physical and thermal properties of the phase change material used in this work.

The initial and boundary conditions for the material and enthalpy balances are as follows: At time $t = 0$:

$$\left.\begin{aligned} c_j &= c_{j0} \\ T &= T_0 \\ p &= p_0 \\ u_{\mathrm{z}} &= u_{\mathrm{s}} \\ \rho_{\mathrm{f}} &= \rho_{\mathrm{f}\,0} \end{aligned}\right\} \quad \forall \text{ values of } z \text{ and } r \tag{5.9}$$

At time $t > 0$:

$$\left.\begin{aligned} c_j &= c_{j1} \\ T &= T_1 \end{aligned}\right\} \qquad \text{at } z = 0 \text{ and } 0 \leq r \leq \frac{d_{\mathrm{t,int}}}{2} \tag{5.10}$$

$$\frac{\partial c_j}{\partial r} = 0 \qquad \text{at } r = 0 \text{ and } r = \frac{d_{\mathrm{t,int}}}{2}, \quad \forall\, z \tag{5.11}$$

$$\frac{\partial T}{\partial r} = 0 \qquad \text{at } r = 0, \quad \forall\, z \tag{5.12}$$

$$\frac{\partial T}{\partial r} = -\frac{h_{\mathrm{w}}}{\kappa_r}(T_{\mathrm{react}} - T_{\mathrm{w}}) \qquad \text{at } r = \frac{d_{\mathrm{t,int}}}{2}, \quad \forall\, z \tag{5.13}$$

5.1.2 Chemical kinetics and reaction on commercial iron catalyst

Industrial scale, heterogeneous, fixed bed reactors operate in the region of influence of mass and heat transport limitations. It is therefore necessary to modify intrinsic reaction rate equations obtained in the laboratory to account for transport resistances in order to accurately model the reaction process. Kuntze [93] and Raak [94] in their research measured the intrinsic rate of consumption of hydrogen gas on a typical iron catalyst (ARGE cat.), using a bench scale fixed bed reactor with small particles (< 0.2mm diameter), and fitted their reaction rate expression to a Langmuir-Hinshelwood-Hougen-Watson (LHHW) type equation (see equation 5.14), which considers the inhibiting effect of water vapour on the Fischer Tropsch reaction rate per unit mass of catalyst:

$$\Re^{\mathrm{m}}_{\mathrm{FT}} = k_{\mathrm{H_2,\,HW}} \frac{c_{\mathrm{H_2,g}}}{\left(1 + K_{\mathrm{HW}} \dfrac{c_{\mathrm{H_2O,\,g}}}{c_{\mathrm{CO,\,g}}}\right)} \tag{5.14}$$

The intrinsic reaction rate constant, $k_{\mathrm{H_2,\,HW}}$ and the LHHW coefficient, K_{HW} are given by equations 5.15 and 5.16:

$$k_{\mathrm{H_2,\,HW}} = 1.2 \times 10^7 \exp\left(\frac{-109000}{R_{\mathrm{g}} T}\right) \left[\frac{\mathrm{m}^3}{\mathrm{kg\,s}}\right] \tag{5.15}$$

$$K_{\mathrm{HW}} = 0.2 \exp\left(\frac{8800}{R_{\mathrm{g}} T}\right) \tag{5.16}$$

For an industrial scale reactor (particle diameter, $d_{\mathrm{p}} > 1$mm), however, the effect of catalyst pore diffusion must be considered, as such, the intrinsic reaction rate, (equation 5.14) needs to be modified using an effectiveness factor, η_{pore} as shown below:

$$\Re^{\mathrm{m}}_{\mathrm{FT,\,eff}} = \eta_{\mathrm{pore}} \left(\frac{k_{\mathrm{H_2,\,HW}}}{1 + K_{\mathrm{HW}} \dfrac{c_{\mathrm{H_2O,g}}}{c_{\mathrm{CO,g}}}}\right) c_{\mathrm{H_2,g}} = \eta_{\mathrm{pore}}\, k_{\mathrm{H_2}}\, c_{\mathrm{H_2,\,g}} \tag{5.17}$$

The quantity in parenthesis may be defined as some quasi-first order reaction rate constant, $k_{\mathrm{m,\,H_2}}$. The pore diffusion effectiveness factor is given by the expression:

$$\eta_{\mathrm{pore}} = \frac{\Re^{\mathrm{m}}_{\mathrm{FT,\,eff}}}{k_{\mathrm{m,\,H_2}}\, c_{\mathrm{H_2,g}}} = \frac{\tanh\phi}{\phi} \approx \frac{1}{\phi} \quad (\text{for } \phi \geq 2) \tag{5.18}$$

where, the Thiele modulus ϕ for the Fischer Tropsch synthesis is given by:

$$\phi = \frac{V_{\mathrm{p}}}{A_{\mathrm{p,\,ext}}} \sqrt{\frac{k_{\mathrm{m,\,H_2}}\, \rho_{\mathrm{p}}\, c_{\mathrm{H_2,g}}}{D_{\mathrm{eff,\,H_2,l}}\, c_{\mathrm{H_2,l}}}} \tag{5.19}$$

The Thiele modulus which is akin to the 2nd Damköhler number (Da_{II}) in expression, accounts for the species transport from the surface of the catalyst pellet to the inside of the catalyst pellet. The ratio $V_{\mathrm{p}}/A_{\mathrm{p,ex}}$ is the ratio of the volume of the catalyst pellet to its external surface area, and $c_{\mathrm{H_2,l}}$ is the concentration of dissolved hydrogen gas in the liquid wax. The quantity $c_{\mathrm{H_2,l}}$ was computed using Henry's law, with a Henry's coefficient ($\mathcal{H}_{\mathrm{H_2,c}} \approx 20,000 \mathrm{Pa\,m^3\,mol^{-1}}$)[5]:

$$c_{\mathrm{H_2,l}} = \frac{p_{\mathrm{H_2,g}}}{\mathcal{H}_{\mathrm{H_2,c}}}\, c_{\mathrm{H_2,g}} \tag{5.20}$$

Combining equations (5.19) and (5.20), the expression for the Thiele modulus becomes:

$$\phi = \frac{V_{\mathrm{p}}}{A_{\mathrm{p,ex}}} \sqrt{\frac{k_{\mathrm{m,H_2}}\, \rho_{\mathrm{p}}}{D_{\mathrm{eff,H_2,l}} \dfrac{R_{\mathrm{g}} T}{\mathcal{H}_{\mathrm{H_2,c}}}}} \tag{5.21}$$

where $D_{\mathrm{eff,H_2,l}}$ is the effective diffusion coefficient of hydrogen in the liquid filled porous catalyst. This takes into account that only a fraction of the pellet is permeable to fluids (through the particle porosity, ϵ_{p}) and that the path of travel through the pellet is random and tortuous (through the particle tortuosity, τ_{p}). The ratio $\dfrac{\epsilon_{\mathrm{p}}}{\tau_{\mathrm{p}}} = 0.3$ [93, 94]. The effective diffusion coefficient is calculated using the molecular diffusivity of H_2 as follows:

$$D_{\mathrm{eff,H_2,l}} = \frac{\epsilon_{\mathrm{p}}}{\tau_{\mathrm{p}}} D_{\mathrm{mol,H_2,l}} \approx 0.3 D_{\mathrm{mol,H_2,l}} \tag{5.22}$$

The molecular diffusivity, $D_{\mathrm{mol,H_2,l}}$ is calculated using the Wilke-Chang equation [184]

$$D_{\mathrm{mol}} = 1.173 \times 10^{-16} \left(\Psi_{\mathrm{a}}\, MW_{\mathrm{wax}}\right)^{\frac{1}{2}} \frac{T}{\mu_{\mathrm{wax}}\, V_{\mathrm{H_2}}^{0.6}} \left[\frac{\mathrm{m^2}}{\mathrm{s}}\right] \tag{5.23}$$

whence, Ψa is an association parameter of the solvent wax, which has a value of 1.0 for unassociated solvents (such as the FT wax in this case) [185], MWwax is the molecular weight of the solvent Fischer-Tropsch wax (The Fischer-Tropsch wax in this work, has

been assumed to be octacosane with chemical formula $C_{28}H_{58}$), T is the absolute temperature, μ_{wax} is the viscosity of the Fischer-Tropsch wax and V_{H_2} is the molar volume of hydrogen at the normal boiling point, obtained from Le Bas [186].

An accurate modelling of the Fischer-Tropsch reaction in a fixed bed reactor may be achieved using three principal reactions namely, the main Fischer-Tropsch reaction, the methanation reaction and the water gas shift reaction [5].

$$\text{CO} + 2\,\text{H}_2 \longrightarrow (-\text{CH}_2-) + \text{H}_2\text{O} \qquad \Delta H^{\theta}_{298} = -152\,\text{kJ mol}^{-1} \tag{5.24}$$

$$\text{CO} + 3\,\text{H}_2 \longrightarrow \text{CH}_4 + \text{H}_2\text{O} \qquad \Delta H^{\theta}_{298} = -206\,\text{kJ mol}^{-1} \tag{5.25}$$

$$\text{CO} + \text{H}_2\text{O} \longrightarrow \text{CO}_2 + \text{H}_2 \qquad \Delta H^{\theta}_{298} = -41\,\text{kJ mol}^{-1} \tag{5.26}$$

The intrinsic rates of these three reactions (equations 5.24 - 5.25) were experimentally determined by Popp [92]. The aforementioned transport limitations have been imposed on the intrinsic reaction rates so that the equations (5.27 - 5.29) represent the effective reaction rates ($\text{mol}\,\text{m}^{-3}\,\text{s}^{-1}$), valid for a fully developed catalyst pore diffusion effect $\left(T > 220^{\text{o}}\text{C},\ \dfrac{V_{\text{p}}}{A_{\text{p,ex}}} = 5 \times 10^{-3}\text{m}\right)$ [54, 89]. The water gas shift reaction rate expression, (equation 5.29), was taken from Lox et al [54].

$$\Re_{\text{FT}} = \rho_{\text{b}} \frac{5.1 \exp\left(\dfrac{-52000}{R_{\text{g}}T}\right)}{\left(1 + 1.6\dfrac{c_{\text{H}_2\text{O}_{\text{g}}}}{c_{\text{CO}_{\text{g}}}}\right)} c_{\text{H}_{2,\text{g}}} \tag{5.27}$$

$$\Re_{\text{M}} = 27.3\,\rho_{\text{b}} \exp\left(\frac{-70000}{R_{\text{g}}T}\right) c_{\text{H}_{2,\text{g}}} \tag{5.28}$$

$$\Re_{\text{WGS}} = \rho_{\text{b}} \times \frac{10^3 \times k_{\text{v}} (R_{\text{g}}T)^{\frac{3}{2}} \left(\dfrac{c_{\text{CO}}\, c_{\text{H}_2\text{O}}}{c_{\text{H}_2}^{\frac{1}{2}}} - \dfrac{1}{K_{\text{ewg}}}\, c_{\text{CO}_2}\, c_{\text{H}_2}^{\frac{1}{2}}\right)}{\left(1 + K_{\text{v}} (R_{\text{g}}T)^{\frac{1}{2}} \dfrac{c_{\text{H}_2\text{O}}}{c_{\text{H}_2}^{\frac{1}{2}}}\right)^2} \tag{5.29}$$

The water gas shift equilibrium constant, K_{ewg} is given by the expression of Lox et al[54]:

$$\exp\left(\frac{5078.0045}{T} - 5.8972089 + 13.958689 \times 10^{-4}T - 27.592844 \times 10^{-8}T^2\right) \tag{5.30}$$

Finally, the consumption or production rate laws based on the reaction stoichiometry (equations 5.24 - 5.26), are as follows:

$$\Re_{H_2} = -\Re_{FT} - 3\Re_M + \Re_{WGS} \tag{5.31}$$

$$\Re_{CO} = -\Re_{FT} - \Re_M - \Re_{WGS} \tag{5.32}$$

$$\Re_{CH_4} = \Re_M \tag{5.33}$$

$$\Re_{C_{cn}H_{2cn+2}} = x_{(cn>2)} \times N_{tot} \times V_{react} \times \frac{1}{(1+\gamma_{FT})} \tag{5.34}$$

$$\Re_{C_{cn}H_{2cn}} = x_{(cn>2)} \times N_{tot} \times V_{react} \times \frac{\gamma_{FT}}{(1+\gamma_{FT})} \tag{5.35}$$

$$\Re_{H_2O} = \Re_{FT} + \Re_M - \Re_{WGS} \tag{5.36}$$

$$\Re_{CO_2} = \Re_{WGS} \tag{5.37}$$

where, cn is the number of carbon atoms in the hydrocarbon in question, α_{FT} is the constant carbon chain growth probability factor and γ_{FT} is the olefin to paraffin ratio,

The total number of moles of hydrocarbon (N_{tot}) produced per unit time as reported by Panahi et al [168] is given by:

$$N_{tot} = \frac{\left(\frac{-\Re_{FT} - \Re_M - \Re_{WGS}}{MW_{CO}} + \frac{\Re_{WGS}}{MW_{CO_2}}\right) V_{react}}{\frac{x_{(cn=1)}}{MW_{CH_4}} + \sum_{cn=2}^{cn} cn \times x_{cn} \times \left(\frac{1}{(1+\gamma_{FT})} . \frac{1}{MW_{C_{cn}H_{2cn+2}}} + \frac{\gamma_{FT}}{(1+\gamma_{FT})} . \frac{1}{MW_{C_{cn}H_{2cn}}}\right)} \tag{5.38}$$

5.2 Product distribution with increasing molecular weight

Figure 5.2 shows the distribution of a selection of straight chain aliphatic alkane/paraffin products in the reactor. As may be observed, the reaction products are minimal at the reactor inlet (top of the reactor) and increase as the reactants travel further down the reactor. It is also worthy of note that as the molecular weight of the product hydrocarbon increases, the preponderance of the product seems to be synthesised close to walls of the reactor as opposed to the reactor core. This behaviour is particularly pronounced in the case of heavier hydrocarbons such as, C_{5+} in Figure 5.2.

The core of the reactor is the hottest part of the reactor, while the walls, which are kept at near isothermal conditions by saturated water, are the coolest part of the reactor. From the Clausius-Clayperon equation, (see equation 5.39), which relates the vapour pressure (p_{vap}) of a substance to its molecular weight (MW) and enthalpy of vaporisation

(ΔH_{vap}), it can be deduced that a concomitant of increasing the molecular weight of a substance is a reduction in its vapour pressure. In the reactor, the gaseous hydrocarbon molecules which have vapour pressures far above the prevalent total

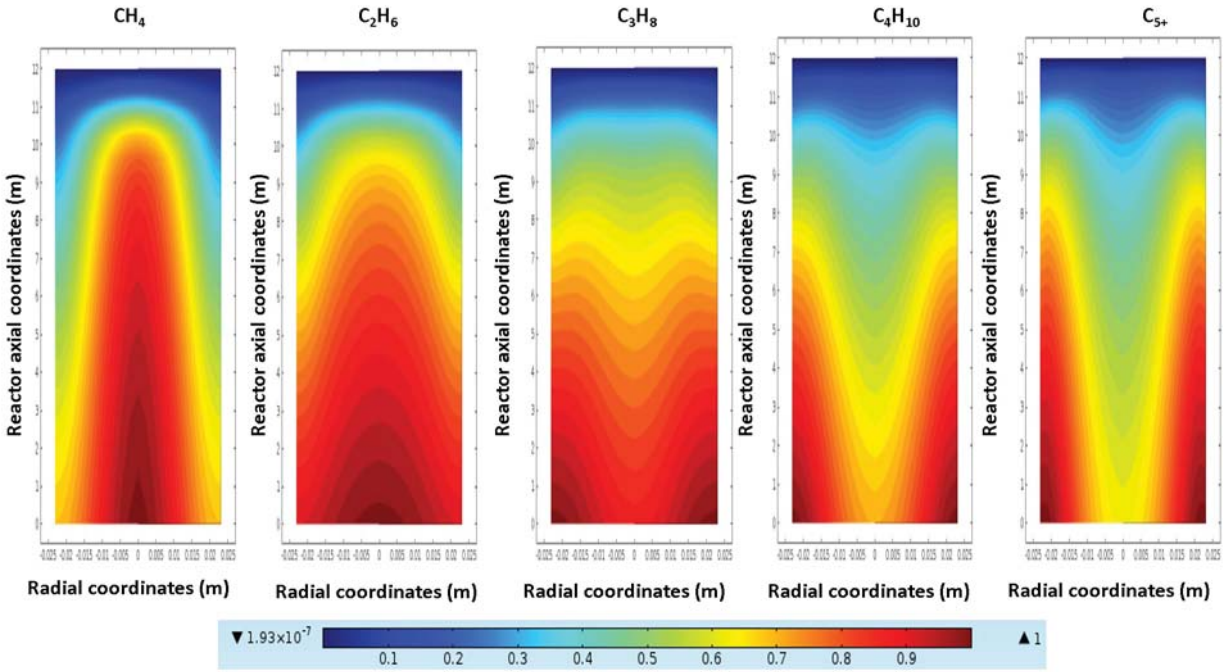

FIGURE 5.2: Hydrocarbon mole fraction in fixed bed Fischer-Tropsch reactor; molecular weight increases by 0.014kg mol^{-1} successively from (CH_4) through to (C_{5+}): As molecular weight increases, there is more of the synthesised hydrocarbon present at the reactor walls than at the axis.

$$\frac{\partial \log_e(p_{\text{vap}})}{\partial T} = \frac{MW \Delta H_{\text{vap}}}{R_{\text{g}} T^2} \tag{5.39}$$

pressure in the reactor, persist in the reactor as gases, e.g. methane. The heavier hydrocarbons (C_{5+}) which, tend to be liquids at normal temperature and pressure, with high molecular weights, have lower vapour pressures, and in addition, the weak intermolecular forces of alkanes also means they are readily vaporised. The existing chemical species gradients, which are perpendicular to the direction of reactant flow in the reactor and are aggravated by the external radial cooling of the reactor, have the effect of transporting away from the catalyst surface, the products that are formed on, and desorbed from the catalyst active sites, towards the reactor walls. At the walls, the heavier vaporised hydrocarbon molecules are condensed, while the lighter hydrocarbons are displaced towards the centre of the reactor. This explains concentration of the heavier hydrocarbons at the walls and their lighter counterparts at the core of the reactor as seen in Figure 5.2.

The subsequent sections in this chapter look at the effect of changes in process conditions or design parameters on the performance of the reactor in terms of the reactant conversion, the productivity of desired and undesired products and thermal controllability. The mitigating effect of the homogeneously distributed phase change material in the catalyst bed will also be presented and discussed.

5.3 Effect of varying the catalyst mass fraction.

5.3.1 Effect on reactant conversion and representative hydrocarbon productivity

This section looks at the effect of diluting the catalyst bed with different mass fractions of encapsulated phase change material on the reactor temperature profile and other key performance indices of the reactor including: reactant conversion, representative hydrocarbon productivity, etc. Figure 5.3a-d depicts the conversion of CO and H_2 and the productivities of C_5+ and CH_4 as functions of the reactor axial length respectively after 7200s of reaction time. The coefficient, σ represents the fraction by mass of catalyst pellets present in the reactor, while the balance, $(1-\sigma)$ represents the fraction by mass of encapsulated phase change material present in the reactor as diluent. As such, an increase in the value of $(1-\sigma)$ corresponds to a pronounced buffering effect of the phase change material on the maximum temperature attained within the reactor.

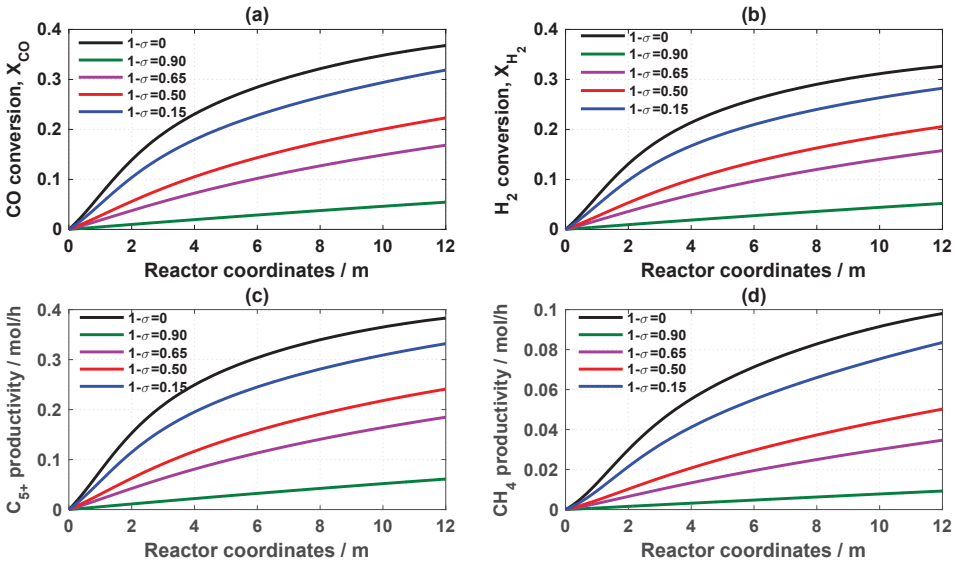

FIGURE 5.3: Reactant conversion and representative hydrocarbon productivity profiles for Fischer-Tropsch synthesis for varying concentrations by mass of phase change material at: $t = 7200$s, $T_{\text{in,cool}} = 230^{\circ}$C and $R_{\text{t}} = 0.023$m

TABLE 5.2: Carbon based selectivity of hydrocarbon products with varying concentrations by mass of phase change material diluent

$1-\sigma$	$\mathbf{S}_{C_{5+}}$ (%)	$\mathbf{S}_{CH_4}$ (%)
0	83	6.9
0.15	83.5	6.8
0.5	86.3	5.82
0.65	87.6	5.29
0.9	89.8	4.4

Expectedly, the extent of conversion of CO and H_2, as seen in Figure 5.3a-b, reduces with increasing the fraction of phase change material; maximum conversion is achieved at $(1-\sigma{=}0)$ and conversion is at a minimum at $(1-\sigma{=}0.9)$. The conversion per pass of H_2 is slightly less than that of CO for each corresponding catalyst activity coefficient, for example, at $T_{\text{in,cool}} = 230^{\circ}\text{C}$, $(1-\sigma{=}0)$, $X_{H_2} \approx 32\%$ while $X_{CO} \approx 38\%$- this is due to the water gas shift reaction which consumes additional CO to produce water and CO_2. This behaviour persists irrespective of the fraction of phase change material present in the bed.

Figure 5.3c-d shows the productivity of C_{5+} and CH_4 respectively, with and without catalyst dilution. As in the case of the reactant conversion, the productivity of both representative desired and undesired products reduce with an increase in the fraction of phase change material present in the reactor. On average, for the same reaction conditions, for every unit molar reduction in C_{5+} productivity, there is a corresponding 1.5 moles reduction in the productivity of methane. This shows that the phase change material, by restricting rapid temperature rise in the reactor impedes the production of methane more than it does the heavier hydrocarbon molecules. Furthermore, an interesting pattern emerges with regards to the selectivity of both products as the concentration by mass of the phase change material in the catalyst bed increases. Table 5.2 shows the carbon-based selectivity for both of the representative products of the reaction, calculated using equation (5.40). The table reveals that as the quantity $(1-\sigma)$ increases, and the temperature rise in the reactor becomes more restricted, the selectivity of the catalyst towards the heavier hydrocarbon molecules increase, while the selectivity towards the lighter hydrocarbons wanes. There is almost a 7% increase in selectivity towards the C_{5+} and a 2.5% reduction in selectivity towards CH_4 over the inequality $0 \leq (1-\sigma) \leq 0.9$.

$$\mathrm{S}_{\mathrm{C_nH_{2n+2}}}(\%) = \frac{\text{moles of } \mathrm{C_nH_{2n+2}} \text{ produced} \times cn}{\text{moles of CO removed}} \times 100 \tag{5.40}$$

As will be shown later in chapter 7, the phase change material and catalyst could be optimally distributed in such a fashion that maximises the productivity of the heavier hydrocarbon molecules while minimising the methane production. The remainder of this chapter will however maintain focus on the general ramifications of catalyst dilution with phase change material under varied process conditions.

5.3.2 Effect on temperature profile in the reactor

Figure 5.4 shows the axial and radial temperature distribution in the reactor after 7200s of reaction time for the base case of $T_{\text{in,cool}} = 230^{\text{o}}\text{C}$, obtained from the 2D quasi-homogeneous model. As may be observed, there is a hotspot generated within the first 2.5m of the axial length of the reactor as is customary with carrying out an exothermic reaction in a wall-cooled packed bed reactor. The maximum axial temperature difference

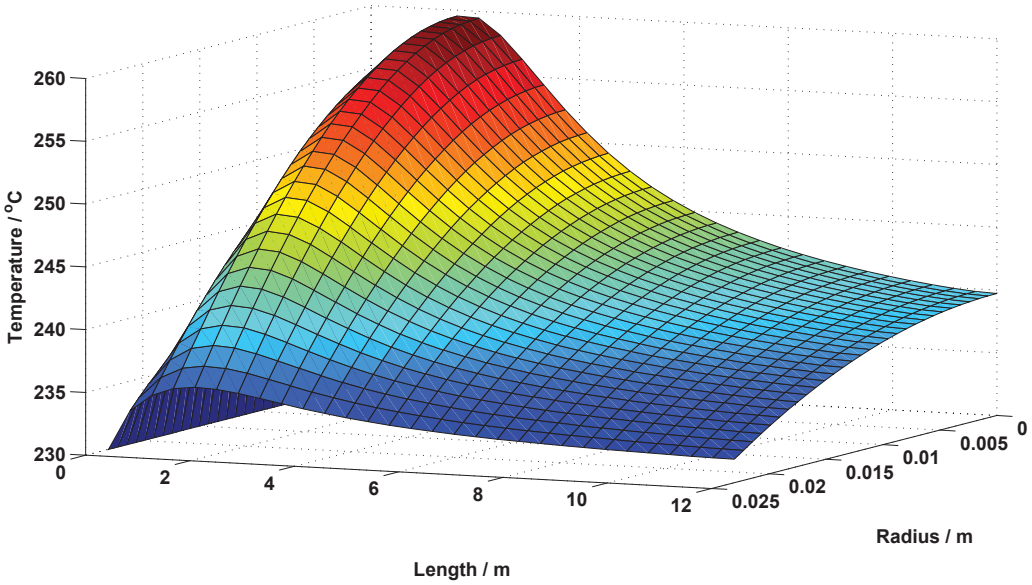

FIGURE 5.4: Axial and radial temperature profiles along the reactor using 2D quasi-homogeneous model for Fischer-Tropsch synthesis at: $t = 7200$s, $T_{\text{in,cool}} = 230^{\text{o}}\text{C}$ and $R_{\text{t}} = 0.023$m

in the reactor is 30°C. The radial wall cooling also produces a temperature gradient in the radial direction and as depicted in Figure 5.4, there is a 10°C temperature difference in the radial direction. Figure 5.5a-d shows the effect of different phase change material concentrations on the axial and radial temperature profiles in the reactor.

The catalyst mass fraction, σ increases from 0.1 to 0.85 in Figure 5.5a to d respectively and by extension, the mass fraction of the phase change material, $(1 - \sigma)$ decreases respectively from 0.9 to 0.15. There is a significant change in the temperature profile in the reactor as the catalyst bed dilution is gradually increased. As an example, at

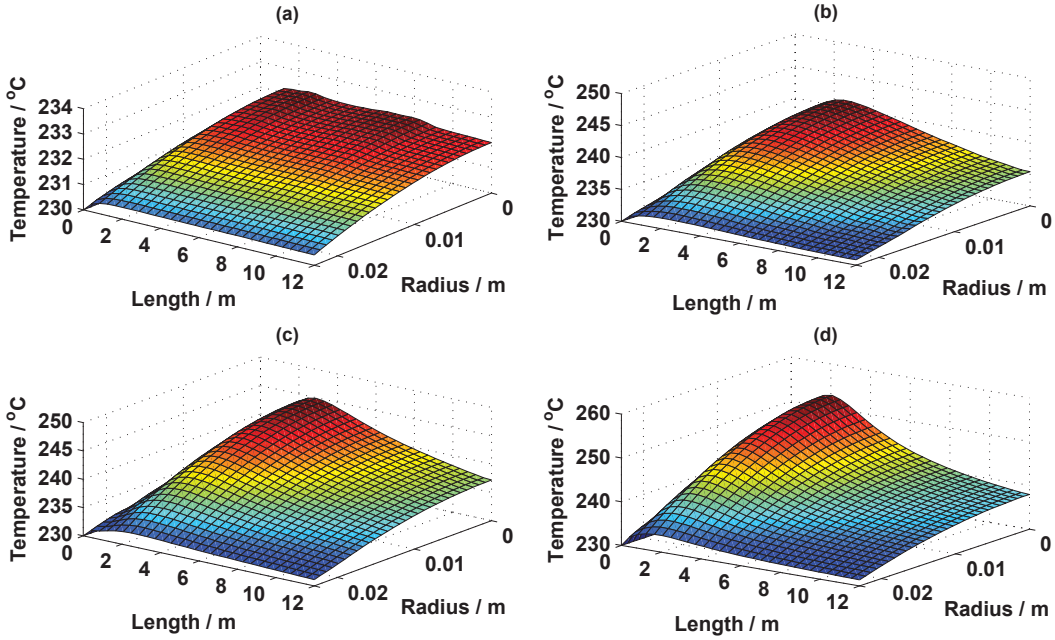

FIGURE 5.5: Axial and radial temperature profiles along the reactor using 2D quasi-homogeneous model for Fischer-Tropsch synthesis for varying concentrations by mass of phase change material at $t = 7200$s, $T_{\text{in,cool}} = 230^{\text{o}}$C and $R_{\text{t}} = 0.023$m: (a) $1 - \sigma = 0.9$ (b) $1 - \sigma = 0.65$ (c) $1 - \sigma = 0.50$ (d) $1 - \sigma = 0.15$

maximum catalyst dilution ($1-\sigma = 0.9$) in Figure 5.5a, the amplitude of the temperature difference on the axial axis has been reduced from 30°C to approximately 1°C and the maximum radial temperature difference has been reduced from 10°C to about 2°C, thus ensuring a near isothermalisation of the reactor. As the diluent concentration by mass falls, in Figure 5.5b-d, the temperature differences in the reactor begin to rise with a corresponding increase in both the conversion of syngas and hydrocarbon productivity. In a practical situation, the requirement of maximising the productivity of the long chain hydrocarbon molecules would serve as the discriminant for the upper limit of the amount of phase change material that should be introduced into the process. The lower limit will depend upon what maximum temperatures can be tolerated by the catalyst and the temperature distribution within the reactor.

5.3.3 Radial profiles of temperature, heat removed and reaction rate at hotspot location

Figure 5.6a-d represents the radial profiles of the reactor sectioned at the location of the hotspot, ($\approx$ 2m from the reactor entrance), for inlet conditions of 230°C and 2.4MPa at different catalyst dilutions. The temperature difference between the reactor core (hottest part of reactor) and circumference (coolest part of reactor) diminishes with an increase in the concentration by mass of the phase change material in the reactor.

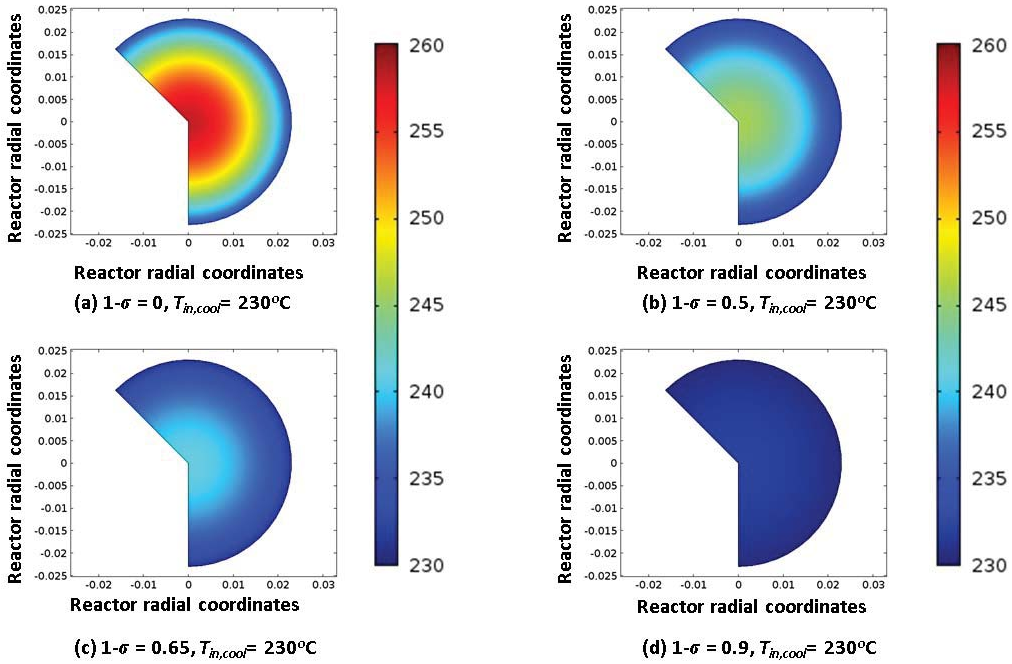

FIGURE 5.6: Plan view of the Fischer-Tropsch reactor at the hotspot location, showing the radial temperature profiles (°C) for varying concentrations by mass of phase change material at: $t = 7200$s, $T_{\text{in,cool}} = 230$°C and $R_{\text{t}} = 0.023$m

Figure 5.7 presents a summary of how the respective ratios of reaction rate at the reactor centre to that at the wall, heat flux at the reactor centre to that at the wall, and temperature at the reactor centre to that at the wall, all at the hotspot location and as a function of the concentration by mass of the phase change material. As the temperature ratio falls due to the buffering effect provided by the phase change material, both the heat flux and reaction rate ratios also fall. For the same fall of 8% in temperature ratio over $0 \leq (1 - \sigma) \leq 1$, the dip in reaction rate is more severe at 28%, compared to a corresponding 9% dip in the heat flux ratio, thus highlighting the exponential and linear temperature dependent nature of the reaction rate and heat flux respectively.

5.4 Effect of varying the inlet or coolant temperature.

5.4.1 Effect on reactant conversion and representative hydrocarbon productivity

Figure 5.8a-d presents the results of varying the inlet/coolant temperature on the reactant conversion and the productivity of selected hydrocarbons both with and without phase change material. Where the phase change material has been taken into account, the base case scenario of catalyst activity, $\sigma = 0.6$ has been considered. Similar to what

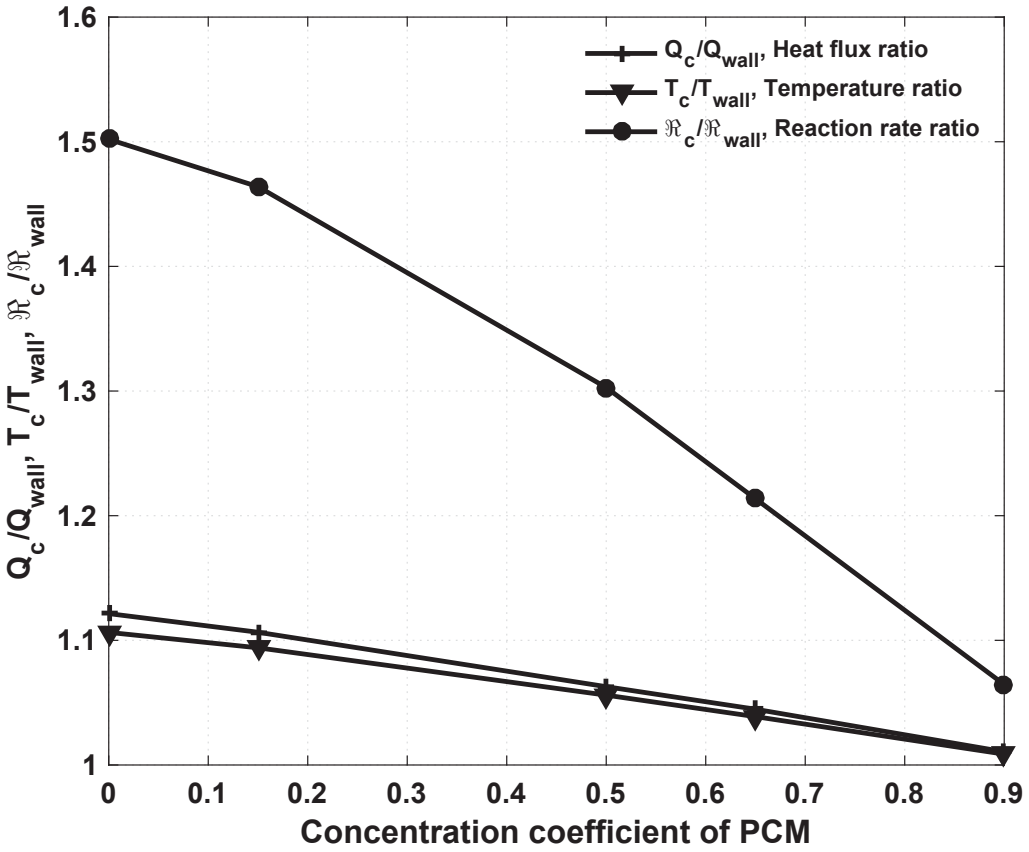

FIGURE 5.7: Ratios of physical quantities $(Q, T, \Re)$ at the reactor core to that at the reactor wall, as a function of varying concentrations by mass of phase change material

was noticed in the previous section, both conversion and productivity were reduced when the effect of the phase change material was included. The conversions of CO, X_{CO} and hydrogen $X_{\mathrm{H_2}}$ at 224°C (Figure 5.8a and b), without phase change material are respectively 32% and 30%, whereas with phase change material, $X_{\mathrm{CO}} = 25\%$ and $X_{\mathrm{H_2}} = 24\%$. On increasing the temperature to 245°C without phase change material, there was increased conversion with $X_{\mathrm{CO}} = 54\%$ and $X_{\mathrm{H_2}} = 41\%$ and on diluting the catalyst bed, the corresponding conversions are: $X_{\mathrm{CO}} = 41\%$ and $X_{\mathrm{H_2}} = 35\%$.

In Figure 5.8c-d, the influence of temperature (and its control) can be seen on the species productivity of the more valuable $\mathrm{C_{5+}}$ and less desirable $\mathrm{CH_4}$. Expectedly, there is a corresponding acceleration of the reaction kinetics with successive step increments in $T_{\mathrm{in,\,cool}}$. As the temperature increases and the reactor becomes more sensitive and more prone to thermal runaway, (at about 245°C), there is a significant rise in the $\mathrm{CH_4}$ production by about 63% compared to a more modest 17% increase in the $\mathrm{C_{5+}}$ for the same step change in temperature from 224°C to 245°C. This observation, i.e. increased production for $\mathrm{CH_4}$ at higher temperatures, is consistent with thermodynamic predictions in literature [13] [187]. This excessive methanation may be put down to

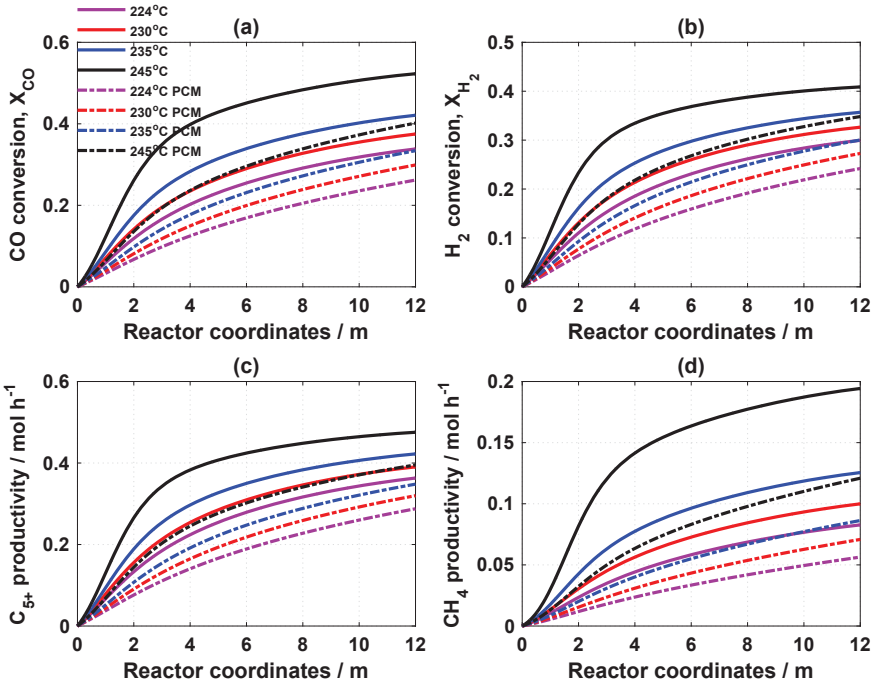

FIGURE 5.8: Reactant conversion and representative hydrocarbon productivity profiles for Fischer-Tropsch synthesis with or without phase change material for varying inlet/coolant temperatures at: $t = 7200$s, $\sigma = 0.6$ and $R_t = 0.023$m

the early desorption of the surface species rather than the continued attachment to the active sites and propagation to higher molecular weight hydrocarbon products [187]. It is equally pertinent to note that this sudden spike in methane production is perhaps the most reliable way of detecting a thermal runaway as it is not practical to place thermocouples in each individual tube of the multi-tubular fixed bed reactor. This is one of the reasons why on-line product analysis is carried out in industry, so as to monitor a "key" product, such as methane in this case. If the concentration of this "key" product exceeds a pre-set limit, the reactor must be shut down and allowed to cool before operation is re-commenced.

As the effect of the phase change material is brought to bear on the process, (Figure 5.8c-d), it can be seen that CH_4 production has been reduced by as much as 34% (at 245°C for example) and the C_{5+} productivity fell by about 15% (at 245°C); in other words, the methane synthesis fell by more than twice as much as did the production of the heavier hydrocarbons. The reason for this observation may be put down to the heat extraction form the reactor augmented by the phase change material, limiting the exponential increase of the reaction rate of the methanation process. The apparent tardy rise of the phase change material influenced C_{5+} productivity curves is brought about because the phase change material delays and controls the temperature ramp rate in the

reactor. The reaction rate is thus slowed down and this is reflected in how quickly the reactants are converted to products (C_{5+}).

5.4.2 Effect on maximum temperature (T_{max}) in the reactor

Figures 5.9a-d and Figures 5.10a-d depict the axial and radial temperature profiles in the reactor after 7200s of reaction time, with and without phase change material respectively. As the inlet/coolant temperature is increased, there is a corresponding increase in the maximum axial temperature (T_{max}) in the reactor. For example, in Figure 5.9a where $T_{in,\,cool} = 224^{o}C$, there is a corresponding $T_{max} \approx 249^{o}C$, and for a step change of $11^{o}C$ in $T_{in,\,cool}$, the corresponding $T_{max} \approx 278^{o}C$ as shown in Figure 5.9c.

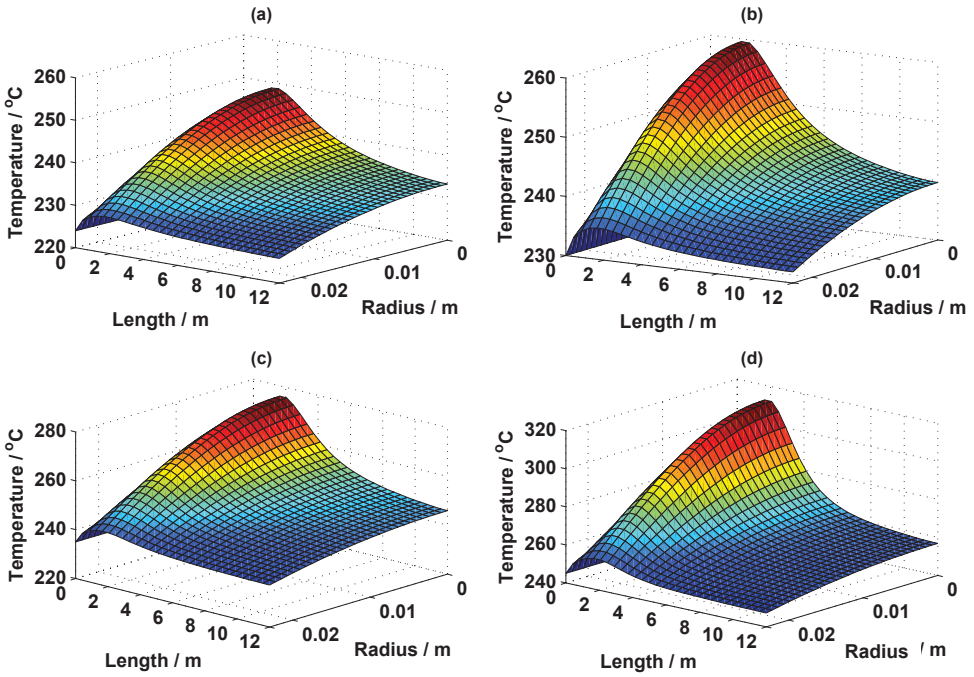

FIGURE 5.9: Axial and radial temperature profiles along the reactor using 2D quasi-homogeneous model for FTS without phase change material diluent, for varying inlet/coolant temperatures at $t = 7200$s, $\sigma = 1.0$ and $R_t = 0.023$m: (a) $T_{in,\,cool} = 224^{o}C$ (b) $T_{in,\,cool} = 230^{o}C$, (c) $T_{in,\,cool} = 235^{o}C$ (d) $T_{in,\,cool} = 245^{o}C$

The observed increase in the productivity of both representative hydrocarbons in Figure 5.8c-d and the exacerbation of the maximum axial temperature in the reactor (Figure 5.9a-d) due to the increase in feed temperature is known as parametric sensitivity. This phenomenon, which is typical of high activation energy, exothermic reactions such as the Fischer Tropsch Synthesis, occurs as a result of the exponential dependency of the rate of reaction on temperature increase (Arrhenius equation) while, the rate of heat removal by the jacket cooling fluid increases linearly (Newton's law of cooling). It follows

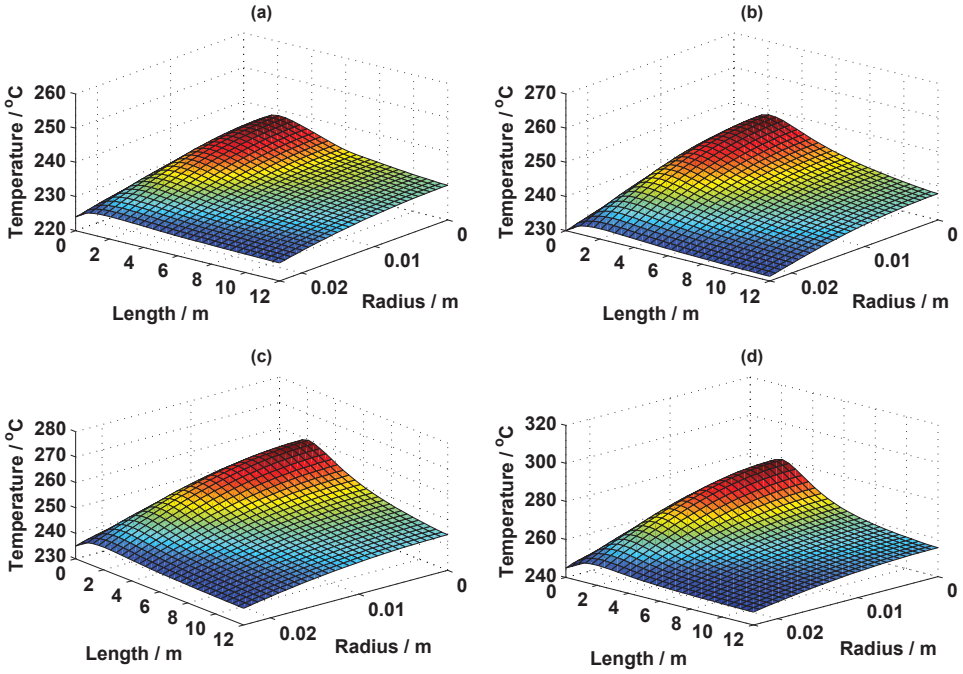

FIGURE 5.10: Axial and radial temperature profiles along the reactor using 2D quasi-homogeneous model for FTS with phase change material diluent, for varying inlet/coolant temperatures at $t = 7200$s, $\sigma = 0.6$ and $R_t = 0.023$m: (a) $T_{in,\,cool} = 224$°C (b) $T_{in,\,cool} = 230$°C, (c) $T_{in,\,cool} = 235$°C (d) $T_{in,\,cool} = 245$°C

therefore, that on the one hand, when an upper temperature threshold is exceeded, the heat released will exceed that removed, the reaction will "ignite" and proceed at a tremendous rate. On the other hand, if a lower temperature limit is reached, the heat removal overtakes evolution and the reaction is extinguished altogether. These two scenarios depict the extremes of multiple stationary states that could be brought about by thermal instabilities.

The effect of the temperature control brought about by the phase change material on the reaction system is evident in Figure 5.10a-d, with much flatter profiles compared to those in Figure 5.9a-d. It is also of interest to note that the phase change material still controls temperature at $T_{in,\,cool}$ values greater than the phase transition temperature of the phase change material (=231.9°C). As an example at $T_{in,\,cool} = 245$°C (Figure 5.10d), $T_{max} \approx 280$°C compared to $T_{max} \approx 315$°C observed for the same inlet/coolant temperature without phase change material modulation in Figure 5.9d. This control is achieved as follows: as the reaction proceeds and heat is generated, the temperature of the evenly dispersed encapsulated phase change material located in the catalyst bed is raised to its fusion temperature, whereupon it begins to melt. The melting process which occurs at near isothermal conditions provides a near isothermal sink into which the enthalpy of reaction may be dissipated temporarily. In other words the phase change

material serves as a buffer which provides thermal inertia in the reaction system and delays any excessive temperature rise in the reactor in a manner proportional to the fractional concentration by mass of the diluent present in the reactor. The temperature control action of the phase change material serves as an auxiliary system under the supervisory cooling mechanism of the jacketed coolant, thus preventing the phase change material from being overwhelmed under a continuous reaction system.

A useful inference to draw from this study is that the less dramatic reduction in the productivity of the C_{5+} compared to the productivity of CH_4 (as noted in subsection 5.4.1 when the influence of the phase change material is considered) is achieved without the comparatively large temperature spikes observed without the use of phase change material. This potentially opens up the possibility of the catalyst activity being promoted to favour selectivity towards the heavier hydrocarbons, e.g. by the addition of oxides of alkali and transition metals [188] [36]. Thus, increasing the conversion per pass with reduced heat transport penalties. The next section of this chapter will look at the results of running simulations using increased catalyst activity with higher selectivity towards the heavier hydrocarbon molecules.

5.5 Effect of using promoted catalyst

5.5.1 Effect on reactant conversion and representative hydrocarbon productivity

Li et al [188] in their experimental work noted that the synthesis of high surface area catalyst precursors based on precipitated Fe–Zn oxides and their promotion with Cu, Ru, and K led to high Fischer–Tropsch synthesis rates and low CH_4 selectivities. They also pointed out that the catalysts can be operated at milder conditions (200°C, 2.0MPa) typically used for the more expensive cobalt based catalysts and that they showed similar heavier hydrocarbon synthesis rates per catalyst mass (or volume) than representative Co-based Fischer Tropsch Synthesis catalysts. The low reaction temperatures made possible by the high Fischer Tropsch Synthesis activity of these Fe-based catalysts also led to lower CO_2 production than on Fe-based catalysts previously reported in literature. This section looks at the effect of promoting the catalyst, thus accelerating the reaction rate by a factor of between 20% and 100% of the original, unpromoted value at $T_{\text{in,cool}} = 230$°C. This catalyst promotion is simulated under conditions of no phase change material modulation and with phase change material modulation. Figure 5.11a-b show the conversion of CO and H_2 at different reaction rates with (broken lines) or without (solid lines) phase change material. The phase change material modulated

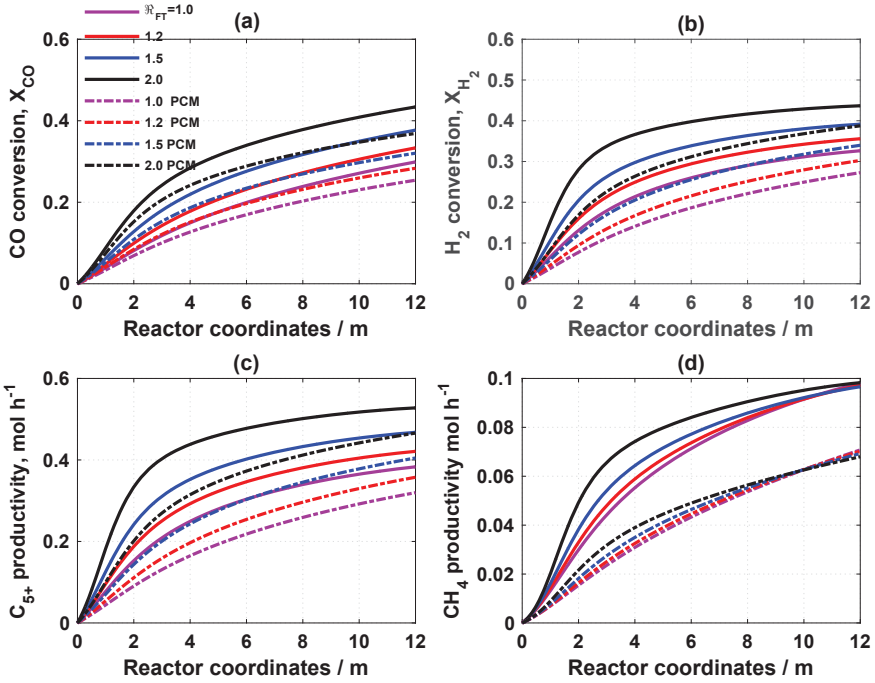

FIGURE 5.11: Reactant conversion and representative hydrocarbon productivity profiles for Fischer-Tropsch synthesis with and without phase change material for varying reaction rates at: $t = 7200$s, $T_{\text{in,cool}} = 230$°C and $R_{\text{t}} = 0.023$m

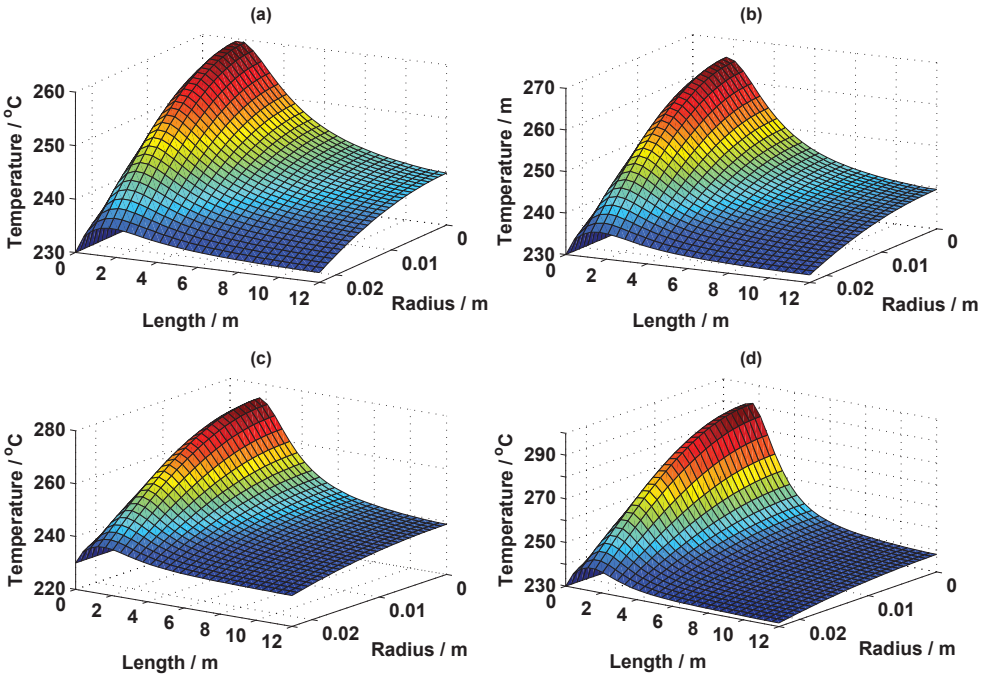

FIGURE 5.12: Axial and radial temperature profiles along the reactor using 2D quasi-homogeneous model for Fischer-Tropsch synthesis without phase change material for varying reaction rates at $t = 7200$s, $T_{\text{in,cool}} = 230$°C, $\sigma = 1.0$ and $R_{\text{t}} = 0.023$m: (a) $\Re_{\text{FT}} = \Re_{\text{FT}}$ (b) $\Re_{\text{FT}} = 1.2\Re_{\text{FT}}$ (c) $\Re_{\text{FT}} = 1.5\Re_{\text{FT}}$ (d) $\Re_{\text{FT}} = 2.0\Re_{\text{FT}}$

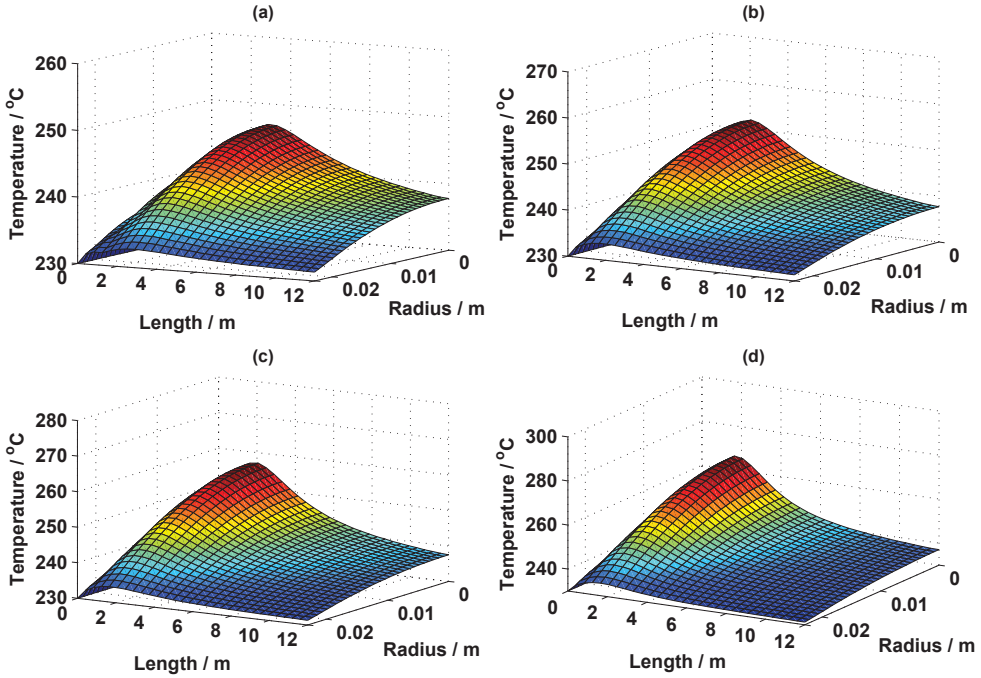

FIGURE 5.13: Axial and radial temperature profiles along the reactor using 2D quasi-homogeneous model for Fischer-Tropsch synthesis with phase change material for varying reaction rates at $t = 7200$s, $T_{\text{in,cool}} = 230^{\circ}$C, $\sigma = 0.6$ and $R_{\text{t}} = 0.023$m: (a) $\Re_{\text{FT}} = \Re_{\text{FT}}$ (b) $\Re_{\text{FT}} = 1.2\Re_{\text{FT}}$ (c) $\Re_{\text{FT}} = 1.5\Re_{\text{FT}}$ (d) $\Re_{\text{FT}} = 2.0\Re_{\text{FT}}$

curves fall behind the non-modulated curves because of the temperature rise restriction imposed by the presence of the phase change material.

When the Fischer Tropsch synthesis reaction rate is increased by a factor of 100% i.e. from $\Re_{\text{FT}} = 1.0$ to $\Re_{\text{FT}} = 2.0$ without considering the phase change material, the conversion per pass values of the respective reactants changed as follows: X_{CO} increased from 33% to 42% and X_{H_2} increased from 32% to 44%. In the case of phase change material, for the same two-fold increase or 100% step change in Fischer-Tropsch reaction rate, the conversion per pass values changed as follows: X_{CO} increased from 24% to 38% and X_{H_2} increased from 26% to 39%. These values show that there is no significant departure from the two sets of figures for the two scenarios. The productivity of C_{5+} for the two fold increase in the reaction rate (i.e. $\Re_{\text{FT}} = 2.0$) without and with the phase change material modulation are respectively $0.54\text{mol}\,\text{h}^{-1}$ and $0.48\text{mol}\,\text{h}^{-1}$ up 31.5% and 29% respectively from the corresponding values at $\Re_{\text{FT}} = 1.0$; again, this shows that the benefit of the promoted catalyst is not significantly retarded by the presence of the phase change material.

The productivity of CH_4 (Figure 5.11d) in the case of no phase change material (solid lines) generally increases, although without as much distinction between the step change

values of the reaction rate ($\Re_{\mathrm{FT}}$) as in the case of the productivity of C_{5+}. All the productivity curves also seem to converge at a particular value of $0.1\mathrm{mol\,h^{-1}}$ at the exit point of the reactor, i.e. at reactor coordinate 12m. This blurring distinction between productivity curves for the various reaction rate values becomes even more pronounced in the case of the phase change material modulated process and the curves converge at reactor coordinates value of 10m. The emerging productivity curves for the higher reaction rates, $\Re_{\mathrm{FT}} \in \{1.2, 1.5, 2.0\}$ actually fall slightly below the $\Re_{\mathrm{FT}} = 1.0$ curve. In both scenarios, this observed behaviour is due to the increased catalyst selectivity towards the heavier hydrocarbons C_{5+}, to the disadvantage of the methane synthesis process. It may be imagined that the catalyst has been better conditioned for the production of heavier, long chain hydrocarbons with less affinity for short chain molecules. In the case of the reaction with phase change material influence, the temperature in the reactor is lower than would have been the case without phase change material being present. The higher reaction rate productivity curves rise faster than their lower counterparts owing to the catalyst promotion, however, a combination of quick reactivity and limited temperature rise in the reactor results in the reaction approaching extinction faster. This phenomenon occurs to different degrees for all the $\Re_{\mathrm{FT}}$ productivity curves and explains why all the reaction rate scenarios seem to converge at a point. The lower reaction rate productivity curves however emerge from the convergence point slightly (but not significantly) higher than their higher reaction rate counterparts because a combination of moderate temperature and moderate reactivity seems to deplete less reactants.

5.5.2 Effect on temperature profile in the reactor

Figures 5.12a-d and 5.13a-d respectively depict the axial and radial temperature profiles in the reactor at different $\Re_{\mathrm{FT}}$ for the without and with phase change material scenarios at reaction time of 7200s, $\sigma = 0.6$ and $T_{\mathrm{in,\,cool}} = 230^{\mathrm{o}}\mathrm{C}$. As expected, as the rate of the reaction is increased through catalyst promotion, there is an increase in the amplitude of the hotspot in the reactor; for example, $T_{\max} \approx 260^{\mathrm{o}}\mathrm{C}$ at $\Re_{\mathrm{FT}} = 1.0$ and $T_{\max} \approx 290^{\mathrm{o}}\mathrm{C}$ at $\Re_{\mathrm{FT}} = 2.0$. As in previous cases, at the reactor entrance, a radial temperature gradient with a maximum at the centre was observed in all cases. In addition, the bulk of the reaction occurs near the reactor inlet when there is no phase change material present in the reactor.

In Figure 5.13, where the effect of the phase change material is brought to bear on the reactor, the axial and radial temperature profiles are generally flatter (showing a more even distribution) in comparison to the base case in Figure 5.12. The maximum temperature at $\Re_{\mathrm{FT}} = 2.0$ is about $260^{\mathrm{o}}\mathrm{C}$ in Figure 5.13d compared to about $290^{\mathrm{o}}\mathrm{C}$ for the same reaction condition without phase change material as in Figure 5.12. An interesting

observation that may be elicited from this arrangement is that the productivity of C_{5+} may be increased from $0.33 mol\,h^{-1}$ to $0.46 mol\,h^{-1}$, about a 39% increase, using a promoted catalyst ($\Re_{FT} = 2.0$)under the influence of phase change material, but without the penalty of excessive temperature spikes in the reactor.

It can be expected that further promoting the catalyst with a fixed amount of phase change material will prove ineffective as the phase change material will be overwhelmed, resulting in large temperature gradients in the reactor.

5.6 Effect of varying internal radius of reactor tube

5.6.1 Effect on reactant conversion and representative hydrocarbon productivity

Heat removal from the Fischer-Tropsch process is critical in order to maintain near isothermal conditions inside the reactor tube. The heat is removed from the catalyst surface to the tube walls where the heat is absorbed by the cooling fluid. Typically, small tube radii are recommended in literature in order to ensure the ease of removal of heat from the reaction system [9, 18, 28]. The effect of the reactor tube radius on the reactant conversion and on the productivity of the representative hydrocarbons is studied in this section.

Figure 5.14a-d depicts the reactant conversion and hydrocarbon productivity for different tube radii without and with phase change material, after 7200s of reaction time, $T_{in,\,cool} = 230^{o}C$ and $\sigma = 0.6$. The phase change modulated conversion and productivity curves lag behind their counterparts without any phase change influence, because of the thermal inertia introduced into the system by the phase change material.

As the tube radius, R_t was increased from 0.013m to 0.033m, the conversion of the reactants changed as follows: X_{CO} increased from 30% to 58% without phase change material (and increased from 24% to 31% for the same step change in reactor tube radius, with phase change material). In the case of hydrogen, X_{H_2} increased from 29% to 42% as the reactor radius was increased from 0.013m to 0.033m without phase change material (and increased from 24% to 29% for the same step change in reactor tube radius under the influence of phase change material).

In Figure 5.14c, the productivity of C_{5+} increases with increasing reactor tube radius, both with and without phase change material. The increase in C_{5+} productivity is however dwarfed by the sharp rise in the productivity of CH_4 by as much as 96% for an increase in the tube radius from 0.013m to 0.033m without phase change material (and

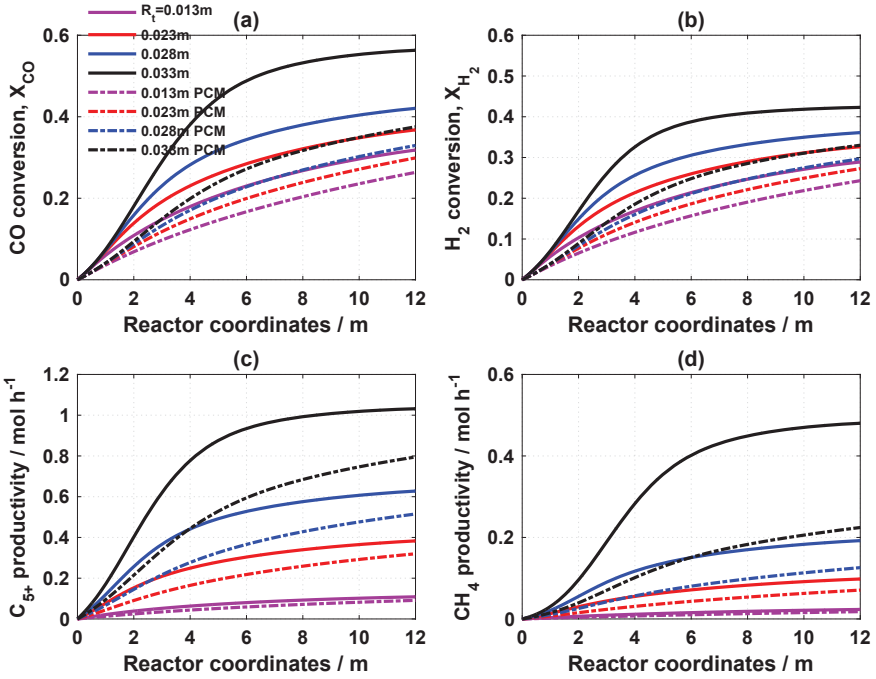

FIGURE 5.14: Reactant conversion and representative hydrocarbon productivity profiles for Fischer-Tropsch synthesis with and without phase change material for varying reactor tube internal radii at: $t = 7200$s, $T_{\text{in,cool}} = 230$°C and $\sigma = 0.6$

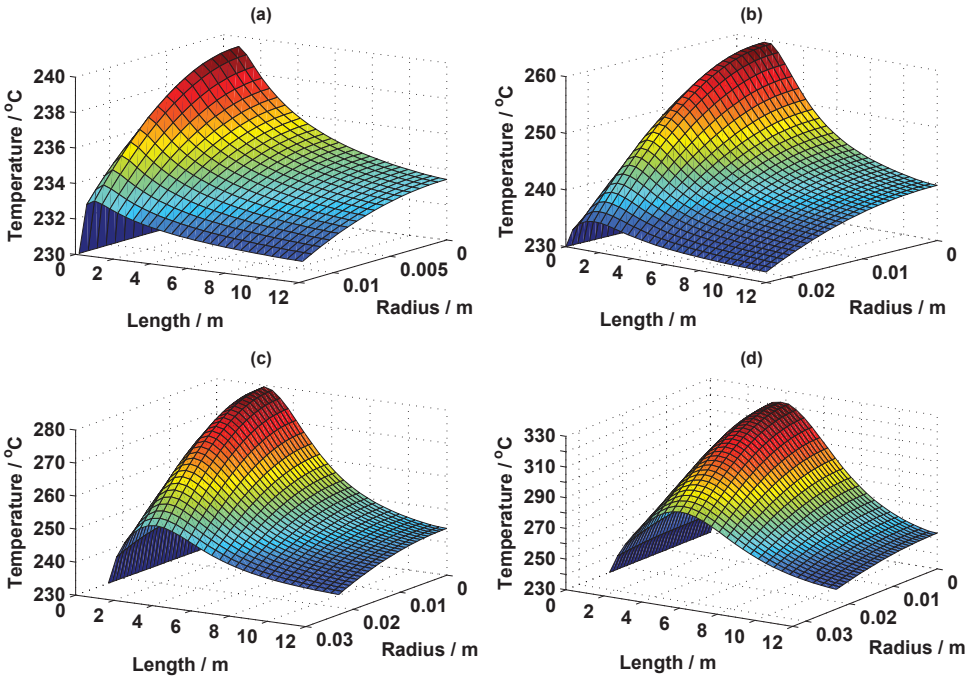

FIGURE 5.15: Axial and radial temperature profiles along the reactor using 2D quasi-homogeneous model for Fischer-Tropsch synthesis without phase change material for varying reactor tube internal radii at $t = 7200$s, $T_{\text{in,cool}} = 230$°C and $\sigma = 1.0$: (a) $R_{\text{t}} = 0.013$m (b) $R_{\text{t}} = 0.023$m (c) $R_{\text{t}} = 0.028$m (d) $R_{\text{t}} = 0.033$m

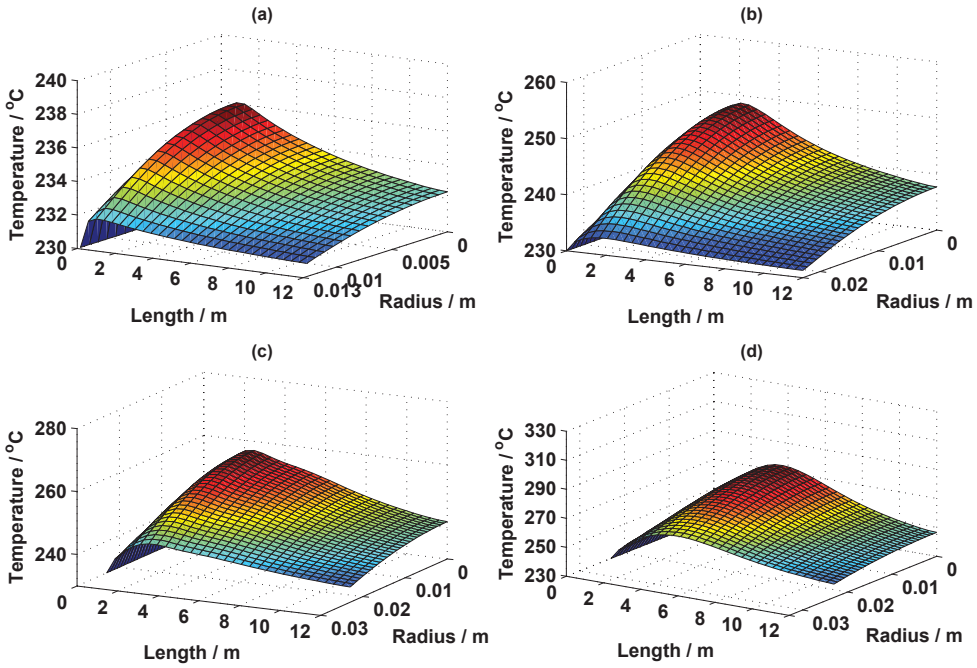

FIGURE 5.16: Axial and radial temperature profiles along the reactor using 2D quasi-homogeneous model for Fischer-Tropsch synthesis with phase change material for varying reactor tube internal radii at $t = 7200$s, $T_{\text{in,cool}} = 230^{\circ}$C and $\sigma = 0.6$: (a) $R_{\text{t}} = 0.013$m (b) $R_{\text{t}} = 0.023$m (c) $R_{\text{t}} = 0.028$m (d) $R_{\text{t}} = 0.033$m

90% without phase change material over the same step change in tube radius). As will be pointed out in subsection 5.6.2, this sharp increase in the methanation process with increasing tube radius can be attributed to the accumulation of heat in the reactor tube, which in turn raises the temperature in the tube. The heat accumulates within the tube with a larger radius because the heat transport resistance (i.e. the distance between the catalyst surface and the heat exchange walls) has been significantly increased, thus making heat removal from the reaction system increasingly difficult.

5.6.2 Effect on temperature profile in the reactor

Figures 5.15a-d and 5.16a-d show the axial and radial temperature profiles in the reactor without and with phase change material respectively for different tube radii. In Figure 5.15a-d, the amplitude of the axial hotspot temperature increases with increasing tube radius, and there is a simultaneous migration of the hotspot position away from the reactor entrance towards the centre of the reactor; thus increasing the exit temperature from the reactor. For the same $T_{\text{in, cool}} = 230^{\circ}$C, the hotspot temperature and position are translated from the temperature-position (T_{max}, z) coordinates of (239.6°C, 1.5m) for tube radius 0.013m to (324°C, 4m) for tube radius of 0.033m. The phase change material does not have any significant effect on restricting the migration of the hotspot

temperature, but reduces the severity in the rise of the temperature in the reactor as seen in Figure 5.16a-d. The temperature-position (T_{max}, z) coordinates of the hotspot from Figure 5.16 are (236°C, 1.5m) at $R_t = 0.013$m and (270°C, 4m) at $R_t = 0.033$m.

As referred to earlier, a larger tube radius implies that the distance between the catalyst pellets at the centre of the reactor and the heat exchange tube walls is significantly increased. This increased distance increases the resistance to heat transport in the reactor, thus making heat removal from the system more difficult. Since heat cannot be removed quickly enough, it accumulates in the reactor, this accumulated heat has an undesirable feed-back loop effect, wherein it drives up the temperature within the reactor, thus accelerating the reaction kinetics exponentially, further driving up the reactor temperature, etc. and possibly leading to a thermal excursion and an uncontrollable reactor. This state of conditions within the reactor creates the ideal recipe for the inordinate production of methane, as recorded in Figure 5.14d, and signals thermal runaway.

An increase in the tube radius, R_t implies a larger throughput of products through the reactor, as evidenced by Figure 5.14c-d. A step change in R_t from 0.013m to 0.033m may be considered, where both tubes have constant cross sectional areas (based on their respective R_t values). If the same entry conditions of temperature and pressure are maintained for each tube scenario, then, the only physical quantity which adjusts in order to compensate for the tube with a larger R_t, such that it delivers a larger throughput commensurate with its cross sectional area, is the superficial velocity of the entry fluid. It is this increased superficial velocity which pushes the reaction fluids further into the reactor, causing the development of a hotspot nearer the middle of the reactor (as this is where any significant reaction first occurs), and prevents any reaction at the entrance. This action of pushing the reactant fluids far into the reactor on entry means that the cooling provided to the first half of the tube is not utilised in any heat removal, resulting in the temperature runaway occurring towards the rear of the reactor, thus leading to the elevation of the hotspot temperature as seen in Figure 5.15d. It is thus clear from the results of this section that increasing the tube radius is not favourable for rapid heat removal from the Fischer-Tropsch synthesis carried out in a multi-tubular fixed bed reactor.

5.6.3 Summary

In summary, this chapter has compared the effect of varying process conditions and design parameters in the Fischer-Tropsch reaction without and with the influence of phase change material, using the rigorous 2D quasi-homogeneous reactor model platform. In

particular, these varied scenarios have been analysed in the light of the reactor performance, i.e. productivity and conversion, as well as the implications for temperature control. The next chapter will look at developing a less computationally cumbersome, yet sufficiently accurate reactor model platform, which lays the groundwork ready for subsequent phase change material regulated reactor optimisation challenges to be addressed in chapter 7.

Chapter 6

Improved One Dimensional Model for The Fixed Bed Fischer Tropsch Reactor: A modified α-model

"The simplification of anything is always sensational."

G.K. Chesterton, (1874-1936).

In chapter 5, a rigorous 2-dimensional model was used in simulating the Fischer-Tropsch fixed bed reactor. Two-dimensional models of this nature are often useful for detailed reactor design because of the high level of accuracy which they provide. In situations where the computational efforts are required to be small such as in the development of control laws for the reaction process control, reactor dynamics flow-sheeting and optimisation of a reactor design [114, 189], two dimensional models become computationally cumbersome and unwieldy; it therefore becomes necessary to have a simplified model which trades off as little accuracy as possible for computational convenience.

One dimensional models, such as the conventional one-dimensional pseudo-homogeneous model, come in handy in such situations where less computational expense is desired. They are however largely unreliable because of their underlying assumptions which completely neglect temperature gradients in the radial direction. Some work has been done in the area of improving one dimensional models in order that they might better approximate two dimensional models. Irrespective of what modifications are made to one

dimensional models to improve their accuracy, the cardinal prerequisite for their adoption is that their ability to approximate the radial temperature gradient must be superior to that of the conventional or standard one-dimensional model where radial gradients are done away with entirely.

There are in the main, three types of one dimensional models available in open literature based on the quasi-homogeneous reactor model assumption, namely: the conventional one dimensional quasi/pseudo-homogeneous model [114], the α-model derived using the Karman-Pohlhausen procedure by Hagan et al [161] and the δ-model based on the Frank-Kamanetskii approximation by Koning et al [143, 190]. Koning et al [143, 190] have carried out a thorough model comparison between the three models for exothermic reactions against the 2D-quasi-homogeneous model. They concluded in their work that where reactors are operated at close to thermal runaway conditions, the α-model best approximates the 2D quasi-homogeneous model. Exothermic commercial packed bed reactors like the Fischer-Tropsch synthesis, are often operated near thermal runaway conditions in order to deliver economically worthwhile conversions [126]. On this basis, the α-model of Hagan et al [161, 191, 192] has been adopted in this chapter for simulating the reactor in place of the more rigorous 2D model.

The outline for this chapter is as follows: section 6.1 will briefly review the conventional one dimensional quasi-homogeneous and the α-models and their underlying assumptions vis-à-vis the 2D quasi-homogeneous model. Section 6.2 compares the reactor performance simulated using three reactor models namely, the 2D quasi-homogeneous model, the α-model and the 1D quasi-homogeneous model in the context of the Fischer-Tropsch synthesis. Section 6.3 presents the modification of the enthalpy balance of the α-model in order to take into account the heat sink effect of the phase change material. Section 6.4 shows results obtained using the modified α-model (with and without phase change material) to investigate reactor response to fluctuations in the feed gas molar ratio.

6.1 Review of approximate one dimensional reactor models

This section looks at the conventional quasi-homogeneous one dimensional model and the α-model and their underlying assumptions. The one dimensional heterogeneous model has not been considered here in order to ensure a common basis of comparison, i.e. maintaining the "quasi-homogeneous theme". Both of the outlined models will be discussed succinctly and it is pertinent to state that as far as this chapter is concerned, the benchmark for the accuracy of the one dimensional models considered will be the

two dimensional quasi-homogeneous model, which has already been discussed at length in chapters 3 to 5.

6.1.1 One dimensional quasi-homogeneous model

It will be recalled from section 3.3 of chapter 3 that the 2D quasi-homogeneous material and enthalpy balances (without axial dispersion) for a chemical species j in the set of reactions $i \in \{1, 2, ...N\}$ are as follows respectively:

$$-\frac{\partial c_j}{\partial t} + \epsilon D_{\text{eff, r}} \left(\frac{\partial^2 c_j}{\partial r^2} + \frac{1}{r} \frac{\partial c_j}{\partial r} \right) - \frac{\partial (u_s \, c_j)}{\partial z} - \sum_{i=1}^{N} \nu_{i,j} \, \Re_{i,j}(c, T) = 0 \tag{6.1}$$

$$-\rho_{\text{f}} C_{\text{p}} \frac{\partial T}{\partial t} + \kappa_{\text{eff, r}} \left(\frac{\partial^2 T}{\partial r^2} + \frac{1}{r} \frac{\partial T}{\partial r} \right) - \rho_{\text{f}} u_{\text{s}} C_{\text{p}} \frac{\partial T}{\partial z} + \sum_{i=1}^{N} \nu_{i,j} \, \Re_{i,j}(c, T) \, (-\Delta H_{\text{r},\, i} + \Delta H_{\text{pcm}}) = 0 \tag{6.2}$$

Pivotal to the conventional 1D model is the assumption that the average reaction rate over a cross section of the reactor is the same as the reaction rate at some average temperature over the same cross section [143, 190]:

$$\overline{\Re(T)} \approx \Re(\overline{T}) \tag{6.3}$$

The one dimensional quasi-homogeneous material and enthalpy balances with neither axial dispersion nor axial conduction for a fixed bed reactor are as follows [114]

$$\epsilon \frac{\partial \overline{c_j}}{\partial t} = -u_{\text{z}} \frac{\partial \overline{c_j}}{\partial z} - \sum_{i=1}^{N} \nu_{i,j} \, \Re_i(\overline{\mathbf{c}}, \overline{T}) \tag{6.4}$$

$$\epsilon \, \rho_{\text{f}} \, C_{\text{p, f}} \frac{\partial \overline{T}}{\partial t} = -u_{\text{z}} \, \rho_{\text{f}} \, C_{\text{p, f}} \frac{\partial \overline{T}}{\partial z} - \frac{2 U_{\text{wall}}}{R_{\text{t}}} (\overline{T} - T_{\text{in, cool}}) - \sum_{i=1}^{N} \nu_{i,j} \, \Re_i \, (\overline{\mathbf{c}}, \overline{T}) \, \Delta H_{\text{r},\, i} \tag{6.5}$$

where $\overline{c_j}$ is the average concentration of species j, $\overline{\mathbf{c}}$ is the vector of the average concentrations of reactants and products, $\overline{T}$ is the average temperature and $\nu_{i,j}$ is the stoichiometric coefficient of chemical species j in any reaction i. The overall heat transfer coefficient, U_{wall}, resulting from the heat transfer resistance inside the catalyst bed and that at the wall may be estimated from the correlation of Dixon [193]:

$$\frac{1}{U_{\text{wall}}} = \frac{1}{h_{\text{wall}}} + \frac{R_{\text{t}}}{3 \, \kappa_{\text{eff, r}}} \frac{Bi + 3}{Bi + 4} \tag{6.6}$$

and the Biot number (Bi) is given by:

$$Bi = \frac{h_{\text{wall}} \, R_{\text{t}}}{\kappa_{\text{eff, r}}} \tag{6.7}$$

6.1.2 The α-Model

The exhaustive derivation of the α-model using the Karman-Pohlhausen procedure can be found in the works of Hagan et al [161, 191, 192]. Hagan et al [161, 191, 192] modified the conventional 1D quasi-homogeneous model and transformed it into the new α-model which accounted for the radial temperature profile by correcting for the effective heat transfer coefficient. The α-model was derived using an approximate solution of the radial temperature profile and a reaction rate approximated by a truncated, second order Taylor's expansion series of the reaction Arrhenius temperature term:

$$\Re(c,\, T) = k_0 c^n \exp\left(\frac{E_{\text{act}}}{R_{\text{g}} T}\right) \approx k_0 c^n \exp\left(A(T-\overline{T}) + B(T-\overline{T})\right)^2 \tag{6.8}$$

where k_0 is the pre-exponential factor, n is the order of the reaction, and A and B are Taylor expansion coefficients. According to Hagan et al [161], the convective terms may be neglected far from the inlet, where the axial concentration and temperature gradients are small. Convective heat transport is particularly insignificant at the hotspot of the reactor, where the enthalpy balance is most sensitive, and this makes the α-model well suited to the description of the radial temperature profile at that position in the reactor [143, 190]. The α-model also distinguishes between heat transport average temperature, $\overline{T}$ and a reaction average temperature, $\overline{T_{\Re}}$, such that:

$$\Re(\overline{T_{\Re}}) = \overline{\Re(T)} \tag{6.9}$$

In making this distinction, the α-model is again distinguished from the conventional 1D quasi-homogeneous model which, completely neglects the radial temperature profile. The α-model computes the reaction averaged temperature, $T_{\Re}$ by applying the integral average value theorem to the heat transport average temperature, $\overline{T}$, over the radial length of the reactor tube (R_{t}), such that:

$$f(\overline{T_{\Re}}(z,t)) = \frac{1}{R_{\text{t}} - 0}\int_0^{R_{\text{t}}} f(\overline{T}(z,r,t)).2r\,\mathrm{d}r \tag{6.10}$$

For a reaction which follows the Arrhenius temperature dependency, such as the Fischer-Tropsch synthesis, the functions of temperature in equation (6.10) may be replaced with the Arrhenius number to give:

$$\exp\left(-\frac{E_{\text{act}}}{R_{\text{g}}\overline{T_{\Re}}(z,t)}\right) \equiv \frac{2}{R_{\text{t}}}\int_0^{R_{\text{t}}} \exp\left(-\frac{E_{\text{act}}}{R_{\text{g}}\overline{T}(z,r,t)}\right) r\,\mathrm{d}r \tag{6.11}$$

The reaction average temperature is used in the material and enthalpy balances which are given respectively by:

$$\epsilon \frac{\partial \overline{c_j}}{\partial t} = -u_z \frac{\partial \overline{c_j}}{\partial z} - \sum_{i=1}^{N} \nu_{i,j}\, \Re_i(\overline{\mathbf{c}}(z,t), \overline{T_\Re}(z,t)) \tag{6.12}$$

$$\epsilon \rho_f\, C_{p,f} \frac{\partial \overline{T_\Re}(z,t)}{\partial t} + u_z\, \rho_f\, C_{p,f} \frac{\partial \overline{T_\Re}(z,t)}{\partial z} = -\frac{8\alpha\, \kappa_{eff,r}}{A R_t^2} + \sum_{i=1}^{N} \nu_{i,j}\, \Re_i \Delta H_{r,i} \tag{6.13}$$

where α is a dimensionless heat loss parameter which is determined from the implicit expression:

$$A(\overline{T_\Re}(z,t) - T_{in,cool}) = \frac{4\alpha}{Bi} - \log_e(1-\alpha) + \frac{1}{3}\left(\frac{B}{A^2}\right) \log_e^2(1-\alpha) \tag{6.14}$$

6.1.3 Numerical Implementation of the α-model

The material and energy balances and all other differential and non-linear algebraic equations were implemented and solved using the finite element package, COMSOL Multi-physics 4.4 [21]. The balances were space-discretised by the backward finite differential (BFD) method. The discretisation of the system of partial differential equations entailed converting them to a system of ordinary differential equations which, are in turn solved by the software. The α-model required the implicit solution of α at each discretisation point, z_n along the axial length of the reactor, z; one iterative Newton step was found to be sufficient for updating α based on its previous value. The phase transition of the phase change material also had to be solved at each discretised node. The sudden "jump" in the physical properties of the phase change material during phase transition often results in numerical discontinuities and non-convergence of the solver. This was avoided through the use of the in-built smoothed Heaviside function with continuous second order derivative; this facility allows for a seamless transition from one set of phase properties to the other e.g. solid to liquid.

The mesh and convergence tests conform with the methods described in chapter 4 and will not be repeated here.

6.2 Reactor model comparison

This section compares the prediction of the reactor performance using the 2D quasi-homogeneous model, α-model and the conventional 1D quasi-homogeneous models. Reactor models are usually compared using bifurcation diagrams as shown in Figure 6.1.

Before discussing this figure in detail, a brief background to reactor thermal run away will be provided.

6.2.1 Thermal runaway in a fixed bed reactor

Thermal runaway in a chemical system refers to a situation where a reaction generates heat faster than it can be rejected. This has the effect of raising the temperature of the reacting system further, leading to favourable conditions for undesired side reactions (e.g. the inordinate production of methane gas and the coking of reaction fluids in the case of the Fischer-Tropsch synthesis [13]) taking place to the detriment of the principal reaction, reactor uncontrollability and ultimately temperature excursions [17, 161]. Paradoxically, in order to deliver commercially useful conversions, strongly exothermic, non-isothermal reactions are usually operated at close to thermal runaway conditions in industrial fixed bed reactors [126]. This implies that the hotspot temperature lies very close to the unstable region, such that a slight perturbation of the process conditions could quite easily result in an exponential increase in temperature within the reactor.

According to the works of Hagan et al [161, 192], thermal runaway may be avoided if the following relationship holds true:

$$\Theta_{\text{ad}} = \frac{\Delta T}{\Delta T_{\text{ad}}} = \frac{T - T_{\text{in, cool}}}{\left(\dfrac{(-\Delta H_{\text{r},i}) \times c_{j,\,\text{in}}}{\rho_{\text{f}}\, C_{\text{p,f}}} \right)} \equiv \frac{t_{\text{dif}}}{t_{\text{rxn}}} << 1.0 \tag{6.15}$$

where, ΔT_{ad} is the adiabatic temperature rise, $c_{j,\,\text{in}}$ is the inlet concentration of the of a chemical species j, ρ_{f} is the density of the inlet reaction mixture, t_{dif} is the time scale on which heat escapes from the reactor by diffusing radially to the cooled reactor walls and t_{rxn} is the time scale on which the reaction occurs. A corollary of equation (6.15) is: if the reaction time scale is held relatively constant at near thermal runaway conditions, while the heat removal capability is enhanced such that the temperature difference $(T - T_{\text{in, cool}})$ is kept to a minimum, then as time approaches infinity and both reactants and reaction heat wane, the ratio of the two time scales necessarily remains a fraction less than 1.0. The physical interpretation of this is that the reactor stays within a "safe" or "stable" zone and avoids thermal runaway.

Generally, phase change materials melt under near-isothermal conditions owing to their latent enthalpy of fusion. The amount of heat which they can absorb without significant temperature change at the critical point is larger (because of the latent enthalpy of fusion) relative to that at the sensible heat capacity, hence they could potentially serve as good candidates for catalyst dilution in exothermic reactions. If properly selected and engineered, the phase change materials melts when required and provides a thermal

"buffer" effect within the reacting system by delaying any significant temperature rise thereby keeping the temperature difference $(T - T_{\text{in, cool}})$ in the reactor to a minimum as required by equation (6.15).

6.2.2 Comparison of one dimensional reactor models

Figure 6.1 is a bifurcation diagram showing Θ_{ad}, reactor temperature normalised using the adiabatic temperature rise, as expressed in equation 6.15, as a function of $\Re_0$, the dimensionless reaction rate at inlet conditions for the 2D quasi-homogeneous, 1D quasi-homogeneous and α-models. The dimensionless reaction rate at inlet conditions is given by:

$$\Re_0 = Pe_{\text{h, r}} \frac{R_{\text{t}}}{u_{\text{s}}\, c_{j,\,\text{in}}} \Re_i \tag{6.16}$$

In the main, there is very good agreement between the bifurcation curves of the 2D model and the α-model and less so between the conventional 1D model and the 2D model. The critical temperatures (i.e. temperatures at the hotspot) of the 2D and α-models, which occur at the respective turning points of the curves, coincide, i.e. $(\Theta^{\text{cr}}_{\text{ad, 2D}} \approx \Theta^{\text{cr}}_{\text{ad, }\alpha} \approx 0.0213)$, while the critical normalised temperature of the 1D model, $\Theta^{\text{cr}}_{\text{ad, 1D}}$ occurs at about 0.0148. For each of the three curves, there are two corresponding solutions of Θ_{ad} for each dimensionless reaction rate at inlet conditions $(\Re_0)$, except at the turning points/critical points of the curves. These solutions are categorised into "stable" and "unstable" solutions as depicted in Figure 6.1. The lower lines, below the critical points of the individual curves represent the stable regime. The physical meaning of this is that

after a temperature perturbation of the reaction system, e.g. a rapid temperature rise due to reaction or increase in the coolant temperature, the system returns to its original state once the cause of the perturbation is removed. This region is characterised by the fact that the heat removal rate increases faster than the heat generation rate.

The upper line and the region above it for the respective curves, in Figure 6.1 depict the unstable solutions. In this regime, the rate of heat generation overwhelms the heat removal process, thus causing the continued increase in the system's temperature. Mathematically, this situation corresponds to a slope with an infinite value on a plot of temperature against the axial length and physically translates to "runaway". Below this upper line, within the envelopes created by the curves, heat removal still prevails and the system is still able to transition to stable solutions after any momentary disturbance to the system is removed. This is depicted by the arrows (a) and (b) in Figure 6.1.

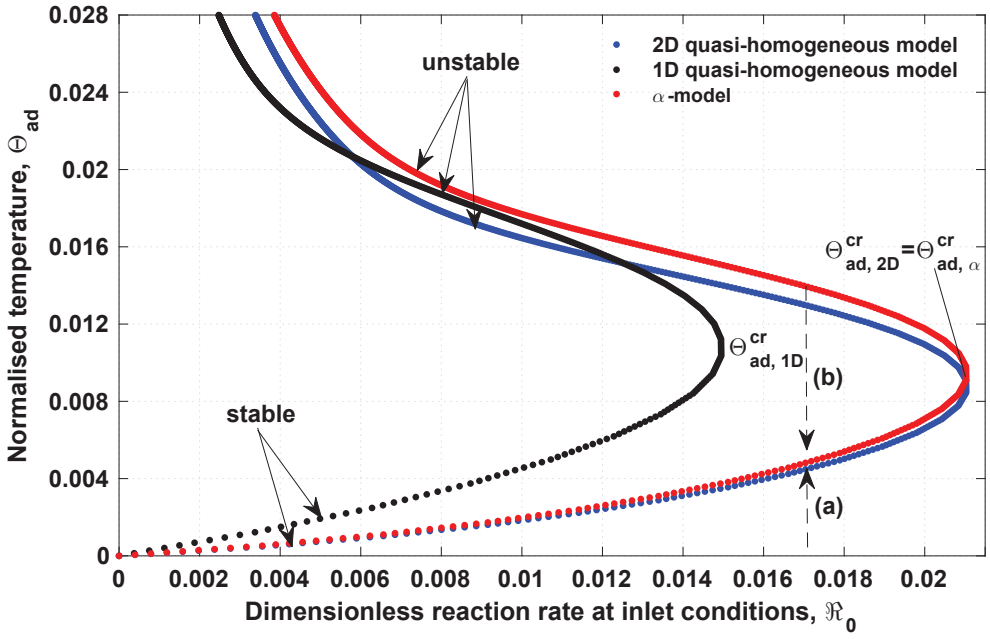

FIGURE 6.1: Comparison of one dimensional models with the numerical solution of the two-dimensional model for the Fischer-Tropsch reaction.

Figure 6.2a compares the plots of the reactor temperature against the normalised bed length using the 2D quasi-homogeneous, α and 1D quasi-homogeneous reactor models. The 2D-quasi-homogeneous model which, in this work, is considered to be the base case has been benchmarked against the work of Jess and Kern [5] for an Fe-catalysed reaction with inlet/coolant temperature of 230°C. It is pertinent to note that although Hagan et al [161] derived and applied their α-model under steady state conditions, this work has extended its use to transient conditions and as may be seen in Figure 6.2a, the agreement between the α and 2D pseudo-homogeneous models is within 4% error.

This shows that the α-model can be extended to space-time models with minimal errors. The standard 1D model is in good agreement with the 2D pseudo-homogeneous model at the beginning and towards the end of the reactor temperature profile. It performs poorly in the estimation of the hotspot temperature however, under-predicting by about 10°C. In general, Figure 6.2a shows that the α-model accurately predicts the hotspot, where the reactor's enthalpy balance is generally at its most sensitive.

The accuracy of the α-model is better illustrated in Figure 6.2b which shows the loci of maximum temperatures in the reactor as a function of different values of the catalyst activity for the three reactor models in question. The catalyst activity was varied by multiplying the reaction rate by increasing constant factors. Then for each factor, the 2D-pseudo-homogeneous, α-, and standard 1D models were solved. The maximum temperatures for each simulation and each model were subsequently located and plotted.

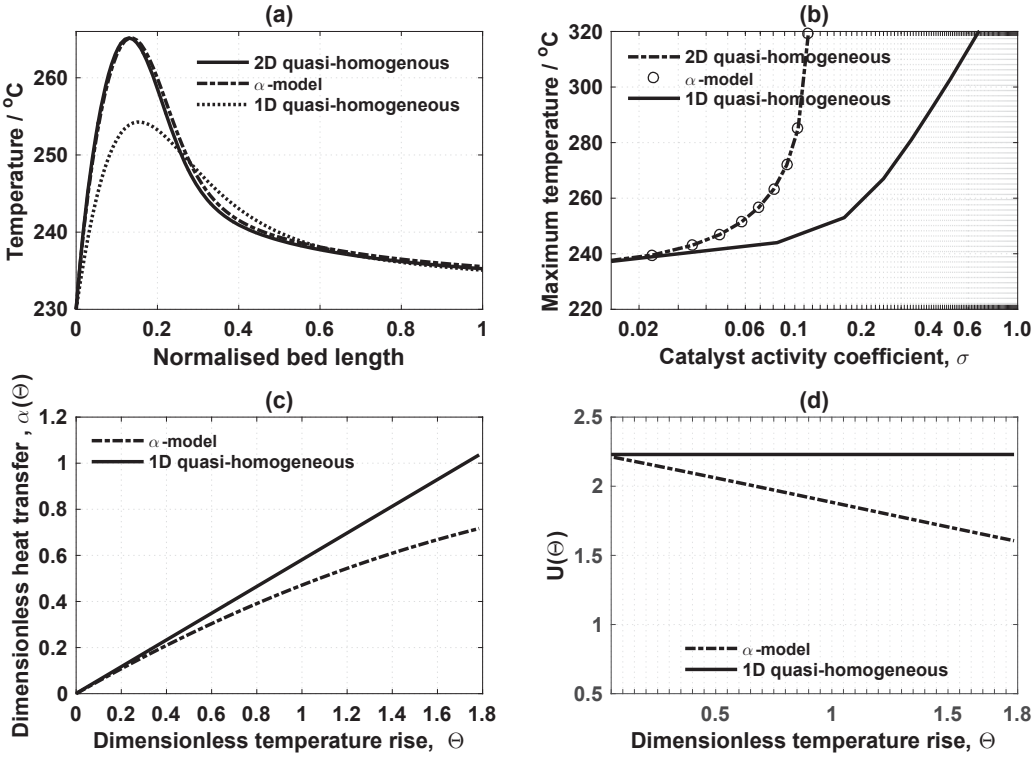

FIGURE 6.2: Comparison of 2D quasi-homogeneous, α- and standard 1D quasi-homogeneous reactor models for $T_{\text{in, cool}}$=230°C: (a) Reactor temperature profiles (b) Reactor maximum temperatures (c) Dimensionless heat transfer versus the dimensionless temperature rise (d) Dimensionless heat transfer coefficient versus the dimensionless temperature rise

As presented in Figure 6.2b, the α-model predicts the 2D pseudo-homogeneous reactor hotspot temperatures within 1.0% error. Remarkably, it does so consistently in spite of the progressive increase in the reactor's sensitivity and exponential rise in the amplitude of the hotspot, due to increasing catalyst activity. The standard 1D model on the other hand significantly departs from the base case model with increasing catalyst activity and by extension, increasing reaction temperature. It over-predicts the reactor's performance by consistently under predicting the maximum temperature in the reactor. In other words, a 1D design model will incorrectly suggest that the feed/coolant temperature could be increased, presumably to drive conversion to much higher values, without suffering thermal runaway. For example, at an intrinsic activity value of 0.07 in Figure 6.2b, the standard 1D model predicts a maximum temperature of about 243°C compared with 257°C predicted by the α-model.

Figures. 6.2c and 6.2d respectively show the dimensionless heat transfer and dimensionless overall heat transfer coefficient against the dimensionless temperature rise for both the standard 1D and α-models. Where the dimensionless heat transfer parameter $\alpha(\Theta)$

is implicitly defined as:

$$\Theta = \frac{4\alpha(\Theta)}{Bi} - \log_e(1-\alpha(\Theta)) - \frac{R_g\overline{T_\Re}(z,t)}{3\overline{E_{act}}}\log_e^2(1-\alpha(\Theta)) \tag{6.17}$$

The dimensionless temperature rise is given by:

$$\Theta = \frac{\overline{E_{act}}(\overline{T_\Re}(z,t) - T_{in,\,cool})}{R_g(\overline{T_\Re}(z,t))^2} \tag{6.18}$$

Matching equation (6.5) with (6.13) shows that the equivalence relationship between the overall heat removal through the reactor walls in the standard 1D model and the α-model is given by:

$$2U_{wall}(\overline{T}(z,t) - T_{in,\,cool}) \equiv \frac{8\alpha\,\kappa_{eff,\,r}}{AR_t^2} \tag{6.19}$$

The heat removal term, $\frac{8\alpha\,\kappa_{eff,\,r}}{AR_t^2}$ in equation (6.13)is what stands the α-model apart from the standard 1D pseudo-homogeneous model (equation 6.5). The overall heat transfer coefficient, U_{wall} in the standard 1D model, is a constant averaged value which, does not change over the reactor axial length, whereas the overall heat transfer coefficient in the α-model is a decreasing function of the radial temperature rise $(\overline{T}(z,t) - T_{in,\,cool})$ (see Figures 6.2c-d). This decrease is as a result of the heat generation becoming progressively accentuated at the reactor axis, away from the walls, as the reactor approaches runaway conditions.

6.2.3 Effect of varying Biot number

Figures 6.3a-c shows the normalised temperature Θ_{ad} plotted against the normalised bed length ξ for the 2D, 1D-quasi-homogeneous and the α-model at different Biot numbers. The dimensionless axes are defined as follows:

$$\Theta_{ad} = \frac{T - T_{in,\,cool}}{\Delta T_{ad}} \tag{6.20}$$

$$\xi = \frac{\text{axial coordinates}}{\text{reactor length}} = \frac{z}{L} \tag{6.21}$$

The Biot number (Bi) is a dimensionless ratio of the conductive heat transport resistance within a solid body, to the convective heat transport resistance at the interface between the solid body and the fluid in which it is immersed[194]. Typically, as the Biot number rises above 0.1, the temperature distribution within the body in question becomes less uniform. In Figure 6.3a-c, three values of Bi, i.e. $Bi \in \{3.0, 5.0, 10.0\}$ are explored using the three reactor models under consideration. As expected, increasing the Biot number results in the exacerbation of the dimensionless hotspot temperature in all cases

of the reactor models used. For example, in the case of the 2D quasi-homogeneous model: $\Theta_{ad} \approx 0.0147$ at $Bi = 3.0$, $\Theta_{ad} \approx 0.021$ at $Bi = 5.0$ and $\Theta_{ad} \approx 0.046$ at $Bi = 10.0$. The reason for this is that radial diffusion of heat across the reactor radius becomes increasingly difficult with rising Biot number and thus becomes the rate determining step for the heat transport process, compared to the convective heat transport resistance at the tube wall. Physical interpretations of increasing the Biot number include: increasing the tube radius, drop in the coolant flow rate, increasing the coolant temperature or fluctuations in feed temperature.

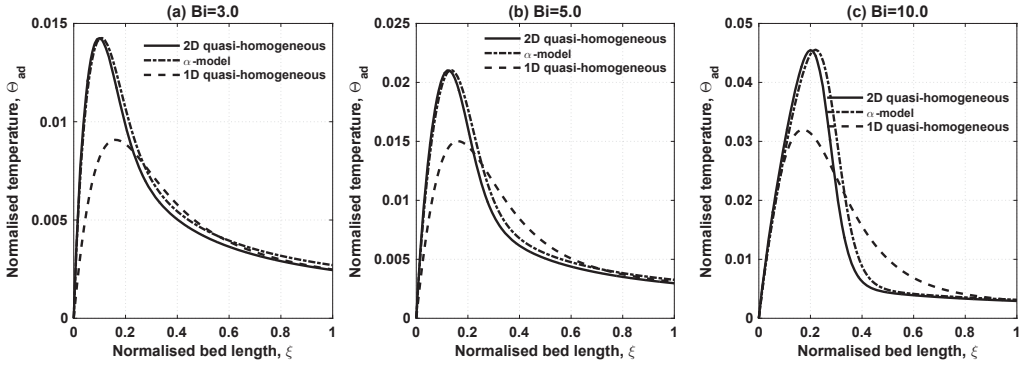

FIGURE 6.3: A comparison of the adiabatic temperature normalised reactor temperature as a function of normalised bed length of the one-dimensional models with the numerical solution of the 2D quasi-homogeneous model, for different Biot numbers: (a) $Bi = 3.0$ (b) $Bi = 5.0$ (c) $Bi = 10.0$

In all three cases, the α-model approximates the 2D quasi-homogeneous remarkably well with increasing Bi. The normalised hotspot temperature in particular is predicted to within 1% error. The conventional one dimensional quasi-homogeneous model is however less accurate, particularly in the prediction of the hotspot temperature of the reactor. This is due to the underlying assumption of the 1D model, which completely ignores any radial diffusion of heat across the tube radius. The effect of this radial diffusive heat transfer (i.e. radial heat conduction) becomes more pronounced as the Biot number increases. It may be observed from Figure 6.3 that the 1D model is most accurate at the lowest Biot number in Figure 6.3a. Figure 6.4a-c shows the fractional conversion of the limiting reactant, CO over the bed length using the three reactor models at different Biot numbers. As in the case of the temperature profiles, the α-model better approximates the 2D model compared to the conventional 1D model. The α-model, however slightly over-predicts the fractional conversion, while the 1D model consistently under-predicts. The conversion increases with increasing Bi values for all three reactor models. This is because the higher temperature within the reactor (with increasing Biot number) drives up conversion.

The last part of this subsection considers the dimensionless heat transfer parameter $\alpha(\Theta)$. In Figure 6.5a, $\alpha(\Theta)$ traces out a similar profile to the dimensionless temperature,

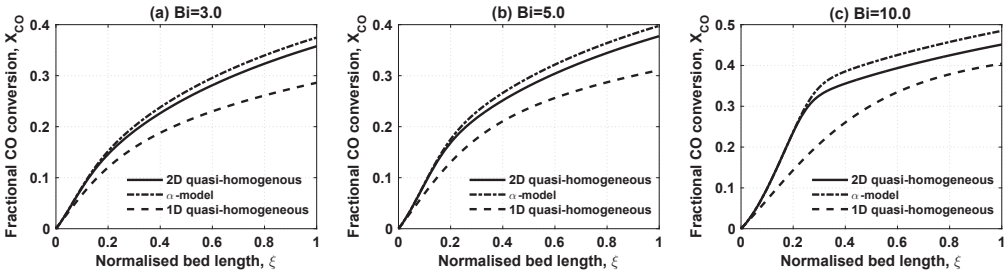

FIGURE 6.4: A comparison of the fractional conversion of CO as a function of normalised bed length of the one-dimensional models with the numerical solution of the 2D quasi-homogeneous model, for different Biot numbers: (a) $Bi = 3.0$ (b) $Bi = 5.0$ (c) $Bi = 10.0$

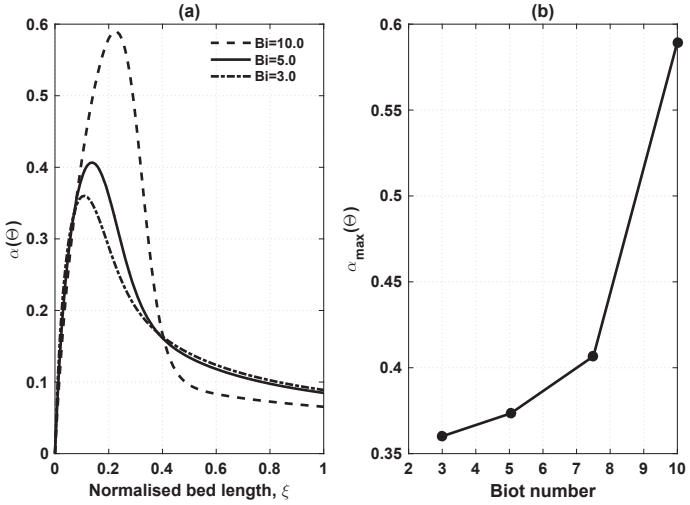

FIGURE 6.5: Effect of varying Biot number on the dimensionless heat loss parameter, α: (a) Variation of the dimensionless heat loss parameter, $\alpha(\Theta)$ as a function of the normalised bed length for different Biot number values (b) Maximum dimensionless heat loss parameter values, $\alpha_{\max}(\Theta)$ as a function of varying Biot number

Θ over the normalised bed length. This is hardly surprising as α is a function of Θ. As Bi increases, Θ also increases, as such the maximum value of $\alpha(\Theta)$ increases. Figure 6.5b shows the maximum value of the dimensionless heat transfer parameter ($\alpha_{\max}(\Theta)$). The values of $\alpha_{\max}(\Theta)$ correspond to the amplitude values of the $\alpha(\Theta)$-curves in Figure 6.5a. In their analyses, Hagan et al[161] noted that a reactor enters runaway domain whenever $\alpha(\Theta) \geq 0.5$, which occurs at about $Bi \geq 8.8$ in Figure 6.5b.

6.3 The modified α-model

This section attempts to incorporate the heat sink effect of the phase change material into the enthalpy balance of the α-model (equation 6.13) in the context of the Fischer-Tropsch synthesis, starting from the enthalpy balance of the 2D quasi-homogeneous model (equation 6.2). The intended end result of this is to provide a modified α-model

which can be used to predict reactor performance, etc. for a catalyst bed diluted with phase change material.

From the general asymptotic analysis of Hagan et al [161], it was shown that radial diffusion of mass occurs much more rapidly than reaction (i.e. $t_{\text{dif}} > t_{\text{rxn}}$), therefore, the radial concentration gradient may be assumed to be negligible such that the concentration in the radial direction is a constant i.e.

$$c_j(z, r, t) \equiv c_j(z, t) \tag{6.22}$$

The radial temperature gradient is however much more significant than its concentration counterpart. This is especially true when the heat generation term is not balanced by the radial diffusion of heat, during which the reactor temperature change undergoes a sharp transition which may lead to runaway.

From the foregoing explanation, assuming there is radial concentration symmetry and negligible radial concentration gradient for any component j within the reactor tube, so that $\dfrac{\partial c_j}{\partial r} = 0$, then the high rate of heat rejection at the reactor walls can be accounted for using an approximate radial temperature distribution profile. The total heat released (Q_{rel}), i.e. the last term on the RHS in equation 6.2, in a reactor with multiple reactions as in the case of the Fischer-Tropsch synthesis, may be represented as:

$$Q_{\text{rel}}(\overline{\mathbf{c}}(z,t),\, \overline{T}(z,r,t)) = -\sum_{i=1}^{N} \nu_{i,j}\, \Re_i(\overline{\mathbf{c}}(z,t),\, \overline{T}(z,r,t))\, \Delta H_{\text{r},\,i} \tag{6.23}$$

By performing a Taylor's series expansion and truncating the same at the second order term around some reaction average temperature, $\overline{T_{\Re}}$ the heat released may be approximated by:

$$\begin{aligned} Q_{\text{rel}}(\overline{\mathbf{c}}(z,t),\, \overline{T}(z,r,t)) = -\sum_{i=1}^{N} \nu_{i,j}\, \Re_i(\overline{\mathbf{c}}(z,t),\, \overline{T}(z,r,t))\, \Delta H_{\text{r,i}} \times \exp[A(\overline{T}(z,r,t) - \overline{T_{\Re}}(z,t)) \\ + B(\overline{T}(z,r,t) - \overline{T_{\Re}}(z,t))^2] \end{aligned} \tag{6.24}$$

The two Taylor expansion coefficients, A and B, are defined as follows:

$$A = \left.\frac{\partial \log_e Q_{\text{rel}}}{\partial \overline{T}(z,r,t)}\right|_{\overline{T}(z,r,t)=\overline{T_{\Re}}(z,t)} \quad \text{and} \quad B = \left.\frac{1}{2}\frac{\partial^2 \log_e Q_{\text{rel}}}{\partial \overline{T}\,((z,r,t))^2}\right|_{\overline{T}(z,r,t)=\overline{T_{\Re}}(z,t)} \tag{6.25}$$

The reaction average temperature, $\overline{T_{\Re}}(z,t)$ for a reaction which follows Arrhenius kinetics is given by the expression:

$$\exp\left(-\frac{E_{\text{act}}}{R_{\text{g}}\overline{T_{\Re}}(z,t)}\right) \equiv \frac{2}{R_{\text{t}}}\int_0^{R_{\text{t}}} \exp\left(-\frac{E_{\text{act}}}{R_{\text{g}}\overline{T}(z,r,t)}\right) r\, \mathrm{d}r \tag{6.26}$$

And satisfies the equation:

$$Q_{\mathrm{rel}}(\overline{\mathbf{c}}(z,t),\, \overline{T_{\Re}}(z,t)) = \frac{2}{R_{\mathrm{t}}} \int_0^{R_{\mathrm{t}}} Q_{\mathrm{rel}}(\overline{\mathbf{c}}(z,t),\, \overline{T}(z,r,t)) r \, \mathrm{d}r \tag{6.27}$$

where R_{t} is the internal radius of the tube. Substituting the Arrhenius temperature term with a first order Taylor's series expansion, and assuming that the reactor walls are kept at some constant temperature, $T_{\mathrm{in,\,cool}}$, by the cooling fluid, then an approximated two-dimensional temperature profile may be obtained by solving the following differential equation

$$\frac{1}{r}\frac{\partial}{\partial r}\left(r\frac{\partial \overline{T}(z,r,t)}{\partial r}\right) + \frac{1}{\kappa_{\mathrm{eff,\,r}}} Q_{\mathrm{rel}}(\overline{\mathbf{c}}(z,t),\, \overline{T_{\Re}}(z,t) \times \exp(A(\overline{T}(z,r,t)) - \overline{T_{\Re}}(z,t))) = 0 \tag{6.28}$$

with its attendant initial and boundary conditions at time $t \geq 0$:

$$\left.\frac{d\overline{T}(z,r,t)}{dr}\right|_{r=0} = 0 \quad \text{and} \quad \left.\frac{d\overline{T}(z,r,t)}{dr}\right|_{r=R_{\mathrm{t}}} = -Bi \times (\overline{T}(z,r,t) - T_{\mathrm{in,\,cool}}) \tag{6.29}$$

and the Biot number, Bi is given by:

$$Bi = \frac{h_{\mathrm{wall}}\, R_{\mathrm{t}}}{\kappa_{\mathrm{eff,r}}} \tag{6.30}$$

The exact solution of equations (6.28) and (6.29) is given by equation (6.31), where α is a dimensionless heat loss parameter [195]:

$$\overline{T}(z,r,t) = T_{\mathrm{in,\,cool}} + \frac{1}{A}\left(\frac{4\alpha}{Bi} - 2\log_e\left(1 - \alpha + \alpha\frac{r^2}{R_{\mathrm{t}}^2}\right)\right) \tag{6.31}$$

Substituting the Taylor's expansion in equation (6.24) into equation (6.27) yields:

$$\frac{2}{R_{\mathrm{t}}} \int_0^{R_{\mathrm{t}}} \exp\left(-\frac{E_{\mathrm{act}}}{R_{\mathrm{g}}\overline{T}(z,r,t)}\right) r \, \mathrm{d}r = 1 \tag{6.32}$$

Substituting the temperature profile, equation (6.31) into equation (6.32) and integrating the resultant expression over r, the following equation which implicitly defines α along the reactor axial dimension is obtained:

$$A \times (\overline{T_{\Re}}(z,t) - T_{\mathrm{in,\,cool}}) = \frac{4\alpha}{Bi} - \log_e(1-\alpha) + \frac{1}{3}\left(\frac{B}{A^2}\right)\log_e^2(1-\alpha) \tag{6.33}$$

The temperature T may be replaced by the average temperature, $\overline{T}$, the concentration term, c by the vector of concentrations $\overline{\mathbf{c}}$, while the ΔH_{pcm} term in the enthalpy balance

of the 2D quasi-homogeneous model (equation 6.2) may be expanded as follows:

$$
\begin{aligned}
&-\epsilon\rho_{\mathrm{f}}C_{\mathrm{p}}\frac{\partial\overline{T}(z,r,t)}{\partial t}+\kappa_{\mathrm{eff,\,r}}\left(\frac{\partial^2\overline{T}(z,r,t)}{\partial r^2}+\frac{1}{r}\frac{\partial\overline{T}(z,r,t)}{\partial r}\right)-\rho_{\mathrm{f}}u_{\mathrm{s}}C_{\mathrm{p}}\frac{\partial\overline{T}(z,r,t)}{\partial z}\\
&+\sum_{i=1}^{N}\nu_{i,j}\,\Re_{i,j}(\overline{\mathbf{c}},\overline{T}(z,r,t))\times\left(-\Delta H_{\mathrm{r},\,i}+(1-\sigma)\int_0^t(m_{\mathrm{pcm}}\,C_{\mathrm{p,\,pcm}}(\overline{T}(z,r,t)))\mathrm{d}\overline{T}(z,r,t)\right)\\
&=0
\end{aligned}
\tag{6.34}
$$

where σ is the catalyst activity coefficient, which turns on/off and moderates the effect of the phase change material at any fractional value lying within the region described by: $0<(1-\sigma)\leq 1$ and the integral term $\int_0^t(m_{\mathrm{pcm}}\,C_{\mathrm{p,\,pcm}}(\overline{T}(z,r,t)))\mathrm{d}\overline{T}(z,r,t)$ represents the heat absorbed by the phase change material over time. The temperature explicit heat capacity of the phase change material is as defined in equation (3.62) in chapter 3.

By putting equation (6.31) into equation (6.34), and applying the radial averaged heat release in equation (6.26), the two dimensional equation reduces to a one dimensional transient enthalpy balance:

$$
\begin{aligned}
\epsilon\rho_{\mathrm{f}}\,C_{\mathrm{p,f}}\frac{\partial\overline{T_{\Re}}(z,t)}{\partial t}+u_z\,\rho_{\mathrm{f}}\,C_{\mathrm{p,f}}\frac{\partial\overline{T_{\Re}}(z,t)}{\partial z}=&-\frac{8\alpha\,\kappa_{\mathrm{eff,\,r}}}{A\,R_{\mathrm{t}}^2}-\sum_{i=1}^{N}\nu_{i,j}\,\Re_{i,j}(\overline{\mathbf{c}}(z,t),\,\overline{T_{\Re}}(z,t))\\
&\times(\Delta H_{\mathrm{r},i}+(1-\sigma)\Delta H_{\mathrm{pcm}})
\end{aligned}
\tag{6.35}
$$

The Fischer-Tropsch reaction comprises several reactions which follow Arrhenius temperature dependence kinetics. Using the averaging rule proposed by Hagan et al [161], the weighted heat release by each reaction is given by:

$$
w_i=\frac{\Re_{i,j}\Delta H_{\mathrm{r},i}}{\sum_{i=1}^{N}\Re_{i,j}\Delta H_{\mathrm{r},i}}
\tag{6.36}
$$

The Taylor's expansion parameters defined in equation (6.25) are given as:

$$
A=\frac{\overline{E_{\mathrm{act}}}}{R_{\mathrm{g}}(\overline{T_{\Re}}(z,t))^2}
\tag{6.37}
$$

The average activation energy of the reactions is given by:

$$
\overline{E_{\mathrm{act}}}=\sum_{i=1}^{N}E_{\mathrm{act}}^{i}\,w_i
\tag{6.38}
$$

where E^i_{act} is the individual activation energy for each reaction i

$$\frac{B}{A^2} = -\frac{R_{\text{g}}\overline{T_{\Re}}(z,t)}{\overline{E_{\text{act}}}} + \frac{1}{2}\sum_{i=1}^{N}\left(\frac{E^i_{\text{act}} - \overline{E_{\text{act}}}}{\overline{E_{\text{act}}}}\right)^2 w_i \tag{6.39}$$

The final form of the transient material and enthalpy balances for the modified α-model thus respectively become:

$$\epsilon\frac{\partial\overline{c_j}}{\partial t} = -u_{\text{z}}\frac{\partial\overline{c_j}}{\partial z} - \sum_{i=1}^{N}\nu_{i,j}\,\Re_i(\overline{\mathbf{c}}(z,t), \overline{T_{\Re}}(z,t)) \tag{6.40}$$

$$\epsilon\rho_{\text{f}}\,C_{\text{p,f}}\frac{\partial\overline{T_{\Re}}(z,t)}{\partial t} + u_z\,\rho_{\text{f}}\,C_{\text{p,f}}\frac{\partial\overline{T_{\Re}}(z,t)}{\partial z} = -\frac{8\alpha\,\kappa_{\text{eff,r}}}{A\,R_{\text{t}}^2} - \sum_{i=1}^{N}\nu_{i,j}\,\Re_{i,j}(\overline{\mathbf{c}}(z,t),\,\overline{T_{\Re}}(z,t)) \times (\Delta H_{\text{r},i} + (1-\sigma)\Delta H_{\text{pcm}}) \tag{6.41}$$

6.4 Reactor performance using α-model

6.4.1 Reactor time response

Figure 6.6 shows an example of how the reactor temperature evolves over the axial bed length with time for $T_{\text{in, cool}}$ without any catalyst dilution. Characteristic of a highly exothermic reaction, with high activation energy in a wall cooled reactor, a maximum temperature occurs near the inlet of the reactor (normalised axial position 0.14 in this case). The amplitude of this maximum temperature is aggravated by small changes to the process/operating parameters e.g. decrease in coolant flow rate, fluctuation in feed concentration, etc. [196]. Such disproportionate temperature increments affect the yield of desired products adversely. On the time scale, it can be seen that the temperature of the reactor ramps up at the start of the reaction and then eventually settles at some steady state temperature. If the dimensionless axial position 0.14 (i.e. the hotspot) is considered as an example, a steady state temperature of about 265.5°C is reached after approximately 718s of reaction.

Figures 6.7a and b show time responses of the maximum reactor temperature to a 5% step increase in the feed H_2 concentration at different values of coolant temperatures. Figure 6.7a depicts how the reactor responds without any catalyst dilution. In the main, there is a monotonic and rapid rise in the temperature of the reacting system for all of the coolant temperature scenarios. The system temperature eventually attains steady state after about 718s. As may be appreciated from the series of plots, the "new" maximum

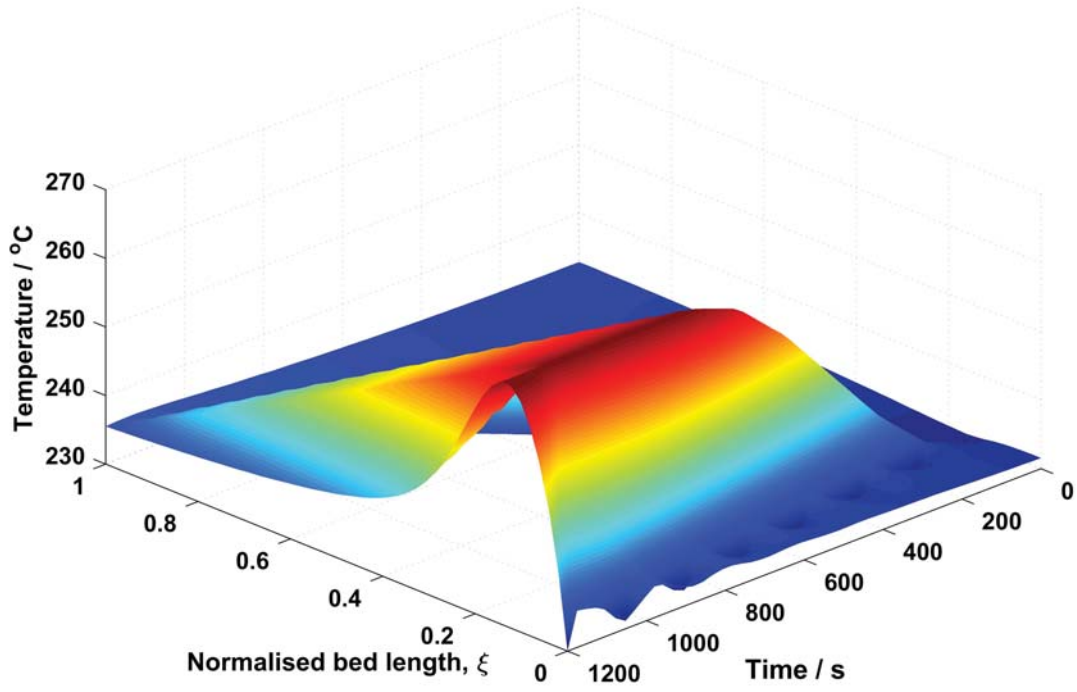

FIGURE 6.6: Evolution of reactor temperature profile along the normalised axial bed length as a function of time for $T_{\text{in, cool}} = 230^{\text{o}}\text{C}$

TABLE 6.1: Modified residence time for various inlet/cooling temperatures

Inlet/coolant temperature, $T_{\text{in, cool}}(^{\text{o}}\text{C})$	**Volumetric flow rate, at STP** $V_{\text{f}}(\text{m}^3\,\text{s}^{-1})$	**Modified residence time,** $\tau = \dfrac{m_{\text{cat}}}{V_{\text{f}}}$ $(\text{kg}\,\text{s}\,\text{m}^{-3})$
224	0.01190	1328
230	001175	1344
235	0.01164	1358
245	0.01141	1384

steady state temperatures reached by the reactor increases with the coolant temperature. This is because the modified residence time of the reactants, $\left(\tau = \dfrac{m_{\text{cat}}}{V_{\text{f, STP}}}\right)$ increases with increasing coolant temperature as depicted in Table 6.1.

Figure 6.7b which features a 40% by weight phase change material dilution of the catalyst bed, presents the same monotonic, rapid temperature rise, although the increments are a lot less aggressive. For instance, the steady state temperature attained at $T_{\text{in, cool}}$= 230°C in Figure 6.7a is about 274.3°C, compared to 246.7°C in Figure 6.7b. This clearly demonstrates how the phase change material adds thermal mass to the system and potentially reins in temperature excursions. If the safe catalyst temperature threshold of 260°C [93] is imposed as an operational constraint, it becomes clear that the arrangement

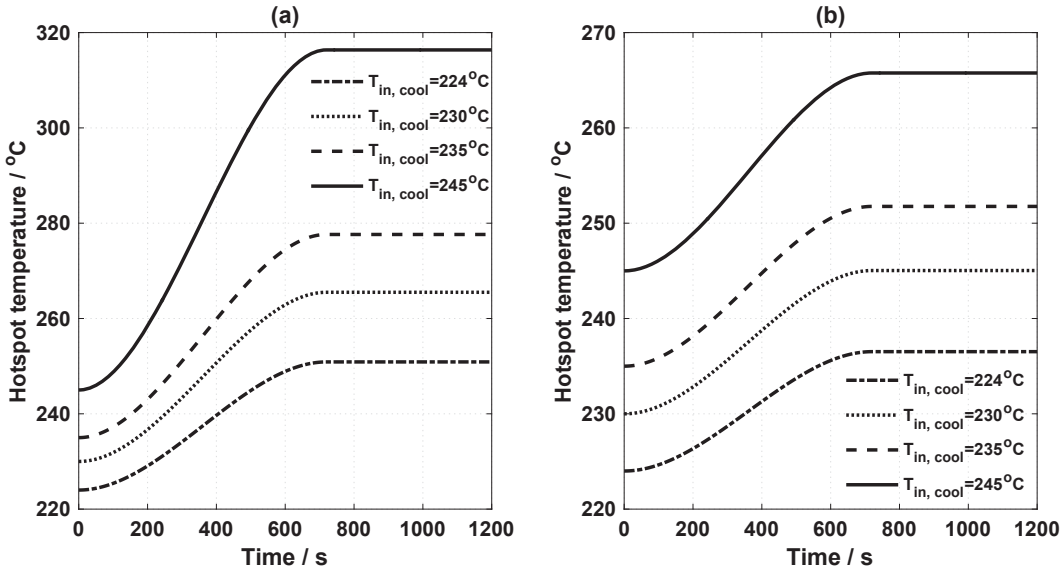

FIGURE 6.7: Reactor response to a 5% step increase in reactant (H_2) concentration: (a) Hotspot response at various coolant temperatures without phase change material (b)Hotspot response at various coolant temperatures with phase change material (40% by weight)

in Figure 6.7b provides for more flexibility in terms of the available coolant temperature range for process operation, without suffering runaway or catalyst destruction. From Figure 6.7a, the reaction (without catalyst dilution) will have to be restricted to $T_{\text{in, cool}}$ = 224°C in order to prevent the catalyst from sintering. It is interesting to note that even when the coolant temperature is greater than the melting temperature of the phase change material e.g. at $T_{\text{in, cool}}$ = 235°C, the phase change material is still able to control the temperature rise in the reactor.

6.4.2 Reactor productivity

Figure 6.8a–d depict the productivities of methane and C_{5+} at t = 7200s. Figure 6.8a and c respectively show the methane and C_{5+} productivities without phase change material dilution. As may be seen from Figure 6.8a, the CH_4 production increases in a monotonic fashion with increasing coolant temperatures. In the case of $T_{\text{in, cool}}$ =245°C, the CH_4 production seems to exhibit a local peak at axial position of 0.25 and subsequently through a point of inflection at position 0.3 before resuming the sharp rise observed in the previous curves. Figure 6.8c portrays a rather interesting phenomenon. There is an initial sharp rise consistent with CH_4 productivity, however, upon increasing $T_{\text{in, cool}}$ beyond 224°C, the C_{5+} production begins to decline such that the C_{5+} productivity at a given coolant temperature falls below that recorded at the coolant temperature value immediately preceding it. For example, in the cases of $T_{\text{in, cool}}$ = 224°C, 230°C and 235°C, the productivity curves seem to converge at about the 0.8 reactor axial

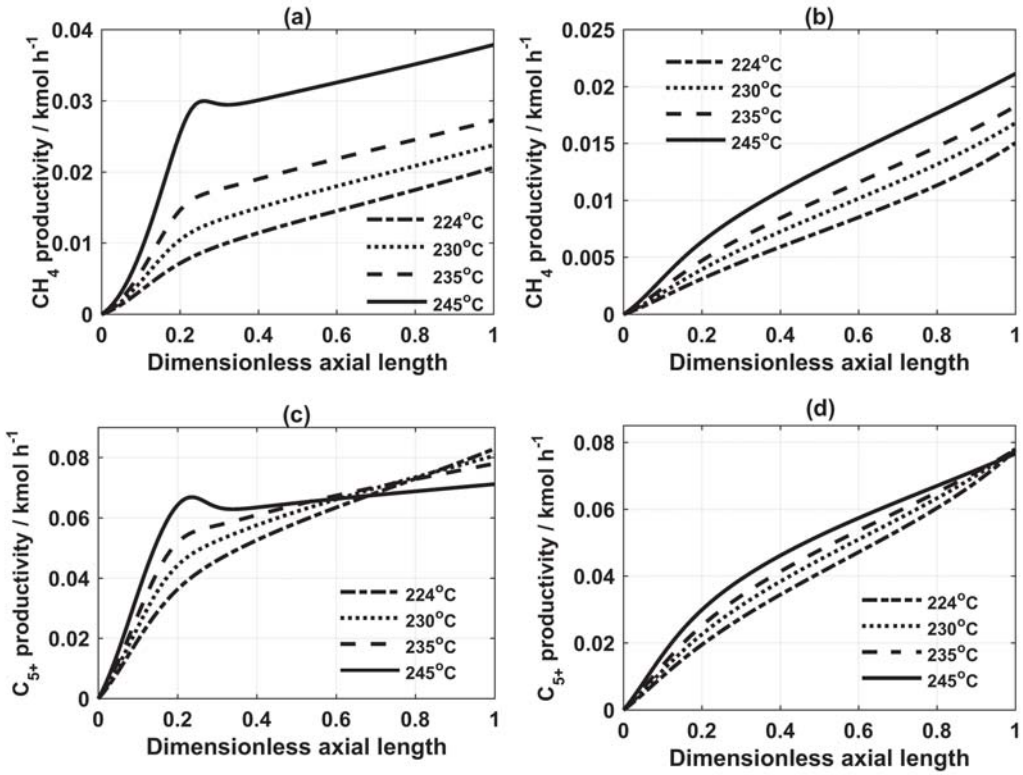

FIGURE 6.8: Reactor response to a 5% step increase in reactant (H_2) concentration: (a) Methane productivity at various coolant temperatures without phase change material at $t = 7200s$ (b) Methane productivity at various coolant temperatures with phase change material (40% by weight)at $t = 7200s$ (c) C_{5+} productivity at various coolant temperatures without phase change material at $t = 7200s$ (d) C_{5+} productivity at various coolant temperatures with phase change material (40% by weight)at $t = 7200s$

position, after which they emerge and diverge with 3.8% reduction in C_{5+} (at $T_{\text{in, cool}} = 230^{\circ}C$) and 7.1% reduction in C_{5+} (at $T_{\text{in, cool}} = 235^{\circ}C$) compared to the productivity at 224°C in both cases. Similar to the methane productivity, the C_{5+} (at $T_{\text{in, cool}} = 245^{\circ}C$) exhibits a local peak at position 0.25 and an inflection point at position 0.3, however unlike in the case of CH_4 (Figure 6.8a), the productivity starts to fall at a rate faster than those exhibited by the previous curves at about halfway through the reactor and beyond. Ultimately, there is a 15.5% reduction in C_{5+} production compared to that recorded at 224°C.

The aforementioned phenomena may be explained by the exponential increase in temperature with reaction. According to Chernobaev et al [187] and Depoorter et al [197], the increased temperature brings about the carbidization of the catalyst surface which in turn results in: (I) a reduced disproportionation of CO, (II) a decreased extent of hydrogenation and (III) the cracking (i.e. decomposition) of long chain hydrocarbons (C_{5+}) to form simpler molecules. The overall effect is a change in the selectivity of the

catalyst for short chain molecules regardless of the high reactant conversion that may be recorded at high temperatures. Thus at 245°C, for example, there is less C_{5+} produced overall and some of that which is produced is decomposed into methane as the reactor temperature increases, hence the dipping of the C_{5+} curve for $T_{\text{in, cool}}$=245°C in Figure 6.8c matched by the ascent of the corresponding CH_4 curve in Figure 6.8a.

Figures 6.8b and 6.8d show the influence of the phase change material dilution. Although there is still an exponential rate of production of CH_4 (Figure 6.8b) in comparison to Figure 6.8a, there is up to a 28.6% reduction in CH4 productivity at $T_{\text{in, cool}}$= 224°C. In Figure 6.8d, the productivity values converge to about the same value at the exit of the reaction. Although there is a 7% decrease in the overall C_{5+} produced with the influence of the phase change material at $T_{\text{in, cool}}$= 224°C compared with no phase change material effect, this is far outweighed by a corresponding four-fold reduction in methane production at the same coolant temperature.

6.4.3 Summary

In summary, this chapter has considered the so-called α reactor model of Hagan et al [161] against the more rigorous 2D quasi-homogeneous model for predicting the reactor performance in the context of the Fischer-Tropsch reaction. The α-model was re-cast to cater for the heat sink effect of phase change diluent within the reactor. The various tests the modified α-model was subjected to, revealed its superiority to the conventional one dimensional model while approximating the 2D model with considerably less computational effort and satisfactory accuracy. This modified, simpler model provides a handy tool to be used in the optimisation exercise carried out in the next chapter.

Chapter 7

Optimal distribution of phase change material diluents and active catalyst in a fixed bed Fischer-Tropsch reactor

"It isn't that they can't see the solution. It is that they can't see the problem."

G.K. Chesterton, (1874-1936).

Hitherto, only one arrangement has been considered in the reactor, namely: a flat catalyst activity profile involving the homogeneous mixing of the active catalyst pellets and encapsulated phase change material. As seen in previous chapters, although this arrangement had the effect of controlling the reactor temperature, the temperature restriction also had the effect of reducing the productivity of both the long chain hydrocarbons as well as methane. In this chapter, the graded or zoned reactor bed technique in the axial direction is examined and adopted. The idea behind this arrangement is to simultaneously improve the reactor performance while balancing the reactor heat generation and heat rejection by optimally distributing the encapsulated phase change material and active catalyst within the reactor.

The outline for this chapter is as follows: section 7.1 presents a background into graded catalyst dilution and the choice of phase change material as the diluent, section 7.2 looks at the mathematical formulation and governing equations based on the modified

α-model including the formulation of the optimisation problem. Section 7.3 looks at the numerical implementation of the optimisation problem, while section 7.4 presents the results and discussion.

7.1 Background into graded zone catalyst dilution

Graded catalytic beds could help improve the performance of a fixed bed reactor in terms of key performance indices such as productivity, selectivity and conversion [198]. The technique entails the use of non-uniform catalyst distribution, which have been diluted with some inert material e.g. silicon dioxide, silicon carbide, etc. in different compositions. Two perceived benefits of this arrangement are:

(i) The average temperature of the catalytic bed may be raised efficiently owing to the carefully engineered non-uniform catalyst mass fraction distribution profile, whilst the hotspot temperature is simultaneously kept within the stable and catalyst actively selective region [198].

(ii) Improved reactor controllability under constrained cooling capacities [19]. It will be recalled that while the reaction, and by extension the heat it generates, scales up volumetrically, the heat removal scales up superficially; this catalyst dilution strategy therefore brings about improved control by delaying any significant temperature rise.

Figure 7.1 shows a schematic of a graded fixed bed reactor with four catalytic zones. As may be observed, the feed enters at the top of the reactor while the products are collected at the bottom of the reactor. The degree to which each graded catalytic zone is diluted is indicated by the catalyst mass fraction, σ_q, where $q \in \{1, 2, 3, 4, ..., q_n\}$ is an index representing the catalytic zone(s) of interest. The variation of σ_q along the reactor axial length is also shown in Figure 7.1. This chapter focuses on the determination of the optimal distribution of the catalyst activity along the reactor axial length which maximises the productivity of long chain hydrocarbon molecules, whilst controlling temperature rise, subject to pre-specified reactor condition constraints. In particular, the inert diluent will be the encapsulated phase change material (metallic tin).

A number of authors have adopted mathematical optimisation methods in chemical reactor designs and packed bed reactors with non-uniform catalyst distributions. Hillestad [199, 200] put forward conceptual analytical and numerical [201] solutions to optimal control problems. The attainable region concept, a geometric approach, was examined by Glasser et al [202], Hildebrandt et al [203] and Feinberg et al [204, 205]. Lee et al [206]

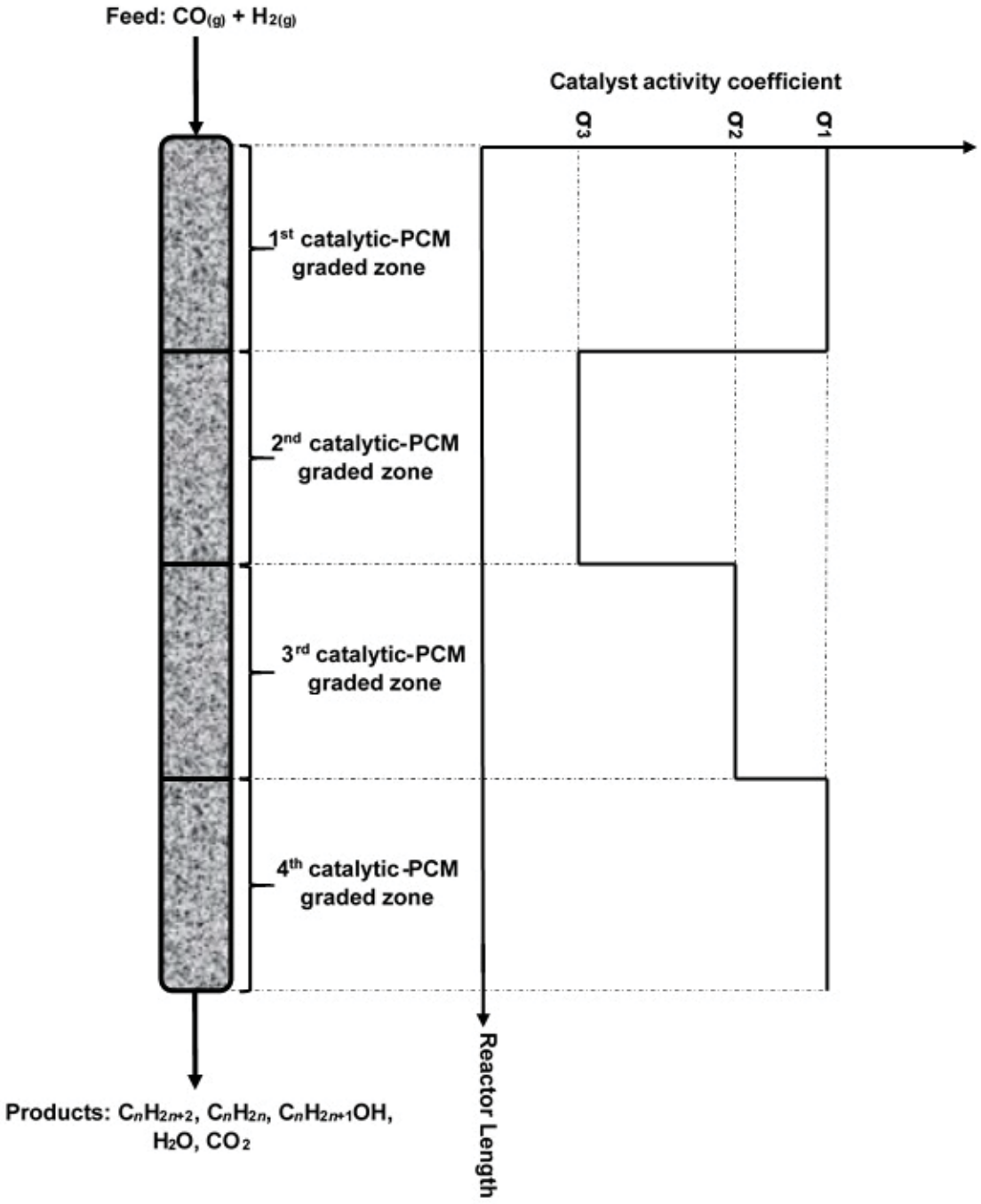

FIGURE 7.1: Schematic of graded zone catalytic reactor (not to scale).

proposed a dual zone mathematical model, formulated by applying Dirac-δ functions at catalytic zone breaks in an isothermal reactor. They went on to conclude from both their model and experimental validations, that the overall reactor conversion could be enhanced with appropriate sequential arrangement of different catalytic materials. Melis et al [207] considered the complex problem of obtaining optimal distribution profiles for inter-dependent homogeneous and heterogeneous reactions. Khanaev et al [199, 208] recast the optimal catalyst distribution problem as a variational one, thus facilitating the determination of continuous distribution profiles for different economic objective functions from analytical solutions. Hwang et al [209–211] considered non-uniform catalysts by which a zoned reactor bed can be implemented with different types of layered catalysts. The recurring theme in the previously outlined works is that they have either assumed isothermal or adiabatic conditions. Both assumptions are largely unrepresentative of strongly exothermic, non-isothermal reactions, which are usually operated near thermal runaway conditions in fixed bed reactors [126].

In contrast to the previous arrangement of homogeneously distributed, encapsulated phase change material in the FT catalyst bed adopted in chapters 5 and 6, this work examines an optimal arrangement of the catalyst and encapsulated phase change material through the use of a graded zoned reactor under non-isothermal conditions. The phase change material brings with it the added advantage of its latent enthalpy of fusion, acting as a temperature buffer and delaying any significant temperature rise in the reactor in the course of the reaction. The optimisation problem is formulated by setting the objective function to maximise the C_{5+} product yield. The constraints consist of pre-specified requirements (usually in inequality form) of the carbon monoxide conversion, C_{5+} product selectivity and a set of differential and non-linear algebraic equations from the reactor model. The modified α-model presented in section 6.3 will be used in the optimisation exercise. This problem formulation is the subject of the next section.

7.2 Mathematical formulation and governing equations

The transient form of the modified α-model material and enthalpy balances are as follows (with the usual definitions of the terms):

$$\epsilon \frac{\partial \overline{c_j}}{\partial t} = -u_z \frac{\partial \overline{c_j}}{\partial z} - \sum_{i=1}^{N} \nu_{i,j}\, \Re_i(\overline{\mathbf{c}}(z,t), \overline{T_{\Re}}(z,t)) \tag{7.1}$$

$$\epsilon\rho_{\mathrm{f}}\, C_{\mathrm{p,f}}\frac{\partial\overline{T_{\Re}}(z,t)}{\partial t} + u_z\,\rho_{\mathrm{f}}\, C_{\mathrm{p,f}}\frac{\partial\overline{T_{\Re}}(z,t)}{\partial z} = -\frac{8\alpha\,\kappa_{\mathrm{eff,r}}}{A\,R_{\mathrm{t}}^2} - \sum_{i=1}^{N}\nu_{i,j}\,\Re_{i,j}(\overline{\mathbf{c}}(z,t),\,\overline{T_{\Re}}(z,t)) \times (\Delta H_{\mathrm{r},i} + (1-\sigma)\Delta H_{\mathrm{pcm}}) \tag{7.2}$$

where, α is implicitly obtained from the following expression:

$$A \times (\overline{T_{\Re}}(z,t) - T_{\mathrm{in,\,cool}}) = \frac{4\alpha}{Bi} - \log_e(1-\alpha) + \frac{1}{3}\left(\frac{B}{A^2}\right)\log_e^2(1-\alpha) \tag{7.3}$$

A and B are the Taylor's expansion parameters as defined respectively in equations (6.37 and 6.39) of chapter 6.

The pressure balance is approximated using the Ergun equation [162]

$$-\frac{\partial p}{\partial z} = \frac{1-\epsilon}{\epsilon^3}\left(1.75 + 4.2\,Re_{\mathrm{p}}^{\frac{5}{6}}\,\frac{1-\epsilon}{Re_{\mathrm{p}}}\right)\frac{\rho_{\mathrm{f}}\,u_{\mathrm{z}}^2}{d_{\mathrm{p}}} \tag{7.4}$$

The three principal reaction schemes considered in the optimisation formulation are the main Fischer-Tropsch synthesis, methanation and water gas shift reactions; the respective equations of reaction are as follows:

$$\mathrm{CO} + 2\,\mathrm{H_2} \longrightarrow (-\mathrm{CH_2}-) + \mathrm{H_2O} \qquad \Delta H_{298}^{\theta} = -152\,\mathrm{kJ\,mol^{-1}} \tag{7.5}$$

$$\mathrm{CO} + 3\,\mathrm{H_2} \longrightarrow \mathrm{CH_4} + \mathrm{H_2O} \qquad \Delta H_{298}^{\theta} = -206\,\mathrm{kJ\,mol^{-1}} \tag{7.6}$$

$$\mathrm{CO} + \mathrm{H_2O} \longrightarrow \mathrm{CO_2} + \mathrm{H_2} \qquad \Delta H_{298}^{\theta} = -41\,\mathrm{kJ\,mol^{-1}} \tag{7.7}$$

The reaction rate equations re-expressed in terms of the α-model reaction averaged temperature ($\overline{T_{\Re}}(z,t)$) and the catalyst activity coefficient, σ are as shown in equations (7.8-7.10):

$$\Re_{\mathrm{FT}} = \rho_{\mathrm{b}}\,\sigma\frac{5.1\exp\left(\dfrac{-52000}{R_{\mathrm{g}}\overline{T_{\Re}}(z,t)}\right)}{\left(1+1.6\dfrac{c_{\mathrm{H_2O_g}}}{c_{\mathrm{CO_g}}}\right)}c_{\mathrm{H_{2,g}}} \tag{7.8}$$

$$\Re_{\mathrm{M}} = 27.3\,\rho_{\mathrm{b}}\,\sigma\,\exp\left(\frac{-70000}{R_{\mathrm{g}}\overline{T_{\Re}}(z,t)}\right)\,c_{\mathrm{H_{2,g}}} \tag{7.9}$$

$$\Re_{\mathrm{WGS}} = \rho_{\mathrm{b}}\,\sigma\frac{10^3\times k_{\mathrm{v}}(R_{\mathrm{g}}\overline{T_{\Re}}(z,t))^{\frac{3}{2}}\left(\dfrac{c_{\mathrm{CO}}\,c_{\mathrm{H_2O}}}{c_{\mathrm{H_2}}^{\frac{1}{2}}} - \dfrac{1}{K_{\mathrm{ewg}}}\,c_{\mathrm{CO_2}}\,c_{\mathrm{H_2}}^{\frac{1}{2}}\right)}{\left(1+K_{\mathrm{v}}(R_{\mathrm{g}}\overline{T_{\Re}}(z,t))^{\frac{1}{2}}\,\dfrac{c_{\mathrm{H_2O}}}{c_{\mathrm{H_2}}^{\frac{1}{2}}}\right)^2} \tag{7.10}$$

The water gas shift equilibrium constant, K_{ewg} is given by the expression of Lox et al [54]:

$$\exp\left(\frac{5078.0045}{\overline{T_{\Re}}(z,t)} - 5.8972089 + 13.958689\times10^{-4}\overline{T_{\Re}}(z,t) - 27.592844\times10^{-8}\left(\overline{T_{\Re}}(z,t)\right)^2\right) \tag{7.11}$$

The respective rate laws of the constituent chemical species, obtained from the reaction stoichiometry are as follows:

$$\Re_{\text{H}_2} = -\Re_{\text{FT}} - 3\Re_{\text{M}} + \Re_{\text{WGS}} \tag{7.12}$$

$$\Re_{\text{CO}} = -\Re_{\text{FT}} - \Re_{\text{M}} - \Re_{\text{WGS}} \tag{7.13}$$

$$\Re_{\text{CH}_4} = \Re_{\text{M}} \tag{7.14}$$

$$\Re_{\text{C}_{\text{cn}}\text{H}_{2\text{cn}+2}} = x_{(cn>2)} \times N_{\text{tot}} \times V_{\text{react}} \times \frac{1}{(1+\gamma_{\text{FT}})} \tag{7.15}$$

$$\Re_{\text{C}_{\text{cn}}\text{H}_{2\text{cn}}} = x_{(cn>2)} \times N_{\text{tot}} \times V_{\text{react}} \times \frac{\gamma_{\text{FT}}}{(1+\gamma_{\text{FT}})} \tag{7.16}$$

$$\Re_{\text{H}_2\text{O}} = \Re_{\text{FT}} + \Re_{\text{M}} - \Re_{\text{WGS}} \tag{7.17}$$

$$\Re_{\text{CO}_2} = \Re_{\text{WGS}} \tag{7.18}$$

where, cn is the number of carbon atoms in the hydrocarbon in question, α_{FT} is the constant carbon chain growth probability factor and γ_{FT} is the olefin to paraffin ratio,

The total number of moles of hydrocarbon (N_{tot}) produced per unit time as reported by Panahi et al [168] is given by:

$$N_{\text{tot}} = \frac{\left(\dfrac{-\Re_{\text{FT}} - \Re_{\text{M}} - \Re_{\text{WGS}}}{MW_{\text{CO}}} + \dfrac{\Re_{\text{WGS}}}{MW_{\text{CO}_2}}\right)V_{\text{react}}}{\dfrac{x_{(cn=1)}}{MW_{\text{CH}_4}} + \displaystyle\sum_{cn=2}^{cn} cn \times x_{cn} \times \left(\frac{1}{(1+\gamma_{\text{FT}})}.\frac{1}{MW_{\text{C}_{\text{cn}}\text{H}_{2\text{cn}+2}}} + \frac{\gamma_{\text{FT}}}{(1+\gamma_{\text{FT}})}.\frac{1}{MW_{\text{C}_{\text{cn}}\text{H}_{2\text{cn}}}}\right)} \tag{7.19}$$

The catalyst mass fraction, σ, varies along the catalyst bed between values of 0 and 1. This mass fraction varies over the bed length as a piece-wise, constant function and will be the chief control variable for the optimisation problem. The manipulated variables used in obtaining the optimum catalyst distribution include the inlet/coolant temperature, $T_{\text{in, cool}}$ and the feed factor multiplier (β_{f}), for controlling the inlet feed flow rate; the feed composition remains the same at all times. The optimisation constraints are the pre-specified conditions which the product must meet, as defined by the C_{5+} selectivity and overall conversion of CO (the limiting reactant) and the constraints from the reactor

model as a whole (i.e. all the foregoing equations outlined). On this basis, it is now possible to proceed to set up the multi-period, non-linear-programming (NLP) optimisation problem statement. The objective function (Φ_{obj}) is to maximise the productivity i.e. the C_{5+} production per unit time per tube:

$$\begin{aligned} \underset{C_{5+}}{\text{Maximise:}} \quad & \{\Phi_{\text{obj}} = c^{\text{out}}_{C_{5+}}\, u_z\, A_c\} \\ \text{subject to:} \quad & S_{C_{5+}} = \frac{c^{\text{in}}_{C_{5+}}}{c^{\text{in}}_{CO} - c^{\text{out}}_{CO}} \geq 78\% \\ & X_{CO} = \frac{c^{\text{in}}_{CO} - c^{\text{out}}_{CO}}{c^{\text{in}}_{CO}} \geq 32\% \\ & \text{model equations } (7.1 - 7.19) \end{aligned} \tag{7.20}$$

where A_c is the tube cross sectional area. Both the C_{5+} selectivity ($S_{C_{5+}}$) and CO conversion per pass (X_{CO}) are end point constraints which are only applicable at the exit point of the reactor. The conversion per pass of CO which is specified as 32% corresponds to almost complete conversion at a recycle ratio of 2. Typically, graded packed bed reactors used in industry are designed with only a few catalytic zones of different but constant relative activity levels as opposed to a continuously varying activity profile [126, 127]. Therefore, a multi-zone optimisation formulation approach will be adopted by dividing the reaction bed into $N \geq 1.0$ catalytic zones. It is also pertinent to note that while the boundaries of the graded bed zones may change, the continuity of reactor temperature and molar flow rates are facilitated at the break points through the piecewise, continuous and constant nature of the activity coefficient σ.

7.3 Implementation of optimisation problem

The continuous, non-linear programming optimisation problem and its constraints, comprising differential and non-linear algebraic equations, were treated as a simultaneous optimal control problem based on the work of Cuthrell et al [212]. In other words, the principal decision variable (σ_q in this case) was represented by an approximate function, specifically, a piecewise, constant parameterisation- as shown schematically in Figure 7.1. In this method, the differential algebraic equations (DAEs) are automatically embedded into the non-linear programming problem after discretisation, as opposed to the sequential approach where the DAEs are treated as an extrinsic black box, requiring external numerical integration packages for the optimisation searches. According to Nie et al [126], the latter method is heavily dependent upon repeated integration of DAEs, thus rendering the optimisation task prone to failure for unstable systems in which the integrators fail to converge.

The optimisation problem was implemented and solved via the optimisation module of the finite element method package, COMSOL Multi-physics 4.4 [21], using the gradient based Sparse Non-Linear Optimiser (SNOPT), on a desktop with Intel Core i7, CPU 2.5GHz, Quad-core and 16GB RAM. The influence of finer zoning was explored by considering $N \in \{1, 2, 3, 4, 5\}$ zones. The mass and enthalpy balances were space-discretised by the backward finite differential (BFD) method. SNOPT handles general optimisation problems with many and/or difficult constraints and by default uses the adjoint method to simultaneously compute all analytic derivatives for the problem in question. The underlying algorithm of the SNOPT method [213, 214] is the implementation of sequential quadratic programming (SQP), i.e. the objective function is approximated by a quadratic polynomial and the constraints treated as linear; steps in this sequence are referred to as the "outer" iterations. Each approximate quadratic programming (QP) problem is equally solved iteratively (requiring inner iterations). The QP solver communicates a step direction to the outer SQP algorithm, which in turn determines the step length and updates the QP approximation before going on to the next outer iteration [215]. The optimality tolerance was set at 1×10^{-6}; oscillatory behaviour of the numerical optimisation task was prevented by avoiding a high resolution discretisation of the control/manipulated variables.

The modified α- model required the implicit solution of α at each discretisation point, z_n along the axial length of the reactor, z. One iterative Newton step was found to be sufficient for updating α based on its previous value. In the diluted catalyst zones, the phase change material energy balance also had to be solved at each discretised node. The sudden "jump" in the physical properties of the phase change material during phase transition often results in numerical discontinuities and non-convergence of the solver. This was overcome through the use of the in-built smoothed Heaviside function with continuous second order derivative. The initial guesses for the optimisation problem in all cases were as follows: feed factor, $\beta_{\mathrm{f}} = 2.0$, inlet/coolant temperature, $T_{\mathrm{in,\,cool}} = 230^{\mathrm{o}}\mathrm{C}$, while the multiple zones were initialised as having equal lengths of equal catalytic activity coefficient $\sigma = 0.6$. Mesh and convergence tests were carried out in the same manner as described in chapter 4.

7.4 Results and discussion

The model was validated by comparing the results of the modified reactor model to that reported by Jess and Kern [5] for the uniform reactor catalyst scenario. Figure 7.2a shows the effect of increasing the coolant temperature, i.e. the exacerbation of the amplitude of the hotspot. Figure 7.2b compares the predicted maximum temperatures

using the modified α reactor model with the results of Jess and Kern [5] and shows that they both agree within 1.5%. Figure 7.2c shows an average 4.8% error between the

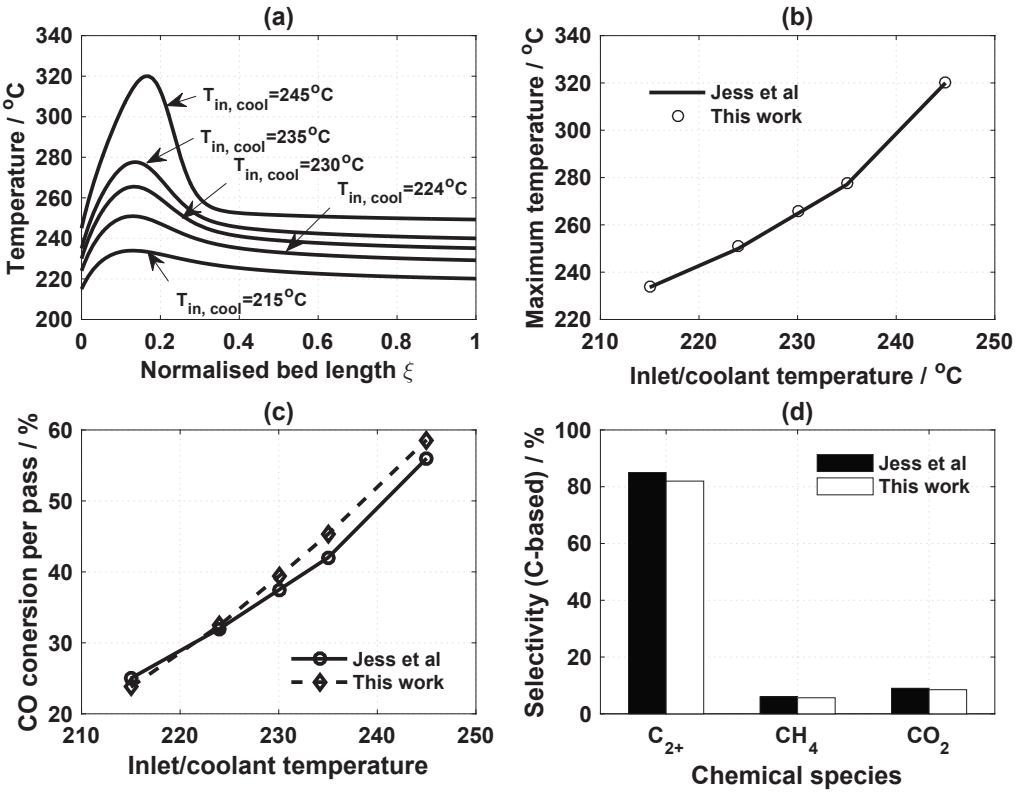

FIGURE 7.2: Model validation (a) Influence of cooling temperature on axial temperature profile using the modified model (b) Reactor maximum temperature at various cooling temperatures- a comparison between 2D model by Jess et al [5] and modified α-model (c) Comparison of percentage conversion per pass of CO between 2D model by Jess et al [5] and modified model at 224°C (d) Comparison of percentage, carbon-based selectivity between 2D model by Jess et al [5] and modified model at 224°C.

two sets of conversion per pass data at $T_{\text{in, cool}}$= 224°C. Figure 7.2d indicates that the literature and predicted values of the carbon based selectivities of the chemical species at $T_{\text{in, cool}}$= 224°C agreed within 5%. The minimal deviation of the results of the modified reactor model from those obtained from literature provided the confidence and basis to explore other optimal catalyst-diluent arrangements in the reactor.

Table 7.1 summarises the results from the optimisation study. It can be seen that the productivity of the C_{5+} increases as the hotspot temperature, T_{max}, is systematically brought under control through an efficient combination of increasing the number of phase change material-diluted catalytic zones, slightly elevating the cooling/inlet temperature and increasing feed flow rate. The increase in productivity tailed off after three catalytic zones.

TABLE 7.1: Optimization results for the different numbers of catalytic zones

Number of zones, N	$\mathbf{C_{5+}}$ **productivity** ($\mathrm{kmol\,h^{-1}\,tube^{-1}}$)	**Feed factor,** β_f	$T_{in,cool}$(°C)	**Maximum temperature,** T_{max} (°C)
1	0.08247	1.85	230.01	265.51
2	0.09580	2.02	231.05	248.76
3	0.09841	2.16	231.2	249.98
4	0.09888	2.19	231.4	250.60
5	0.09890	2.20	231.63	250.71

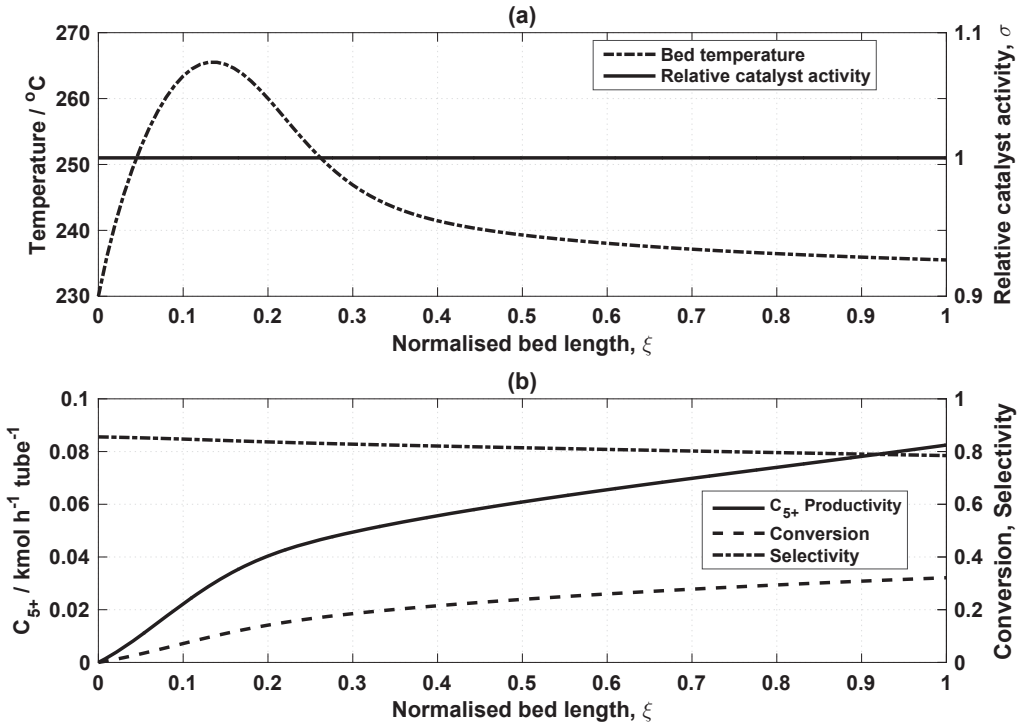

FIGURE 7.3: Optimal profile for uniform ($N = 1$) catalyst distribution.

Figure 7.3a-b is the reference case for a flat catalyst activity profile that contains no phase change material diluent, i.e. $\sigma = N = 1.0$. Specifically, Figure 7.3a is the typical temperature profile over the dimensionless bed length for a high activation energy, exothermic reaction taking place in a wall cooled reactor. The characteristic single hotspot temperature, circa 266°C in this case, occurs near the reactor inlet. Figure 7.3b depicts the objective function, C_{5+} productivity, and the additional process constraints: C_{5+} selectivity and CO conversion over the dimensionless bed length.

Figure 7.4a-b portrays the effect of using a catalytic bed with two activity zones. In Figure 7.4a, the first part of the bed has an optimised catalyst activity of about 0.7 and a uniform catalyst activity of 1.0 in the second part. This arrangement results in a 16% increase in the C_{5+} productivity when Figures 7.3b and 7.4b are compared, (see

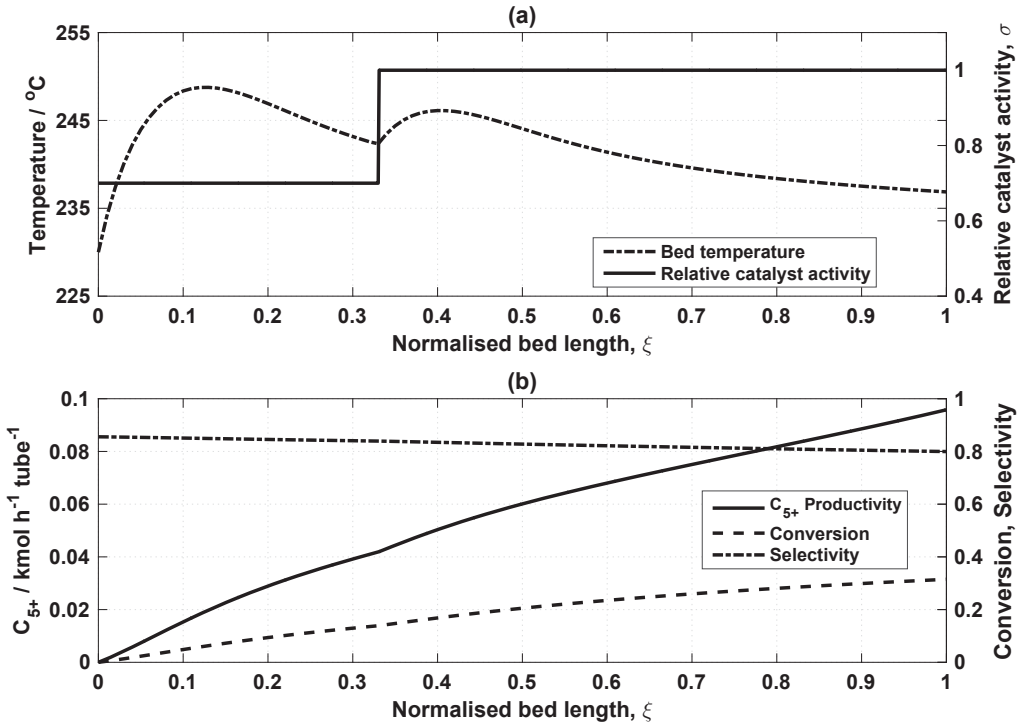

FIGURE 7.4: Optimal profile$N = 2$ catalyst distribution.

summary in Table 7.1). The presence of the phase change material in the first part of the zoned bed ensures that part of the reaction heat generated near the reactor inlet is absorbed, thus resulting in a lower maximum temperature of about 249°C, which is about 17°C lower than that observed in Figure 7.3a. It follows therefore, that diluting the catalyst in this fashion momentarily reduces but does not extinguish the "reaction momentum." This arrangement pushes the reaction front further into the catalytic bed, thus ensuring a more economical use of the bed as well as the "re-ignition" of the reaction when the reactants reach the second part of the bed characterised by $\sigma = 1.0$. This catalyst-diluent distribution is responsible for the double-humped profile observed in Figure 7.4a. The productivity curve in Figure 7.4b also shows a steady increase along the bed with a slight kink occurring at the catalytic bed zone boundary.

Figure 7.5a-b depicts the optimised three-zone catalytic bed. In Figure 7.5a, the first of the three zones of the graded reaction bed features the maximum activity, $\sigma = 1.0$ over a minimal normalised bed length $\xi = 0.032$. The effect of this is that the reactor temperature is ramped up very quickly to a controlled maximum temperature, but because of the combination of the short length of this zone and the lower activity of the second catalytic zone, $\sigma = 0.7$, there is a resultant attenuation of the reaction rate and thermal runaway is prevented at the reactor inlet. The third activity zone again features the maximum activity coefficient which provides any remnant reactant with the

opportunity to be converted to products. A further 3% increase in the C_{5+} productivity is observed when Figure 7.5b is compared with Figure 7.4b, thus underpinning the effectiveness of this strategy. Figures 7.6a-b respectively show the optimised temperature

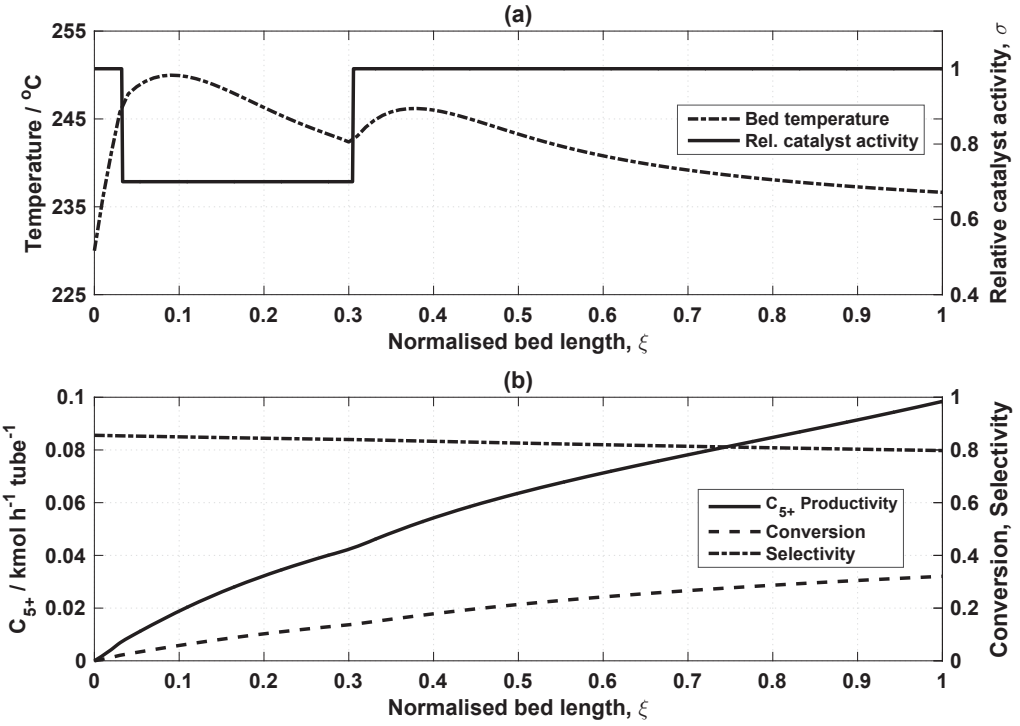

FIGURE 7.5: Optimal profile$N = 3$ catalyst distribution.

and catalytic activity coefficient profiles for the other multi-zone case studies, $N = 4$ and $N = 5$. The same approach as in $N = 3$ is adopted where the maximum catalyst activity with minimal grade length is used in the first part of the reactor. Subsequent, intermediate diluted catalytic zones seemed to form a continuous curve but had little effect on the C_{5+} productivity. As summarised in Table 7.1, there is no significant increase in the C_{5+} productivity with increasing number of the catalytic zones. It therefore shows that an optimised three-zone reactor suffices for maximising the C_{5+} productivity, while minimising the value of the hotspot temperature.

Figure 7.7 is a summary of the optimised C_{5+} productivity and the maximum reactor temperature as functions of the number of diluted catalytic zones. As shown in the graph, the hot spot temperature is reduced by up to 17°C and the enhancing effect of the graded bed on productivity becomes less apparent beyond the three zone scenario.

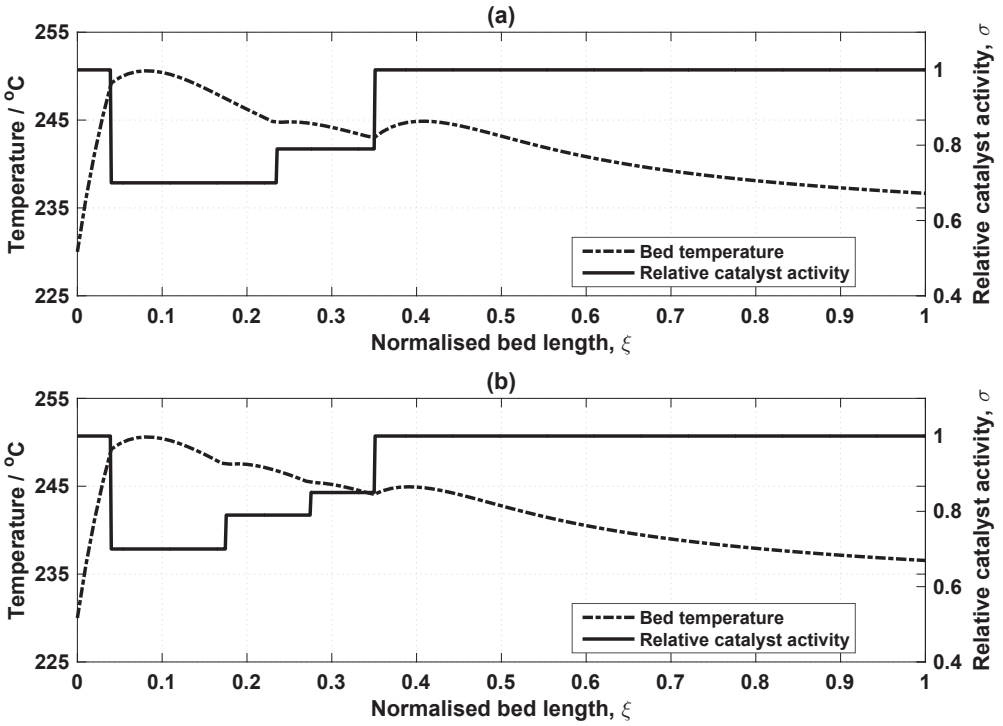

FIGURE 7.6: Optimal profile: (a) $N = 4$ catalyst distribution and (b) $N = 5$ catalyst distribution

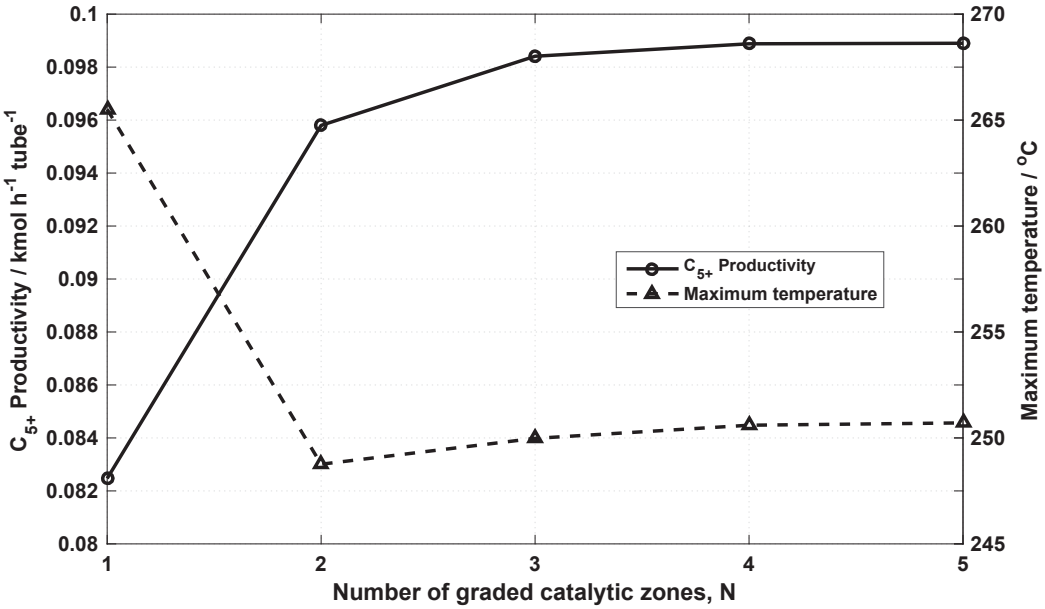

FIGURE 7.7: Optimal productivity and maximum temperature as functions of graded zone numbers

7.5 Summary

The modified α-model approximated the more rigorous, computationally expensive and accurate 2D quasi-homogeneous model within acceptable error limits. The combined accuracy and less expensive computational requirements of the modified α-model made it a suitable candidate for the reactor optimisation problem in hand.

The concept of diluting a catalytic bed using encapsulated phase change material in carefully optimised zones was also presented. The latent enthalpy of fusion of the phase change material was exploited by homogeneously mixing them with promoted catalysts in optimised graded zones. A 16% increase in the desired C_{5+} productivity was observed in the two-zone reactor compared to the uniform catalyst arrangement with no phase change material dilution. A further 3% increase in the C_{5+} productivity was observed with a three zone arrangement. Beyond this, there was a minimal increment in the productivity as the number of zones was increased.

A well balanced combination of promoted catalysts, optimally diluted with encapsulated phase change material in a graded, catalytic-zone, fixed bed reactor could help:

(I) increase productivity of long chained hydrocarbon molecules and

(II) simultaneously control the temperature rise in the Fischer-Tropsch reactor.

The latent enthalpy of the metallic phase change material combined with its good thermal conductivity could possibly push the limits of the catalyst bed by increasing the conversion per pass beyond the typical 32% reported in literature, with less likelihood of either early catalyst deactivation or thermal unreliability of the reacting system. It does this by delaying any significant temperature rise in the catalyst bed owing to its large thermal capacity and at the same time facilitates heat conduction out of the reaction bed as a result of its good thermal conductivity.

Chapter 8

Conclusion and future work

"Life can only be understood backwards; but it must be lived forwards."

Søren Kierkegaard, (1813-1855).

This chapter presents the conclusions of this thesis and puts forward recommendations for possible future work.

8.1 Concluding remarks

The Fischer-Tropsch synthesis technology, despite nearly one hundred years of its existence, remains uniquely placed within the energy/fuel mix to meet the global energy demands. The wide variety of precursors for obtaining syngas (including biomass, stranded natural/shale gas, CO_2, etc.) to which the Fischer-Tropsch process is amenable, and the ultra-clean nature of the product liquid fuels (devoid of aromatics, particulates, sulphur and nitrogen based compounds), both position the chemical process ready to cater for the changing tastes in energy sources, stricter environmental policies and the growing global energy requirements. The latterly renewed interest in the catalytic process has seen the implementation of the Fischer-Tropsch synthesis in both traditional (e.g. fixed bed reactors) and more novel forms (e.g. the use of micro-reactors, mobile bio-refineries, etc.). Irrespective of the adaptations made to the technology, the need to control the reactor temperature and optimise the reactor performance in order to maximise the productivity of long chain hydrocarbon molecules remain pivotal. The optimal reactor configuration could on the one hand be arrived at, through the classical design route of: laboratory bench scale experiments, pilot plant scale tests and full scale

implementation. On the other hand, computer simulations could serve as a less time consuming and less expensive route. The fixed bed reactor configuration of all reactors available on the market, presents the most significant heat transport challenges and has been selected for this study. In addition to the co-current recycling of the liquid and gaseous effluents from the reactor at high velocities in order to generate turbulence, the reduction of tube diameters in order to reduce heat transport resistance, the dilution of the catalyst bed with inert materials could help control temperature within a fixed bed reactor. The dilution of the catalyst bed with encapsulated phase change material, in conjunction with an external supervisory cooling mechanism, was adopted as a strategy for temperature control and reactor performance regulation in a fixed bed Fischer-Tropsch reactor. This strategy is central to this thesis. The fusion temperature of the phase change material lies between some nominal operating temperature and a maximum safe operating temperature. This approach of using phase change material diluents to regulate temperature in a multi-tubular fixed bed Fischer-Tropsch reactor has not been recorded in available open literature. It was therefore important to develop a model which accurately predicts the reactor behaviour without and with the influence of the encapsulated phase change material. To this end, simulations were run using the commercial Finite Element Analysis (FEA) tool, COMSOL Multiphysics.

The underlying governing two dimensional quasi-homogeneous conservation equations for the Fe-catalysed Fischer-Tropsch synthesis in a fixed bed reactor including the: material balance, enthalpy balance, momentum balance, chemical kinetics and the additional phase change material enthalpy balance were presented in chapter 3. A single, representative tube within a multi-tubular fixed bed reactor was found to be sufficiently accurate to model the entire reactor. The initial conditions, boundary conditions and constitutive relationships for the relevant physical properties were developed and set out. The simplifying assumptions and discretisation schemes of FEA software were also detailed. The full description of the implementation of the mathematical models developed in chapter 3 as numerical models, their numerical solution, validation and verification were set out in chapter 4 using the COMSOL Multi-physics platform. A necessary feature for the implementation of the models in COMSOL was the ability of each physics module to be dependent upon one another. The rigorous validation and verification exercise entailed three test cases, which were benchmarked against the experimental and modelling works of other authors as reported in literature. The grid/convergence refinement studies were carried out for each test case based on the Grid Convergence Index (GCI).

Chapters 5-7 set out the principal contributions of this thesis to the study of the Fischer-Tropsch process with regards to temperature control and reactor performance. In chapter 5, it was demonstrated using two-dimensional models that the addition of carefully chosen and engineered, encapsulated phase change materials into the catalyst bed of

a heterogeneous, strongly exothermic reaction as the Fischer-Tropsch synthesis, can quench local hot spots, prevent thermal runaway through the introduction of thermal inertia to the reacting system and change the product distribution to favour the production of long chain hydrocarbons. The robustness of the temperature control which the phase change material brings to bear on the chemical process was tested by varying the process and design variables including the reactor coolant temperature, diameter of the reactor tube, etc.

Chapter 6 was focussed on developing a one-dimensional model, which while providing relative computational convenience, traded off as little accuracy as possible in predicting the reactor performance (selectivity to chemical species, conversion, productivity, etc.). The steady state α-model originally developed using the Karman-Pohlhausen procedure was re-cast to account for transient operations, as well as the heat sink effect of the phase change material and benchmarked against the two dimensional quasi-homogeneous models set out in chapter 5. A very good agreement was found between both sets of models. As in the case of the two dimensional models, a flat, homogeneous catalyst activity profile was used for all simulation scenarios considered.

In chapter 7, the catalyst arrangement in the reactor was changed. The previously flat, homogeneous catalyst activity profile was supplanted with a graded, multi-zonal packed bed arrangement. Each of the graded catalytic zones was diluted with encapsulated phase change materials to different degrees. Whereas a two dimensional model would have proven unwieldy in the repetitive non linear programming optimisation computations needed to locate the best catalyst dilution and distribution strategy for simultaneously maximising the productivity of long chain hydrocarbon molecules whilst preventing thermal runaway, the modified α-model proved to be better suited to the task in hand. The objective function of the optimisation problem was the maximisation of the productivity of the long chain hydrocarbon molecules (C_{5+}), the main decision variable was the relative catalyst activity profile (σ), while the manipulated variables included: the inlet/coolant temperature, the feed flow rate factor (β_f). The optimisation problem was constrained by all the constituent and constitutive equations of the modified α-model as well as the additional pre-specified minimum product selectivity and minimum CO conversion per pass. The multi-zonal dilution of the catalytic bed using encapsulated phase change material brought about a 16% increase in the desired C_{5+} productivity in the two-zone reactor compared to the uniform catalyst arrangement with no phase change material dilution. A further 3% increase in the C_{5+} productivity was also recorded with a three zone arrangement. Beyond three zones, there was no significant increment in the C_{5+} productivity.

8.2 Future work

The current work presented in this thesis could benefit from further work in three principal areas:

(I) **Experimental validation**: Carrying out the experiment for the phase change material modulated Fischer-Tropsch reaction, that was simulated, could serve to provide further information (such as actual reactor data) which may be compared with and fed back into the mathematical model in order to improve its ability to predict the reactor performance. For instance, the effect of thermal hysteresis (i.e. if and by how much the fusion temperature departs from the "normal fusion temperature") during its repeated phase transition may be ascertained. Experimenting may also help determine how well and how soon the phase change materials are regenerated and the life span of the phase change material in the reactor. It may also be of interest to investigate the use of other inert materials as diluents instead of phase change materials.

(II) **Increasing the model robustness**: The quasi-homogeneous model has been used in this thesis. This model may be improved if the chemical and physical phenomena could also be predicted at the micro (catalyst) scale and the results projected on to, and used by the macro-scale. A single pellet (or a group of pellets) model incorporating the conservation equations in and around the pellet(s) could be used as the representative micro-scale. The model presented in this thesis has also not accounted for deviations from the Anderson-Schulz Flory distribution of products. It is known from literature that olefins may be formed as intermediates or final products and be re-adsorbed onto the catalyst active sites for further reaction. This phenomenon is likely to have an effect on the product distribution and the model could be updated to reflect this.

(III) **Exploring other reactor configurations**: This thesis has chosen the fixed bed reactor configuration, principally because of its challenging heat transfer characteristics. Other configurations may also be considered, particularly those which allow for the easy regeneration of the phase change material, such as the micro-fluidised beds, modular catalytic plate reactors, etc. These configurations may also be explored with the deliberate intention to intensify (i.e. shrink the footprint) of the Fischer-Tropsch process as mobile, "on-demand", scalable and modular Fischer-Tropsch units are almost certain to play a crucial role in delivering clean energy and petrochemical feedstock for the future.

References

[1] A. de Klerk, editor. *Fischer-Tropsch Process in Kirk Othmer Encyclopedia of Chemical Technology*. John Wiley & Sons, 6:791-827, 2013.

[2] BP Energy Outlook. Technical report, BP Plc., 2016. URL https://www.bp.com/content/dam/bp/pdf/energy-economics/energy-outlook-2016/bp-energy-outlook-2016.pdf.

[3] C. Zhang, K.W. Jun, K.S. Ha, Y.J. Lee, and S.C. Kang. Efficient Utilization of Greenhouse Gases in a Gas-to-Liquids Process Combined with CO_2/ Steam-Mixed reforming and Fe-Based Fischer-tropsch Synthesis. *Environ. Sci. Technol.*, 48:8251–8257, 2014.

[4] Velocys® Plc. 2016. URL http://www.velocys.com/.

[5] A. Jess and C. Kern. Modeling of multi-tubular reactors for Fischer-Tropsch synthesis. *Chemical Engineering and Technology*, 32(8):1164–1175, 2009. ISSN 09307516 15214125.

[6] H. Schulz. Trends in Research and Development of Coal Conversion to Liquid Fuels and Basic Chemicals in Europe. *Pure & Appl. Chem.*, 51:2225, 1979.

[7] M. Röper. *in Catalysis in C_1 Chemistry*. Reidel, Dordrecht, W. Keim edition, 1983.

[8] X. W. Zhu, X. J. Lu, X. Y. Liu, D. Hildebrandt, and D. Glasser. Study of Radial Heat Transfer in a Tubular Fischer-Tropsch Synthesis Reactor. *Industrial & Engineering Chemistry Research*, 49(21):10682–10688, 2010. ISSN 08885885.

[9] M. E. Dry. The Fischer-Tropsch Process - Commercial aspects. *Catalysis Today*, 6(3):183–206, 1990. ISSN 0920-5861.

[10] M. E. Dry. The Fischer-Tropsch process: 1950-2000. *Catalysis Today*, 71(3-4): 227–241, 2002. ISSN 0920-5861.

[11] A.P. Steynberg, M.E. Dry, B.H. Davis, and B.B. Breman. *in Fischer Tropsch Technology, Studies in Surface Science and Catalysis*. Elsevier B.V, Amsterdam, 2004.

[12] S. T. Sie and R. Krishna. Fundamentals and selection of advanced Fischer Tropsch reactors. *Applied Catalysis*, 186:55, 1999. ISSN 0926-860X.

[13] R.M. De Deugd. *Fischer-Tropsch Synthesis Revisited; Efficiency and Selectivity Benefits from Imposing Temporal and/or Spatial Structure in the Reactor*. PhD thesis, Technische Universiteit Delft, 2004.

[14] I. V. Derevich, V. S. Ermolaev, V. Z. Mordkovich, and D. D. Galdina. Simulation of fluid dynamics in a microchannel Fischer-Tropsch reactor. *Theoretical Foundations of Chemical Engineering*, (1):8, 2012. ISSN 0040-5795.

[15] I. V. Derevich, V. S. Ermolaev, and V. Z. Mordkovich. Modeling of hydrodynamics in microchannel reactor for Fischer-Tropsch synthesis. *International Journal of Heat and Mass Transfer*, 55:1695–1708, 2012. ISSN 0017-9310.

[16] R. L. Espinoza, A. P. Steynberg, B. Jager, and A. C. Vosloo. Low temperature Fischer Tropsch synthesis from a Sasol perspective. *Applied Catalysis*, 186:13–26, 1999. ISSN 0926-860X.

[17] G. Eigenberger. *Fixed-Bed Reactors*, volume B4 of *Ullmann's Encyclopedia of Industrial Chemistry*, pages 199–238. VCH Publishers Inc., 5 edition, 1992.

[18] B. Jager and R. Espinoza. Advances in low temperature Fischer Tropsch synthesis. *Catalysis Today*, 23(1):17, 1995. ISSN 09205861.

[19] W.L. Luyben. Catalyst dilution to improve dynamic controllability of cooled tubular reactors. *Computers & Chemical Engineering*, 37:184–190, 2012. ISSN 0098-1354.

[20] M.M. J. Quina, F. Quinta, and M. Rosa. Model comparison and sensitivity analysis for a fixed bed reactor with two catalytic zones. *Chemical Engineering Journal*, 75:149–159, 1999. ISSN 1385-8947.

[21] COMSOL. Comsol multiphysics 4.4, 2014. URL www.comsol.com.

[22] J. Ansorge. Shell Middle Distillate Synthesis: Fischer-Tropsch Catalysis in Natural Gas Conversion To High Quality Products. *American Chemical Society; Div. Fuel Chem.*, 43(2):654–663, 1997.

[23] H. Schulz. *Chemierohstoffe aus Kohle*. Georg Thieme Verlag, Stuttgart, Germany, 1977.

[24] F. Fischer and H. Tropsch. Uber die Herstellung synthetischer ölgemische (Synthol) durch Aufbau aus Kohlenoxyd und Wasserstoff. *Brennstoff-chemie*, 4:276, 1923.

[25] P.M. Maitlis and A. de Klerk, editors. *Greener Fischer Tropsch processes for fuels and feedstocks*. Wiley-VCH Verlag GmbH & Co. KGaA, 2013.

[26] G.P. van der Laan and A. A. C. M. Beenackers. Kinetics and selectivity of the Fischer Tropsch synthesis: A literature review. *Catalysis Review: Science and Engineering*, 41(3&4):255–318, 1999. ISSN 0009-2509.

[27] S.T. Sie. Process Development and Scale-Up: IV. Case History of the Development of a Fischer-Tropsch Synthesis Process. *Reviews in Chemical Engineering*, 14:109, 1998.

[28] A. P. Steynberg, R. L. Espinoza, B. Jager, and A. C. Vosloo. High temperature Fischer Tropsch synthesis in commercial practice. *Applied Catalysis*, 186:41–54, 1999. ISSN 0926-860X.

[29] A. de Klerk and Furimsky E. *Catalysis in the refining of Fischer-Tropsch syncrude*. RSC Publishing, Cambridge UK, 2010.

[30] B. Eisenberg, R.A. Fiato, C.H. Mauldin, G.R. Say, and S. Soled. EXXON's Advanced Gas-to-Liquids Technology. *Studies in Surface Science and Catalysis*, 119: 943, 1998.

[31] T. Knott. Alchemy in Alaska. *BP Frontiers*, 14, 2002.

[32] Rentech PDU. URL http://www.rentechinc.com.

[33] J. W. Pratt. A Fischer Tropsch synthesis reactor model framework for liquid biofuels production, 2012.

[34] V.U.S. Rao, G.J. Stiegel, G.J. Cinquegrane, and R.D. Srivastave. Iron-based catalysts for slurry-phase Fischer-Tropsch process: Technology review. *Fuel Process. Technol.*, 30:83, 1992.

[35] H. Kölbel and M. Ralek. The Fischer-Tropsch Synthesis in the Liquid Phase. *Catal. Rev.-Sci. Eng.*, 21(2):225, 1980.

[36] M. E. Dry. Fischer tropsch synthesis over iron catalysts. *Catalysis Letters*, 7(1-4): 241–251, 1990.

[37] M.E. Dry. *Chemical concepts used for engineering purposes in Fischer-Tropsch technology*. Elsevier B.V., Amsterdam, 2004.

[38] P.F. Mako and W.A. Samuel, editors. *in Meyers, R.A. Handbook of Synfuels Technology*. McGraw, New York, N.Y., 1984.

[39] F.J.M. Schrauwen, editor. *in Meyers, R.A. Handbook of Petroleum Refining Process*. McGraw, New York, N.Y., 2004.

[40] S.T. Sie, M.M.G. Senden, and H.M.H. van Wechum. Conversion of natural gas to transportation fuels via the shell middle distillate synthesis process (SMDS). *Catal. Today*, 8(3):371, 1991.

[41] M.J. van der Burgt, C.J. van Leeuwen, J.J delÁmico, and S.T. Sie. *in Methane Conversion*. Elsevier Science, New York, 1988.

[42] R.J. Madon, E. Iglesia, and S.C. Reyes. Selectivity in catalysis. *American Chemical Society*, 1993.

[43] M.E. Dry. *in Catalysis- Science and Technology*, volume 1. Springer-Verlag, New York, 1981.

[44] M.A. Vannice. The catalytic synthesis of hydrocarbons from H_2/CO mixtures over the Group VIII metals: V. The catalytic behavior of silica-supported metals. *Journal of Catalysis*, 50(2):228–236, 1977.

[45] R.B. Anderson. *Catalysts for the FFischer-Tropsch Synthesis*, volume 4. Van Nostrand Reinhold, 1956.

[46] E. S. Lox, G.B. Marin, E. de Graeve, and P. Bussière. Characterization of a promoted precipitated iron catalyst for Fischer-Tropsch synthesis. *Appl. Catal.*, 40:197–218, 1988.

[47] H.B. Zhang and G.L. Schrader. Characterization of a fused iron catalyst for Fischer-Tropsch synthesis by *in situ* laser Raman spectroscopy. *J. Catal.*, 95(1): 325–332, 1985.

[48] K.R.P.M. Rao, F.E. Huggins, V. Mahajan, G.P. Huffman, V.U.S. Rao, B.L. Bhatt, D. B. Bukur, B.H. Davis, and R.J. O'Brien. Mössbauer spectroscopy study of iron-based catalysts used in Fischer-Tropsch synthesis. *Top. Catal.*, 2(1):71–78, 1995.

[49] M.D. Shroff, D.S. Kalakkad, K.E. Coulter, S.D. Kòhler, M.S. Harrington, N.B. Jackson, A.G. Sault, and A.K. Datye. Activation of Precipitated Iron Fischer-Tropsch Synthesis Catalysts. *J. Catal.*, 156(2):185–207, 1995.

[50] D. B. Bukur, L. Nowicki, R.K. Manne, and X. Lang. Activation Studies with a Precipitated Iron Catalyst for Fischer-Tropsch Synthesis: II. Reaction Studies. *J. Catal.*, 155(2):366–375, 1995.

[51] C.N. Satterfield and Jr. G.A. Huff. Usefulness of a slurry-type Fischer-Tropsch reactor for processing synthesis gas of low Hydrogen-Carbon monoxide ratio. *Can. J. Chem. Eng.*, 60:159, 1982.

[52] W.H. Zimmerman and D.B. Bukur. Reaction kinetics over iron catalysts used for the Fischer-Tropsch synthesis. *Can. J. Chem. Eng.*, 68(2):292, 1990.

[53] D.S. Newsome. The Water-Gas Shift Reaction. *Catal. Rev.-Sci. Eng.*, 21(2):275, 1980.

[54] E. S. Lox and G. F. Froment. Kinetics of the Fischer-Tropsch reaction on a precipitated promoted iron catalyst. II Kinetic modeling. *Industrial and Engineering Chemistry Research*, 32(1):71–82, 1993. ISSN 0888-5885.

[55] D.G. Rethwisch and J.A. Dumesic. Adsorptive and catalytic properties of supported metal oxides: III. Water-gas shift over supported iron and zinc oxides. *J. Catal.*, 101(1):35–42, 1986.

[56] K.R.P.M. Rao, F.E. Huggins, V. Mahajan, G.P. Huffman, and V.U.S. Rao. The role of magnetite in Fischer-Tropsch synthesis. *Hyperfine Interact.*, 93(1):1745–1749, 1994.

[57] J.P. Hindermann, G.J. Hutchings, and A. Kiennemann. Mechanistic Aspects of the Formation of Hydrocarbons and Alcohols from CO Hydrogenation. *Catal. Rev.-Sci. Eng.*, 35(1):1, 1993.

[58] M.E. Dry. in Int. Conf. on Catal. and Catal. Proc. Cape Town, South Africa, 1993.

[59] M.E. Dry. Practical and theoretical aspects of the catalytic Fischer-Tropsch process. *Appl. Catal. A*, 138(2):319–344, 1996.

[60] A.A. Adesina. Hydrocarbon synthesis via Fischer-Tropsch reaction: travails and triumphs. *Appl. Catal. A.*, 138(2):345–367, 1996.

[61] R.B. Anderson. *The Fischer-Tropsch Synthesis.* Academic Press, Orlando, 1984.

[62] S. Novak, R.J. Madon, and H. Suhl. Models of hydrocarbon product distributions in Fischer-Tropsch synthesis. *J. Chem. Phys.*, 74:6083, 1981.

[63] S. Novak, R.J. Madon, and H. Suhl. Secondary effects in the Fischer-Tropsch synthesis. *J. Catal.*, 77(1):141–151, 1982.

[64] B.W. Wojciechowski. The Kinetics of the Fischer-Tropsch Synthesis. *Catal. Rev.-Sci. Eng.*, 30(4):629–702, 1988.

[65] A.T. Bell. Catalytic Synthesis of Hydrocarbons over Group VIII Metals. A Discussion of the Reaction Mechanism. *Catal. Rev.-Sci. Eng.*, 23(1-2):203–232, 1981.

[66] J.P. Hovi, J. Lahtinen, Z.S. Liu, and R.M. Nieminen. Monte Carlo study of CO hydrogenation on cobalt model catalysts. *J. Chem. Phys.*, 102:7674, 1995.

[67] M.A. Vannice. The Catalytic Synthesis of Hydrocarbons from Carbon Monoxide and Hydrogen. *Catal. Rev.-Sci. Eng.*, 14(1):153–191, 1976.

[68] G. Bub, M. Baerns, B. Büssemeier, and C. Frohning. Prediction of the performance of catalytic fixed bed reactors for Fischer-Tropsch Synthesis. *Chem. Eng. Sci.*, 35 (1-2):348–355, 1980. ISSN 0009-2509.

[69] M.A. Vannice. The catalytic synthesis of hydrocarbons from H2CO mixtures over the group VIII metals: II. The kinetics of the methanation reaction over supported metals. *J. Catal.*, 37(3):462–473, 1975.

[70] G.A. Huff Jr and C.N. Satterfield. Stirred autoclave apparatus for study of the Fischer-Tropsch synthesis in a slurry bed. 2. Analytical procedures. *Ind. Eng. Chem. Des. Dev.*, 22(2):258–263, 1983.

[71] B. Sarup and B.W. Wojciechowski. Studies of the Fischer-Tropsch synthesis on a cobalt catalyst II. Kinetics of carbon monoxide conversion to methane and to higher hydrocarbons. *Can. J. Chem. Eng.*, 67:62, 1989.

[72] H. Nettelhoff, R. Kokuun, S. Ledakowicz, and W.D. Deckwer. Studies on the kinetics of Fischer-Tropsch synthesis in slurry phase. *Ger. Chem. Eng.*, 8:177, 1985.

[73] M.E. Dry, T. Shingles, L.J. Boshoff, and G.J. Oosthuizen. Rate of the Fischer-Tropsch reaction over iron catalysts. *J. Catal.*, 25(1):99–104, 1972.

[74] W.J. Shen, J.L. Zhou, and B. J. Zhang. Kinetics of Fischer-Tropsch synthesis over precipitated iron catalyst. *J. Nat. Gas Chem.*, 4:385, 1994.

[75] M.E. Dry. Advances in Fischer-Tropsch Chemistry . *Ind. Eng. Chem. Prod. Res. Dev.*, 15(4):282–286, 1976.

[76] W.D. Deckwer, R. Kokuun, E. Sanders, and S. Ledakowicz. Kinetic studies of Fischer-Tropsch synthesis on suspended iron/potassium catalyst - rate inhibition by carbon dioxide and water. *Ind. Eng. Chem. Process. Des. Dev.*, 25(3):643–649, 1986.

[77] H.P. Whiters Jr and J.W. Eleizer, K.F. andMitchell. Slurry-phase Fischer-Tropsch synthesis and kinetic studies over supported cobalt carbonyl derived catalysts. *Ind. Eng. Chem. Res.*, 29(9):1807–1814, 1990.

[78] S. Ledakowicz, H. Nettelhoff, R. Kokuun, and W.D. Deckwer. Kinetics of the Fischer-Tropsch synthesis in the slurry phase on a potassium-promoted iron catalyst. *Top. Catal.*, 24:1043–1049, 1985.

[79] R.S. Dixit and L.L. Tavlarides. Kinetics of the Fischer-Tropsch synthesis. *Ind. Eng. Chem. Process. Des. Dev.*, 22(1):1–9, 1983.

[80] I.C. Yates and C.N. Satterfield. Intrinsic kinetics of the Fischer-Tropsch synthesis on a cobalt catalyst. *Energy Fuels*, 5:168–173, 1991.

[81] W.H. Zimmerman. *Kinetic modelling of the Fischer-Tropsch synthesis*. PhD thesis, Texas A&M University, College Station, Texas, USA, 1990.

[82] C.N. Satterfield, R.T. Hanlon, S.E. Tung, Z. Zou, and G.C. Papaefthymiou. Initial behavior of a reduced fused-magnetite catalyst in the Fischer-Tropsch synthesis. *Ind. Eng. Chem. Prod. Res. Dev.*, 25(3):401–407, 1986.

[83] C.D. Frohning, editor. *Chemical Feedstocks from Coal*. Wiley, New York, 1982.

[84] H. E. Atwood and C.O. Bennett. Kinetics of the Fischer-Tropsch Reaction over Iron. *Ind. Eng. Chem. Process. Des. Dev.*, 18(1):163–170, 1979. ISSN 0196-4305.

[85] G.A. Huff Jr and C.N. Satterfield. Intrinsic kinetics of the Fischer-Tropsch synthesis on a reduced fused-magnetite catalyst. *Ind. Eng. Chem. Process. Des. Dev.*, 23(4):696–705, 1984.

[86] M.E. Dry, T. Shingles, L.J. Boshoff, and G.J. Oosthuizen. Heats of chemisorption on promoted iron surfaces and the role of alkali in Fischer-Tropsch synthesis. *J. Catal.*, 15(2):190–199, 1969.

[87] J.H. Boelee. *The Fischer-Tropsch synthesis in slurry phase reactors*. PhD thesis, University of Eindhoven, 1988.

[88] I.C. Yates and C.N. Satterfield. Effect of carbon dioxide on the kinetics of the Fischer-Tropsch synthesis on iron catalysts. *Ind. Eng. Chem.Res.*, 28(1):9–12, 1989.

[89] A. Jess, R. Popp, and K. Hedden. Fischer-Tropsch-synthesis with nitrogen-rich syngas: Fundamentals and reactor design aspects. *Applied Catalysis*, 186(1-2): 321–342, 1999. ISSN 0926860X.

[90] A. Jess and C. Kern. Influence of Particle Size and Single-Tube Diameter on Thermal Behavior of Fischer-Tropsch Reactors. Part I. Particle Size Variation for Constant Tube Size and Vice Versa. *Chemical Engineering & Technology*, 35(2): 369, 2012. ISSN 09307516.

[91] A. Jess and C. Kern. Influence of particle size and single-tube diameter on thermal behavior of Fischer-Tropsch reactors: Part II: Eggshell catalysts and optimal reactor performance. *Chemical Engineering and Technology*, 35(2):379–386, 2012. ISSN 09307516 15214125.

[92] R. Popp. *Ergebnisse halbtechnischer Untersuchungen zur Fischer-Tropsch-Synthese mit stickstoffreichem Synthesegas*. PhD thesis, University of Karlsruhe, Germany, 1996.

[93] T. Kuntze. *Kinetik der Fischer-Tropsch-Synthese an einem Eisenfällungskatalysator unter Druck bei Einsatz eines stickstoffreichen Synthesegases*. PhD thesis, University Karlsruhe, Germany, 1991.

[94] H. Raak. *Reaktionskinetische Untersuchungen in der Anfangsphase der Fischer-Tropsch-Synthese an einem technischen Eisenfällungskatalysator*. PhD thesis, University of Karlsruhe, Germany, 1995.

[95] M.E. Dry. Catalytic aspects of industrial Fischer-Tropsch synthesis. *J. Mol. Catal.*, 17(2-3):133–144, 1982.

[96] A. de Klerk and E. Furimsky. *Catalysis in the Refining of Fischer-Tropsch Syncrude*. RSC Publishing, Cambridge UK, 2010.

[97] T.J. Donnelly and C.N. Satterfield. Product distributions of the Fischer-Tropsch synthesis on precipitated iron catalysts. *Appl. Catal. A.*, 52(1):93–114, 1989.

[98] R.A. Dictor and A.T. Bell. Fischer-Tropsch synthesis over reduced and unreduced iron oxide catalysts. *J. Catal.*, 97(1):121–136, 1986.

[99] H. H. Storch, N. Golumbic, and R.B. Anderson. *The Fischer-Tropsch and Related Syntheses*. Wiley, New York, N.Y., 1951.

[100] E.W. Kuipers, C. Scheper, J.H. Wilson, and H. Oosterbeek. Non-ASF Product Distributions Due to Secondary Reactions during Fischer-Tropsch Synthesis. *J. Catal.*, 158(1):288–300, 1996.

[101] E. Iglesia, S.C. Reyes, and R.J. Madon. Transport enhanced $\alpha-$ olefin readsorption pathways in Ru catalysed hydrocarbon synthesis. *J. Catal.*, 129:238–256, 1991.

[102] D.B. Bukur, S. A. Patel, and X. Lang. Fixed Bed and Slurry Reactor Studies of Fischer-Tropsch Synthesis on Precipitated Iron Catalyst. *Appl. Catal.*, 61:329, 1990.

[103] K.M. Vanden Bussche and G.F. Froment. A Steady-State Kinetic Model for Methanol Synthesis and the Water Gas Shift Reaction on a Commercial $Cu/ZnO/Al_2O_3$ Catalyst. *J. Catal.*, 161:1–10, 1996.

[104] D.B. Bukur, M. Koranne, X. Lang, K.R.P.M. Rao, and G.P. Huffman. Pretreatment effect studies with a precipitated iron Fischer-Tropsch catalyst. *Appl. Catal. A.*, 126(1):85–113, 1995.

[105] D.B. Bukur, X. Lang, J.A. Rossin, W.H. Zimmerman, M.P. Rosynek, E.B. Yeh, and C. Li. Activation studies with a promoted precipitated iron Fischer-Tropsch catalyst. *Ind. Eng. Chem.Res.*, 28(8):1130–1140, 1989.

[106] D.B. Bukur, K. Okabe, M.P. Rosynek, C. Li, D. Wang, K.R.P.M. Rao, and G.P. Huffman. Activation Studies with a Precipitated Iron Catalyst for Fischer-Tropsch Synthesis: I. Characterization Studies. *J. Catal.*, 155(2):353–365, 1995.

[107] D.B. Bukur, L. Nowicki, and S. A. Patel. Activation studies with an iron Fischer-Tropsch catalyst in fixed bed and stirred tank slurry reactors. *Can. J. Chem. Eng.*, 74(3):399–404, 1996.

[108] M.P. Dudukovic. Opaque multiphase flows: experiments and modeling. *Experimental Thermal and Fluid Science*, 26(6-7):747–761, 2002.

[109] M.H. Al-Dahhan and M.P. Dudukovic. Catalyst wetting efficiency in trickle bed reactors at high pressure. *Chemical Engineering Science*, 50:2377–2389, 1995.

[110] M.R. Khadilkar, Y.X. Wu, M.H. Al-Dahhan, M.P. Dudukovic, and M. Colakyan. Comparison of ttrickle-bed and upflow reactor performance at high pressure: Model predictions and experimental observations. *Chemical Engineering Science*, 51:213–2148, 1996.

[111] J.F. Richardson and D.G. Peacock, editors. *Coulson and Richardson's Chemical Engineering: Chemical and Biochemical Reactors and Process Control*, volume 3. Pergamon, 3rd edition, 1994. ISBN 0080410030.

[112] J.H. Yang, H.K. Kim, D.H. Chun, H.T. Lee, J.C. Hong, H. Jung, and J. Yang. Mass transfer limitations on fixed-bed reactor for Fischer-Tropsch synthesis. *Fuel Process. Technol.*, 91(3):285–289, 2010. ISSN 0378-3820.

[113] P.F. Schubert, C.A. Bayens, and L. Weick. GTL: Progress and Prospects- Development progresses for GTL fuels, specialty products. *Oil Gas J.*, 99(11):69, 2001.

[114] G.F. Froment and K.B. Bischoff. *Chemical reactor analysis and design.* Wiley, 2nd edition, 1990. ISBN 0471521906.

[115] B. Jager. Development of Fischer Tropsch Reactors. *The AIChE Spring Meeting, New Orleans*, pages 1–9, 2003.

[116] H.M. Naim. *Analysis of the Dynamics and Stability of Fixed Bed Reactors*. PhD thesis, 1974.

[117] Y.N. Wang, Y.Y. Xu, Y.W. Li, Y.L. Zhao, and B.J. Zhang. Heterogeneous modeling for fixed-bed Fischer Tropsch synthesis: Reactor model and its applications. *Chem. Eng. Sci.*, 58(3-6):867–875, 2003. ISSN 0009-2509.

[118] M. A. Marvast, M. Sohrabi, S. Zarrinpashne, and G. Baghmisheh. Fischer-Tropsch Synthesis: Modeling and Performance Study for Fe-HZSM5 Bifunctional Catalyst. *Chemical Engineering & Technology*, 28(1):78–86, 2005.

[119] J.W.A De Swart, R. Krishna, and S.T. Sie. *in Natural gas conversion IV, Studies in Surface Science and Catalysis*, volume 107. Elsevier, Amsterdam, 1997.

[120] R. Philippe, M. Lacroix, L. Dreibine, C. Pham-Huu, D. Edouard, S. Savin, F. Luck, and D. Schweich. Effect of structure and thermal properties of a Fischer Tropsch catalyst in a fixed bed. *Catalysis Today*, 147:S305–S312, 2009. ISSN 0920-5861.

[121] R. Guettel and T. Turek. Comparison of different reactor types for low temperature Fischer-Tropsch synthesis: A simulation study. *Chem. Eng. Sci.*, 64(5):955–964, 2009. ISSN 0009-2509.

[122] M. H. Rafiq, H. A. Jakobsen, R. Schmid, and J. E. Hustad. Experimental studies and modeling of a fixed bed reactor for Fischer-Tropsch synthesis using biosyngas. *Fuel processing technology*, 92(5):893–907, 2011. ISSN 03783820.

[123] E. Mears. Tests for transport limitations in experimental catalytic reactors. *Industrial and Engineering Chemistry Process Design and Development*, 10(4):541, 1971.

[124] E. Mears. On criteria for axial dispersion in nonisothermal packed bed catalytic reactors. *Industrial and Engineering Chemistry Fundamentals*, 15(1):20, 1976.

[125] H.A. Jakobsen. Fixed Bed Reactors: Lecture notes in subject TKP4145 Reactor Technology. 2011.

[126] Y. Nie, P.M. Witt, A. Agarwal, and L.T. Biegler. Optimal Active Catalyst and Inert Distribution in Catalytic Packed Bed Reactors: ortho-Xylene Oxidation. *Ind. & Eng. Chem. Res.*, 52(44):15311–15320, 2013. ISSN 0888-5885.

[127] E. M. Calverley, P. M. Witt, and J. D. Sweeney. Reactor runaway due to statistically driven axial activity variations in graded catalyst beds. *Chem. Eng. Sci.*, 80:393–401, 2012. ISSN 0009-2509.

[128] R. C. Pattison and M. Baldea. A thermal flywheel approach to distributed temperature control in microchannel reactors. *AIChE Journal*, (6):2051, 2013. ISSN 0001-1541.

[129] R. C. Pattison and M. Baldea. Robust autothermal microchannel reactors. *Computers & Chemical Engineering*, 81:171–179, 2015. ISSN 0098-1354.

[130] A. Mittal, S. Roy, and F. Larachi. Modeling of heat uptake and release with embedded phase change materials in monolithic microfluidized bed reactors. *Industrial and Engineering Chemistry Research*, 49(3):1086–1097, 2009. ISSN 0888-5885.

[131] M. Zhang, Y. Hong, S. Ding, M. Su, J. Hu, A. A. Voevodin, and Y. Fan. Encapsulated nano heat sinks for thermal management of heterogeneous chemical reactions. *Nanoscale*, 2(12):2790–2797, 2010. ISSN 20403364 20403372.

[132] S. Krishnan, S. V. Garimella, and S. S. Kang. A novel hybrid heat sink using phase change materials for transient thermal management of electronics. *IEEE Transactions on Components and Packaging Technologies*, 28(2):281–289, 2005. ISSN 15213331.

[133] W.J. Cole, K.M. Powell, and T.F. Edgar. Optimisation and advanced control of thermal energy storage systems. *Reviews in Chemical Engineering*, 28(2-3):81–99, 2012.

[134] C. Konstantinidis, W. Lang, and A. Novoselac. Integration of phase change materials in lightweight buildings in order to optimize the conditions for thermal comfort and to improve the building energy performance. In *Proceedings of Clima*, 2010.

[135] A. Sharma, V.V. Tyagi, C.R. Chen, and D. Buddhi. Review on thermal energy storage with phase change materials and applications. *Revnewable and Sustainable Energy Reviews*, 13(2):318–345, 2009.

[136] W.C Chan, N. Russell, J. Swithenbank, and V. Sharifi. ESPRC Thermal management of Industrial Process: Literature review. Technical report, Department of Chemical and Biological Engineering, University of Sheffield, 2011.

[137] A report of IEA Solar heating and Cooling Programme (SHC)-Task 32: Advanced storage concepts for solar and low energy buildings. Technical report, The International Energy Agency (IEA), 2005.

[138] R. Tamme. Optimised industrial process heat and power generation with thermal energy storage final report. Technical report, Deutsches Zentrum fur Luft-und Raumfarht: The international Energy Agency (IEA), 2010.

[139] Y. Hong, S. Ding, W. Wu, J. Hu, A.A. Voevodin, L. Gschwender, E.d Snyder, L. Chow, and M. Su. Enhancing Heat Capacity of Colloidal Suspension Using Nanoscale Encapsulated Phase-Change Materials for Heat Transfer. *ACS Applied Materials & Interfaces*, 2(6):1685–1691, 2010. ISSN 1944-8244.

[140] T. Yokota, M. Murayama, and J. Howe. Transmission-Electron-Microscopy Investigation of Melting in Submicron Al-Si Alloy Particles under Electron-Beam Irradiation. *Physical Review Letters*, 91(26):265504, 2003.

[141] D.B. Bukur, D. Mukesh, and S. A. Patel. Promoter effects on precipitated iron catalysts for Fischer-Tropsch synthesis. *Industrial & Engineering Chemistry Research*, 29(2):194–204, 1990. ISSN 0888-5885.

[142] K. Keyvanloo, W.C. Hecker, B.F. Woodfield, and C.H. Bartholomew. Highly active and stable supported iron Fischer-Tropsch catalysts: Effects of support properties and SiO_2 stabilizer on catalyst performance. *J. of Catal.*, 319(0):220–231, 2014. ISSN 0021-9517.

[143] G.W. Koning. *Heat and mass transport in tubular packed bed reactors at reacting and non reacting conditions: Experiments and models.* Thesis, University of Twente, The Netherlands, 2002.

[144] PSE. Reactor modelling, simulation and optimisation, 2014. URL http://www.psenterprise.com/chemicals/reaction.

[145] A.H. Benneker, A.E. Kronberg, J.W. Post, A.G.J. van der Ham, and K.R. Westerterp. Axial dispersion in gases flowing though a packed bed at elevated temperatures. *Chem. Eng. Sci.*, 51:2099, 1996.

[146] A.H. Benneker, A.E. Kronberg, I.C. Lansbergen, and K.R. Westerterp. Mass dispersion in liquid flow through packed beds. *Ind. Eng. Chem. Res.*, 41:1716, 2002.

[147] D. Vortmeyer and E. Haidegger. Discrimination of three approaches to evaluate heat fluxes for wall-cooled fixed bed chemical reactors. *Chem. Eng. Sci.*, 46:2651, 1991.

[148] H. S. Fogler. *Elements of chemical reaction engineering.* Harlow Pearson, 2014.

[149] E. Fontes. Modeling approaches in heterogeneous catalysis, 2015. URL https://www.comsol.com/blogs/modeling-approaches-in-heterogeneous-catalysis.

[150] A. Stanckiewicz. Advances in modeling and design of multitubular fixed-bed reactors. *Chem. Eng. Technol.*, 1989.

[151] M.E. Davis and R.J. Davis. *Fundamentals of Chemical Reaction Engineering.* McGraw, Boston, 2003.

[152] R.B. Anderson, B. Seligman, J.F. Schultz, R. Kelly, and M.A. Elliot. Fischer-Tropsch synthesis: Some important variables of the synthesis on iron catalysts. *Ind*, 44:391, 1952.

[153] R.J. Madon and E. Iglesia. Hydrogen and CO intrapellet diffusion effects in Ruthenium-catalyzed hydrocarbon synthesis. *J. Catal.*, 149:428–437, 1994.

[154] E. Iglesia, S.L. Soled, J.E. Baumgartner, and S.C. Reyes. Synthesis and ccatalytic properties of eggshell cobalt catalysts for the Fischer-Tropsch synthesis. *J. Catal.*, 153:108–122, 1995.

[155] E.W. Kuipers, I.H. Vinkenburg, and H. Oosterbeek. Chain length dependence of 1-Olefin re-adsorption in FFischer-Tropsch synthesis. *J. Catal.*, 152:137–146, 1995.

[156] E. Iglesia, S.C. Reyes, and S.L. and Soled. *Reaction transport selectivity models and the design of Fischer-Tropsch catalysts.* in Computer-Aided Design of Catalysts and Reactors. Marcel Dekker, New York, 1993.

[157] H. Raak. A pressurized reactor wwith integrated load cell for measuring the activities of Fischer-Tropsch synthesis: Their loading with liquid reaction products (wax). *Edrol-Erdgas-Kohle*, 114:251, 1998.

[158] J.J. Marano and G.D. Holder. Characterization of Fischer-Tropsch liquids for vapor-liquid equilibria calculations. *Fluid Phase Equilibria*, 138(1-2):1–21, 1997. ISSN 0378-3812.

[159] O. Levenspiel. *Chemical Reaction Engineering.* John, 3rd edition, 1999.

[160] R. Aris. On shape factors for irregular particles-I. The steady-state problem. Diffusion and reaction. *Chem. Eng. Sci.*, 6:262–268, 1957.

[161] P. Hagan, M. Herskowitz, and C. Pirkle. A simple approach to highly sensitive tubular reactors. *SIAM J. Appl. Math.*, 48(5):1083–1101, 1988.

[162] S. Ergun. Fluid flow through packed columns. *Chem. Eng. Prog.*, 48(2):89, 1952.

[163] D. Nemec and Levec J. Flow through packed bed reactors: 1. Single-phase flow . *Chemical Engineering Science*, 60:6947–6957, 2005.

[164] S.H. Skaare. *Reaction and heat transfer in a wall cooled fixed bed reactor.* PhD thesis, Norwegian University of Science and Technology, 1993.

[165] J. Xu and G.F. Froment. Methane steam reforming, methanation and water-gas shift: intrinsic kinetics. *AIChE Journal*, 35:88–96, 1989. ISSN 00011541. doi: 10.1002/aic.690350109. URL http://search.ebscohost.com/login.aspx?direct=true&db=asf&AN=501613279&site=eds-live.

[166] R. B. Anderson, R. A. Friedel, and H. H. Storch. Fischer Tropsch mechanism involving stepwise growth of carbon chain. *J. Chem. Phys.*, 19:313–319, 1951.

[167] Schanke D. Personal Communication. Technical report, Statoil Research Center, Trondheim, 2010.

[168] M. Panahi, A. Rafiee, S. Skoestad, and M. Hillestad. A Natural Gas to LLiquid Process Model for Optimal Operation. *Ind. Eng. Chem. Res.*, 51:425–433, 2012.

[169] N. Vitorino, J.C.C. Abrantes, and J.R. Frade. Numerical solutions for mixed controlled solidification of phase change materials. *International Journal of Heat and Mass Transfer*, 53(23):5335, 2010.

[170] N. Vitorino, J. C. C. Abrantes, and J. R. Frade. Solutions for heat or cold discharge from encapsulated phase change materials. *Numerical Heat Transfer*, 64(6):421, 2013. ISSN 1040-7790.

[171] V. Alexiades and A.D. Solomon. *Mathematical modeling of melting and freezing processes*. Hemisphere Publishing Corporation, 1993.

[172] Matlab and simulink ^{TM} release 2015b, the mathworks inc., 2015. URL uk.mathworks.com.

[173] P.J. Roache. *Verification and validation in computational science and engineering*. Hermosa Publishers, Albuquerque, 1998.

[174] P.J. Roache, editor. *A method for uniform reporting of grid refinement studies: Proceedings of quantification of uncertainty in computational fluid dynamics*, volume 158, 1993. ASME Fluids Engineering Division Spring Meeting, Washington D.C.

[175] L.E. Schwer. Is your mesh refined enough? Estimating discretization error using GCI. 2008.

[176] M.J. Keyser, R.C. Everson, and R.I. Espinoza. Fischer Tropsch kinetic studies with cobalt manganese oxide catalysts. *Ind. Eng. Chem. Res.*, 39:48–54, 2000.

[177] S. Cingarapu, D. Singh, E.V. Timofeeva, and M.R. Moravek. Nanofluids with encapsulated tin nanoparticles for advanced heat transfer and thermal energy storage. *International Journal of Energy Research*, (1):51, 2014. ISSN 0363-907X.

[178] H. Bake, S.F. Zaman, Y.A. Alhamed, A.A. Al-Zahrani, M.A. Daous, S.U. Rather, H. Driss, and L.A. Petrov. Partial oxidation of methanol over $Au/CeO_2 - ZrO_2$ and $Au/CeO_2 - ZrO_2 - TiO_2$catalysts. *RSC Advances*, 6(27):22555–22562, 2016.

[179] R. W. McCabe and D. F. McCready. Kinetics and reaction pathways of methanol oxidation on platinum. *The Journal of Physical Chemistry*, 90(7):1428–1435, 1986. ISSN 0022-3654.

[180] A. Lordanidis. *Mathematical modelling of catalytic fixed bed reactors*. PhD thesis, University of Twente, 2002.

[181] S.J. Gentry, A. Jones, and P.T. Walsh. Kinetics of methanol oxidation over platinum wire catalysts. *Journal of the Chemical Society, Faraday Transactions 1: Physical Chemistry in Condensed Phases*, 76(0):2084–2095, 1980. ISSN 0300-9599.

[182] T.S. Lee. *Numerical modeling and simulation of Fischer Tropsch packed bed reactor and its thermal management*. PhD thesis, University of Florida, 2011.

[183] A. O. Odunsi, T.S. O'Donovan, and D.A. Reay. Temperature stabilisation in Fischer Tropsch reactors using phase change material (PCM). *Applied Thermal Engineering*, 93:1377–1393, 2016. ISSN 1359-4311.

[184] C.R. Wilke and P. Chang. Correlation of diffusion coefficients in dilute solutions. *AIChE Journal*, 1:264, 1955.

[185] C.J. Geankoplis. *Transport processes and unit operations*. Prentice-Hall International, Inc., 3rd edition, 1993.

[186] G. Le Bas. *The molecular volumes of liquid chemical compounds*. New York: David McKay Co., Inc.,, 1915.

[187] I.I. Chernobaev, M.N. Yakubovich, A.I. Tripolskii, N.V. Pavlenko, and V.L. Struzkho. Investigation of the mechanism of methane formation in the Fischer-Tropsch synthesis on a $CO/SiO_2\,Zr^{IV}$ catalyst. *Theor. Exp. Chem.*, 33:38–40, 1997.

[188] Krishnamoorthy S. Li A. Meitzner G.D. Iglesia E. Li, S. Promoted iron based catalysts for the fischer tropsch synthesis: Design, synthesis, site densities, and catalytic properties. *Journal of Catalysis*, 206:202–217, 2002.

[189] K.R. Westerterp, W.P.M. van Swaaij, and A.A.C.M. Beenackers. *Chemical reactor design and operation*. Wiley, New York, 1984.

[190] G. W. Koning, A.E. Kronberg, and W. P. M. van Swaaij. Improved one-dimensional model of a tubular packed bed reactor. *Chemical Engineering Science*, 61:3167–3175, 2006. ISSN 0009-2509.

[191] P.S. Hagan, M. Herskowitz, and C. Pirkle. Equilibrium temperature profile in highly sensitive tubular reactors. *SIAM J. Appl. Math.*, 47(6):1287–1305, 1987.

[192] P.S. Hagan, M. Herskowitz, and C. Pirkle. Runaway in highly sensitive tubular reactors. *SIAM J. Appl. Math.*, 48(6):1437–1450, 48.

[193] A.G. Dixon. An improved equation for the oveover heat transfer coefficient in packed beds. *Chemical Engineering and Proceedings*, 35:323–331, 1996.

[194] Y.A. Çengel. *Heat transfer: A practical approach*. WCB/McGraw-Hill, 1998.

[195] T.R. Goodman. *Application of Integral Methods to Transient Nonlinear Heat Transfer*, volume Volume 1, pages 51–122. Elsevier, 1964. ISBN 0065-2717.

[196] A. Stankiewicz and G. Eigenberger. Dynamic modeling of multi-tubular catalytic reactors. *Chem. Eng. Technol.*, 14:414–420, 1991.

[197] C.K.R. Depoorter. A comprehensive mechanism for the fischer tropsch synthesis. *Chem. Rev.*, 81:447–474, 1981.

[198] P. Sadhukhan and E. E. Petersen. Oxidation of naphthalene in packed-bed reactor with catalyst activity profile: A design scheme for improved reactor stability and higher product yield. *AIChE Journal*, 22(4):808, 1976. ISSN 00011541.

[199] M. Hillestad. A systematic generation of reactor designs: I. isothermal conditions. *Computers and Chemical Engineering*, 28:2717–2726, 2004. ISSN 0098-1354.

[200] M. Hillestad. A systematic generation of reactor designs: II. non-isothermal conditions. *Computers and Chemical Engineering*, 29:1101–1112, 2005. ISSN 0098-1354.

[201] M. Hillestad. Systematic staging in chemical reactor design. *Chemical Engineering Science*, 65:3301–3312, 2010. ISSN 0009-2509.

[202] D. Glasser, D. Hildebrandt, and C. Crowe. A geometric approach to steady flow reactors: The attainable region and optimization in concentration space. *Industrial & Engineering Chemistry Research*, 26:1803–1810, 1987. ISSN 08885885.

[203] D. Hildebrandt and D. Glasser. The attainable region and optimal reactor structures. *Chemical Engineering Science*, 45(8):2161–2168, 1990. ISSN 00092509.

[204] M. Feinberg and D. Hildebrandt. Optimal reactor design from a geometric viewpoint: I. universal properties of the attainable region. *Chemical Engineering Science*, 52(10):1637–1665, 1997. ISSN 00092509.

[205] M. Feinberg. Optimal reactor design from a geometric viewpoint: Part II. critical sidestream reactors. *Chemical Engineering Science*, 55:2455–2479, 2000. ISSN 0009-2509.

[206] C. Lee and A. Varma. *An isothermal fixed bed reactor with non uniformly active catcatalysts: Experiments and theory*, pages 1995–2000. Pergamon, 1988. ISBN 978-0-08-036969-3.

[207] S. Melis, A. Varma, and C. J. Pereira. Optimal distribution of catalyst for a case involving heterogeneous and homogeneous reactions. *Chemical Engineering Science*, 52(2):165–169, 1997. ISSN 00092509.

[208] V. M. Khanaev, E. S. Borisova, and A. S. Noskov. Optimization of the active component distribution through the catalyst bed. *Chemical Engineering Science*, 59:1213–1220, 2004. ISSN 0009-2509.

[209] S. Hwang and R. Smith. Heterogeneous catalytic reactor design with optimum temperature profile i: Application of catalyst dilution and side-stream distribution. *Chemical Engineering Science*, 59(20):4229–4243, 2004. ISSN 0009-2509.

[210] P. Hwang, S.and Linke and R. Smith. Heterogeneous catalytic reactor design with optimum temperature profile II: Application of non-uniform catalyst. *Chemical Engineering Science*, 59(20):4245–4260, 2004. ISSN 0009-2509.

[211] S. Hwang and R. Smith. Optimum reactor design in methanation processes with non uniform catalysts. *Chem. Eng. Commun.*, 196:616–642, 2008.

[212] J. Cuthrell and L. Biegler. On the optimization of differential algebraic process systems. *AIChE J.*, 33(1257-1270), 1987.

[213] P.E. Gill, W. Murray, and M.A. Saunders. SNOPT: An SQP algorithm for large scale constrained optimisation. *SIAM Review*, 47(1):99–131, 2005.

[214] P.E. Gill, W. Murray, and M.A. Saunders. User's guide for SNOPT version 7: Software for large scale nonlinear programming. Systems Optimization Laboratory (SOL), Stanford University 2006.

[215] COMSOL Multiphysics Optimization user's guide (version 4.4). 2013.

[216] R.H. Perry. *Perry's chemical engineers' handbook.* McGraw-Hill New York, 8 edition, 2008. ISBN 0071593136 9780071593137.

[217] R.C. Reid, J.M. Prausnitz, and B.E. Poling. *The properties of gases and liquids.* McGraw, New York, 5th edition, 1988.

[218] C.L. Yaws. *Yaw's handbook of thermodynamic and physical properties of chemical compounds.* Knovel, 2003.

[219] A.L. Lydersen. *Fluid flow and heat transfer.* John Wiley & Sons, New York, 1979.

[220] J. Xu and G.F. Froment. Methane steam reforming, methanation and water gas shift II: Diffusional limitations and reactor simulations. *AIChE Journal*, 35:97–103, 1989.

Appendix A

Constitutive equations and correlation of physical properties

TABLE A.1: Correlations of physical properties

Parameters	**Equation**	**Reference**
Component heat capacity	$c_{\mathrm{p},j} = c_1 + c_2 \left[\frac{\left(\frac{c_3}{T}\right)}{\sinh\left(\frac{c_3}{T}\right)}\right]^2 + c_4 \left[\frac{\left(\frac{c_5}{T}\right)}{\cosh\left(\frac{c_5}{T}\right)}\right]^2$	[216]
Mixture heat capacity	$c_{\mathrm{p,f}} = \sum_{j=1}^{N_j} (y_j \times c_{\mathrm{p},j})$	-
Component thermal conductivity	$\kappa_j = A_{j1} + B_{j2}T + C_{j3}T^2 + D_{j3}T^3$	[217, 218]
Mixture thermal conductivity	$\kappa_{\mathrm{f}} = \sum_{j=1}^{N_j} (y_j \times \kappa_j)$	-
Component viscosity	$\mu_j = \frac{c_1 T^{c_2}}{1 + \left(\frac{c_3}{T}\right) + \left(\frac{c_4}{T^2}\right)}$	[216, 218, 219]
Mixture viscosity	$\mu_{\mathrm{f}} = \sum_{j=1}^{N_j} (y_j \times \mu_j)$	-
Average molecular weight	$MW_{\mathrm{av}} = \sum_{j=1}^{N_j} (y_j \times MW_j)$	-
Reaction enthalpy	$\Delta H_{\mathrm{r}}(T) = \Delta H^{\theta}_{298\mathrm{K}} + \int_{298\mathrm{K}}^{T} c_{\mathrm{p,av}}\,\mathrm{d}T - \Delta H_{\mathrm{vap}}$	-
Void to void radiation coefficient	$\alpha_{\mathrm{rv}} = \frac{0.227 \times 10^{-3}}{\left(1 + \frac{\epsilon}{2(1-\epsilon)} \frac{1-\lambda_{em}}{\lambda_{em}}\right)} \left(\frac{T + 273.15}{100}\right)^3$	[114, 220]
Catalyst radiation coefficient	$\alpha_{\mathrm{rs}} = 0.227 \times 10^{-3} \frac{\lambda_{em}}{2 - \lambda_{em}} \left(\frac{T + 273.15}{100}\right)^3$	[114, 220]
Static radial thermal conductivity	$\kappa^0_{\mathrm{eff,r}} = \kappa_{\mathrm{f}} \left[\epsilon \left(1 + \beta \frac{d_{\mathrm{p}}\,\alpha_{\mathrm{rv}}}{\kappa_{\mathrm{f}}}\right) + \frac{\beta(1-\epsilon)}{\left(\frac{1}{\Phi} + \frac{\alpha_{\mathrm{rs}}\,d_{\mathrm{p}}}{\kappa_{\mathrm{f}}}\right)} + \gamma \frac{\kappa_{\mathrm{f}}}{\kappa_{\mathrm{s}}}\right]$	[114, 220]
Effective radial thermal conductivity	$\kappa_{\mathrm{eff,r}} = \kappa^0_{\mathrm{eff,r}} + 0.14\,\kappa_{\mathrm{f}}\,Re_{\mathrm{p}}\,Pr$	[114, 220]